Quantitative Scanning Transmission Electron Microscopy for III-V Semiconductor Heterostructures Utilizing Multi-Slice Image Simulations

Dissertation

zur
Erlangung des Doktorgrades
der Naturwissenschaften
(Dr. rer. nat.)

dem

Fachbereich Physik
der Philipps-Universität Marburg

vorgelegt von

Pirmin Kükelhan, M.Sc.

aus

Minden (Westf.)

Marburg (Lahn), 2019

Vom Fachbereich Physik der Philipps-Universität Marburg
als Dissertation angenommen am: 01.07.2019
Erstgutachterin: Prof. Dr. Kerstin Volz
Zweitgutachter: Prof. Dr. Wolfram Heimbrodt
Tag der mündlichen Prüfung: 22.08.2019
Hochschulkennziffer: 1180

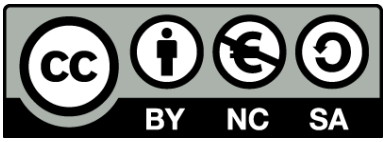

Contents

1 Introduction

Modern semiconductor devices play an important role in everyday life. Particularly, III-V semiconductors have a large variety of applications due to advantageous material properties. These applications include transistors, photo diodes, solar cells, scintillators, light emitting diodes and lasers. Ongoing research and development aims for further improvements of device performance. For these improvements, an efficient interplay of theoretical predictions of material properties, growth of the actual devices and their characterization - in particular structural characterization - is important.

The size of modern devices is continuously decreasing leading to more compact devices and possibly new functionalities. Consequently, there is a demand for structural characterization at atomic scale. This can be provided by transmission electron microscopy (TEM). In particular, annular dark field scanning transmission electron microscopy (ADF-STEM) enables directly interpretable atomic resolution imaging [1, 2, 3]. The images provide dominant atomic-number contrast [4, 5, 6] and are therefore sensitive to both thickness and composition of the specimen. Advances in electron optics and aberration correction further improve the attainable resolution [7, 8, 9, 10].

With this, quantitative characterization at atomic scale is possible. The goal is to locate, count and distinguish atoms in nano-structures [11]. Locating atoms is possible with very high precision [12, 13]. For counting and distinguishing atoms by ADF-STEM, there are two main approaches.

One is based on statistical parameter estimation theory [14] that was also applied to TEM [15, 16] and electron energy loss spectroscopy [17] before. Within this framework, accurate atom counting is possible [18, 19]. Combining the approach with image simulations, the accuracy is increased [20]. Composition determination on a relative scale is possible [14] and through combination with simulations it can be brought to an absolute scale [21]. The recently proposed atomic lensing model can also be used for composition determination [22, 23].

The other main approach that is followed in this work is the comparison of experimental and simulated ADF-STEM results. To allow this comparison, first scaling of experimental data was necessary [24, 25, 26, 27]. Then, the normalization of experimental data on an

absolute scale enabled the direct comparison [28, 29]. Now, there are several additional methods for a normalization of the experimental intensity [30, 31, 32, 33, 34]. Hence, composition determination [30, 35] as well as atom counting [36] by direct comparison of experiment and simulation is possible. For this direct comparison, accurate image simulations are needed. They have to model the electron probe, the specimen, the electron probe-specimen interaction and the detector characteristics precisely. Image simulations are mainly based on the Bloch-wave approach [2, 3] or the multi-slice algorithm [37, 38] that is used in this work. Considering all parameters correspondingly, excellent modeling is possible [11].

In particular, for ternary III-V semiconductors composition determination was conducted in this way [30, 35, 39, 40, 41]. This established method is enhanced in this work to explore the capabilities of single-atom accuracy (cf. section 4.2). Atomic level investigations of growth mechanisms like surface segregation are possible (cf. section 4.3). It is found that for accurate composition determination the thickness has to be known very precisely. Therefore, a method is developed to truly determine thickness and composition locally from a single ADF-STEM image of ternary III-V semiconductors (cf. section 4.4). For quaternary III-V semiconductors which also become important technologically, usually several methods [42, 43, 44] or several ADF-STEM images [45] are combined to determine the composition. In this work, a method is shown to determine the composition of a quaternary III-V semiconductor with two elements on each sub lattice from a single ADF-STEM image (cf. section 4.5).

To present these results in a comprehensive way, the first properties of III-V semiconductors (chapter 2) and the principles of STEM (chapter 3) are introduced. Then, the results that are shown in original published and submitted manuscripts in chapter 6 are summarized (chapter 4). Conclusions of the work are drawn in chapter 5.

2 III-V Semiconductors

In this chapter, the interest in III-V semiconductors and their quantitative characterization is motivated through their material properties. These material properties make III-V semiconductors technologically highly relevant and lead to a large variety of applications. First, the crystal structure which is investigated by STEM is introduced in section 2.1. Then, the band structure (section 2.2) and consequential optical properties (section 2.3) that are very important for applications are discussed. How crystal structure and band structure behave in heterostructures, is explained in section 2.4. Additionally, there is a short introduction of the heterostructures investigated in this work. Finally, growth of these heterostructures by MOVPE (section 2.5) and structural characterization by X-ray diffraction (section 2.6) are considered. Sections 2.1 to 2.4 are based on [46]. Section 2.5 is based on [47, 48] and section 2.6 on [49].

2.1 Crystal Structure

All III-V semiconductors investigated in this work are present in a crystalline structure. Hence, they consist of identical building blocks that are repeating periodically. The crystal structure of the III-V semiconductors investigated in this work is the so-called zinc blende structure. This is a face centered cubic (fcc) lattice with a diatomic base. There are two sub lattices that are shifted by a quarter of the fcc lattice diagonal. One sub lattice consists only of group III elements while the other sub lattice consists only of group V atoms. All atoms are tetrahedrally coordinated. The cubic unit cell of the III-V zinc blende structure is shown in Fig. 2.1(a). Here, group III atoms are depicted in blue, group V atoms in red.

All STEM investigations performed in this work show a projection of the crystal structure along [010]-direction. The resulting projection is shown in Fig. 2.1(b). Group III atomic columns are depicted in blue, group V atomic columns in red.

If different III-V semiconductors are mixed, the formation of random alloys, super lattices with periodically ordered structures and clusters due to non-miscibility is possible. The materials investigated in this work form random alloys but may show some degree

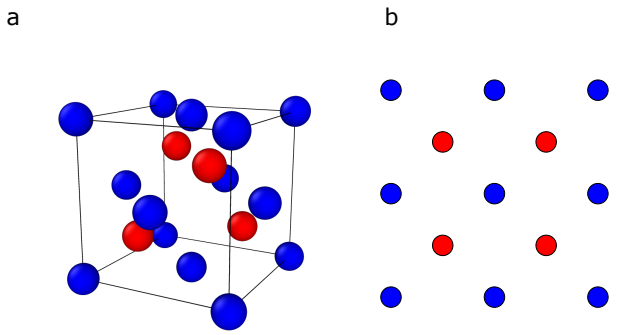

Figure 2.1: (a) Cubic unit cell of III-V zinc blende structure generated with [50] and (b) projection along [010]-direction. Group III atoms and atomic columns are depicted in blue, group V atoms and atomic columns in red.

of clustering. Investigated alloys are ternary and quaternary. In ternary alloys, mixing of two elements occurs on one sub lattice while in quaternary alloys mixing can either occur on one sub lattice with three different elements or on both sub lattices with two elements each. To identify properties of alloys, in the virtual crystal approximation properties are determined with pseudo-atoms that have linearly interpolated properties. With Vegard's law, for the lattice constant of a ternary material this yields

$$a_{A_xB_{1-x}C} = x a_{AC} + (1-x)\, a_{BC}. \tag{2.1}$$

Here, the material ABC is assumed to consist out of material AC with fraction x and material BC with fraction $1-x$.

In reality, the atoms in the crystal are displaced from their average position and lattice deformation takes place on a nanoscopic scale. These deformations are called static atomic displacements.

2.2 Band Structure

The band structure is determined by the periodic arrangement of the atoms and their atomic number. The band with the highest energy that is fully filled at a temperature $T = 0\,\mathrm{K}$ is the valence band, while the first empty band is the conduction band. The difference in energy between both bands is the band gap energy E_g. Usually, the maximum of the valence band is at the Γ-point in k-space. If the minimum of the conduction band is at the same k-vector, a direct band gap is present. Otherwise, the band gap is

called indirect. *GaAs* on which the materials investigated in this work are based has a direct band gap.

In alloys, size and character of the band gap depend on the composition. The dependence is non-linear and can be expressed with the bowing parameter b as

$$E_g\left(A_xB_{1-x}C\right) = E_g\left(BC\right) + x\left[E_g\left(AC\right) - E_g\left(BC\right)\right] - bx\left(1-x\right). \tag{2.2}$$

In certain cases, instead the valence band anti-crossing model is suitable [51].

General influences on the band gap are: volume deformation of the band structure with the lattice constant where generally the band gap decreases with increasing lattice constant, charge exchange in the alloy where the band gap increases with increasing ionicity, relaxation of the cation anion bond lengths and disorder. Depending on the composition in the alloy, a transition between a direct band gap and an indirect band gap is possible.

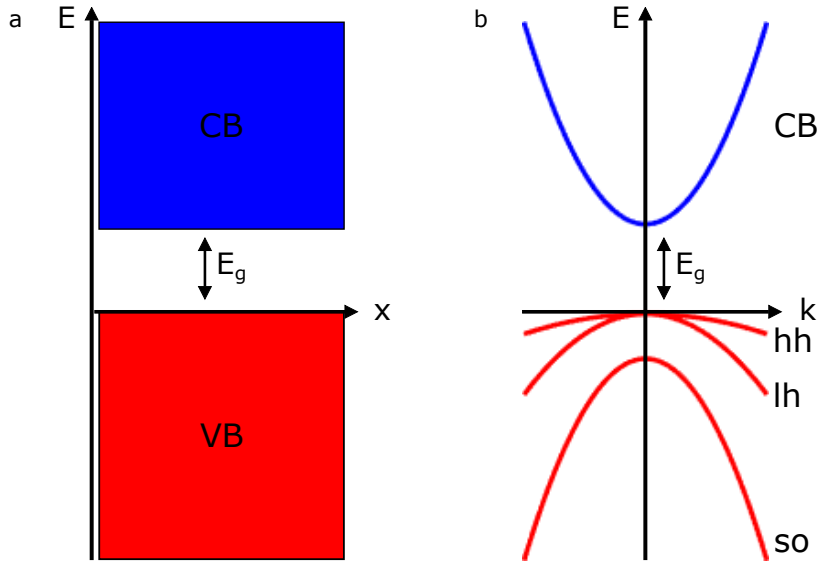

Figure 2.2: Band structure of direct III-V semiconductor in real (a) and reciprocal space (b). The formation of conduction band (CB) and valence band (VB) is shown in real space with band gap E_G. In reciprocal space, the splitting of the valence band into heavy hole band (hh), light hole band (lh) and split-off band (so) is depicted.

The valence band is 3-fold degenerate at the Γ-point where spin-orbit coupling leads to the formation of a heavy hole, a light hole and a split-off hole band.

Other influences on the band gap are temperature and strain. With increasing temperature, the band gap decreases. Strain changes the bond length and thus is also changing

the band gap. Here, compressive strain lifts the heavy hole band above the light hole and tensile strain leads to a strong mixing of bands.

2.3 Optical Properties

If III-V semiconductors are interacting with light, reflection, transmission and absorption are possible. During absorption, energy is transferred from the electric field to the semiconductor. In the absorption spectrum, transitions between valence band and conduction band, interaction with excitons which are bound electron hole pairs, valence band-donor and conduction band-acceptor transitions, phonon interaction, impurities to band edge transitions and a background due to free-carrier absorption show up. In direct semiconductors, a rapid increase in absorption is found in vicinity of the band gap. In indirect semiconductors, the necessary momentum transfer is provided by phonons which leads to a change in absorption energy.

Absorption of light and carrier injection can lead to excess carriers that then relax into energetically lower states. Most important is the transition from conduction band to valence band which for a direct band gap is an optical transition and for an indirect band gap is phonon-assisted. These transitions can be caused by spontaneous emission, absorption and stimulated emission provoked by an incoming photon. Additionally, the recombination of bound excitons, impurity recombinations and recombinations at defects like surfaces, grain boundaries and dislocations are possible.

In contrast to radiative recombination where a photon is released, Auger recombination is non-radiative. The energy due to the recombination is transferred to a third particle like an electron or hole and can eventually be released as a phonon. Auger recombination is likely for high carrier density or a small band gap.

Their optical properties allow an application of III-V semiconductors in devices for light-to-electricity conversion like photo diodes and solar cells or for electricity-to-light conversion like scintillators, light emitting diodes and lasers.

2.4 Heterostructures

Heterostructures consist of at least two different materials. The heterostructures investigated in this work are pseudomorphic, i.e. the lattice constant perpendicular to the growth direction remains constant. If for the epitaxial layer the lattice constant parallel to the growth direction is decreased, the layer is compressively strained. If the lattice constant parallel to the growth direction is increased, tensile strain is present. Tetragonal

distortion is caused in both cases. The possible mismatch in lattice constants between the materials and strain building up leads to a critical layer thickness, i.e. width in cross-sectional TEM perspective, above which plastic relaxation occurs and defects arise.

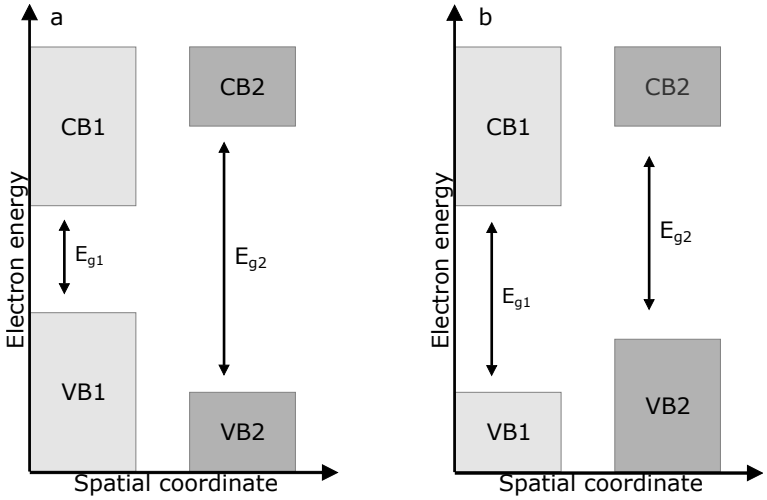

Figure 2.3: Type-I (a) and type-II band alignment (b). In a type-I band alignment, the highest valence band and the lowest conduction band are present in one material. In a type-II band alignment, they are present in different materials.

The motivation for heterostructures is the combination of materials with different band gaps and therefore the possibility of band gap engineering. In a type-I band alignment, the highest valence band and the lowest conduction band are both present in the same material so that electrons and holes are both localized in this material. In a type-II band alignment, the highest valence band and the lowest conduction band are present in different materials. Hence, electrons and holes are localized in different materials and have to recombine across the interface. Both band alignments are shown schematically in Fig. 2.3.

A quantum well (QW) is built of a thin layer of one material with smaller band gap between barriers of a second material with larger band gap. The wave function of the carriers is mostly localized in the QW but there is also tunneling into the barrier. In plane, the carriers are free. There is a thickness, i.e. width in cross-sectional TEM perspective, dependent blue shift of the recombination energy due to excitons.

The heterostructures investigated in this work are presented in Table 2.1. These are mainly QW heterostructures (QWHs) and, additionally, one multi QWH. This is *GaAs/(GaIn)As/Ga(AsSb)/(GaIn)As/GaAs*. Type-II laser application in the infrared wave length regime at 1.3 μm was demonstrated successfully for this structure [52]. Type-

$GaAs/(GaIn)As/GaAs$
$GaAs/Ga(AsSb)/GaAs$
$GaAs/Ga(AsBi)/GaAs$
$GaAs/(GaIn)(AsBi)/GaAs$
$GaP/Ga(PAs)/GaP$
$Si_{0.2}Ge_{0.8}/Si_{1-x}Ge_x/Si_{0.2}Ge_{0.8}$
$GaAs/(GaIn)As/Ga(AsSb)/(GaIn)As/GaAs$

Table 2.1: Heterostructures investigated in this work.

II band alignment suppresses Auger losses that would be prominently present in type-I band alignment due to the long wave length [53, 54]. The "W"-QWH design (cf. Fig. 2.4) allows sufficient overlap of the wave functions in the type-II system as a hole QW is embedded between two electron QWs [55, 56]. The name "W" resembles the resulting band structure of the QWH.

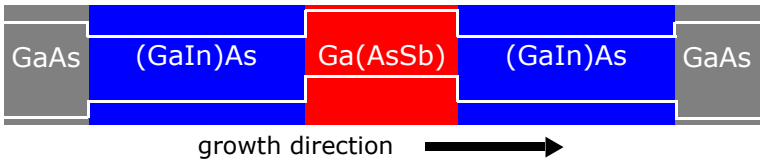

Figure 2.4: Structure of "W"-QWH. The different materials are shown. In addition, the band structure with valence and conduction band is presented (white).

2.5 Growth by Metal Organic Vapor Phase Epitaxy

The III-V semiconductor heterostructures investigated in this work are grown by metal-organic vapor phase epitaxy (MOVPE). The name follows from the metalorganic precursors that are used for the process. These precursor molecules contain the group III and group V atoms. The precursor molecules are diluted in a carrier gas which typically is H_2 to be transported to the heated substrate surface (several hundreds °C). The MOVPE process is far from thermodynamic equilibrium. Thus, decomposition and deposition are caused.

Thereby, the process carries out as follows (cf. Fig. 2.5): The precursor molecules are transported to the substrate and decompose due to the high temperature. Group III and group V elements are adsorbed and diffuse on the surface to be incorporated into the crystal. Excess group III and group V atoms not incorporated and organic molecules are transported to the exhaust system.

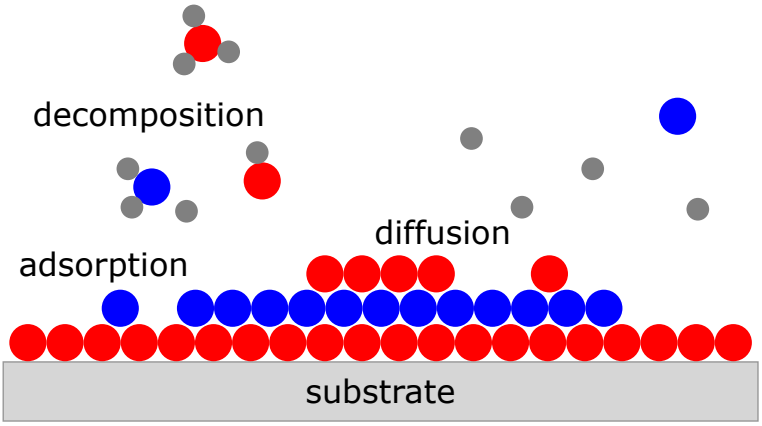

Figure 2.5: Important processes during MOVPE. Group III atoms are shown in blue, group V atoms in red and organic molecules in gray (not to scale).

Depending on the temperature, there are three growth regimes. At low temperatures, growth is thermally activated and the growth rate increases with temperature. In an intermediate temperature range, the growth rate is independent of temperature and controlled by mass transport (diffusion). At high temperatures, the growth rate decreases again due to adsorption and enhanced parasitic prereactions.

Mostly, MOVPE is performed in the mass transport-limited temperature regime. Typically, the diffusion of group III elements and therefore their supply is the limiting factor here. Hence, the V/III ratio is important to control the growth.

Following precursor molecules are used for the growth of the investigated heterostructures: triethylgallium and trimethylindium as group III precursors and tertiarybutyarsine, triethylantimony, trimethylbismuth and tributylphosphat as group V precursors.

2.6 Structural Characterization by X-Ray Diffraction

X-ray diffraction (XRD) can be used for a structural characterization of III-V semiconductor heterostructures. Box-like one-dimensional concentration profiles without atomic resolution can be obtained in contrast to two-dimensional atomic resolution composition information attainable by STEM.

In XRD, the lattice constant parallel to the growth direction is probed. As discussed in section 2.4, the lattice constant parallel to the growth direction is changed due to compressive and tensile strain depending on the material grown. Scattering incident X-rays at the specimen leads to constructive and destructive interference. Constructive interference occurs if the path length difference between X-rays scattered from two atoms

is a multiple of the X-ray wavelength λ_X. This can be expressed by Bragg's law

$$2d \sin(\Theta) = n\lambda_X, \tag{2.3}$$

with distance d between the lattice planes, incident angle Θ and natural number n.

Typically, the reflex belonging to the (004) lattice planes is probed due to its high intensity. By measuring the angle dependent diffracted intensity, information about the distance of the (004) lattice planes in the epitaxial layer and the layer width in multi QW structures can be gained. The distance of the lattice planes leads to the lattice constant for cubic crystal structures

$$a = d\sqrt{h^2 + k^2 + l^2}, \tag{2.4}$$

with Miller indices h, k and l. Tetragonal distortion can be considered by

$$\frac{a' - a_0}{a_0} = \frac{C_{11}}{C_{11} + 2C_{12}} \frac{a - a_0}{a_0} \tag{2.5}$$

to determine the relaxed lattice constant a' from the tetragonally distorted one a that is measured. Here, a_0 is the lattice constant of the substrate and C_{11} and C_{12} are elastic constants. With Vegard's law, the composition can be determined.

3 Scanning Transmission Electron Microscopy

In this chapter, the basic principles of STEM and in particular ADF-STEM are explained. Therefore, after a first introduction (section 3.1) there are remarks about specimen preparation in section 3.2. The interaction of the electron probe and the specimen is discussed in section 3.3. Then, the design of a scanning transmission electron microscope (section 3.4) that is necessary to gain information from this interaction is outlined. Image aberrations (section 3.5) and their corrections (section 3.6) are explained since they strongly influence the imaging process as discussed in section 3.7. Characteristics of ADF imaging are examined in section 3.8. Finally, the principles of multi-slice image simulations (section 3.9) and concepts for the modeling of electron probe, specimen and detector (section 3.10) are presented.

3.1 Introduction to Scanning Transmission Electron Microscopy

STEM emerged as a powerful tool to gain atomic-scale information about nano-materials. In STEM, a high energy convergent electron probe that is a demagnified image of the electron source is focused on the specimen. By scanning the electron probe over the sample, an image can be formed. At every scan position, the electron probe is interacting with the specimen. Electrons are scattered elastically and in-elastically giving rise to a large variety of signals that can form an image by detecting them for every scan position. In the far field behind the specimen, the scattered electrons form a convergent beam electron diffraction (CBED) pattern. The appearance of this CBED pattern is determined by the lattice spacing of the (crystalline) specimen and the convergence angle [57].

This work focuses on electrons scattered into large angles and detected by an annular detector, i.e. annular dark field (ADF) imaging. This is discussed in detail in section 3.8. Other available imaging modes include but are not limited to bright field imaging, nano-

diffraction, electron energy loss spectroscopy and energy dispersive X-ray spectroscopy [58]. Imaging modes can also be used simultaneously to gain complementary information about the investigated specimen.

In general, the resolution of STEM images is determined by the size of the electron probe and its convergence angle given by an aperture. Hence, the formation of the electron probe is crucial for STEM and aberration correction plays an important role to enhance its capabilities.

3.2 Specimen Preparation

For investigation by STEM, specimens have to be thin enough to be electron transparent. Quantitative STEM may have even higher restrictions for the specimen thickness. Next to thickness restrictions, it is necessary to limit surface defects, e.g. amorphous layers induced during specimen preparation and oxide layers.

All specimens in this work are prepared in cross-sectional view in [010]-direction. Two different ways of specimen preparation are performed.

One is based on conventional grinding and polishing [59] conducted with the help of a MultiPrep (Allied High Tech Products, Inc., Rancho Dominguez, CA, United States). Final thicknesses are reached by single-sector Ar ion milling [60] that is used trying to limit the resulting thickness gradient of the specimen. For this, a precision ion polishing system (model 691, Gatan Inc., Pleasanton, CA, United States) is used with ion energies of 5 keV to 1.2 keV. From this preparation procedure, amorphous layers with a thickness of 3.5 nm result for $GaAs$ based materials [61].

To further limit these amorphous layers and the thickness gradient of the specimen, specimen preparation is also performed in a different manner. Ga ion milling is performed with a dual beam scanning electron microscope focused ion beam machine (JEOL JIB-4601F, JEOL Ltd., Tokyo, Japan) with ion energies of 30 keV to 10 keV [62]. Afterwards, the specimen is further thinned using Ar ion milling and polishing with voltages of 900 V to 250 V. For this, a NanoMill (model 1040, E. A. Fischione Instruments, Inc., Export, PA, United States) is employed [63]. The lower ion energy limits surface damage.

3.3 Interaction of Electron Probe and Specimen

In the following, the interaction of electron probe and specimen is discussed using dynamical diffraction based on [3, 64, 65].

The electron probe has a high energy due to high acceleration voltage and therefore has to be treated relativisticly. For the wavelength of the electrons, this leads to

$$\lambda = \frac{hc}{\sqrt{eU\left(2m_0c^2 + eU\right)}}, \tag{3.1}$$

with the acceleration voltage U, electron charge e and mass m_0, velocity of light c and Planck's constant h. Relativistic effects would demand for the Dirac equation to handle the electron wave function. However, it is accepted to use the Schrodinger equation with relativistic wavelength and mass which is ignoring the electron spin. During the interaction of electron probe and specimen, the effect of the magnetic field of the objective lens is neglected [64]. The Schrodinger equation for the electron wave function in the electrostatic potential of the specimen $V\left(\mathbf{R}, z\right)$ is

$$\left[-\frac{\hbar^2}{2m}\nabla^2 - eV\left(\mathbf{R}, z\right)\right]\Psi\left(\mathbf{R}, z\right) = E\Psi\left(\mathbf{R}, z\right). \tag{3.2}$$

Here, m is the relativistic electron mass, E is the energy of the electron wave and z is parallel to the optical axis while $\mathbf{R}$ is the transverse component.

The specimen is assumed to be crystalline and thus to have a periodic potential. In the Bloch wave formulation, the Schrodinger equation can be solved by Bloch waves

$$\Phi\left(\mathbf{r}\right) = \sum_g \Phi_g \exp\left[-2\pi i\left(\mathbf{k} + \mathbf{g}\right)\cdot\mathbf{r}\right], \tag{3.3}$$

with reciprocal lattice vector $\mathbf{g}$ and wave vector $\mathbf{k} = (\mathbf{K}, k_z)$.

In STEM, the illuminating probe is a cone that is a sum of partial plane-waves. The probe wave function can be given as

$$\Psi_P = \int A\left(\mathbf{K_i}\right)\exp\left[-2\pi i\mathbf{K_i}\cdot\mathbf{R} + 2\pi i\mathbf{K_i}\cdot\mathbf{R_0}\right]d\mathbf{K_i}, \tag{3.4}$$

with the probe location vector $\mathbf{R_0}$, the incident transverse wave vector $\mathbf{K_i}$ and the aperture function $A\left(\mathbf{K_i}\right)$. The aperture function depends on the size of the aperture and the lens aberrations. The influence of lens aberrations is discussed in detail in sections 3.5 and 3.6. The wave function within the crystal is then given as an integration over all incident plane waves and a sum of many Bloch states as

$$\Psi\left(\mathbf{R}, z, \mathbf{R_0}\right) = \int \sum_j \sum_g A\left(\mathbf{K_i}\right) \bar{\Phi}_0^{(j)}\left(\mathbf{K_i}\right) \Phi_{\mathbf{g}}^{(j)}\left(\mathbf{K_i}\right) \times \exp\left\{-2\pi i \left[\left(\mathbf{K_i} + \mathbf{g}\right) \cdot R - \mathbf{K_i} \cdot \mathbf{R_0} + k_z^{(j)}\left(\mathbf{K_i}\right) z\right]\right\} d\mathbf{K_i}. \tag{3.5}$$

Thereby, $\Phi_0^{(j)}\left(\mathbf{K_i}\right)$ is the amplitude of excitation of the j-th Bloch state for an incoming plane wave. The different Bloch states have different propagation speed inside the crystal which leads to constructive and destructive interference. The electron wave inside the specimen depends on both probe position and depth in the crystal. In a physical interpretation, this is connected to local phase shifts of the wavefront. Disruptions in the periodicity of the crystal such as thermal diffuse scattering (cf. section 3.8) lead to scattering away from the Bloch states.

An important feature of dynamical diffraction is the channeling effect. In a specimen aligned along a zone axis, the atomic columns act as channel for the wave function that oscillates periodically with depth [66]. This is caused by the more attractive potential of the atomic column than in interstitial regions that confines the electron wave. Due to the more attractive potential, the wave length is shorter in the atomic column than in the interstitial region. In an optical fiber analogy, the index of refraction is inversely proportional to the wavelength which then leads to reflection at the interface between atomic column and interstitial region and hence a confinement of the electron wave.

3.4 Design of a Scanning Transmission Electron Microscope

To enable information gain from the interaction of electron probe and specimen, the design of a state-of-the-art scanning transmission electron microscope consists of several parts: an electron source, a condenser lens system, a condenser aperture, an aberration corrector, scan coils, an objective lens, the specimen holder and at least one detector. In the following, the specific design of the microscope used in this work is described. This microscope is an aberration-corrected JEOL JEM-2200FS (JEOL Ltd., Tokyo, Japan).

Commonly, in the electron microscope round electromagnetic lenses are used. Round electromagnetic lenses are built of a wound coil that creates a magnetic field by passing a current. A pole piece can enhance the resulting magnetic field while the current is determining the focusing power. The force that an electron feels within the lens is according to the Lorentz force

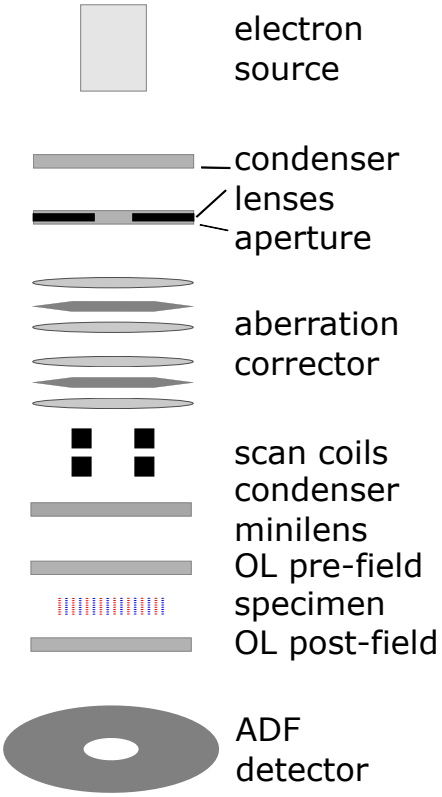

Figure 3.1: Design of a scanning transmission electron microscope. The representation is limited to the most important optical elements. These are further discussed in the main text.

$$F = -e\left(\mathbf{E} + \mathbf{v} \times \mathbf{B}\right), \tag{3.6}$$

with the electron charge e, the electric field $\mathbf{E}$, the electron velocity $\mathbf{v}$ and the magnetic field $\mathbf{B}$. The electric field is zero for a purely magnetic lens and the magnetic field causes electrons at an angle to the optical axis to spiral around the optical axis. If the field changes along the optical axis, a focusing effect can be achieved [58]. However, this comes along with various image aberrations that are discussed in detail in section 3.5.

As an electron source, a Schottky emitter is used. This offers a high brightness of the electron beam that fundamentally determines the noise level of the images acquired [58]. A single crystal tungsten tip is warmed while also applying an extraction voltage with the help of a first anode. Warming lowers the work function that is required to overcome for electron extraction. A second anode accelerates the electrons with the desired voltage that is 200 kV in the case of this work. Both anodes together yield a field that produces

a cross-over after the electron gun [67].

The condenser lens system is using this cross-over and forms an image of the gun cross-over that has the necessary size for probing the specimen, i.e. it demagnifies the electron source. Additionally, one can independently change the probe convergence angle. The image of the gun cross-over has to be at a fixed plane in front of the corrector system [58]. To fulfill these requirements, at least three independent condenser lenses are necessary [68]. In a simplistic picture, the first condenser lens is defining the current in the probe and the second and third condenser lens together are controlling probe convergence angle and spot size [58]. The condenser aperture is eventually defining the convergence angle of the electron probe.

For the microscope at hand, the aberration corrector is based on a combination of two extended hexapole fields. Its principles are described in detail in section 3.6.

The scan coils consist of a set of double deflection coils that scan the electron probe by magnetic deflection. The ratio of the deflection of the upper and lower coils is set in a way such that the axial ray is crossing the optical axis at the focal point of the objective lens [58]. The pre-field of the objective lens (OL) is then focusing the electron probe on the specimen.

After interaction with the specimen, scattered electrons are detected by an annular detector for ADF imaging. The detection angles of this detector can be set by means of the camera length, i.e. the effective distance between specimen and detector. The detector is based on a scintillator/photomultiplier combination.

3.5 Image Aberrations

Image aberrations of the electromagnetic lenses influence the probe formation. An image aberration in the image plane is defined based on Gaussian optics: It is the distance between the location where the Gaussian ray intersects the Gaussian image plane and the location where the aberrated ray is intersecting the Gaussian image plane. In the aperture plane, a wave aberration is defined as the deviation between the aberrated wave and a spherical wave that is brought to a point focus for an infinitely small wavelength. Descriptions in this section are based on [57] and [58].

In the following, coherent and incoherent aberrations will be discussed. Coherent aberrations are the inherent geometric aberrations of an electromagnetic lens. In contrast to that, chromatic aberrations are incoherent. Parasitic aberrations can be both coherent and incoherent. While geometric aberrations limit the resolution of an image, chromatic aberrations restrict the information transfer.

The deviation between a wave affected by geometric aberrations and a spherical wave can be described by the wave aberration function χ. Geometric aberrations are symmetry permitted for round electromagnetic lenses. Considering only axial aberrations, χ can be written as an expansion of the position in the aperture plane ω up to fifth order as

$$\begin{aligned}\chi(\omega) = \mathbb{R}\{&A_0\bar{\omega} + \frac{1}{2}C_1\omega\bar{\omega} + \frac{1}{2}A_1\bar{\omega}^2 + B_2\omega^2\bar{\omega} + \frac{1}{3}A_2\bar{\omega}^3 \\ &+\frac{1}{4}C_3(\omega\bar{\omega})^2 + S_3\omega^3\bar{\omega} + \frac{1}{4}A_3\bar{\omega}^4 \\ &+B_4\omega^3\bar{\omega}^2 + D_4\omega^4\bar{\omega} + \frac{1}{5}A_4\bar{\omega}^5 \\ &+\frac{1}{6}C_5(\omega\bar{\omega})^3 + S_5\omega^4\bar{\omega}^2 + R_5\omega^5\bar{\omega} + \frac{1}{6}A_5\bar{\omega}^6\}. \end{aligned} \tag{3.7}$$

The expansion coefficients are the aberration coefficients of the geometric axial aberrations that are summarized in Table 3.1. Their order that refers to the image aberration is given by the respective subscript.

Aberration	Symbol	Symmetry N
Beam/Image shift	A_0	1
Defocus	C_1	0
Twofold astigmatism	A_1	2
Second-order axial coma	B_2	1
Threefold astigmatism	A_2	3
Third-order spherical aberration	C_3	0
Third-order star aberration	S_3	2
Fourfold astigmatism	A_3	4
Fourth-order axial coma	B_4	1
Fourth-order three-lobe astigmatism	D_4	3
Fivefold astigmatism	A_4	5
Fifth-order spherical aberration	C_5	0
Fifth-order star aberration	S_5	2
Fifth-order rosette aberration	R_5	4
Sixfold astigmatism	A_5	6

Table 3.1: Geometric axial aberrations up to fifth order. Based on [57].

In the following, the most important axial geometric aberrations, i.e. third-order spherical aberration C_3, two- and threefold astigmatism A_1 and A_2 and second-order axial coma B_2, are discussed.

Third-order spherical aberration causes electron rays that are hitting the lens away

from the optical axis to come to focus on a different plane than rays close the optical axis. If the third-order spherical aberration is positive, this focus point is closer to the lens. If it is negative, then it is further away. According to Scherzer's theorem all electromagnetic lenses that are rotationally symmetric, constant in time and charge free have positive third-order spherical aberration [69]. As a consequence, a point in the object plane is imaged as a disk of finite size in the image plane, i.e. the disk of least confusion. The radius of this disk is given as

$$r_s = C_3|\omega|^3. \tag{3.8}$$

A focusing power of the lens that is depending on the azimuthal angle causes astigmatism. For twofold astigmatism, this focusing power differs in two orthogonal directions while for threefold astigmatism it differs in three directions that stand at an angle of 60° to each other. On different focal planes of the lens, line foci result while a disk of least confusion is located between these focus planes.

Coma leads to an aberration figure in the image plane that resembles the shape of a comet. It is caused by non-axial or crooked rays. A disk is imaged as radially displaced circles leading to the characteristic figure.

In addition to these coherent geometric aberrations, there are also incoherent chromatic and parasitic aberrations.

Chromatic aberrations are aberrations where the effect of the lens depends on the electron energy, i.e. the wavelength of the electrons. Differing electron wavelengths result from the electron source itself and from non-constant acceleration voltages. The most prominent chromatic aberration is the axial chromatic aberration C_C which causes the focal point of the lens to change with electron wavelength. In the image plane, a disk of

$$r_C = C_C|\omega|\frac{\delta E}{E_0}. \tag{3.9}$$

results with the nominal electron energy E_0 and a deviation of δE.

While geometric and chromatic aberrations are inherent to ideal round electron lens, parasitic aberrations result from non-ideal round electron lenses. Parasitic aberrations lead to a huge variety of aberrations because no lens is perfectly manufactured. They are caused by mechanical imperfection or inhomogeneities of the materials used. Additionally, mechanical and electrical instabilities can be treated as parasitic aberrations.

3.6 Aberration Correction

The achievable electron probe size in STEM is limited by present aberrations and therefore limiting the possible resolution. Hence, effort is made to be able to correct as many image aberrations as possible. Descriptions in this section are based on [57].

In most scanning transmission electron microscopes, the third-order spherical aberration C_3 of the probe forming system is the decisive aberration limiting the resolution. According to Scherzer's theorem [69], the third-order spherical aberration of the round electromagnetic lenses used is positive. To correct this, it can be made use of the addition theorem stating that geometric aberrations can be added [70]. Hence, one can correct for the positive third-order spherical aberration of the probe forming lenses by adding an optical element with negative third-order spherical aberration. For an optical element with negative third-order spherical aberration, one condition of Scherzer's theorem has to be broken. This can be achieved by using multi-pole lenses that break the rotational symmetry. A multi-pole lens consists of $2m$ magnetic poles under equidistant azimuthal angles where m is a natural number. The polarity of neighboring poles is opposite. The primary effect of such a multi-pole lens is m-fold astigmatism of order $m-1$. Hence, for example a quadrupole lens is inducing twofold astigmatism A_1. Therefore, it can be used as a so called stigmator that is a simple aberration corrector correcting twofold astigmatism. Additionally, multi-pole lenses can be used to balance positive third-order spherical aberration.

For the correction of third-order spherical aberration, two corrector designs exist. One is based on a quadrupole-octupole combination [71] and the other one on a hexapole combination [72]. In the microscope at hand, a hexapole based aberration corrector is employed. Hence, this work focuses on its operation principles.

A hexapole lens does not have a first-order effect but its primary effect is to induce second-order threefold astigmatism. Nonetheless, one can make use of combination aberrations. Combining optical elements can lead to aberrations that are not characteristic for the optical elements incorporated and are also not the sum of present aberrations [73]. A combination of thin hexapoles gives negative third-order spherical aberration C_3 which can also be achieved by an extended hexapole lens [74]. However, there is still threefold astigmatism present for a hexapole lens that has to be taken care of. The threefold astigmatism of a single extended hexapole lens would destroy the benefit of correcting the spherical aberration. In addition to threefold astigmatism, also fourth-order three-lobe aberration D_4 and sixfold astigmatism A_5 are generated.

If a cross-over of the electron beam would be induced at the center of a single extended

hexapole field, still negative third-order spherical aberration C_3 results due to its even azimuthal symmetry. However, the threefold astigmatism A_2 of the first half of the hexapole would be canceled by the threefold astigmatism of the second half due to the odd azimuthal symmetry. A design based on such a single extended hexapole field was proposed [75] but not workable in practice. The only workable hexapole based corrector design is based on two extended hexapole fields and four round transfer lenses [76]. The design of this aberration corrector for STEM is shown in Fig. 3.2.

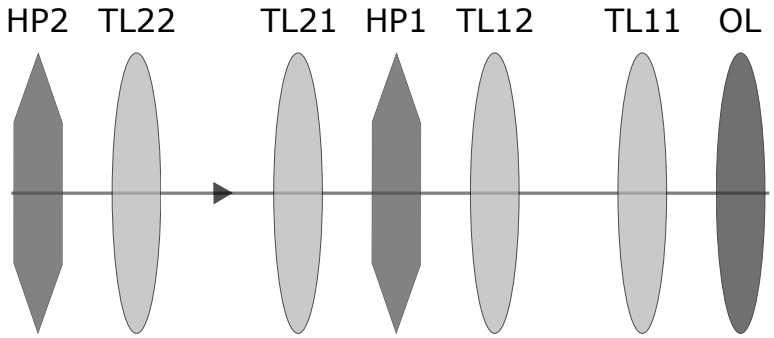

Figure 3.2: Design of hexapole aberration corrector for STEM. Based on [77]. It is built of two hexapole lenses (HP) and four round transfer lenses (TL). Afterwards, electrons are coupled into the objective lens (OL).

The hexapole aberration corrector is built of a first hexapole lens followed by two round transfer lenses that induce the cross-over of the beam in front of the second hexapole field. This second hexapole field has the same azimuthal orientation than the first hexapole field. Finally, two round transfer lenses couple the beam into the objective lens pre-field. In this way, both hexapole fields give negative third-order spherical aberration C_3, but the threefold astigmatism A_2 cancels out. Additionally, also the three-lobe aberration D_4 cancels out while the sixfold astigmatism A_5 adds up and remains as residual aberration of the hexapole aberration corrector. The transfer doublets give the flexibility to account for side effects and mechanical imperfections. Furthermore, parasitic aberrations of the lenses of the whole microscope can be accounted for by deflectors and stigmators.

With the corrector design described, geometric axial aberrations of first-, second- and third-order can be corrected while fourth-order aberrations can be minimized. Thus, remaining geometric axial aberrations that are limiting the resolution are of fifth-order: fifth-order spherical aberration C_5 and sixfold astigmatism A_5 [78]. The effects of fifth-order aberrations can be partially compensated for by setting lower-order aberrations to suitable values. However, due to the additional lenses of the corrector the influence of chromatic aberrations is increased which decreases the information limit.

To be able to correct for and counterbalance geometric aberrations requires for precise measurements of these aberrations. This can be achieved based on the Zemlin tableau method for conventional high resolution transmission electron microscopy [79, 80]. Here, the characteristic change of the coherent contrast transfer under tilted illumination is employed. For STEM, this is realized by comparing over- and under-focused images to an isotropic image to obtain a blurring function for convolution that is the electron probe. This allows for measuring defocus C_1 and twofold astigmatism A_1. Under tilted illumination, higher order aberrations show as effective defocus $\tilde{C_1}$ and as effective twofold astigmatism $\tilde{A_1}$. From these, higher order aberrations can be determined which eventually allows for correcting geometric aberrations and measuring residual ones. The parameters as determined for the microscope at hand are shown in Table 3.2.

Electron energy E_0	200 keV
Energy width ΔE	0.42 eV
Aperture angle α	21.3 mrad
Defocus C_1	0 nm
Twofold astigmatism A_1	0 nm
Third-order spherical aberration C_3	2 μm
Fifth-order spherical aberration C_5	5 mm
Axial chromatic aberration C_C	1.5 mm

Table 3.2: Parameters as determined for microscope at hand.

3.7 Imaging Principles

The characteristics of the electron probe and hence the information transfer in STEM are determined by the (condenser) aperture function, residual geometric aberrations and the partial coherence of the electron beam. In the following, these influences are discussed based on [57].

The size of the aperture determines the maximum attainable resolution due to the diffraction limit. An aperture of finite size is needed for optimization of the electron probe because of residual image aberrations present. This finite aperture size leads to the formation of an Airy pattern-type electron probe. In an Airy pattern, there is a central maximum of highest intensity together with concentric rings with lower intensity. The first zero of this Airy pattern is taken as the radius δ_D of the diffraction-limited electron probe

$$\delta_D = 0.61\frac{\lambda}{\alpha}, \tag{3.10}$$

where λ is the relativistic wavelength of the electrons and α is the semi-angle of the aperture. This gives the diffraction-limited resolution of an electron probe corresponding to the Rayleigh criterion for small α. Descriptively, to resolve a certain lattice spacing the diffraction limit requires the corresponding diffraction disk to partially overlap with the disk of the direct beam. Hence, the aperture size has to be chosen large enough to yield an electron probe that is small enough to give the desired resolution.

Residual geometric aberrations alter the shape of the Airy pattern. This is caused by a change of the phase of the electron wave inside the aperture due to these residual geometric aberrations. The most dominant geometric aberration has the strongest influence on the electron probe. For a non-corrected microscope this would be the third-order spherical aberration C_3 that would therefore also be the limiting factor for the resolution. However, with an aberration function $\chi = 0$ the electron probe becomes optimal. As discussed in the previous section 3.6, with third-order aberration correction the residual aberrations are of fifth-order and the limiting aberration is the fifth-order spherical aberration C_5.

If a phase shift of $\gamma = \frac{2\pi\chi}{\lambda} = \frac{\pi}{4}$ inside the aperture is tolerated, one can determine the optimum aperture semi-angle and the attainable probe size considering the diffraction-limited electron probe. For a C_5-limited electron probe, the optimum aperture semi-angle is given as

$$\alpha_{C_5} = \sqrt[6]{a_2\frac{\lambda}{C_5}}, \tag{3.11}$$

with $a_2 = 0.75$ and the probe size is given as

$$\delta_{C_5} = a_1\sqrt[6]{\lambda^5 C_5}, \tag{3.12}$$

with $a_1 = 0.64$.

With third-order aberration correction, it is also possible to set aberrations up to third order to partially compensate higher-order aberrations. Doing so for the defocus C_1 and the third-order spherical aberration C_3, fifth-order spherical aberration C_5 can be counterbalanced by setting

$$C_1 = -1.56\sqrt[3]{\lambda^2 C_5} \tag{3.13}$$

and

$$C_3 = -2.88\sqrt[3]{\lambda C_5^2} \tag{3.14}$$

according to [81]. With these settings, values of $a_1 = 0.4$ and $a_2 = 12$ result [82]. Hence, a higher convergence semi-angle α and therefore a smaller electron probe size and a better resolution result.

As a side effect, a higher convergence semi-angle α compared to non-corrected electron microscopes allows for a higher beam current and thus a better signal to noise ratio.

The effects of aperture size and residual geometric aberrations are coherent. Additionally, there are also incoherent effects. If instabilities of the instrument are small, there are partial temporal and partial spatial coherence.

Partial temporal coherence is present because of the finite energy spread of the electron probe ΔE and the axial chromatic aberration C_C that can also be used to describe the influence. As already explained in section 3.5, a blurring of the electron probe in lateral direction and primarily parallel to the optical axis is present. The partial temporal coherence does not have the strongest effect on the maximum on the Airy patter but on the side lobes. Hence, it does not lead to a loss in resolution but to a loss of contrast. Since the intensity of these side lobes increases with increasing aperture semi-angle α, the aperture size has to be chosen in a way to give optimized spatial resolution and adequate image contrast. An optimum aperture semi-angle was found as

$$\alpha_C = 1.2\sqrt{\lambda\frac{E_0}{C_C\Delta E}} \tag{3.15}$$

where the side lobes contain 25 % of the total intensity of the electron probe. With this aperture semi-angle, the attainable resolution is

$$\delta_C = 0.51\sqrt{\lambda\frac{C_C\Delta E}{E_0}} \tag{3.16}$$

which can give a stronger limitation than residual geometric aberrations.

The partial spatial coherence of the electron probe is caused by the finite size of the electron source. Since the electron probe is an image of the electron source, it always has a finite size. The incoherently broadened electron probe is obtained by a convolution of the coherent probe with the effective source size [83]. Hence, information with high spatial frequency show less contrast. Partial spatial coherence is only influential if the effective source size is on the same scale as the size of the coherent electron probe. However, this is the case for aberration-corrected instruments and hence, the effective source size has to be considered as it is always decreasing the resolution.

All effects discussed cannot be treated separately from each other but are all influential on the formation of the electron probe and have to be considered. Nonetheless, one effect

will be dominant and therefore determine the attainable resolution and the choice of the aperture semi-angle α. In this work, mainly $\alpha = 21.3\,\mathrm{mrad}$ is used.

While a larger aperture semi-angle increases the lateral resolution, it decreases the depth of field that is connected to the extension of the electron probe along the optical axis. Considering geometric limitations and the partial temporal coherence, an effective depth of field is estimated as

$$\Delta_{eff} \approx \sqrt{\left(\frac{\lambda}{\alpha^2}\right)^2 + \left(\frac{C_C \Delta E}{E_0}\right)^2}. \tag{3.17}$$

However, influences of dynamic scattering effects like channeling also have to be considered. The depth of field can be smaller than the thickness of the specimen so that only a fraction of the specimen is significantly contributing to image formation.

3.8 Annular Dark Field Imaging

Annular dark field (ADF) imaging is the most popular STEM imaging mode. Electrons scattered to an annular detector are collected. The inner angle of the detector is one the order of tens of milliradians but larger than the angles of Bragg diffraction ($10 - 20\,\mathrm{mrad}$). The outer detector angle can extend up several hundred milliradians. The intensity of every image pixel is then given by the intensity detected. This is shown schematically in Fig. 3.3. In the following, Z-contrast and incoherence of ADF imaging as well as the influence of thermal diffuse scattering (TDS) are discussed based on [58].

Detecting electrons in ADF imaging, an atom or atomic column shows bright contrast as scattering is present while vacuum shows no scattering and dark contrast. The scattering of electrons is mostly Rutherford-like with a screened Coulomb potential which decreases the Z-dependence below Z^2. This leads to sensitivity to composition and thickness of the specimen and each atomic column.

The incoherence of ADF imaging is caused by the large detector. A highly coherent electron probe and elastic scattering lead to interference effects in the detector plane. The large detector averages over the interference features so that the detected signal is incoherent. Hence, the intensity on the detector relies only on the intensity of the electron probe and the fraction that is scattered to the angular range of the detector. Dynamical scattering is strongly influencing the scattering of electrons detected in ADF imaging due to multiple scattering and channeling effects. However, the large ADF detector and the consequential incoherence simplify the interpretation of ADF images.

The intensity of the ADF detector is mainly formed from channeling states that are

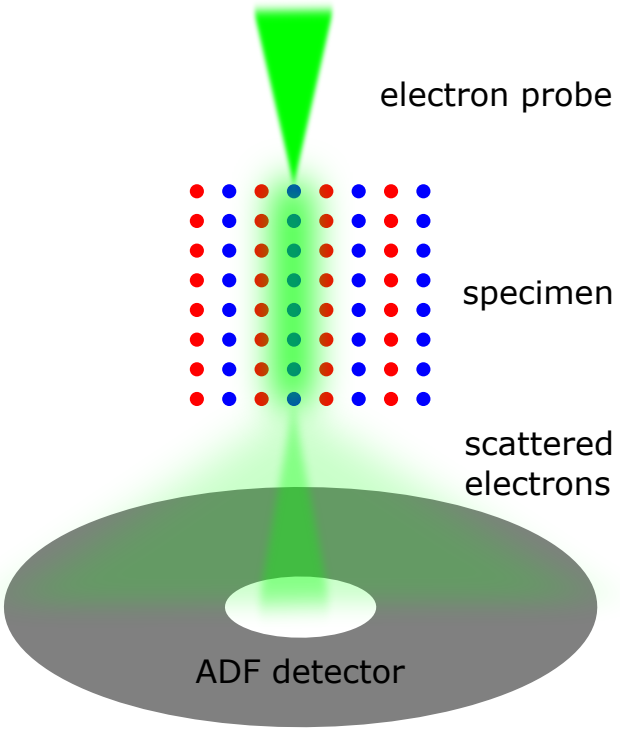

Figure 3.3: Annular dark field imaging. The representation is limited to the electron probe, interaction with the sample and the ADF detector that collects the electrons scattered to a certain angular range.

most localized on the atomic columns [3]. An ADF image shows the strength of channeling depending on the probe position. Therefore, also beam tilt and strain of the specimen influence the contrast of ADF images.

Thermal lattice vibrations, i.e. phonons, redistribute intensity from Bragg beams into diffuse intensity present under ADF detector angles. This attenuation of Bragg beams can be described by Debye-Waller factors. Scattering at phonons is inelastic but with very small energy transfer. In the ADF detector range, there is more intensity of TDS present than by elastic scattering [84] and therefore TDS is important to describe ADF imaging. As inelastic scattering process, TDS additionally destroys the coherence of the ADF signal.

3.9 Multi-Slice Image Simulations

Quantitative STEM can either be achieved by statistics-based methods [14, 18] or by direct comparison to image simulations. Composition determination on an absolute scale

requires complementary image simulations that are discussed in the following based on [64]. Image simulations are typically based on one of two approaches to consider dynamic scattering. On the one hand, the Bloch wave solution [2, 3] uses a numerical solution of the Bloch functions introduced in equation 3.5. On the other hand, in the multi-slice algorithm [37, 38] the specimen is sliced into weak phase objects for which the interaction with the electron probe can be calculated. Between these slices, the electron wave is propagated based on Fresnel diffraction. Thereby, the multi-slice algorithm is more efficient computation-wise and allows to simulate defects and interfaces. It is used in this work and thus focused on in the following.

The wave equation for fast electrons follows from the Schrodinger equation (cf. equation 3.2) assuming only elastic scattering

$$\frac{\partial \Psi\left(x,y,z\right)}{\partial z} = \left[\frac{i\lambda}{4\pi}\nabla_{xy}^{2} + i\sigma V\left(x,y,z\right)\right]\Psi\left(x,y,z\right), \tag{3.18}$$

with the electron wave Ψ, the interaction parameter $\sigma = \frac{2\pi me\lambda}{h^2}$ and the potential inside the specimen $V\left(x,y,z\right)$. The multi-slice solution follows either with a formal operator or a finite difference solution as

$$\Psi\left(x,y,z+\Delta z\right) = \exp\left[\frac{i\lambda}{4\pi}\Delta z\nabla_{xy}^{2} + i\sigma\int_{z}^{z+\Delta z} V\left(x,y,z'\right)dz'\right]\Psi\left(x,y,z\right). \tag{3.19}$$

Thereby, the potential inside the specimen is typically calculated with the isolated atom approximation as a linear superposition of all atoms in the specimen as

$$V(\mathbf{x}) = \sum_{j=1}^{N} V_j\left(\mathbf{x}-\mathbf{x}_j\right), \tag{3.20}$$

with the atomic potential V_j. The transmission function is defined as

$$t\left(x,y,z\right) = \exp\left[i\sigma\int_{z}^{z+\Delta z} V\left(x,y,z'\right)dz'\right] \tag{3.21}$$

and can be seen as an interaction with a weak phase object for the slice of the specimen between z and $z+\Delta z$. Likewise, the propagator function is defined as

$$p\left(x,y,\Delta z\right)\otimes = \exp\left(\frac{i\lambda\Delta z}{4\pi}\nabla_{xy}^{2}\right) \tag{3.22}$$

which resembles Fresnel diffraction over a distance Δz.

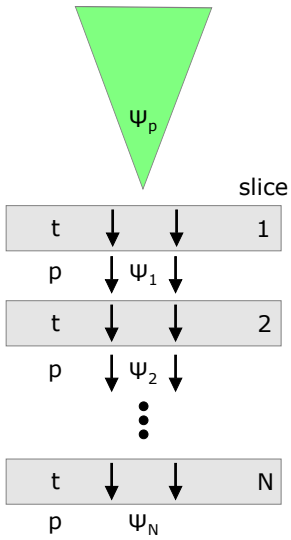

Figure 3.4: Principle of multi-slice image simulation. The specimen is divided into thin slices. Then, the initial probe wave function Ψ_p is transmitted through every slice with the transmission function t and propagated between them with the propagator function p.

With slice thickness Δz and N slices $n = 1, 2, 3, ...$, equation 3.19 can be written as

$$\Psi_{n+1}(x,y) = p_n(x,y,\Delta z_n) \otimes [t_n(x,y)\,\Psi_n(x,y)] + \mathbb{O}\left(\Delta z^2\right). \tag{3.23}$$

The error for one step is caused by the combination of transmission function and propagator and on the order of Δz^2. Performing N steps reduces this order to Δz. Thinner slices reduce the error but if the slice is too thin an error for the potential is caused. The initial wave function is the electron probe wave

$$\Psi_p(\mathbf{x},\mathbf{x}_p) = A_p \int_0^{k_{max}} \exp\left[-i\chi(\mathbf{k}) - 2\pi i\mathbf{k}\cdot(\mathbf{x}-\mathbf{x}_p)\,d^2\mathbf{k}\right], \tag{3.24}$$

with $\lambda k_{max} = \alpha_{max}$ as maximum aperture semi-angle, a normalization constant A_p and the probe position x_p. The principle of multi-slice image simulations is illustrated in Fig. 3.4. Using Fourier transforms, equation 3.23 can be written in reciprocal space as

$$\Psi_{n+1}(\mathbf{k}) = \mathrm{FT}\left[p_n(x,y,\Delta z)\right]\mathrm{FT}\left[t_n(x,y)\,\Psi_n(x,y)\right] + \mathbb{O}\left(\Delta z^2\right). \tag{3.25}$$

This calculation is done for all slices of the super cell and all probe positions. For N

probe positions the calculation scales with $N \ln N$. The ADF signal can be obtained after each slice for every probe position as

$$g(\mathbf{x}_p) = \int D(\mathbf{k}) |\Psi(\mathbf{k})|^2 d^2\mathbf{k} \tag{3.26}$$

where $D(\mathbf{k})$ is the detector function with $D(\mathbf{k}) = 1$ on the detector and $D(\mathbf{k}) = 0$ elsewhere.

There are several implementations of the multi-slice algorithm available [85, 86, 87, 88]. In this work, STEMsalabim [89] which is optimized for highly parallelized computing is used.

3.10 Modeling of Electron Probe, Specimen and Detector

To allow for a direct comparison of experimental and simulated STEM data, precise modeling of the imaging process in the scanning transmission electron microscope is required. Next to the electron probe-specimen interaction discussed in section 3.9, this includes the electron probe and the specimen itself and the detector.

The wave function of the electron probe is given in equation 3.24. Here, the residual geometric aberrations as outlined in sections 3.5 and 3.6 are considered. In addition to these, the partial coherence of the electron probe plays an important role (cf. section 3.7) and has to be taken into account. The partial temporal coherence can be modeled by a defocus series [90] which resembles the blurring of the probe caused in combination with the chromatic aberrations. The chromatic aberration can be measured for example with the method introduced in [91]. Partial spatial coherence, i.e. the finite source size, is taken into account by a convolution of the final ADF image with a Gaussian or Lorentzian. Several methods were proposed to measure the source size distribution [92, 93, 94, 11]. In this work, the ansatz presented in [95] is followed. Here, a Lorentzian is adapted to match experimental and simulated image. This also includes the effect of beam broadening due to amorphous layers.

Next to the general crystal structure of the specimen, the super cell used as input for image simulations is required to resemble the specimen as closely as possible. Static atomic displacements that are caused by different sizes and different electronegativity of the incorporated atoms [96] were found to be very influential on ADF-STEM images [27]. They can be included via a valence force field minimization [97, 98]. Another influential feature of TEM specimens is surface relaxation which occurs in strained heterostructures due to the free surfaces that allow relaxation [99, 100, 101]. Surface relaxation can be

considered by a finite element relaxation [102].

In section 3.8, the importance of TDS for ADF imaging is highlighted. There are several options to include TDS into image simulations. Approaches are based on an absorptive potential [103, 104], molecular dynamics [105] or a frozen lattice [106, 107]. The software package STEMsalabim [89] employed in this work uses the frozen lattice approach. For the frozen lattice approach, for each super cell different atomic configurations are generated. In each atomic configuration, the atoms are randomly displaced considering a root-mean-square displacement that is proportional to Debye-Waller factors. These Debye-Waller factors are taken from [108]. For every atomic configuration, the multi-slice algorithm is applied and the resulting images are averaged.

For a comparison of experimental and simulated STEM data, a normalization of the experimental data is crucial [28]. There are different approaches to accomplish this normalization [29, 30, 33, 34, 31] while the one followed in this wok is outlined in [32]. Here, the calibration of the detector is achieved with the help of a charge coupled device (CCD) camera. For this normalization, it is important to consider the non-uniform detector sensitivity that can be determined by a detector scan [29, 30, 109, 110, 111]. Additionally, knowledge of the detector angles is important. In this work, the angles are determined with help of the detector shadow on a CCD camera [112].

Imperfections of the microscope [34] as well as possible beam tilt [113, 114] also have to be considered.

An important feature of the specimen that is not taken into account in image simulations are amorphous layers that are introduced during specimen preparation. These influence ADF images in several ways [115, 116]. The most important influences on ADF images are beam broadening and added intensity in comparison to crystalline material only. Therefore, amorphous layers should be limited during specimen preparation (cf. section 3.2). One possible way to incorporate amorphous layers into the evaluation procedure is based on CBED [117].

4 Results

In this chapter, the results achieved during this work and presented in detail in original publications in chapter 6 are summarized. This starts with an investigation of the "W"-QWH introduced in section 2.4. This investigation is based on a comparison of experimental and simulated STEM intensity profiles and is combined with concentration results from XRD to yield simplistic one-dimensional layer-by-layer information (section 4.1). Here, simulated STEM intensities are re-scaled in order to match the experimental ones. All other results rely on a direct comparison of simulated and experimental STEM intensities on an absolute scale and give two-dimensional atomically resolved composition information. In section 4.2, a method to determine atomically resolved compositions for ternary III-V semiconductors from STEM intensities is presented. This method is based on the established direct comparison of experimental and STEM intensities but it is further developed towards the potential capability of single-atom accuracy, i.e. counting of substitute atoms. With atomically resolved composition information obtained using this method, the "W"-QWH is analyzed in more detail (section 4.3). In particular, surface segregation during growth is investigated. In section 4.4, a method is shown that enables to determine both thickness and composition locally with atomic resolution from a single STEM image of a ternary III-V semiconductor. A similar method to determine the atomically resolved composition of quaternary III-V semiconductors with two elements on each sub lattice, e.g. *(GaIn)(AsBi)*, from the intensities of a single STEM image is presented in section 4.5. Both methods are based on considering cross scattering between neighboring atomic columns during the evaluation.

4.1 Atomic Structure of "W"-type Quantum Well Heterostructures

The atomic structure of the "W"-QWHs introduced in section 2.4 is investigated with regard to the influence of different growth conditions. This is done by ADF-STEM measurements of two "W"-QWHs grown by MOVPE at 525 °C and 550 °C and a comparison to a simulated STEM image of an "ideal" "W"-QWH. This ideal "W"-QWH is based on

XRD results and box-like concentration profiles. Consequently, the evaluations in this section are based on STEM intensities in combination with XRD concentrations and focus upon one-dimensional profiles.

The dominant Z-contrast in ADF-STEM images reveals the atomic structure of the "W"-QWHs. The Voronoi intensity profiles that are determined from the ADF-STEM images of the two experimental structures and the simulation are shown in Fig. 4.1. To obtain Voronoi intensities, the intensity of all image pixels that are closest to a specific atomic column is averaged and assigned to that atomic column [35]. The profiles are thickness corrected by applying a linear gradient in the profiles and normalized to the intensity of *GaAs* to enable a better comparison despite of slightly different specimen thicknesses. In the Voronoi intensity profiles, the two *(GaIn)As*-QWs can be clearly identified due to an increased intensity on the group III sub lattice. The *Ga(AsSb)*-QW increases the intensity on the group V sub lattice.

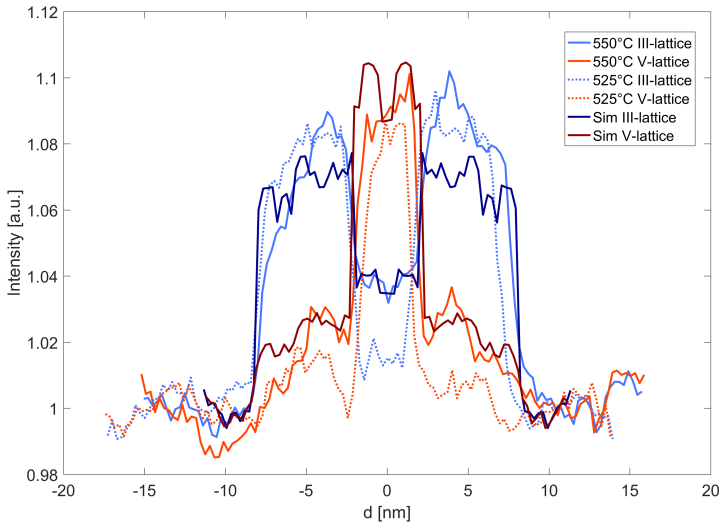

Figure 4.1: Voronoi intensity profiles for experimental and simulated "W"-QWHs. Both group III and group V profiles are shown. The intensity is normalized to the *GaAs* barrier and profiles are thickness corrected. Reprinted from [118].

The simulation for which the interfaces are designed to be abrupt shows graded interfaces. These are caused by strain relaxation and beam broadening due to spatial incoherence. A comparison of the grading of the interfaces in experiment and simulation yields a steeper gradient for the simulated "W"-QWHs which proves that the interfaces are rather graded than abrupt experimentally.

If the width of the QW is defined by a 50 %-criterion for the intensity at the interfaces,

this leads to a slightly higher width of the simulated QWs than actually present in the super cell. The width of the QWs in the experimental "W"-QWHs is smaller than the expected width that is based on XRD results from single QWs. Additionally, the width of the *Ga(AsSb)*-QW is smaller for the "W"-QWH grown at 525 °C. This points to an interaction of the different elements in the "W"-QWH during growth leading to a change of the QW width. The interaction is confirmed by complementary measurements presented in section 4.3.

The Voronoi intensity profiles show increased intensities on the group V sub lattice in the *(GaIn)As*-QWs and on the group III sub lattice in the *Ga(AsSb)*-QW. By analyzing the simulated Voronoi intensity profiles, these increased intensities can be attributed to cross scattering and wide quaternary layers can be ruled out.

The standard deviation of the Voronoi intensity along one lattice plane is a combination of a composition fluctuation and experimental noise:

$$\Delta I = \sqrt{\Delta^2_{composition} + \Delta^2_{noise}}. \tag{4.1}$$

By this, the material homogeneity can be assessed. For all QWs, $\Delta_{composition}$ has a similar value. By comparison to the simulated Voronoi intensities, $\Delta_{composition}$ can be connected to the intensity fluctuation caused by a Poisson-like distribution of the substitute atoms. An atomically resolved concentration profile allows a deeper investigation of the "W"-QWH as presented in section 4.3.

In a first approximation, simplistic concentration profiles can also be obtained from the Voronoi intensity profiles. For this, a linear relationship between Voronoi intensity and concentration is assumed. With a maximum concentration determined by XRD results, it is possible to estimate layer-by-layer concentrations. These concentrations can be used to calculate the expected photo-luminescence (PL) with a fully microscopic theory described by Berger et al. [55]. The expected PL is compared to the one experimentally measured. Experimentally, a two times higher PL intensity is found for the sample grown at 525 °C. For the calculated PL, this factor is decreased to 1.4. Additionally, the emission energies differ between experiment and calculation. This can be explained by a high dependence on the concentration and an uncertainty in the hetero-offsets of the "W"-QWH systems. Considering the simplistic concentration determination, the qualitative trends are reasonable. Improvements can be made with a more reliable concentration determination, e.g. like introduced in section 4.2, and by additional theoretical PL modeling studies.

4.2 Composition Determination of Semiconductor Alloys Towards Atomic Accuracy

STEM combined with complementary image simulations is an established method to determine the two-dimensional atomically resolved composition of nano-structures on an absolute scale [30, 35, 21]. Here, this methodology is extended to explore the capabilities of single-atom accuracy in material systems with one substitute atom.

For this, image simulations are performed for super cells with varying average concentrations of the substitute atom inside a matrix. Inside each super cell, atoms are statistically distributed. Static atomic displacements are considered. For a given thickness, i.e. a given total number of atoms per atomic column, the number of substitute atoms and the Voronoi intensity are evaluated for every atomic column across all super cells. Each number of substitute atoms gives a mean Voronoi intensity that is used for composition determination. These intensity composition relationships are shown for *(GaIn)As*, *Ga(PAs)* and *SiGe* for a thickness of 32 atoms per atomic column in Fig. 4.2.

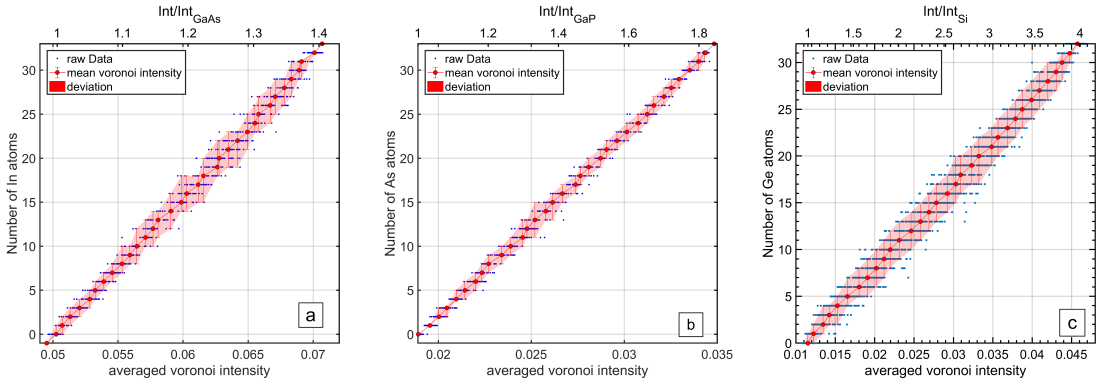

Figure 4.2: Intensity composition relationships for *(GaIn)As* (a), *Ga(PAs)* (b) and *SiGe* (c) for a thickness of 32 atoms per atomic column. Blue data points are present for every atomic column, the red data points give the mean values for every composition with a standard deviation translated to composition. Reprinted from [119].

The spread of Voronoi intensities for one composition is caused by different z-height configurations. The overlap of the intensity spread defines uncertainties for composition determination. For atomic columns with unknown composition, the Voronoi intensity is compared to the intensity composition relationship for its thickness to find the composition.

In a simulation study for $(Ga_{0.8}In_{0.2})As$, the capability of composition determination

with single-atom accuracy is investigated. 810 group III atomic columns are examined. First, the percentage of atomic columns for which the composition is determined correctly is investigated depending on the thickness (cf. Fig. 4.3(a)). Here, the thickness assumed for composition determination is the actual one.

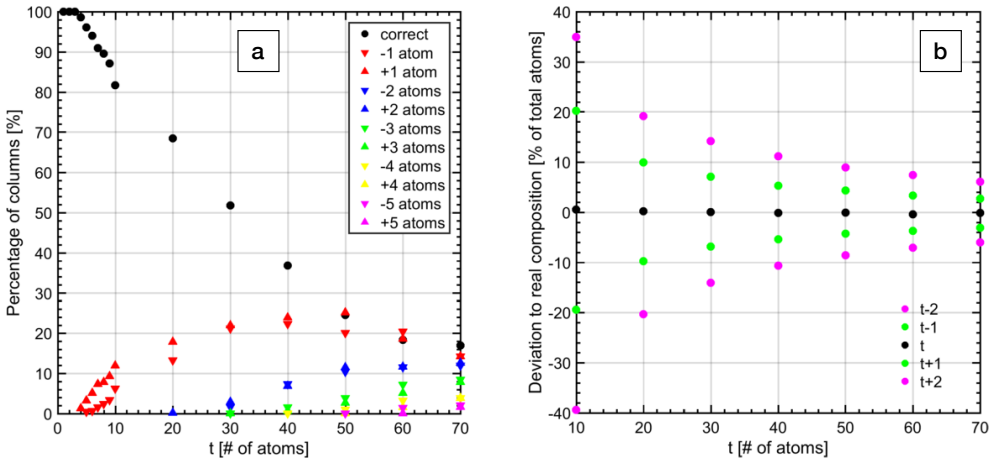

Figure 4.3: Capability of composition determination depending on thickness for the example of $(Ga_{0.8}In_{0.2})As$. In (a), the thickness is assumed correctly and the percentage of correctly determined atomic columns is given. In (b), the deviation of the total concentration is given for correctly and wrongly assumed thicknesses. Reprinted from [119].

For the given material system $(Ga_{0.8}In_{0.2})As$, the composition is determined correctly for all atomic columns up to a thickness of 3 atoms per atomic column. Beyond this thickness, the percentage of atomic columns for which the composition is determined correctly drops down. This is caused by more possible z-height configurations and, consequently, a larger spread in intensity. Deviations to the correct composition increase with thickness but are symmetrically distributed. For a correctly assumed thickness, the overall accuracy of the composition determination is very good (cf. Fig. 4.3(b)) even if locally the single-atom accuracy decreases with thickness. Hence, local statistical deviations cancel each other.

Additionally, the influence of a wrongly assumed thickness is investigated (cf. Fig. 4.3(b)). A wrongly assumed thickness leads to a deviation in the overall concentration determined that decreases with increasing thickness and is symmetric for over- and underestimated thickness. This decrease is caused by the smaller percentage error in thickness. Hence, for accurate local composition determination knowledge of the thickness is important. However, errors due to under- and overestimation of thickness would

cancel each other if under- and overestimation are equally present.

The overall trends discussed are generally representative for all material systems but the exact behavior depends on the material system and the concentration. In particular, the difference in atomic number between the substitute atom and the replaced matrix atom is decisive. Higher concentrations allow more possible z-height configurations.

With this knowledge about capabilities of the method, it is applied to experimental STEM images of a *(GaIn)As*-QW grown by MOVPE on *GaAs*, a *Ga(PAs)*-QW grown by MOVPE on *GaP* and a *SiGe*-QW grown by low-energy plasma-enhanced chemical vapor phase epitaxy on $Si_{0.2}Ge_{0.8}$ [120, 121].

For each sample, the determination of a Lorentzian convolution parameter σ to match simulation and experiment is important [95]. This parameter takes into account the effective source size but is also affected by beam broadening due to residual amorphous layers on the specimen. The determination of σ is achieved by comparison of experimental and simulated average unit cell images of known composition. First, the thickness of the experimental average unit cells is found by comparison of the average intensity to simulations. Then, σ is determined by a two-dimensional comparison of experimental and simulated average unit cell. Good matching with a relative difference of 1.1 % to 1.6 % between experiment and simulation is found for the three STEM images.

As found in the simulation study, knowledge of thickness plays a crucial role for composition determination. For an atomic column of known composition, the thickness can be determined by comparison of the Voronoi intensity to simulations. Therefor, the composition of neighboring atomic columns has to be known or cross scattering, i.e. the influence of neighboring atomic columns on the intensity, has to be negligible. An established way to identify the thickness of every atomic column is to inter- or extrapolate the thickness from a region of known composition, i.e. the barrier [30, 35]. This is applied to the *Ga(PAs)*-QW with an interpolation between the *GaP* barriers and to the *SiGe*-QW with an overall extrapolation due to varying composition within the barrier. These approaches are obviously prone to errors in local thickness and will lead to errors in local composition. Since cross scattering is negligible for the *(GaIn)As*-QW due to the small thickness and the material system, the group V atomic columns containing only *As* atoms are used for thickness determination similar to an approach in [21]. Then, the thickness of group III atomic columns is averaged from their 4 next neighbors (NN) that are group V atomic columns. A method to determine thickness and composition locally from a single STEM image regardless of the presence of cross scattering is presented in section 4.4.

For all three material systems, composition intensity relationships are evaluated for all

present thicknesses. Then, for each atomic column the composition is found considering its thickness. Negative concentrations and concentrations higher than 1 are allowed to take into account experimental noise and local errors in thickness. Composition information is present with two-dimensional atomic resolution. However, for comparison to concentration profiles obtained by XRD and strain state analysis the two-dimensional composition information is reduced to one-dimensional concentration profiles. This is done by averaging along lattice planes and gives mean values and standard deviations for each lattice plane. Local thicknesses are considered for the concentration profiles shown in Fig. 4.4.

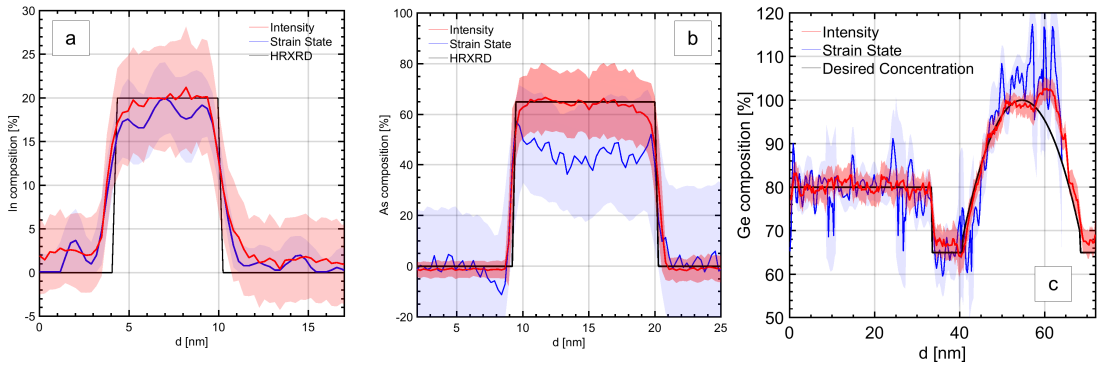

Figure 4.4: Concentration profiles of the *(GaIn)As*-QW (a), the *Ga(PAs)*-QW (b) and the *SiGe*-QW (c). The concentration profile obtained by XRD is shown in black in (a) and (b), in (c) the black profile is the intended concentration. The concentration profiles determined by STEM intensities are shown in red, strain state concentration profiles from evaluation of the same STEM images are shown in blue. Reprinted from [119].

For the *(GaIn)As*-QW, good agreement to both methods is found. For the *Ga(PAs)*-QW, the agreement to XRD is good while surface relaxation is severely affecting composition determination by strain state analysis. For the *SiGe*-QW, reasonable XRD data cannot be obtained but the concentration profile determined is in good agreement with the intended one and the one found by strain state analysis.

The comparison of the concentration profiles determined suggests that local errors in composition due to intrinsic limitations and wrongly assumed thicknesses cancel out when averaging the concentration over a high number of atomic columns. While intrinsic limitations are part of the STEM experiment itself, the problem of local errors in thickness is treated in section 4.4.

To reach these results, accurate knowledge of all experimental parameters is necessary. However, the influence of amorphous layers from specimen preparation is not included in

the evaluation except for beam broadening. Non-zero concentrations in the barriers are assumed to be associated with the influence of amorphous layers. Then, this influence can be decreased by an improvement in specimen preparation.

4.3 Segregation at Interfaces in "W"-type Quantum Well Heterostructures

For the "W"-QWHs introduced in section 2.4 and already discussed in section 4.1, two-dimensional atomically resolved composition information can be obtained by the method introduced in section 4.2. A composition determination across the interfaces of the heterostructure is possible. Due to very thin specimens and consequently negligible cross scattering, the thickness can be determined locally with help of the sub lattice with constant composition. This leads to layer-by-layer concentration profiles for both the *Ga(AsSb)*-QW and the *(GaIn)As*-QWs. To judge influences of other QWs and elements on the growth of the different QWs, additionally single *(GaIn)As*- and *Ga(AsSb)*-QWs grown between *GaAs* barriers with the same growth conditions are analyzed. These growth conditions include a growth temperature of 550 °C in accordance to one sample analyzed in section 4.1. Excellent agreement of the concentration profiles of the *(GaIn)As*-QW to XRD results is found, while for the *Ga(AsSb)*-QW the agreement is reasonable.

Surface segregation is well known to influence the growth at interfaces in III-V semiconductor heterostructures [122, 123, 124]. A well established method to describe its influence on the concentration profile is the Muraki model [124]. According to this model, only a certain fraction of the offered material is incorporated into the crystal, while the rest is segregating to the surface. The concentration of every atomic layer $x(n)$ is described by

$$x(n) = \begin{cases} x_0 \left(1 - S^N\right) & : 1 \leq n \leq N \\ x_0 \left(1 - S^N\right) S^{n-N} & : n > N \end{cases} . \tag{4.2}$$

x_0 is the final concentration of the element segregating, S is the segregation coefficient and N is the number of layers deposited.

In Fig. 4.5, the concentration profiles of all three *(GaIn)As*-QWs are shown together with the fitted Muraki model. In case of the single *(GaIn)As*-QW (cf. Fig. 4.5(a)), the concentration profile is well described by the Muraki model. The segregation coefficient is in good agreement to results for the same MOVPE growth temperature [126]. For the

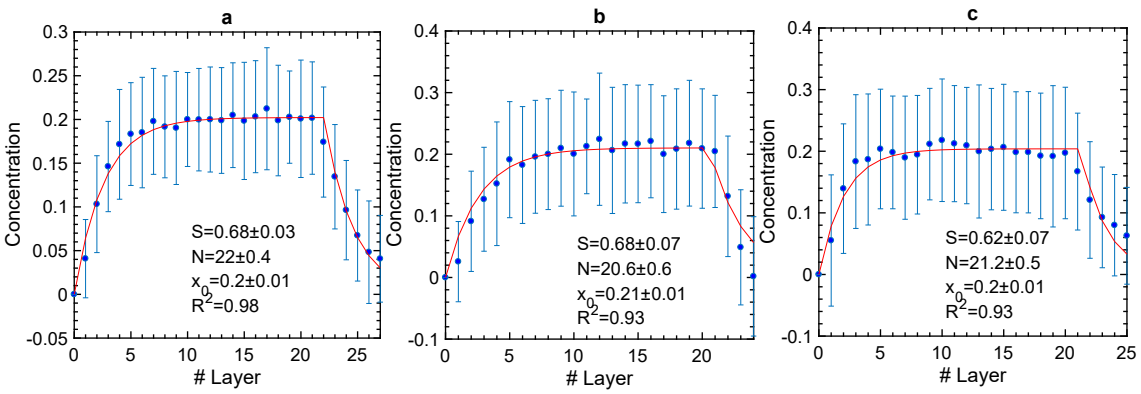

Figure 4.5: Concentration profiles of single *(GaIn)As*-QW (a) and *(GaIn)As*-QWs in "W"-QWH. The first and the second *(GaIn)As*-QW in the "W"-QWH are shown in (b) and (c), respectively. Error bars depict the standard deviation of the concentration within one lattice plane. The parameters for the fitted Muraki model (red) are given as inset. Reprinted from [125].

(GaIn)As-QWs in the "W"-QWH, the description of the concentration profiles by the Muraki model shows some deviations (cf. Fig. 4.5(b) and (c)).

Allowing two different segregation coefficients for the lower and the upper interface of each *(GaIn)As*-QW in the "W"-QWH, a better description can be achieved (cf. Fig. 4.6). Here, the segregation coefficients at interfaces between *(GaIn)As* and *GaAs*, i.e. the lower interface of the first *(GaIn)As*-QW (Fig. 4.6(a)) and the upper interface of the second *(GaIn)As*-QW (Fig. 4.6(b)), are similar to the segregation coefficient for the single *(GaIn)As*-QW. The upper interface of the first *(GaIn)As*-QW to the *Ga(AsSb)*-QW has a smaller segregation coefficient representing the more abrupt interface. This blocking of incorporation of segregating *In* by *Sb* was found before for a similar material system [127]. Blocking of *In* incorporation by *Sb* is also represented by the decreased segregation coefficient for the lower interface of the second *(GaIn)As*-QW. The *Sb* still present at the surface has to vanish before the growth of the *(GaIn)As*-QW can start. In summary, the *Ga(AsSb)* interface changes the interfaces of the *(GaIn)As*-QWs compared to the *GaAs* interface.

Concentration profiles and fitted Muraki models for the single *Ga(AsSb)*-QW and the *Ga(AsSb)*-QW in the "W"-QWH are shown in Fig. 4.7. Here, a good description of both QWs can be achieved. For both QWs, the lower and the upper interface are to the same material so that one segregation coefficient is sufficient. Since the materials are different, the segregation coefficients for both QWs do not totally match.

The concentration of *Sb* is decreased in the *Ga(AsSb)*-QW in the "W"-QWH compared

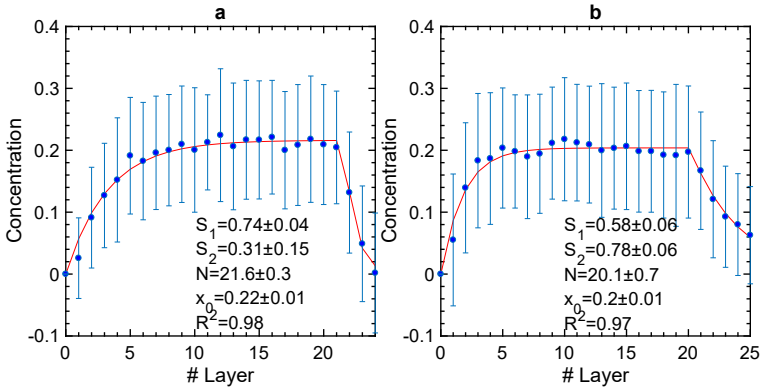

Figure 4.6: Concentration profiles of *(GaIn)As*-QWs in the "W"-QWH and modified Muraki model. The first QW is shown in (a) and the second one in (b). Error bars depict the standard deviation of the concentration within one lattice plane. The parameters for the fitted Muraki model (red) are given as inset. Reprinted from [125].

to the single *Ga(AsSb)*-QW. Growth of the *Ga(AsSb)*-QW on *(GaIn)As* and *In* possibly still floating around on the surface decreases *Sb* incorporation. This is in agreement with previous results [127]. Additionally, the width of the *Ga(AsSb)*-QW in the "W"-QWH is decreased. The strain of the *(GaIn)As*-QW and floating *In* on the surface decrease the growth rate.

The two-dimensional atomically resolved composition information obtained in this section allows a deeper analysis of the "W"-QWH than evaluations based on intensity profiles presented in section 4.1.

4.4 Local Determination of Thickness and Composition for Ternary III-V Semiconductors

As seen in section 4.2, knowledge of the thickness of an atomic column is very important for accurate composition determination for ternary III-V semiconductors. Generally, the thickness of an atomic column can be determined if the composition is known. However, due to cross scattering the use of the sub lattice with constant composition is limited to small specimen thicknesses depending on the material system. Therefore, a common approach for thickness estimation is based on interpolation of thickness between regions of known composition [30, 35] which is obviously prone to errors locally. Another previous method for composition and thickness determination is based on angular resolved STEM where composition and thickness characteristic scattering can be exploited for certain

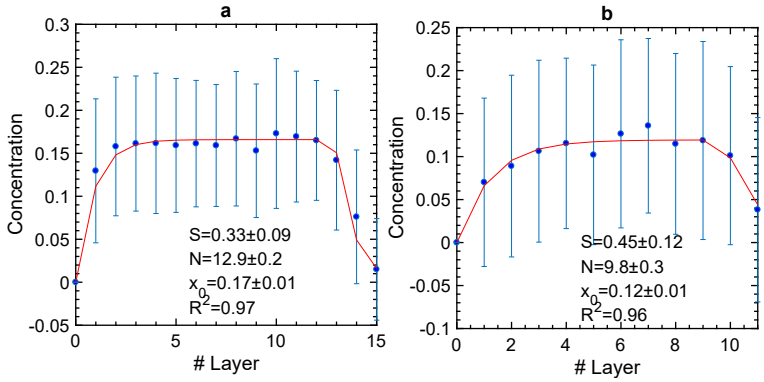

Figure 4.7: Concentration profiles of the single *Ga(AsSb)*-QW (a) and the *Ga(AsSb)*-QW in the "W"-QWH (b) together with Muraki model fitted. Error bars depict the standard deviation of the concentration within one lattice plane. The parameters for the fitted Muraki model (red) are given as inset. Reprinted from [125].

material systems [128]. Then, two STEM images taken at different detector angles are evaluated.

Here, a method is shown that uses the knowledge of cross scattering from image simulations to iteratively determine thickness and composition locally from a single STEM image. The method is explained for the example of *Ga(AsBi)* in the following.

For composition determination, the sub lattice with changing composition is evaluated which is the group V sub lattice in this case. Here, the same intensity composition relationships as explained in section 4.2 are determined from simulations (cf. Fig. 4.8(a)). Additionally, for a range of thicknesses the intensity of the group III sub lattice that has a constant composition in this case is analyzed depending on the average number of *Bi* atoms in the 4 next neighbor (NN) group V atomic columns (cf. Fig. 4.8(b)). This information is used for thickness determination.

Initially, the thickness of group III atomic columns is determined considering zero NN *Bi* atoms, i.e. pure *GaAs*. To figure out the thickness of group V atomic columns, the thickness of the 4 NN group III atomic columns is averaged. For these thicknesses, the composition is determined for every atomic column. These compositions are then used to determine the thickness of group III atomic columns considering the average NN composition. For the thickness of group V atomic columns, group III atomic columns are averaged again. After composition determination with these new thicknesses, these steps can be performed iteratively to find a stable thickness composition configuration.

The feasibility of this method is proven in a simulation study for both *Ga(AsBi)* and

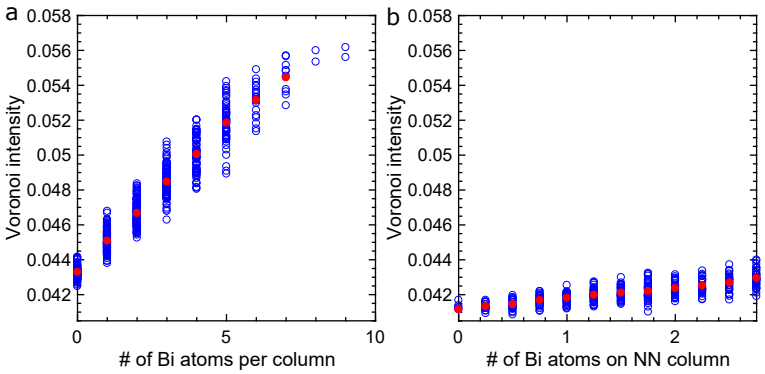

Figure 4.8: Evaluation of simulations for proposed method. (a) The intensities of the group V atomic columns are evaluated depending on the number of *Bi* atoms contained. The value for every column is given in blue, mean values are shown in red. (b) The intensities of group III atomic columns are evaluated depending on the average NN *Bi* composition. Again, all values are shown in blue and the mean values in red. The evaluated thickness is 30 atoms per atomic column and the evaluated detector range is $70 - 280$ mrad. Reprinted from [129].

(GaIn)As. In the case of *Ga(AsBi)*, a simulated STEM image with a thickness of 30 atoms per atomic column and a detector range of $70 - 280$ mrad is evaluated. The thickness is determined correctly for 99 % of the 81 group V atomic columns. This leads to a composition determination being correct for 78 % of the group V atomic columns and a total deviation for the composition of $+2$ *Bi* atoms for 140 *Bi* atoms out of 2430 group V atoms. In the case of *(GaIn)As*, a simulated STEM image with a thickness of 35 atoms per atomic column and a detector range of $70 - 280$ mrad is investigated. Here, the thickness can be determined correctly for 92 % of the 49 group III atomic columns while the composition is correct for 33 % of the group III atomic columns. The total *In* composition is overestimated by 4 *In* atoms for 495 *In* atoms out of 1715 group III atoms. Both results are governed by the statistical character of composition determination discussed in section 4.2 and match closely to results for correctly known thickness everywhere.

In a simulation study for $GaAs_{0.94}Bi_{0.06}$, the influence of detector angles and specimen thickness on the accuracy of the proposed method is investigated (cf. Fig. 4.9). This is performed for inner detector angles of $30 - 100$ mrad while the outer detector angle is four times the inner angle as determined by the geometry of the detector. The specimen thickness is varied from 10 to 35 atoms per atomic column in steps of 5 atoms per atomic column. In Fig. 4.9(a), the total deviation of the *Bi* composition and the percentage of

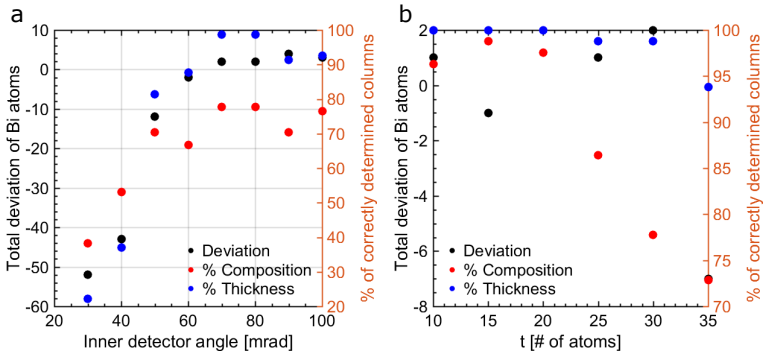

Figure 4.9: Influences of detector angles (a) and thickness (b) on accuracy of proposed method for $GaAs_{0.94}Bi_{0.06}$. To judge the accuracy, the percentage of columns for which thickness (blue) and composition (red) are correctly determined and the deviation of the total composition (black) are evaluated. Reprinted from [129].

atomic columns for which thickness and composition are determined correctly is shown for a thickness of 30 atoms per atomic column. Optimum inner detector angles are found to be $70 - 80$ mrad where the thickness is determined correctly for almost every column and the composition is determined correctly for almost 80 % of the atomic columns. The optimum detector angles depend on the material system and also on the thickness as this changes the total atomic number of atomic columns. Exploiting angular dependencies offers great potential in the future.

For all investigated thicknesses up to 35 atoms per atomic column, thickness and composition can be determined reasonably well. Nonetheless, with increasing thickness the accuracy decreases. This is again caused by the statistical character of composition determination discussed in section 4.2 and the mutual dependence of thickness and composition.

Finally, the proposed method is applied to an experimental STEM image of a *Ga(AsBi)*-QW grown by MOVPE. Considering the results from the simulation study, detector angles are chosen as $67 - 268$ mrad and specimen thickness is also taken care of during specimen preparation. The resulting STEM image is shown in Fig. 4.10(a). The *Ga(AsBi)*-QW and the *GaAs*-barrier are clearly distinguishable. After applying the proposed method for 15 iterations, the thickness and composition maps shown in Fig. 4.10(b) and (c) result. The thickness ranges from 26 to 31 atoms per atomic column while a *Bi* composition of -1 to 6 atoms per atomic column is present. Negative composition values are allowed to account for experimental noise. In the composition map, clustering is apparent which was also found for this material system before [130].

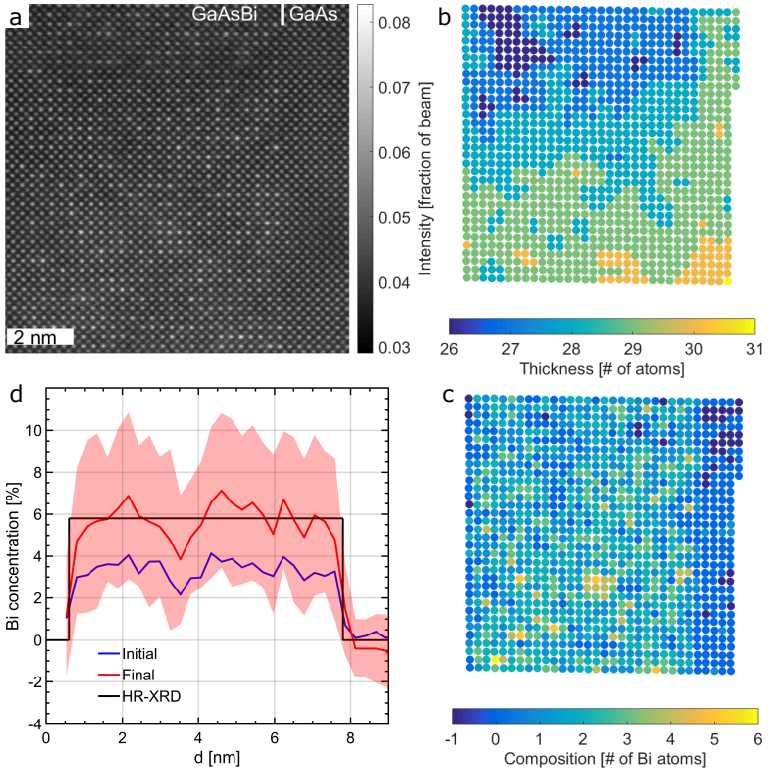

Figure 4.10: Experimental results for *Ga(AsBi)*-QW. (a) In the STEM image, *Ga(AsBi)*-QW and *GaAs*-barrier are clearly distinguishable. (b) The thickness map shows the final thicknesses determined. (c) The final composition map clearly identifies the QW. (d) The concentration profile determined by STEM (red) is in good agreement with the box-like concentration profile obtained by XRD (black). The red shadow gives the standard deviation of the composition along one lattice plane. The initial concentration profile (blue) clearly deviates from the real concentration. Reprinted from [129].

Averaging the composition along the lattice planes and considering the local thickness leads to the concentration profile shown in Fig. 4.10(d). The shaded region represents the standard deviation along one lattice plane. A very good agreement to the box-like concentration profile obtained by XRD with a QW width of 7.2 nm and a *Bi* concentration of 5.8 % is found. However, STEM gives more detailed two-dimensional atomically resolved composition information. For comparison, also the initial concentration profile without applying the iterative determination is shown. This clearly deviates from the real concentration.

Due to improved specimen preparation, amorphous layers are reduced which can lead to the *Bi* concentration in the barrier being closer to zero compared to concentration profiles obtained for conventionally prepared specimens.

4.5 Composition Determination for Quaternary III-V Semiconductors

Composition determination by STEM and complementary image simulations is widespread for ternary III-V semiconductors and an option to develop it towards single-atom accuracy is presented in section 4.2. For quaternary III-V semiconductors, a combination of different STEM methods [44] or several ADF-STEM images [45] was used before. Cross scattering influences the intensity of neighboring atomic columns [131] and has to be taken into account for composition determination by STEM intensity only.

The method presented here considers cross scattering and knowledge about it from image simulations for composition determination similar to the method presented in section 4.4. This is done with a single STEM image and is applicable for quaternary III-V semiconductors with two elements on each sub lattice. Here, *(GaIn)(AsBi)* is evaluated as an example.

A wide range of quaternary compositions is simulated. For each atomic column, the Voronoi intensity is analyzed depending on the in-column composition and the average composition of the four NN atomic columns which belong to the other sub lattice in [010]-viewing direction. If there are at least 10 data points for one event, a mean value is assigned. Missing mean values are obtained by fitting a polynomial function of second degree. The resulting intensity composition data spaces for the group III (a) and the group V atomic columns (b) are shown in Fig. 4.11.

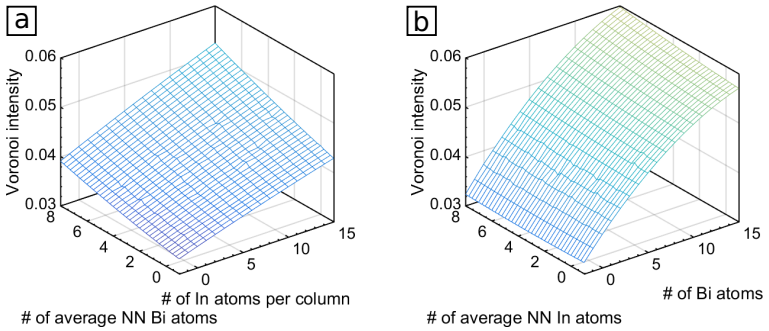

Figure 4.11: Dependence of the Voronoi intensity on the in-column and the average NN composition for the group III (a) and the group V atomic columns (b). Image simulations at a thickness of 25 atoms per atomic columns and for a detector range of $70 - 280$ mrad are evaluated. For the NN composition, quarter atoms are considered. In-column composition is restricted to natural numbers. Mean values for at least 10 events and interpolated values are shown. Reprinted from [132].

The composition is determined iteratively for both sub lattices separately. Knowledge of the thickness of every atomic column is necessary. Since the Voronoi intensity is more strongly depending on the *Bi* composition than on the *In* composition, the composition determination starts with the group V sub lattice. Considering no *In* atoms within the NN atomic columns, i.e. pure *GaAs*, the *Bi* composition is determined by comparison of each atomic column's Voronoi intensity to the simulated mean values. Then, the *In* composition is determined considering the NN *Bi* composition by comparing the Voronoi intensities to the intensity composition relationship for *In* and the correct number of NN *Bi* atoms. Afterwards, the same is done for the *Bi* composition considering the NN *In* composition and then the *In* composition considering the NN *Bi* composition follows. These steps can be performed iteratively.

To prove the feasibility of the method, it is applied to a simulated STEM image. This image is generated for $(Ga_{0.05}In_{0.95})(As_{0.95}Bi_{0.05})$ at a thickness of 25 atoms per atomic column with a virtual detector range of $70 - 280$ mrad. Applying the described method for two composition determination cycles, the composition for every atomic column can be determined. The deviations to the real composition are maximum ± 1 atoms. For 85 % of the atomic columns, the composition is determined correctly. Looking at the overall *Bi* and *In* composition, for 1600 atoms on each sub lattice the *Bi* composition deviates by -1 atom to the real composition of 63 *Bi* atoms and the *In* composition deviates by +2 atoms to the real composition of 65 *In* atoms. Hence, the described method is able to determine the composition of *(GaIn)(AsBi)*. The obtained results represent the statistical character of composition determination already discussed in section 4.2. These effects are enhanced here since the composition determination for one atomic column depends on knowledge of the composition of the NN atomic columns.

In a simulation study, the influence of detector angles and specimen thickness is investigated. Specimen thicknesses are varied from 10 to 35 atoms per atomic columns. The accuracy of the composition determination depends on the detector angles. With increasing thickness, the optimum detector angles increase. This is caused by the non-monotonic increase of scattering cross-sections for low angle ADF-STEM at small thicknesses [133]. For all investigated thicknesses, good accuracy is found. However, the performance decreases with increasing thickness as already found and discussed for ternary material systems (cf. sections 4.2 and 4.4).

Finally, the described method is applied to an experimental image of a *(GaIn)(AsBi)*-QW grown by MOVPE. In the STEM image (Fig. 4.12(a)), the QW is distinguishable due to Z-contrast. To be able to assume a thickness for every atomic column, it is interpolated between the *GaAs* barriers (cf. Fig. 4.12(b)) since there is no sub lattice with constant

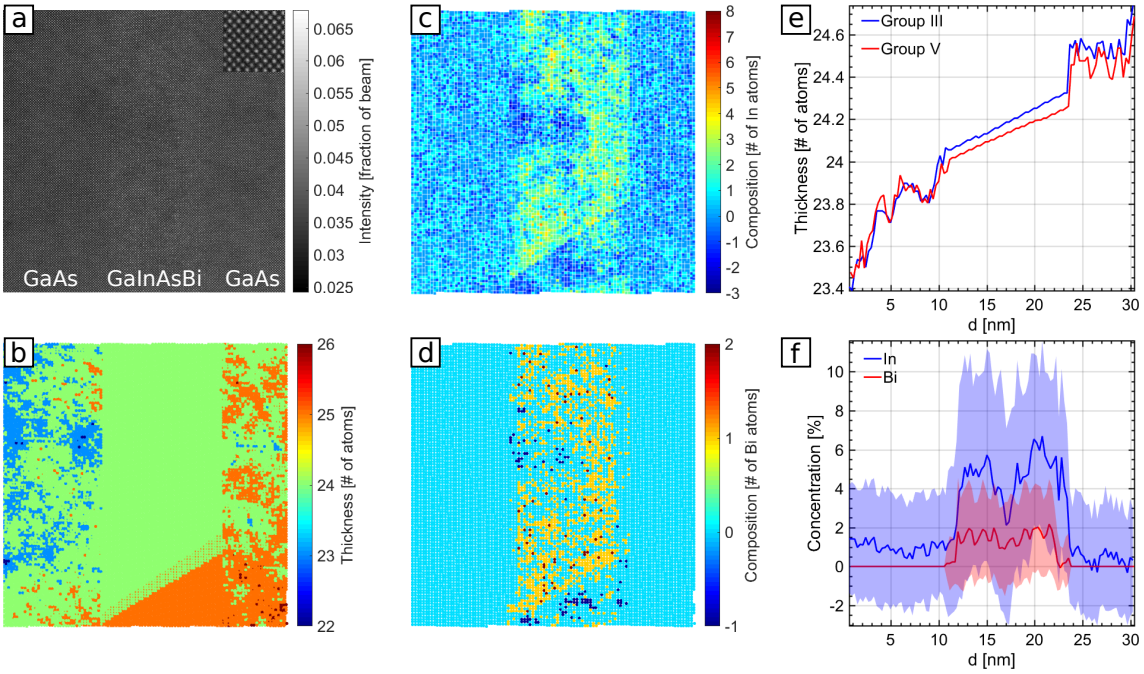

Figure 4.12: Experimental results for *(GaIn)(AsBi)*-QW grown by MOVPE. The STEM image (a) shows *(GaIn)(AsBi)*-QW and *GaAs* barriers. From these barriers, the thickness is interpolated (b, e). With the described method, *In* (c) and *Bi* composition (d) result. The concentration profiles (f) show layer-by-layer concentrations. Reprinted from [132].

composition. Applying the method discussed leads to the *In* and *Bi* composition shown in Fig. 4.12(c) and (d), respectively. Here, the influence of thickness interpolation is visible. In particular, composition determination of *In* is very sensitive to thickness since here adding one *Ga* atom is more influential on the intensity than replacing one *Ga* atom by one *In* atom. However, overall the thickness trend is reasonably represented by the thickness interpolation as can be seen in the thickness profile shown in Fig. 4.12(e). The concentration profile (cf. Fig. 4.12(f)) shows large variations of the concentrations in the QW which is also represented by the standard deviations. *In* growth has continued longer than *Bi* growth since it is the last growth pulse of the pulsed growth. The average concentration within the QW is 4.5 % of *In* and 1.3 % of *Bi*.

A simulation of XRD results for this concentration of the multi QW structure gives good agreement with experimental XRD results (cf. Fig. 4.13). QW and barrier width are adjusted from the difffractogram since they are found to vary locally. A direct comparison to XRD concentrations is not possible since these cannot be obtained from one XRD measurement. However, a comparison to concentration results from a combination

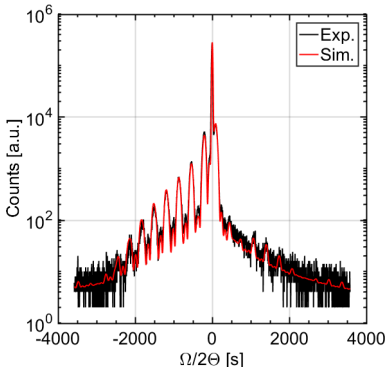

Figure 4.13: Simulated and experimental XRD results. The simulated diffractogram is shown for the concentrations determined by STEM. Thereby, all three QWs are assumed to have the same concentration. QW and barrier width are adjusted as 10.4 nm and 48.1 nm, respectively. Reprinted from [132].

of XRD and PL is conducted. For this combination, many theoretical assumptions are necessary, e.g. the energetic level of Bi impurities in (GaIn)As. The combination of XRD and PL yields concentrations of 3.9 % *In* and 1.3 % *Bi*. STEM indicates a slightly higher *In* concentration. Next to the theoretical assumptions mentioned, reasons for this deviation can be local variations of concentration within the multi QW structure or wrong thickness estimations from the thickness interpolation. The composition determination of *In* is very sensitive to thickness as discussed above. Nonetheless, good agreement of concentration results can be observed while STEM offers superior two-dimensional atomic resolution that can be used to deeply analyze material characteristics, e.g. composition homogeneity.

5 Summary

Quantitative STEM can satisfy the demand of modern semiconductor device development for atomically resolved structural information. Thereby, quantitative evaluations can be based on STEM intensities only, a combination of STEM intensities with different methods or a comparison of STEM intensities to image simulations.

Based on STEM intensities only, quantitative evaluations of the "W"-QWH are conducted and reveal information about its structure. Simplistic one-dimensional layer-by-layer concentration profiles can be assigned through a combination with concentration results from XRD that do not provide layer-by-layer information.

However, the composition can be determined more accurately, i.e. without further assumptions from other methods, and with two-dimensional atomic resolution based on STEM results only. Composition determination by STEM is possible because ADF-STEM images show dominant atomic-number contrast. This can be taken into account by image simulations that are used for a direct comparison to experimental results.

With these more accurate two-dimensional atomically resolved composition results, a deeper analysis of, amongst others, the interfaces of QWHs is possible. For the "W"-QWH, this analysis and comparison to single QWs reveals strong interaction of In and Sb during MOVPE growth. This interaction leads to an alteration of the interfaces compared to single QWs with interfaces to $GaAs$ only.

As the goal of quantitative STEM is to locate, count and distinguish atoms [11] in an atomic column, established composition determination for ternary III-V semiconductors is further developed towards potential capability of single-atom accuracy, i.e. counting substitute atoms. Image simulations are a great tool to explore this capability. The capability of single-atom accuracy is determined by statistics and leads to a probability for correct composition determination of an atomic column: For a given number of substitute atoms in an atomic column, a certain range of intensities can result due to different z-height configurations of the same atoms in that column. The probability for correct composition determination of an atomic column is influenced by the composition, i.e. the number of substitute atoms, and the thickness of that atomic column, i.e. the total number of atoms. Both increase the number of possible z-height configurations and therefore

decrease the probability for correct composition determination. Additionally, the capability for composition determination is strongly influenced by the material system. This manifests in the difference in atomic number of substitute and matrix atom. However, for the characterization of technologically relevant specimens the material system and its composition are dictated by device requirements leaving only specimen thickness as parameter. This is a matter of optimum specimen preparation. Specimen preparation also has to ensure good quality of specimens, e.g. limited surface damage.

While correct composition determination for one atomic column is statistically determined, the overall accuracy as the average over many atomic columns is very good. Statistical deviations cancel each other which leads to an exact overall composition result. This is usually the case experimentally where many atomic columns are evaluated.

To distinguish atoms in an atomic column, one needs to count them first. STEM probes the total atomic number of an atomic column and thus intensity changes by composition and thickness are indistinguishable looking at the intensity. A wrong assumption for the number of atoms impedes accurate composition determination. Therefore, accurate knowledge of the local thickness is necessary. Commonly, the thickness of a QW was interpolated from regions with known composition obviously leading to local errors. A method to achieve local thickness and composition determination for ternary III-V semiconductors from a single STEM image is part of this work. It utilizes the crystal symmetry in [010]-viewing direction and knowledge about cross scattering from image simulations. Then, thickness and composition can be determined iteratively.

Since the effects of thickness and composition on the intensity are interchangeable, the principle of this method can also be applied to quaternary III-V semiconductors with two elements on each sub lattice. The thickness has to be interpolated from regions of known composition or has to be determined in a different manner. Again, the intensity of both sub lattices combined with knowledge about cross scattering from image simulations can be used to determine both compositions iteratively.

All composition determination methods can be optimized with regards to the ADF-STEM detector range. The exploitation of angular dependencies of electron scattering [128] offers great potential for further improvements and developments in the future. In particular, this is made possible by the available experimental hardware, i.e. pixelated detectors. Next to optimizing the composition determination of the material systems investigated in this work, this kind of composition determination which is looking for single-atom accuracy can also be extended to different III/V semiconductors as well as other crystalline materials with unknown composition.

6 Scientific Contributions

6.1 Atomic Structure of "W"-type Quantum Well Heterostructures Investigated by Aberration-Corrected STEM

P. Kükelhan, A. Beyer, C. Fuchs, M. J. Weseloh, S. W. Koch, W. Stolz, K. Volz. *Journal of Microscopy* 268(3) (2017), pp. 259-268. doi: 10.1111/jmi.12647

Abstract The atomic structure of *(GaIn)As/Ga(AsSb)/(GaIn)As*-"W"-type quantum well heterostructures ("W"-QWHs) is investigated by scanning transmission electron microscopy (STEM). These structures were grown by metal organic vapor phase epitaxy and are built for type-II laser systems in the infrared wavelength regime. For two samples grown at 525 °C and 550 °C, intensity profiles are extracted from the STEM images for each sub lattice separately. These intensity profiles are compared to the one obtained from an image simulation of an ideal "W"-QWH that is modeled in close agreement with the experiment. From the intensity profiles, the width of the different quantum wells (QWs) can be determined. Additionally, characteristics connected to the growth of the structures, such as segregation coefficients and material homogeneity, are calculated. Finally, composition profiles are derived from the STEM intensity profiles to a first approximation. For these composition profiles, the expected photo-luminescence (PL) is computed using the semiconductor luminescence equations. The PL spectra are then compared to experimental measurements for both samples.

Contributions of the Author For this work, I performed all STEM investigations and evaluations.

The manuscript was written by me except for three paragraphs dealing with MOVPE and PL theory.

Journal of Microscopy

Journal of Microscopy, Vol. 268, Issue 3 2017, pp. 259–268 doi: 10.1111/jmi.12647
Received 30 May 2017; accepted 7 September 2017

Atomic structure of 'W'-type quantum well heterostructures investigated by aberration-corrected STEM

P. KÜKELHAN, A. BEYER, C. FUCHS, M.J. WESELOH, S.W. KOCH, W. STOLZ & K. VOLZ
Materials Science Center and Faculty of Physics, Philipps-Universität Marburg, Hans-Meerweinstraße 6, Marburg, Germany

Key words. HAADF-STEM, image simulation, photoluminescence, quantum well heterostructure, type-II laser system.

Summary

The atomic structure of (GaIn)As/Ga(AsSb)/(GaIn)As-'W'-type quantum well heterostructures ('W'-QWHs) is investigated by scanning transmission electron microscopy (STEM). These structures were grown by metal organic vapour phase epitaxy and are built for type-II laser systems in the infrared wavelength regime. For two samples grown at 525°C and 550°C, intensity profiles are extracted from the STEM images for each sublattice separately. These intensity profiles are compared to the one obtained from an image simulation of an ideal 'W'-QWH that is modelled in close agreement with the experiment. From the intensity profiles, the width of the different quantum wells (QWs) can be determined. Additionally, characteristics connected to the growth of the structures, such as segregation coefficients and material homogeneity, are calculated. Finally, composition profiles are derived from the STEM intensity profiles to a first approximation. For these composition profiles, the expected photoluminescence (PL) is computed based using the semiconductor luminescence equations. The PL spectra are then compared to experimental measurements for both samples.

Introduction

Modern semiconductor lasers in the infrared wavelength regime are suitable for a variety of applications that especially include telecommunications (Murphy, 2010). Emission wavelengths of 1300 nm enable more efficient optical telecommunications. For this, novel GaAs-based material systems, in particular type-II laser systems, are suggested (Zegrya & Andreev, 1995; Meyer *et al.*, 1998). In these systems, electrons and holes are spatially separated in different quantum wells (QWs). For wavelengths greater than 1200 nm, a design based on a 'W'-type quantum well heterostructure ('W'-QWH) was proposed (Berger *et al.*, 2015) and successfully grown (Fuchs *et al.*, 2017). The active region of this design is a (GaIn)As/Ga(AsSb)/(GaIn)As-QWH. The origin of the name 'W'-QWH comes from the resemblance of the band structure to the letter 'W'. Based on this structure, a vertical-external-cavity surface-emitting laser at 1200 nm has also been realised (Möller *et al.*, 2016).

To achieve laser devices at higher emission wavelengths, an efficient interplay between the theoretical prediction of the optical properties, growth of the designed structure and both the optical and structural characterisation of the realised structure is necessary. The theoretical predictions are based on a fully microscopic theory. These 'W'-QWHs can be grown by metal organic vapour phase epitaxy (MOVPE). For the first optical characterisation, photoluminescence (PL) measurements are suitable. Structural characterisation can be carried out, for example, by X-ray diffraction (XRD) (Fuchs *et al.*, 2017) or conventional transmission electron microscopy (TEM). Although with the first method a quantitative analysis on a larger scale is possible, some TEM techniques offer an atomic resolution of the structure. For a quantitative analysis at an atomic scale, atomically resolved high angle annular dark-field scanning transmission electron microscopy (HAADF-STEM) is an appropriate method. This has been used in the present work for a quantitative characterisation of the grown 'W'-QWHs. In addition, the dominant Z-contrast of atomic resolution HAADF-STEM offers the possibility of quantifying the composition of a sample. Here, the intensity in the image is determined both by the atomic number of the present element (Pennycook & Jesson, 1991) and by the thickness of the sample (Watanabe *et al.*, 2001). Alongside atomic-scale composition determination (Van Aert *et al.*, 2009; Rosenauer *et al.*, 2011), HAADF-STEM has also been successfully applied to the characterisation of interfaces (Han *et al.*, 2017). A good method for the quantitative interpretation of HAADF-STEM images is the comparison to image simulations (Jones, 2016). Image simulation as a comparative tool is widespread and able to reproduce experimental results very precisely (LeBeau *et al.*, 2008). By comparing results obtained both experimentally and through simulations, a more in-depth analysis is possible. When using HAADF-STEM for the investigation of QWHs, it is necessary to consider strain relaxation of the thin TEM specimen for the interpretation of

Correspondence to: Pirmin Kükelhan, Materials Science Center and Faculty of Physics, Philipps-Universität Marburg, Hans-Meerweinstraße 6, 35032 Marburg, Germany. Tel +49 64212825713; fax +49 642128935; e-mail: pirmin.kuekelhan@physik.uni-marburg.de

the resulting HAADF images. This can lead to a severe modification of the intensities in the image (Beyer *et al.*, 2017), thus resulting in a misinterpretation when determining composition. In this work, through the use of linear elastic theory (De Caro *et al.*, 1995) and valence force field (VFF) relaxation (Keating, 1966) this strain relaxation is included in the image simulation. Hence, a comparison to image simulations can prevent a misinterpretation of the experimentally obtained intensities. Furthermore, for the quantitative evaluation procedure of the image intensities the concept of Voronoi-cells is applied to reduce the influence of strain relaxation on the image intensities (E *et al.*, 2013).

With this approach, it is possible to identify the different elements in the respective QWs and determine their spatial distribution. The concept of segregation coefficients of elements during growth by MOVPE, which has previously been used for similar material systems (Muraki *et al.*, 1992; Volz *et al.*, 2009), enables a further quantitative characterisation of both the structure and the growth. Using this, it is possible to correlate the obtained structural properties with both the growth by MOVPE and the optical properties. This can then be combined with theoretical calculations of the optical properties in order to improve material systems for laser applications.

In this work, first the HAADF images of two 'W'-QWHs grown at different temperatures by MOVPE are presented and evaluated quantitatively. This gives rise to both an atomic depiction of the 'W'-QWH and a determination of parameters including both the aforementioned segregation coefficient and the material homogeneity. Finally, the atomic structure is correlated to the optical properties of the samples.

Materials and methods

The epitaxial growth of the 'W'-QWHs was carried out using an AIXTRON AIX 200 GFR (Gas Foil Rotation) (Aixtron SE, Herzogenrath, Germany) metal organic vapour phase epitaxy (MOVPE) reactor system. The growth process was carried out on exactly oriented, semi-insulating GaAs (001) substrates at a reactor pressure of 50 mbar. Triethylgallium (TEGa) and trimethylindium (TMIn) were used as group III precursors, whereas tertiarybutylarsine (TBAs) and triethylantimony (TESb) were used as group V precursors. Here, the reactor pressure is the sum of all partial pressures and the carrier gas, whereas the partial pressures of group III and group V precursor gases are smaller than 1 mbar. High-purity H_2 was used as the carrier gas and a TBAs-stabilised bake-out procedure was applied prior to the sample growth in order to remove the native oxide layer from the substrates. Growth temperatures of 525°C and 550°C were chosen in order to achieve a sufficiently high antimony concentration while preventing the incorporation of impurities into the materials. V/III ratios of 2.5 and 4 were chosen for the growth of Ga(AsSb) at 525°C and 550°C, respectively (Fuchs *et al.*, 2017). Thereby, the ratio of the partial pressures of In to group III elements was 0.75 at both growth temperatures, whereas the ratio of the partial pressures of Sb to group V elements was 0.39 at 525°C and 0.73 at 550°C.

Cross-sectional TEM samples in the [010]-direction were prepared by grinding and polishing with a Multiprep™ System (Allied High Tech Products, Inc., Rancho Dominguez, CA, United States) down to a thickness of around 20 μm. The final thinning and polishing was carried out with a precision ion polishing system (model 691 Gatan, Inc., Pleasanton, CA, United States) using Ar-ions. Acceleration voltages ranged from 4 to 1.2 kV and the inclination angle of the ion beam on the sample surface was set to 4°. This preparation procedure results in wedge-shaped samples. Plasma cleaning (model 1020 E. A. Fischione Instruments, Inc., Export, PA, United States) was performed prior to the STEM measurements.

To characterise the samples with HAADF-STEM, a double C_S-corrected JEOL JEM2200FS (Jeol Ltd., Tokyo, Japan) with an acceleration voltage of 200 kV was used. A condenser aperture size of 40 μm resulted in an electron probe with a convergence semi-angle of $\alpha = 24$ mrad. The nominal camera length was set to 4 cm yielding inner and outer detector angles of 84 and 174 mrad, respectively (JEOL EM-24590YPDFI dark-field image detector). The inner angle was determined by measuring the shadow of the detector on a CCD camera and the outer angle is limited by the geometry of the microscope. Each image is an average of ten images taken with a dwell time of 3 μs and aligned with help of the software Smart Align (Jones *et al.*, 2015). The images were then normalised to the impinging beam which was determined from a beam image (He & Li, 2014) on the CCD camera.

For simulating the expected STEM contrast of the 'W'-QWH, the software package STEMsalabim (Oelerich *et al.*, 2017), based on the multislice method (Kirkland, 2010), was utilised. Thermal diffuse scattering is considered using the frozen phonon approximation (Loane *et al.*, 1991) and different phonon configurations. For each configuration, atomic displacements representing thermal vibration were randomly chosen. To incorporate chromatic aberration, a defocus series (Kuramochi *et al.*, 2009) was carried out with 7 defoci centred on $\Delta f = -2$ nm with a full width half maximum (FWHM) of 7.5 nm. The source size of the simulation was adopted to match that of the experiment using a Lorentzian convolution with $\sigma = 0.048$ nm. Further main parameters were also chosen corresponding to the experiment (cf. Table 1).

Table 1. Parameters for STEM image simulation.

Electron energy	200 kV
Aperture angle	24 mrad
Astigmatism	0 nm
C_S	2 μm
C_5	5 mm
C_C	1.5 mm
Lorentzian convolution	$\sigma = 0.048$ nm

In the simulated supercell, the respective amount of In and Sb was distributed randomly in the respective atomic columns of the QWs. These amounts of In (20.5%) and Sb (25.5%) were chosen as determined by XRD for the sample grown at 550°C. The QWs have a width of 6 nm ((GaIn)As) and 4 nm (Ga(AsSb)), respectively. To reconstruct a thin TEM sample, the supercell was relaxed by finite element calculation with linear elastic theory (De Caro *et al.*, 1995) and valence force field relaxation (Keating, 1966) to account for the lattice mismatch and the strain of the materials. The finite element calculations were realised with COMSOL Multiphysics® (Comsol Multiphysics GmbH, Göttingen, Germany) suite employing the elasticity parameters given in (Vurgaftman *et al.*, 2001) for binary materials, which have been extended for ternary materials using Vegard's law (Denton & Ashcroft, 1991). The parameters used are given in the supplementary material.

The simulated super cell had a width of 10 unit cells, whereas in the growth direction the super cell is only simulated to the centre of the 'W'-QWH in order to reduce computation time. This is possible because the described ideal 'W'-QWH is symmetric when not considering possible experimental effects like segregation. Next, the simulated image was mirrored to get the intensity profile for the whole 'W'-QWH. The thickness of the sample was chosen in accordance to the experimental samples for which the thickness can be determined from a comparison of the intensities of binary regions. Hence, the simulated super cell had a size of 5.7 nm × 12.8 nm × 22.5 nm (width × length × thickness). Additionally, two unit cells were added at the edges in x- and y-direction to exclude edge artefacts.

Photoluminescence (PL) measurements were carried out at room temperature by nonresonantly exciting the samples using a frequency-doubled Nd:YAG laser at a photon wavelength of 532 nm. An excitation power of 100 mW was chosen. The spectral resolution was obtained by dispersing the PL signal using a grating monochromator and detecting the resulting signal with a liquid nitrogen-cooled germanium detector and a lock-in amplifier. The theoretical modelling of the luminescence signal of the 'W'-QWHs is carried out using the fully microscopic theory described by Berger *et al.* (2015) based on the $\mathbf{k} \cdot \mathbf{p}$ model and solving the semiconductor luminescence equations (SLE).

Results and discussion

Both simulated and experimental quantitative HAADF-STEM were used to investigate the atomic structure of the 'W'-QWH. In Figure 1, the obtained images are shown along with a schematic of the 'W'-QWH (Fig. 1A). The origin of the name 'W'-QWH comes from the resemblance of the band structure shown in the schematic to the letter 'W'.

A simulated STEM image of the ideal 'W'-QWH in the [010]-direction (Fig. 1B) reveals the expected contrast and structure of the experimentally grown structures. In the [010]-direction, the sublattices of group III and group V elements can be easily separated, as indicated in the image (Fig. 1C).

Due to Z-contrast, the differences in atomic numbers for different elements in addition to the different QW structures built using these elements can be distinguished. On the group V sublattice, the Sb has the highest atomic number ($Z = 51$) and so causes the highest intensity leading to the detection of the Ga(AsSb)-QW.

Meanwhile, In has the highest atomic number on the group III sublattice and so identifies the (GaIn)As-QWs. On both sides of the 'W'-QWH the GaAs-barriers are the darkest regions.

This is also the case for the experimental STEM images obtained for the samples grown at both 550°C (Fig. 1C) and 525°C (Fig. 1D), where the growth direction is from left to right. The sample grown at 550°C is mentioned first from now on because this is the original growth temperature for the 'W'-QWHs (cf. Fuchs *et al.*, 2017). In addition to the Z-contrast, intensity differences in the GaAs-barriers originate from a thickness gradient introduced during sample preparation. The thickness of the investigated samples was in the range of 20 nm.

The respective intensity profiles were extracted from the images as follows: for each atomic column position, the intensity was averaged with a Voronoi cell (Rosenauer *et al.*, 2011; Jones *et al.*, 2014; Nguyen *et al.*, 2014). The main reason for using this approach is that the strain relaxation of the crystal for a thin TEM sample has been found to have a significant influence on the intensity of atomic columns in HAADF-STEM images (Beyer *et al.*, 2017). The application of Voronoi cells decreases this influence because it is counter-balanced by averaging the intensity of an atomic column over its Voronoi cell and therefore attributing the de-channelled intensity back to the respective column (Rosenauer *et al.*, 2011; E *et al.*, 2013).

Initially, the relaxation of the thin TEM specimen has only a small influence in the centre of the QWH, but this intensity modification effect increases closer to and at the interfaces of the QWs. Due to the long range of this effect, the intensity in the GaAs-barriers is also influenced. These effects must be taken into account when analysing the atomic structure of the 'W'-QWH.

In addition to using Voronoi cells, strain relaxation is also included in the STEM image simulation for the ideal 'W'-QWH. A comparison between simulation and experiment can be made to take into account the strain relaxation of the crystal.

Having determined the column intensities with Voronoi cells, a lattice plane is introduced for each layer of the respective sublattices in the growth direction (cf. Fig. 1D). For these lattice planes, a mean intensity and standard deviation is obtained. This gives layer-resolved intensities of the separate sublattices in the growth direction, which allows for the intensity profiles of both group III and group V sublattices to be deduced (cf. Fig. 2).

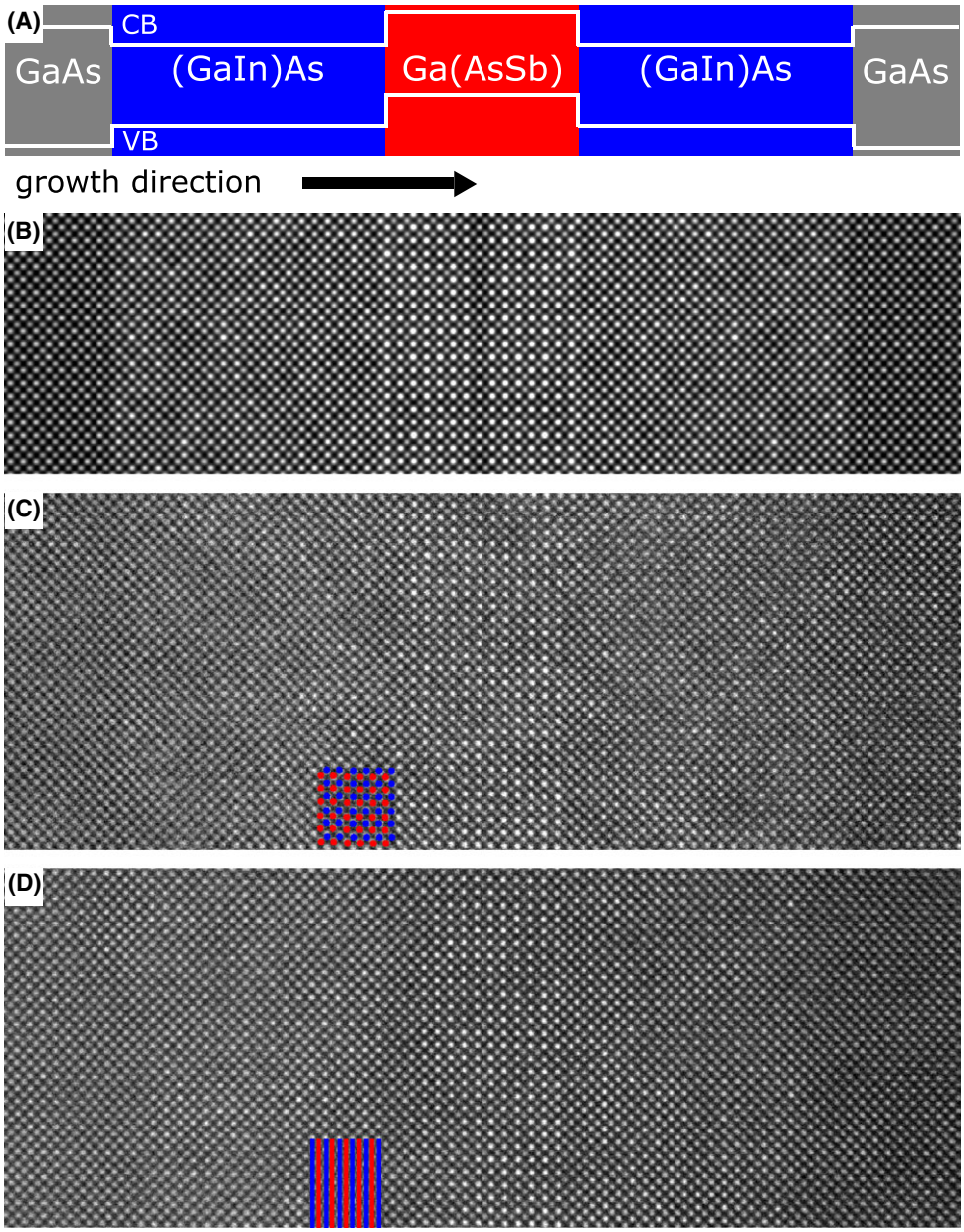

Fig. 1. Simulated and experimental STEM images of the 'W'-QWH. A schematic design of the 'W'-QWH is shown in (A). Additionally, the band structure with conduction (CB) and valence band (VB) is shown. The simulated STEM image (B) is obtained with all main parameters in accordance to the experimental images. Note that the image is mirrored in the centre of the 'W'-QWH. A STEM image of the sample grown at 550°C is shown in (C) together with a small inset illustrating the lattice separation into group III (blue) and group V (red). For the sample grown at 525°C, the STEM image is displayed in (D). Here, a small inset explains the separation into lattice planes. Due to the Z-contrast of the images, the different QWs are detectable.

The intensity profiles of group III and group V sublattices are shown for the simulated STEM image of the ideal 'W'-QWH, as well as for the two samples grown at temperatures of 550°C and 525°C (Fig. 2). The thickness gradient of the experimental samples was corrected by applying a linear background to the intensity in the GaAs-regions for both sublattices independently. Additionally, the intensities were normalised to the intensities in the GaAs-regions, that is to the intensity of Ga for the group III sublattice and the intensity of As for the group V sublattice, respectively. These two steps allow for a better comparison between the different intensity profiles to be made. All profiles are centred on the midpoint of the Ga(AsSb)-QW.

Due to the Z-dependency (Krivanek *et al.*, 2010), the intensities are correlated to the composition of the considered layer. For the group III profile, the intensity in the GaAs-regions is linked to Ga ($Z = 31$). In the (GaIn)As-QWs the higher

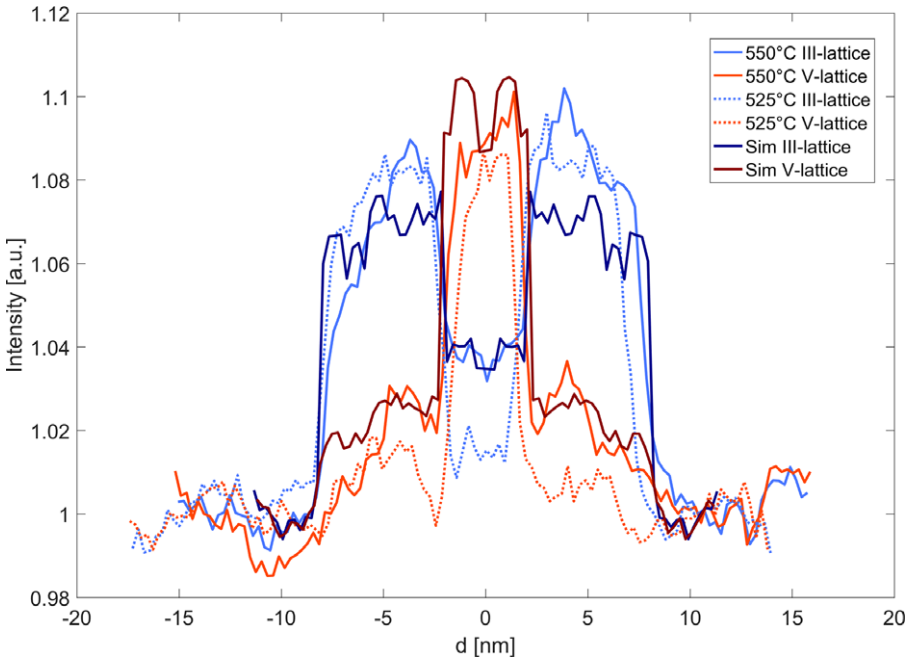

Fig. 2. Intensity profiles deduced from the STEM images. To guide the eye, the intensity values, which are lattice plane resolved, are interpolated linearly. The intensity profiles are thickness corrected and normalised to the intensities of Ga for the group III lattice and As for the group V lattice. For the group III lattice (blue colours), the intensity is increased in the (GaIn)As-QWs due to the higher atomic number of the included In. Similarly, the group V lattice intensity (red colours) is increased in the Ga(AsSb)-QW because of the higher atomic number of Sb. Intensity profiles are shown for the simulated image (solid, dark lines) and the two experimental samples grown at 550°C (solid, light colours) and 525°C (dotted, light colours).

intensity is caused by the In with a higher atomic number ($Z = 49$) being present in addition to the Ga. Similarly, for the group V profile, the intensity in the GaAs-regions is connected to the As-content ($Z = 33$). The Sb-concentration ($Z = 51$) in the Ga(AsSb)-QW causes an increased intensity in the corresponding region.

In addition, the intensity is also influenced by cross scattering from elements on the other sublattice (Nellist & Pennycook, 2000) which will be discussed in more detail later on.

First, the intensity profile of the ideal 'W'-QWH obtained from the simulated STEM image is discussed. From this, the expected intensity profile of the ideal structure is known and deviations of the grown samples can be identified afterwards.

In a simple approach, for the simulated intensity profiles box-like shapes are expected. To some degree, the intensity profile (shown in Fig. 2) agrees with this expectation. Fluctuations within the QW-regions are caused by the random distribution of In and Sb in the crystal in those regions, which lead to statistical fluctuations of the intensity. These can be decreased by using a larger simulation area, because a larger field of view contains more atomic columns for which the composition is statistically varying around the preset values. Therefore, the composition per lattice plane (as seen in the profile) approaches the preset values. A larger field of view, however, increases the computational costs. Furthermore, the edges in the intensity profile are not totally abrupt as designed in the simulated super cell, but slightly graded, which is caused by the included strain relaxation and modelled source size. This also leads to an overlap of the increased group III intensity in the (GaIn)As-QW and the increased group V intensity in the Ga(AsSb)-QW.

A general comparison of the simulated and the experimental intensity profiles shows a qualitative agreement between them. In the following, the width of the QWs and the grading of the QW interfaces are discussed quantitatively for the simulated and experimental data.

In order to define the width of the respective QWs, the positions of the QW edges were determined. For this, a criterion to locate the QW edge was defined: the edge is located at that position, where the intensity has changed by 50% of the total intensity change at the edge. This criterion makes it possible to find the edge positions.

From the QW edge positions, the width of the single QWs can be easily determined. These values are shown in Table 2

Table 2. Width of the different QWs for the simulation and experimental samples. The width is determined by applying a 50% criterion to the intensities.

	Simulation	550°C	525°C
First In-QW	6.1 ± 0.1 nm	5.5 ± 0.1 nm	5.6 ± 0.1 nm
Second In-QW	6.1 ± 0.1 nm	5.5 ± 0.2 nm	5.3 ± 0.1 nm
Sb-QW	4.3 ± 0.1 nm	3.7 ± 0.1 nm	3.0 ± 0.1 nm

for the simulated STEM image and both experimental samples. For the simulated image, the widths of the QWs are slightly higher than the preset ones, which is caused by the strain relaxation and beam broadening leading to a widening of the intensity profiles. Nonetheless, preset and measured widths are in good agreement. The widths of the (GaIn)As-QWs are similar for both experimental samples, but smaller than for the simulation. The widths of the QWs in the supercell were chosen according to the XRD results, which assume box-like composition profiles. This leads to the observed differences between experiment and simulation. These arguments can also be transferred to the Ga(AsSb)-QWs. For the two samples grown at 550°C and 525°C, the widths of the Ga(AsSb)-QWs are significantly different, with the Ga(AsSb)-QW being thinner for 525°C. Because the QW thicknesses have been calibrated by growing Ga(AsSb)/GaAs reference structures, this can be caused by the combination of different segregation behaviour at different temperatures (see below) and the growth on GaAs/(GaIn)As.

In addition, the grading of the interfaces for the simulated and experimental intensity profiles is investigated. The interfaces of the 'W'-QWH in the simulated image are almost box shaped, whereas the experimental edges are more graded. Besides a physically graded interface of the QWs, an apparent graded edge in the intensity profile could also be caused by, for example, beam broadening or the relaxation of the crystal. Because all of these influences are also included in the simulation, these explanations can be excluded and the interfaces of the experimentally grown samples are indeed graded.

The grading of the interfaces is also analysed quantitatively for the experimental samples. For this, the Muraki model for segregation (Muraki *et al.*, 1992) is applied to describe the expected segregation of In and Sb during the growth of the 'W'-QWHs. This segregation leads to the present saw tooth-like segregation profile shape for the experimentally grown samples that is expected from the growth conditions used. There are more complex models than the Muraki model that could be used to describe the segregation (Godbey & Ancona, 1997) as the Muraki model was found to fail in some cases (Walther *et al.*, 1997; Norris *et al.*, 2014). These more complex models will be applied in the future when the composition of the QWs can be determined more reliably to consider the effects of cross scattering, quaternary composition and relaxation on the intensity. By doing this, it should be possible to ensure that a change in the profile is not caused by one of these factors.

In the Muraki model, the concentration of the segregating element at the first interface of the QW (in the growth direction) is described by

$$I_n = x_0\ (1 - S^n)\,. \tag{1}$$

Here, I_n is the concentration in the nth monolayer, x_0 the nominal concentration and S the segregation coefficient characterising the fraction of the supplied element segregating to the next layer. Note, that to a first approximation this concentration is directly connected to the intensity profiles deduced as mentioned before if other influences on the intensity are not taken into account. Hence, the Muraki model is fitted to the intensity profiles even if the exact concentration of each layer is unknown.

The second interface of a QW is modelled by

$$I_m = x_0\ S^m. \tag{2}$$

Segregation leads to an incorporation of the respective element in the mth layer after the supply of this element is stopped. Examples of fits of the Muraki model to the intensity profiles for the sample grown at 525°C, are shown in Figure 3. The group III and V intensity profiles are shown in Figures 3(A) and (B), respectively. In both the figures, the determined intensity values are marked by blue crosses and the obtained fits of the Muraki model to the different QWs are illustrated by red lines. The segregation and R^2-parameters of these fits are shown as well. Additionally, the resulting segregation coefficients for both samples as well as the R^2-parameters of the fits are given in Table 3.

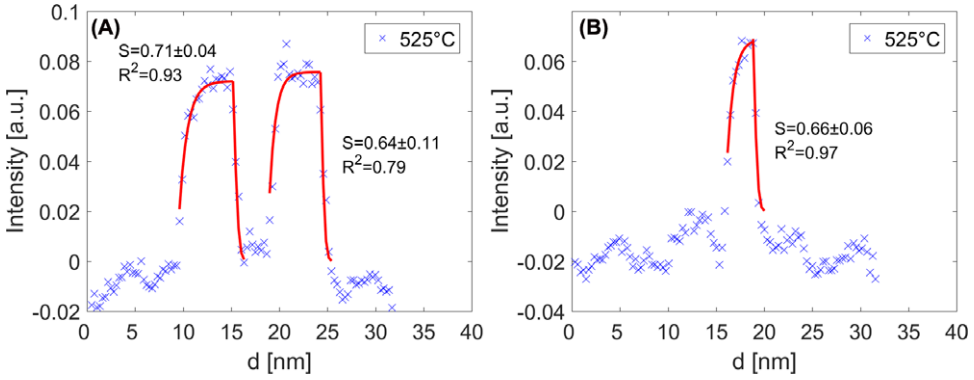

Fig. 3. Muraki model for segregation fitted to the group III (A) and group V (B) intensity profiles of sample grown at 525°C. The In- and Sb-QWs were fitted with the given segregation coefficients yielding the shown R^2-parameters. Between the In-QWs, the intensity values are larger than zero mainly due to cross scattering (see above explanations). The Muraki model is further discussed in the main text.

Table 3. Segregation coefficients for the samples grown at 550°C and 525°C as determined by the Muraki model.

	550°C	525°C
First In-QW	0.83 ± 0.04	0.71 ± 0.04
	$R^2 = 0.89$	$R^2 = 0.93$
Second In-QW	0.49 ± 0.13	0.64 ± 0.11
	$R^2 = 0.63$	$R^2 = 0.79$
Sb-QW	0.52 ± 0.12	0.66 ± 0.06
	$R^2 = 0.77$	$R^2 = 0.97$

Looking at the first (GaIn)As-QW (in the growth direction), the segregation coefficient is higher for the sample grown at 550°C than for the sample grown at 525°C. This finding is in agreement with a higher In-segregation at higher temperatures that was found for (GaIn)As-QWs grown on GaAs before (Schowalter *et al.*, 2006; Han *et al.*, 2015).

Looking at the second (GaIn)As-QW (in the growth direction), the segregation coefficients obtained from the fits are lower than that of the first (GaIn)As-QW. This could be related to the growth of this QW on GaAs/(GaIn)As/Ga(AsSb) instead of only GaAs, and so the growth is taking place on a strained layer. Additionally, the results indicate an unexpected behaviour: at the higher growth temperature (550°C), the fitted segregation coefficient is lower. Considering the related R^2-parameters and accuracies of the fits, the resulting segregation coefficients could hint towards different growth behaviours than those known from the growth of (GaIn)As on GaAs. However, this should be investigated in more detail prior to being trusted. Here, for example, a larger field of view along the QW interfaces appears promising for improving the statistics.

Looking at the Ga(AsSb)-QW, a parallel argument to the second (GaIn)As-QW can be made. Again, the segregation coefficients are lower than for the first (GaIn)As-QW and lower at the higher temperature. Likewise, the accuracy and the R^2-parameters indicate the need for further investigation that will be carried out in the same manner as mentioned before.

To conclude, the results obtained for the first (GaIn)As-QW grown on GaAs are in accordance with former results: Mehrtens *et al.* (2013) found a segregation coefficient of $S = 0.85$ for a sample grown by molecular beam epitaxy at 520°C by using STEM-HAADF. Piscopiello *et al.* (2005) investigated structures grown by MOVPE at 550°C by composition evaluation via the lattice fringe analysis method and determined a segregation coefficient of $S = 0.65$. Results presented by Schowalter *et al.* (2006) approve this value range, as well as segregation coefficients increasing with temperature. However, a direct comparison of results at the same temperature is difficult because the absolute calibration of growth temperature is problematic in general.

The results for the second (GaIn)As- and the Ga(AsSb)-QW are surprising and point towards a different behaviour for the growth on strained layers and in presence of a surface segregation layer. As such, they demand a more detailed investigation.

Another difference between the two experimental profiles is the intensity of the single-element lattice in the respective QW-region: the group III intensity in the Ga(AsSb)-QW and the group V intensity in the (GaIn)As-QW.

Generally, the group III intensity in the Ga(AsSb)-QW region is expected to be comparable to the group III intensity in the GaAs-barriers because there should be only Ga on the group III sublattice. However, this intensity can be increased in two ways: In-segregation in the Ga(AsSb)-QW or cross scattering due to the heavy atoms on the other sublattice being in close proximity, which is Sb in this case. For the increased group V intensity in the (GaIn)As-QWs, a parallel argument can be made. The increased intensities described above will be called 'cross-intensities' in the following discussion.

To find out the origin of the 'cross-intensities', the comparison to the simulated intensity profiles is a promising approach. Here, the QWs are ternary by design so that only cross scattering is present.

The simulation is compared to the intensity profile of the sample grown at 550°C which has the higher 'cross-intensities' of the two experimental samples. This comparison gives a good agreement of the group III intensities in the Ga(AsSb)-QW and the group V intensities in the (GaIn)As-QWs. This supports the idea of 'cross-intensities' being mainly caused by cross scattering, even with some degree of segregation. From this, it can be deduced that the lower 'cross-intensities' of the sample grown at 525°C are caused by less cross scattering rather than by less segregation. Because cross scattering is thickness dependent (Allen *et al.*, 2003), the smaller amount of cross scattering is caused by the smaller thickness of the sample grown at 525°C – the observed decrease was caused by a difference of less than 1 nm. This helps to explain the different 'cross-intensities' of the two samples.

Having determined the respective regions of the different QWs in the intensity profiles, one can also analyse the material homogeneity of the single QWs. This is correlated to the material quality and therefore influences the properties of the final device.

The homogeneity of the QWs is determined separately for each sublattice and QW- or GaAs-region: the standard deviation of the intensity (SDI) of the included lattice planes is averaged. The values for the two GaAs-regions are averaged. Because in these regions there is only Ga on the group III lattice and only As on the group V lattice, the SDI should be zero for both sublattices. As this is not the case, the resulting SDI is caused by experimental noise such as from the detector. The total SDI is assumed to take the following form:

$$\Delta I = \sqrt{\Delta^2_{composition} + \Delta^2_{noise}}. \quad (3)$$

Here, ΔI is the measured SDI of each QW, Δ_{noise} is the contribution from experimental noise and $\Delta_{composition}$ is the

Table 4. Material homogeneity for both samples (standard deviation of the respective chemical composition). The material homogeneity is connected to the intensity homogeneity and derived from statistical properties. Note that values for GaAs represent noise and have already been subtracted to get the homogeneity values for the QWs.

Lattice and QW	550°C	525°C
III-lattice: first In-QW	0.014 ± 0.009	0.014 ± 0.007
III-lattice: second In-QW	0.014 ± 0.009	0.016 ± 0.10
III-lattice: Sb-QW	0.010 ± 0.009	0.008 ± 0.012
III-lattice noise: GaAs	0.014 ± 0.009	0.014 ± 0.07
V-lattice: first In-QW	0.006 ± 0.013	0.005 ± 0.014
V-lattice: second In-QW	0.005 ± 0.014	0.007 ± 0.012
V-lattice: Sb-QW	0.018 ± 0.009	0.020 ± 0.007
V-lattice noise: GaAs	0.014 ± 0.009	0.016 ± 0.010

homogeneity of the QWs correlated to the material quality. Associating the mean SDI for Ga and As with Δ_{noise}, one can determine the homogeneity of the QWs for both sublattices. Additionally, $\Delta_{composition}$ is divided by the mean intensity of each QW-region for normalisation purposes. The uncertainties given for the QW results are due to the standard deviation of the SDI values for the lattice planes involved.

The resulting $\Delta_{composition}$ values for both the two sublattices and samples are shown in Table 4. Considering the statistical uncertainty, these values do not appear to differ between both samples and sublattices. Therefore, the homogeneity of the QWs is the same for both samples grown at different temperatures. Looking at the actual values, a $\Delta_{composition}$ value of below 2% is also quite small compared to other material systems (Wegele *et al.*, 2016).

The homogeneity of the QWs can be further supported by evaluating the standard deviations of the column composition and the column intensity for the simulated super cell. In the (GaIn)As-QW, a standard deviation for the group III intensities (the In-containing columns) is determined to be 0.018, whereas the standard deviation of the composition is 0.321. This is the expected order of magnitude for a Poisson distribution of In on the atomic columns proving that the grown In-QWs are as homogenous as possible by assuming a statistical distribution of In.

In the Ga(AsSb)-QW, the determined values give a standard deviation of 0.020 for the group V intensities (the Sb-containing columns) and a compositional standard deviation of 0.284. As such, the same argument can be made as for the (GaIn)As-QWs showing the homogeneity of the grown Ga(AsSb)-QWs.

Because the investigated 'W'-QWHs are of actual use for laser devices, the determined structures are correlated to the measured optical properties. Therefore, as a first

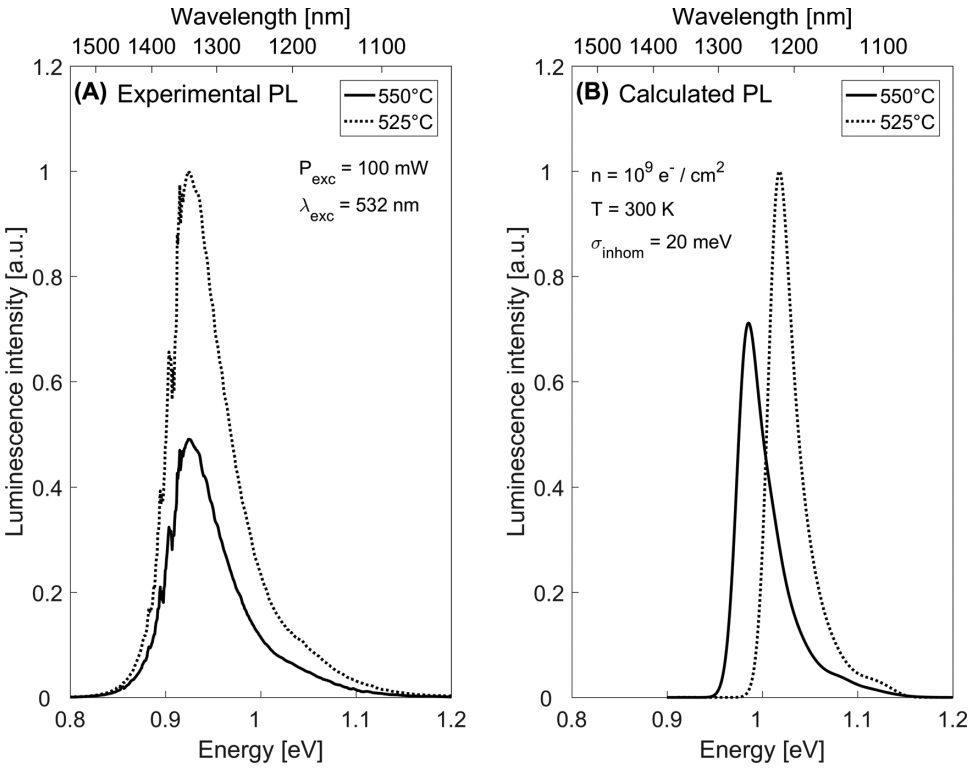

Fig. 4. Experimental and calculated PL of both samples. The experimental PL (A) was measured using the given parameters. For the calculated PL (B), the SLE are solved for approximated composition profiles deduced from the intensity profiles of the STEM images. Both PL spectra are shown on arbitrary intensity scales. Further discussion is taking place in the main text.

approximation composition profiles are deduced from the shown intensity profiles of both samples. The resulting PL of 'W'-QWHs featuring these compositions is calculated by solving the SLE (Berger *et al.*, 2015). This calculated PL is then compared to the experimentally measured PL of both samples.

The evaluation of the composition profiles is carried out in the following way: in the GaAs-regions, there is no In or Sb incorporated. So, the corresponding intensity is set to be the reference level of zero for both compositions. The averaged intensity in the QW-regions is correlated to the respective In- and Sb-concentration as determined by XRD measurements for the sample grown at 550°C (In-content: 20.5%, Sb-content: 25.5%). By these two reference values, the compositions are linearly assigned to the intensities in the respective QW-regions. To match the resolution of the theoretical calculations, these composition profiles are averaged with 1 nm bins. For these structural compositions, the SLE is solved.

In Figure 4(A) the PL measured experimentally for the two samples grown at different temperatures is shown. For visual purposes the PL spectra were smoothed over a span of five data points, as in this wavelength range the water vapour in the laboratory air leads to sharp absorption structures in the experimental PL spectra. Although the peak position of the PL for both samples is only slightly different, the peak intensity is higher by a factor of 2 for the sample grown at 525°C.

The calculated PL that is based on the composition profiles deduced from the STEM images is shown in Figure 4(B). Here, the PL intensity of the sample grown at 525°C is higher than the one of the sample grown at 550°C by a factor of 1.4. Because this result is based on composition profiles determined from the STEM intensity profiles in combination with XRD measurements in a rather simplistic manner, the qualitative trend is reasonable. Current work is aiming to get more precise results based on a quantitative intensity comparison to STEM simulations in addition to taking into account the influence of strain relaxation on these intensities.

In addition to the difference in intensities, the different energies compared to the experiment are notable. For similar 'W'-QWH with Sb-concentrations of around 20% in the central Ga(AsSb) layer, we have observed a deviation in emission energies of 20 meV between experiment and theory (Berger *et al.*, 2015). This is in very good agreement keeping in mind that: (i) a change in absolute chemical concentrations by 1% would already lead to a change in emission wavelength of 15 meV and (ii) that the hetero-offsets in these QWH systems are only determined with a precision of about 50 meV. Increasing the Sb-content to 25% in this study results in an increase in the deviation between experiment and theory to 50 meV. This observation points to a compositional dependence of the hetero-offset ratio between the respective conduction and valence band states of (GaIn)As and Ga(AsSb). Additional theoretical modelling studies are underway to clarify this hetero-offset behaviour in detail and, thus, to further improve the agreement in emission energy between experiment and theory.

Conclusion

In this work, investigations into the atomic structure of (GaIn)As/Ga(AsSb)/(GaIn)As-QWHs by STEM were presented. By evaluating the intensities of each sublattice in the III*V* semiconductor crystal, a determination of the respective QW-regions was possible. The samples grown at 550°C and 525°C have different segregation coefficients of In and Sb, respectively. In both samples, the segregation coefficient of In is different for the two (GaIn)As-QWs grown on GaAs and Ga(AsSb). However, the material homogeneity of both samples is the same. A comparison to a simulated STEM image of the 'W'-QWH proved helpful when evaluating the experimental data and has shown great promise for use in precise quantitative determination of the atomic structure in future investigations. Finally, the calculated PL spectra obtained from first approximations of the experimental composition profiles are in reasonable agreement with the measured PL of both samples.

Acknowledgements

Funding provided by the Deutsche Forschungsgemeinschaft (DFG) in the Framework of Sonderforschungsbereich 1083 – Structure and Dynamics of Internal Interfaces – is gratefully acknowledged.

References

Van Aert, S., Verbeeck, J., Erni, R., Bals, S., Luysberg, M., Van Dyck, D. & Van Tendeloo, G. (2009) Quantitative atomic resolution mapping using high-angle annular dark field scanning transmission electron microscopy. *Ultramicroscopy* **109**, 1236–1244.

Allen, L.J., Findlay, S.D., Oxley, M.P. & Rossouw, C.J. (2003) Lattice-resolution contrast from a focused coherent electron probe. Part I. *Ultramicroscopy* **96**, 47–63.

Berger, C., Möller, C., Hens, P. *et al.* (2015) Novel type-II material system for laser applications in the near-infrared regime. *AIP Adv.* **5**, 1–6.

Beyer, A., Duschek, L., Belz, J., Jandieri, K. & Volz, K. (2017) Influence of surface relaxation of strained layers on atomic resolution ADF imaging. *Ultramicroscopy* **181**, 8–16.

De Caro, L., Giuffrida, A., Carlino, E. & Tapfer, L. (1995) Elastic stress relaxation in HRTEM specimens of strained semiconductor heterostructures and its influence on the image contrast. *Microsc. Microanal. Microstruct.* **6**, 465–472.

Denton, A.R. & Ashcroft, N.W. (1991) Vegard's law. *Phys. Rev. A* **43**, 3161–3164.

E, H., MacArthur, K.E., Pennycook, T.J., Okunishi, E., D'Alfonso, A.J., Lugg, N.R., Allen, L.J. & Nellist, P.D. (2013) Probe integrated scattering cross sections in the analysis of atomic resolution HAADF STEM images. *Ultramicroscopy* **133**, 109–119.

Fuchs, C., Beyer, A., Volz, K. & Stolz, W. (2017) MOVPE growth of (GaIn)As/Ga(AsSb)/(GaIn)As type-II heterostructures on GaAs substrate for near infrared laser applications. *J. Cryst. Growth* **464**, 201–205.

Godbey, D.J. & Ancona, M.G. (1997) Modeling of Ge segregation in the limits of zero and infinite surface diffusion modeling of Ge segregation in the limits of zero and infinite surface diffusion. *J. Vac. Sci. Technol. A* **15**, 976–980.

Han, H., Beyer, A., Belz, J., König, A., Stolz, W. & Volz, K. (2017) Quantitative atomic resolution at interfaces: subtraction of the background in STEM images with the example of (Ga,In)P/GaAs structures. *J. Appl. Phys.* **121**, 1–9.

Han, H., Beyer, A., Jandieri, K., Gries, K.I., Duschek, L., Stolz, W. & Volz, K. (2015) Quantitative characterization of the interface roughness of (GaIn)As quantum wells by high resolution STEM. *Micron* **79**, 1–7.

He, D.S. & Li, Z.Y. (2014) A practical approach to quantify the ADF detector in STEM. *J. Phys.: Confer. Ser.* **522**, 1–4.

Jones, L. (2016) Quantitative ADF STEM: acquisition, analysis and interpretation. *IOP Conf. Ser.: Mater. Sci. Eng.* **109**, 1–20.

Jones, L., Macarthur, K.E., Fauske, V.T., Van Helvoort, A.T.J. & Nellist, P.D. (2014) Rapid estimation of catalyst nanoparticle morphology and atomic-coordination by high-resolution Z-contrast electron microscopy. *Nano Lett.* **14**, 6336–6341.

Jones, L., Yang, H., Pennycook, T.J. *et al.* (2015) Smart Align – a new tool for robust non-rigid registration of scanning microscope data. *Adv. Struct. Chem. Imag.* **1**(8), 1–16.

Keating, P.N. (1966) Effect of invariance requirements on the elastic strain energy of crystals with application to the diamond structure. *Phys. Rev.* **145**, 637–645.

Kirkland, E.J. (2010) *Advanced Computing in Electron Microscopy*. 2nd edn. Springer.

Krivanek, O.L., Chisholm, M.F., Nicolosi, V. *et al.* (2010) Atom-by-atom structural and chemical analysis by annular dark-field electron microscopy. *Nature* **464**, 571–574.

Kuramochi, K., Yamazaki, T., Kotaka, Y., Ohtsuka, M., Hashimoto, I. & Watanabe, K. (2009) Effect of chromatic aberration on atomic-resolved spherical aberration corrected STEM images. *Ultramicroscopy* **110**, 36–42.

LeBeau, J.M., Findlay, S.D., Allen, L.J. & Stemmer, S. (2008) Quantitative atomic resolution scanning transmission electron microscopy. *Phys. Rev. Lett.* **100**, 1–4.

Loane, R.F., Xu, P. & Silcox, J. (1991) Thermal vibrations in convergent-beam electron diffraction. *Acta Crystallogr. Sect. A* **47**, 267–278.

Mehrtens, T., Müller, K., Schowalter, M., Hu, D., Schaadt, D.M. & Rosenauer, A. (2013) Measurement of indium concentration profiles and segregation efficiencies from high-angle annular dark field-scanning transmission electron microscopy images. *Ultramicroscopy* **131**, 1–9.

Meyer, J.R., Felix, C.L., Bewley, W.W. *et al.* (1998) Auger coefficients in type-II InAs/Ga1-xInxSb quantum wells. *Appl. Phys. Lett.* **73**, 2857–2859.

Möller, C., Fuchs, C., Berger, C. *et al.* (2016) Type-II vertical-external-cavity surface-emitting laser with Watt level output powers at 1.2 μm. *Appl. Phys. Lett.* **108**, 1–4.

Muraki, K., Fukatsu, S. & Shiraki, Y. (1992) Surface segregation of In atoms during molecular beam epitaxy and its influence on the energy levels in InGaAs/GaAs quantum wells. *Appl. Phys. Lett.* **61**, 557–559.

Murphy, E. (2010) Enabling optical communication. *Nature Publishing Group* **4**, 287–287.

Nellist, P.D. & Pennycook, S.J. (2000) The principles and interpretation of annular dark-field Z-contrast imaging. *Adv. Imag. Electr. Phys.* **113**, 147–203.

Nguyen, D.T., Findlay, S.D. & Etheridge, J. (2014) The spatial coherence function in scanning transmission electron microscopy and spectroscopy. *Ultramicroscopy* **146**, 6–16.

Norris, D.J., Qiu, Y., Dobbie, A., Myronov, M. & Walther, T. (2014) Similarity of Stranski-Krastanow growth of Ge/Si and SiGe/Si (001). *J. Appl. Phys.* **115**, 1–8.

Oelerich, J.O., Duschek, L., Belz, J., Beyer, A., Baranovskii, S.D. & Volz, K. (2017) STEMsalabim: a high-performance computing cluster friendly code for scanning transmission electron microscopy image simulations of thin specimen. *Ultramicroscopy* **177**, 91–96.

Pennycook, S.J. & Jesson, D.E. (1991) High-resolution Z-contrast imaging of crystals. *Ultramicroscopy* **37**, 14–38.

Piscopiello, E., Rosenauer, A. & Passaseo, A. (2005) Segregation in InGaAs / GaAs Stranski – Krastanow layers grown by metal – organic chemical vapour deposition. *Philos. Magaz.* **85**, 3857–3870.

Rosenauer, A., Mehrtens, T., Müller, K. *et al.* (2011) Composition mapping in InGaN by scanning transmission electron microscopy. *Ultramicroscopy* **111**, 1316–1327.

Schowalter, M., Rosenauer, A., Litvinov, D. & Gerthsen, D. (2006) Investigation of segregation by quantitative transmission electron microscopy. *Opt. Appl.* **XXXVI**, 297–309.

Volz, K., Koch, J., Höhnsdorf, F., Kunert, B. & Stolz, W. (2009) MOVPE growth of dilute nitride III/V semiconductors using all liquid metalorganic precursors. *J. Cryst. Growth* **311**, 2418–2426.

Vurgaftman, I., Meyer, J.R. & Ram-mohan, L.R. (2001) Band parameters for III – V compound semiconductors and their alloys. *J. Appl. Phys.* **89**, 1–6.

Walther, T., Humphreys, C.J. & Robbins, D.J. (1997) Diffusion and surface segregation in thin SiGe/Si layers studied by scanning transmission electron microscopy. *Defect Diffus. Forum* 143–147, 1135–1140.

Watanabe, K., Yamazaki, T., Hashimoto, I. & Shiojiri, M. (2001) Atomic-resolution annular dark-field STEM image calculations. *Phys. Rev. A* **64**, 1–5.

Wegele, T., Beyer, A., Ludewig, P. *et al.* (2016) Interface morphology and composition of Ga(NAsP) quantum well structures for monolithically integrated LASERs on silicon substrates. *J. Phys. D: Appl. Phys.* **49**, 1–9.

Zegrya, G.G. & Andreev, A.D. (1995) Mechanism of suppression of Auger recombination processes in type-II heterostructures. *Appl. Phys. Lett.* **67**, 2681–2683.

Supporting Information

Additional Supporting information may be found in the online version of this article at the publisher's website:

Elasticity parameters used for finite element relaxation

6.2 Composition Determination of Semiconductor Alloys Towards Atomic Accuracy by HAADF-STEM

L. Duschek, P. Kükelhan, A. Beyer, S. Firoozabadi, J. O. Oelerich, C. Fuchs, W. Stolz, A. Ballabio, G. Isella, K. Volz. *Ultramicroscopy* 200 (2019), pp. 84-96.
doi: 10.1016/j.ultramic.2019.02.009

Abstract This paper presents a comprehensive investigation of an extended method to determine composition of semiconductors by scanning transmission electron microscopy (STEM) high angle annular dark field (HAADF) images and using complementary multi-slice simulations. The main point is to understand the theoretical capabilities of the algorithm and address the intrinsic limitations of using STEM HAADF intensities for composition determination. A special focus is the potential of the method regarding single-atom accuracy. All important experimental parameters are included into the multi-slice simulations to ensure the best possible fit between simulation and experiment. To demonstrate the capabilities of the extended method, results for three different technical important semiconductor samples are presented. Overall the method shows a high lateral resolution combined with a high accuracy towards single-atom accuracy.

Contributions of the Author For this work, I contributed to the development of the method and evaluated the capabilities of the method with the simulation study. Additionally, I performed the STEM measurements on the *(GaIn)As*-QW and evaluated the experimental STEM data.

I wrote the sections of the manuscript dealing with the evaluation of experimental data and the discussion.

Ultramicroscopy 200 (2019) 84–96

Contents lists available at ScienceDirect

Ultramicroscopy

journal homepage: www.elsevier.com/locate/ultramic

Composition determination of semiconductor alloys towards atomic accuracy by HAADF-STEM

L. Duschek[a], P. Kükelhan[a], A. Beyer[a,*], S. Firoozabadi[a], J.O. Oelerich[a], C. Fuchs[a], W. Stolz[a], A. Ballabio[b], G. Isella[b], K. Volz[a]

[a] Materials Science Center and Faculty of Physics, Philipps-Universität Marburg, Hans-Meerweinstraße 6, Marburg, Germany
[b] L-NESS, Dipartimento di Fisica, Politecnico di Milano Polo di Como via Anzani, 42 22100 Como Italy

ARTICLE INFO

Keywords:
multislice simulation
scanning transmission electron microscopy
composition determination
towards single atom accuracy

ABSTRACT

This paper presents a comprehensive investigation of an extended method to determine composition of materials by scanning transmission electron microscopy (STEM) high angle annular darkfield (HAADF) images and using complementary multislice simulations. The main point is to understand the theoretical capabilities of the algorithm and address the intrinsic limitations of using STEM HAADF intensities for composition determination. A special focus is the potential of the method regarding single-atom accuracy. All-important experimental parameters are included into the multislice simulations to ensure the best possible fit between simulation and experiment. To demonstrate the capabilities of the extended method, results for three different technical important semiconductor samples are presented. Overall the method shows a high lateral resolution combined with a high accuracy towards single-atom accuracy.

1. Introduction

In the last two decades, scanning transmission electron microscopy (STEM) developed into a very important characterization tool for atomic analysis of crystalline specimens [1,2]. Using high angle annular dark field (HAADF) detectors, this technique can provide directly interpretable atomic resolution images where the measured intensity is highly sensitive to the type and the number of atoms [3–5]. Since the electron-matter interaction as well as the image formation process have been understood in detail, it is nowadays possible to reproduce experimental images via numeric simulations [6]. Through the combination of experimental aberration corrected STEM HAADF images and complementary multislice simulations it is possible to extract important information about the sample such as the thickness, chemical composition or strain fields [7–10]. Since semiconductor devices such as lasers or transistors become constantly smaller, there is an increasing need for the local arrangements of atoms on an atomic scale. To gain such quantitative insights from crystalline structures, a lot of work has been performed to make electron microscopy a quantitative method [6]. Combining all knowledge of the past years of research, several methods have been proposed to gain quantitative information from crystalline samples [11–13]. Van Aert and coworkers have published significant work in the field of statistical model-based quantitative characterization of a $La_{0.7}Sr_{0.3}MnO_3$-$SrTiO_3$ interface [14–17]. Also Grieb et al. demonstrated quantitative composition determination for the samples of Ga(N,As) [18,19] and (Ga,In)(N,As) [10,20,21], using the averaged intensities from STEM multislice simulations and comparing them to experimental images.

This work focuses on the composition determination of ternary III/V and binary group IV semiconductor alloys with atomic precision. The technique to compare experimental intensities with simulated intensities known from literature [10,18,21,22] is extended in this work. All influencing experimental parameters are included and a detailed analysis of the used simulated supercells opens up the possibility to push the precision to single-atom accuracy. This is shown using a detailed simulation study. The evaluation scheme is applied to experimental images of technologically relevant semiconductor samples. The experimental samples are the following: $(Ga_{1-x}In_x)As$ quantum wells (QW) are investigated, potentially being part of a 'W'-type or a multi QW heterostructure used in an infrared laser device [23]. Furthermore a $Ga(P_{1-x}As_x)$ QW structure is analyzed that might be used as a barrier in several different laser designs. Additionally a $Si_{1-x}Ge_x$ QW heterostructure is investigated, where the Ge fraction x is varied in the attempt of obtaining a parabolic confining potential [24]. Especially in devices as lasers, transistors, solar cells and photodetectors a detailed knowledge of the element´s local distribution is a key factor in the

* Corresponding author.
E-mail addresses: lennart.duschek@physik.uni-marburg.de (L. Duschek), andreas.beyer@physik.uni-marburg.de (A. Beyer).

https://doi.org/10.1016/j.ultramic.2019.02.009
Received 9 August 2018; Received in revised form 21 December 2018; Accepted 12 February 2019
Available online 13 February 2019
0304-3991/

optimization process. This work shows, how to determine the exact composition of atomic columns in a ternary/binary alloy with the detailed analysis of STEM HAADF multislice simulations, using the STEMsalabim package [25].

Following this introduction, the samples used as well as the experimental equipment used is explained in detail in Section 2. Furthermore, the complementary simulations used to evaluate the data will be outlined. In Section 3, the method itself is described and explained in detail followed by plots of the resulting intensity composition relationships. A detailed analysis of the limitations with regards to single atom accuracy is the focus of the next paragraph.

Section 4 starts with the description of the raw experimental data. The determination of the local thicknesses is described afterwards, as it is different for every sample used and has an important role in the quantitative analysis. The results are presented in color coded 2D composition maps of the investigated samples that have a lateral resolution of one atomic column. Furthermore line scans in growth direction are presented and compared to well established methods for composition determination such as high resolution X-ray diffraction (HRXRD) and lattice constant analysis. For the latter technique, the lattice constant is derived from the experimental images and combined with Vegard's law and tetragonal distortion due to pseudomorphic growth to determine the composition.

At the end, a discussion points out the potential of single-atom accuracy of the method and the role of experimental influences is assessed.

2. Methods and experiment

The investigated samples include a $(Ga_{1-x}In_x)As$ quantum well (QW) structure between GaAs barriers, which will be referred to as sample I, as well as a $Ga(P_xAs_{1-x})$ quantum well structure between GaP barriers, which will be referred to as sample II. Both of these samples were grown for TEM investigations via metalorganic vapor phase epitaxy (MOVPE) using an AIXTRON AIX 200 GFR reactor (Gas Foil Rotation) (Aixtron SE, Herzogenrath, Germany). Sample I was grown on an exactly oriented, semi-insulating GaAs (001) substrate at a growth temperature of 550 °C [23]. The (Ga,In)As QW structure is 6.1 nm wide with an In concentration of 20%, derived from HRXRD.

Sample II was grown on an exactly oriented, semi-insulating GaP (001) substrate at a growth temperature of 550 °C. The Ga(P,As) QW layer has a width of 11.7 nm and the As content is about 65.5% which was determined by HRXRD [26].

Sample III is a strained SiGe multi-quantum well heterostructure, which was grown via low-energy plasma-enhanced chemical vapor deposition (LEPECVD) on a Si (001) substrate [27]. The buffer layer on which the QW structures are grown, consists of a 2 µm thick $Si_{0.2}Ge_{0.8}$ layer on top of a 11 µm linearly graded buffer [28]. 15 QW layers with a width of 30 nm are grown with a Ge concentration graded between 65% and 100% in a parabolic manner. In this work, only the first QW of the sample is investigated.

All samples were conventionally prepared for cross-sectional TEM investigations in [010] direction. Mechanical grinding and polishing was carried out for all samples utilizing an Allied MULTIPREP system (Allied High Tech Products, Inc., Rancho Dominguez, CA, United States). The final thinning and polishing was done by Ar-ion milling with a precision ion polishing system (model 691 Gatan, Inc., Pleasanton, CA, United States) until electron transparency was achieved. The acceleration voltage of the Ar-ions was progressively reduced from 5 kV to 1.2 kV to limit the amorphous surface layers and damage of the thin specimen. The inclination angle of the ion beam used was 6° resulting in a wedge shape of the TEM samples, which can be seen as a thickness gradient in the STEM images. All samples were treated in a plasma cleaner (model 1020 E. A. Fischione Instruments, Inc., Export, PA, United States) before inserting them into the microscope.

All HAADF measurements shown here were carried out in a double C_s-corrected JEOL JEM 2200FS (JEOL Ltd., Tokyo, Japan) operating at 200 kV acceleration voltage. The annular dark-field detector used (JEOL EM-24590YPDFI) detected electrons scattered to an annular range that was determined for each image using the method proposed by LeBeau and Stemmer [29] namely measuring the physical shadow of the detector on a CCD camera to determine the inner detector angle. For sample I the detector ranges were 63–252 mrad, for sample II 74–174 mrad and for sample III 68–272 mrad. A condenser aperture with a size of 40 µm diameter was used, which led to a semi-convergence angle of 21 mrad of the probe. To improve the signal-to-noise-ratio and to reduce the effect of sample drift on the image, each STEM image is the average of multiple images with a short dwell time (3 µs). The images have been aligned with the Smart Align software [30]. Furthermore the image intensity was normalized to the intensity of the impinging beam applying the approach described in [31]. The peak positions of the atomic columns were found by the 2D peak finding program PeakPairs [12].

2.1. Complementary STEM HAADF simulations

To gain quantitative information from the STEM HAADF images, complementary contrast simulations are necessary. All steps described in the next paragraph are equivalent for the samples introduced above. Structure models were created with dimensions of 5 × 5 unit cells in *X*- and *Y*- direction and with 80 unit cells in *Z*-direction (electron beam direction). The ternary/binary alloys were generated by randomly replacing atoms in the base matrix (e.g. GaAs for sample I) with the substitute atom (e.g. In for sample I). The lattice constant for the corresponding resulting compound material was calculated by Vegards law [32,33]. The composition of the cells was chosen between 0% and 100% in steps of 5% for all three samples. The atom positions for sample I & II were relaxed via a force field, using a Keating potential as described by Rubel et al. [34,35]. This has been done to acknowledge the static atomic displacements (SADs), caused by the different atom sizes and electronegativity [36]. It has already been shown in literature that SADs have a significant influence on the HAADF intensities in STEM [8]. Sample III has not been relaxed in the same way because the differences in covalent radii and electronegativities between Si and Ge are minor compared to the other two systems investigated.

Then these cells were used as input for the simulation software, called STEMsalabim [25], that was used for this investigation. This software package is designed for highly parallelized simulations on high-performance computer clusters and implements the multislice algorithm presented by Kirkland in [37,38]. A more detailed description on the technical implementation and scaling of the code can be found in [25]. Thermal diffuse scattering (TDS) was taken into account using the frozen lattice approach [39], where the atomic positions get displaced statistically (Gaussian distribution) from their resting positions. To include chromatic aberration, a defocus series of 7 defocus values was calculated for every individual simulation cell as described in [40–43]. For each defocus value, 10 phonon configurations were simulated, resulting in 70 individual phonon configurations for one simulation cell. In addition, the detector sensitivity was determined and applied to all simulations as proposed by LeBeau et al. in [44]. The finite source size as well as beam broadening by amorphous layers were included by convoluting a two dimensional Lorentzian distribution to the simulation of the form:

$$S_L = \frac{\sigma}{(x^2 + y^2 + \sigma^2)^{3/2}},$$

where x and y are the spatial coordinates and σ describes the width of the distribution. This step is crucial to match simulation intensities as closely as possible to the experimental images as described in [40]. A detailed explanation on the choice of the width parameter sigma of the Lorentzian function will be given in a later chapter. All simulation

Table 1
Experimental parameters of the used electron microscope. All the parameters were used for the complementary multislice simulations.

Electron beam energy	200 kV
Aperture angle	21 mrad
Cs	2 µm
C_5	5 mm
C_C	1.5 mm
ΔE	0.42 eV

parameters were carefully chosen to fit the experimental setup and are summarized in Table 1.

3. Results

This chapter presents the steps necessary to determine the composition of the investigated samples using HAADF-STEM images and complementary multislice simulations. First, the method itself is explained and it will be shown how the *intensity composition relationships* are extracted from the multislice simulations. The capabilities of the extended method are highlighted afterwards and the intrinsic limitations towards single-atom accuracy are pointed out. Thereafter, the raw experimental STEM images are introduced which are used to demonstrate the composition determination method. Several parameters have to be taken into account to match the simulated STEM intensity to the experimental intensities. The various important parameters are addressed in the upcoming section. Since the thickness determination plays a crucial role to gain accurate results, three different methods to consider thickness locally are explained and demonstrated using the experimental images. Three technologically important semiconductor samples are used to present the method. The color coded 2D composition with a lateral resolution of one atomic column are explained in detail. Line scans are compared to established methods such as HRXRD and lattice constant analysis.

3.1. Intensity composition relationship

The foundation of the method described is to find the dependency between the STEM HAADF intensity and the number of included substitute atoms. Since the method should be as accurate as possible, the analysis is carried out for every atomic column. The first step for analyzing the simulated concentration set is to retrieve STEM HAADF images from the raw simulation data. The experimental parameters needed for this, i.e. sample thickness, detector angles or the sigma parameter of the Lorentzian distribution, can be determined with the method explained in an upcoming chapter. For every STEM image created from the simulated concentration set, the atomic column positions are extracted from the simulation cell and divided into group III and group V (or group IV respectively). The Voronoi intensity [13,45] is determined and correlated to the number of substitute atoms in the column. Since simulated results are processed, the count of substitute atoms in every atomic column is given by design. The value pair of Voronoi intensity and number of substitute atom is determined for every column in every simulation of the concentration set. With this, a dependency between number of substitute atoms and Voronoi intensity is build up gradually. Fig. 1a–c shows the dependencies for a fixed thickness of 32 atoms in total and experimentally used detector angles, as stated in previous chapter, for all three samples used in this work. It is important to derive the *intensity composition relationships* for every column thickness present in the experimental image to be able compare it to every column individually. Every blue dot visible in Fig. 1a–c represents an intensity – number of atoms value pair derived from a simulation of the concentration set. It is noticeable in the plots that there is a deviation in intensity for one fixed number of substitute atoms. For example: for 10 In atoms embedded in GaAs with 32 atoms thickness, the Voronoi intensity ranges from 0.055 to 0.057. This effect is caused by the different heights of the substitute atoms in the crystal in reference to the defocus of the electron beam [46,47]. As already mentioned above, the distribution of the substitute atoms' coordinates is random and thus also the height. Crosstalk between atomic columns can affect the intensity on a specific column as well [48,49]. These two effects are the main reasons why there is a deviation in the Voronoi intensity for a specific amount of substitute atoms. These inherent statistical fluctuations influence the corresponding STEM HAADF images and therefore introduce a fundamental limitation of the achievable accuracy of the composition determination. In addition to this theoretical limit, in experimental STEM HAADF measurements where additional noise is present, the achievable accuracy may be reduced. Further on, the Voronoi intensity as well as the standard deviation is calculated for each number of substitute atom. The red markers in Fig. 1a–c depicts the mean Voronoi intensity for a fixed number of substitute atom. The "errorbars" mark the maximum overlap of the standard deviations for different numbers of substitute atoms. In other words, if the upper maximum of the standard deviation of one specific number overlaps with the minimum of the next higher number, the uncertainty is one atom. This also represents the highest precision possible for each atom number of a specific material. All three sample materials, used in this work, show a maximum precision error of ± 2 atoms at a total thickness of 32 atoms. The deviation in the Voronoi intensity is influenced by the elements, which build up the material, as well as the total thickness and the detector range of interest.

The dependencies that follow from the analysis, described above will be called intensity composition relationship in the following. Each intensity composition relationship depicted in Fig. 1a–c shows an increasing, nearly linear behavior of the Voronoi intensity with increasing number of substitute atoms. This is because a lighter element is substituted with a heavier one and thus increasing the mean atomic number Z of the column. The slope of the plot depends on the atomic number of the substitute atom as well as the difference to the replaced atom, since heavier elements have a higher influence on the STEM HAADF intensity. To visualize this effect more clearly, a second x-axis has been plotted in Fig. 1a–c. There, the plotted intensities were normalized to the surrounding base material, i.e. GaAs for sample I, GaP for sample II and Si for sample III. The limits of the axis reflect the slope of the plot. This means that the intensity difference between pure GaAs and InAs (Fig. 1a) or pure GaP and GaAs (Fig. 1b) is smaller than the difference between pure Si and pure Ge (Fig. 1c). Comparing sample I and II, it is noticeable that the points of pure GaAs do not match in Voronoi intensity. This is due to the different inner detector angles (63 mrad for sample I and 74 mrad for sample II), which affects the intensity strongly. The inner detector angles of sample I and III were 63 mrad and 68 mrad and thus are more comparable. The second axis in Fig. 1c ranges from 1 to 4, whereas the limits of the second axis in Fig. 1a only range from 1 to 1.4. The drastic difference in this limits originates, amongst others, from the different sample structure (diamond, zincblende) of the samples. Since the substitute atoms in the diamond SiGe sample occupy both fcc sub lattices, the fractional compositions of Ge actually reflect twice the absolute number of substitute atoms compared to the zincblende case.

3.2. Capabilities and limitations the method

In the following paragraph, the capabilities and limitations of the presented method are investigated. The subject is the overall accuracy with a special focus on accuracy towards single-atom detection. For this, simulated STEM images with known composition and thickness are used as input. The resulting number of substitute atoms that are determined by the algorithm proposed are verified by the supercell used as input. This is used to derive a percentage of exactly determined atomic columns. Furthermore, the number of columns that differ by a certain number of substitute atoms are extracted and are examined. The

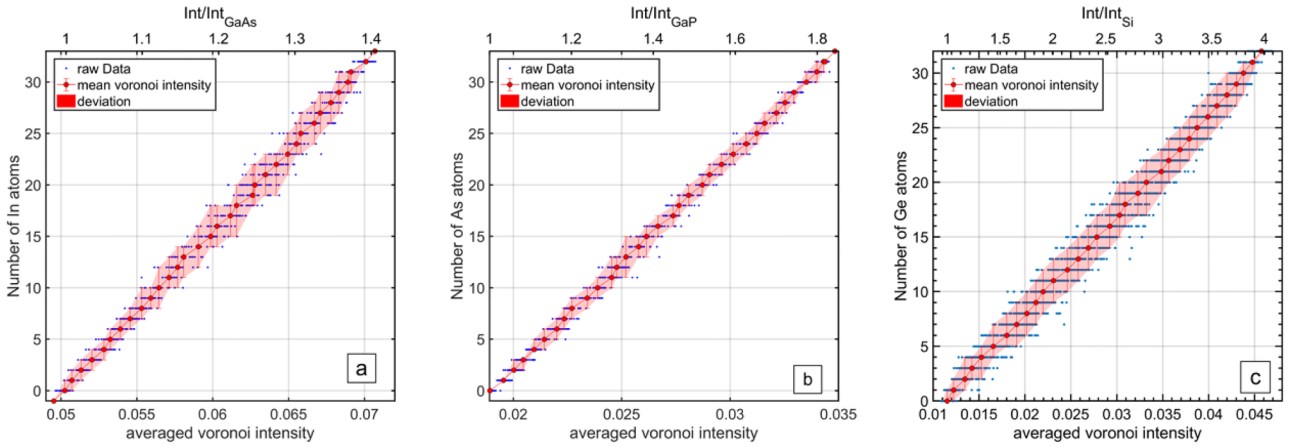

Fig. 1. The figure shows the *intensity composition relationships* for all corresponding samples I and III. The blue dots mark the averaged Voronoi intensity of every atomic column of each concentration set. The red markers illustrate the mean intensity for every atom count, whereas the "errorbars" mark the overlap of the standard deviations, which is the maximum precision achievable. The second *x*-axis shows the intensity normalized to the barrier material. With this a quantitative comparison between all samples is possible. All figures were calculated for total thickness of 32 atoms. (For interpretation of the references to color in this figure legend, the reader is referred to the web version of this article.)

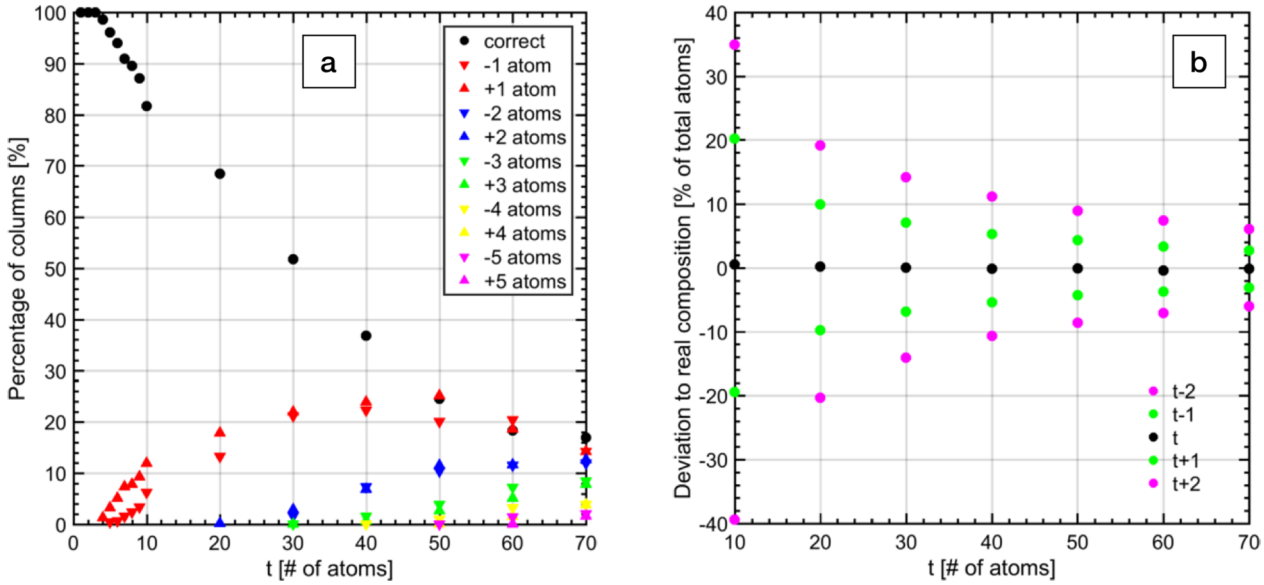

Fig. 2. Percentage of correctly determined atomic columns versus the sample thickness *t* for (Ga,In)As with 20% In concentration (a). With increasing sample thickness, the percentage of correctly determined atomic columns decreases and the number of atomic columns, off by several atoms increases. The number of underestimated columns is nearly the same as the number of overestimated columns, resulting in the correct average composition for all thicknesses. Subfigure (b) shows the deviation of the real composition determined from all atomic columns (810 in total) versus sample thickness. Assumed sample thickness affects the deviation of real composition. The composition deviation is symmetrically distributed around 0, which means that the mean concentration stays mainly correct.

benchmark will be exemplarily done with GaInAs with 20% indium content incorporated. To improve statistics, 10 simulations are used as input with random atom configurations. This ensures, that the benchmark covers a decent amount of indium atoms distributed in e-beam direction. The individual simulations are 5 × 5 unit cells in lateral dimensions which leads to 81 group III atomic columns, edge columns excluded. Overall, the 10 simulations then add up to 810 examined atomic columns. The analysis was also carried out for varying sample thickness. Fig. 2a depicts the results from the benchmark. The y-axis shows the percentage of atomic columns that are either determined correctly or differ by one or up to five substitute atoms. The percentage of atomic columns is plotted against the sample thickness *t* presented in number of atoms in e-beam direction. The black dots depict the number of correctly determined atomic columns, meaning that the exact amount of substitute atoms resulted from the algorithm. The differently colored triangles show the fraction of atomic columns, where the result is off by one or up to five atoms, according to the legend. The upwards facing triangles represent deviation in the positive direction whereas the downwards facing triangles show negative deviation.

The plot, seen in Fig. 2a starts at 1 atom thickness and 100% correctly determined atomic columns. This is not relevant for experimental cases but important to check for the correct operation of the algorithm. The exact number of substitute atoms can be determined correctly on each atomic column up to a sample thickness of 3 atoms. At 10 atoms thickness, the percentage of exactly determined atomic columns drops to 82% with a deviation in one atom of 13% in positive direction and 5% in negative direction. From statistics, these values should be equal since overestimation of the In content is as likely as underestimation according to Fig. 1a. The discrepancy observed is most likely caused by insufficient statistics at a thickness of only 10 atoms. For higher thicknesses, the errors are distributed nearly symmetrically around zero.

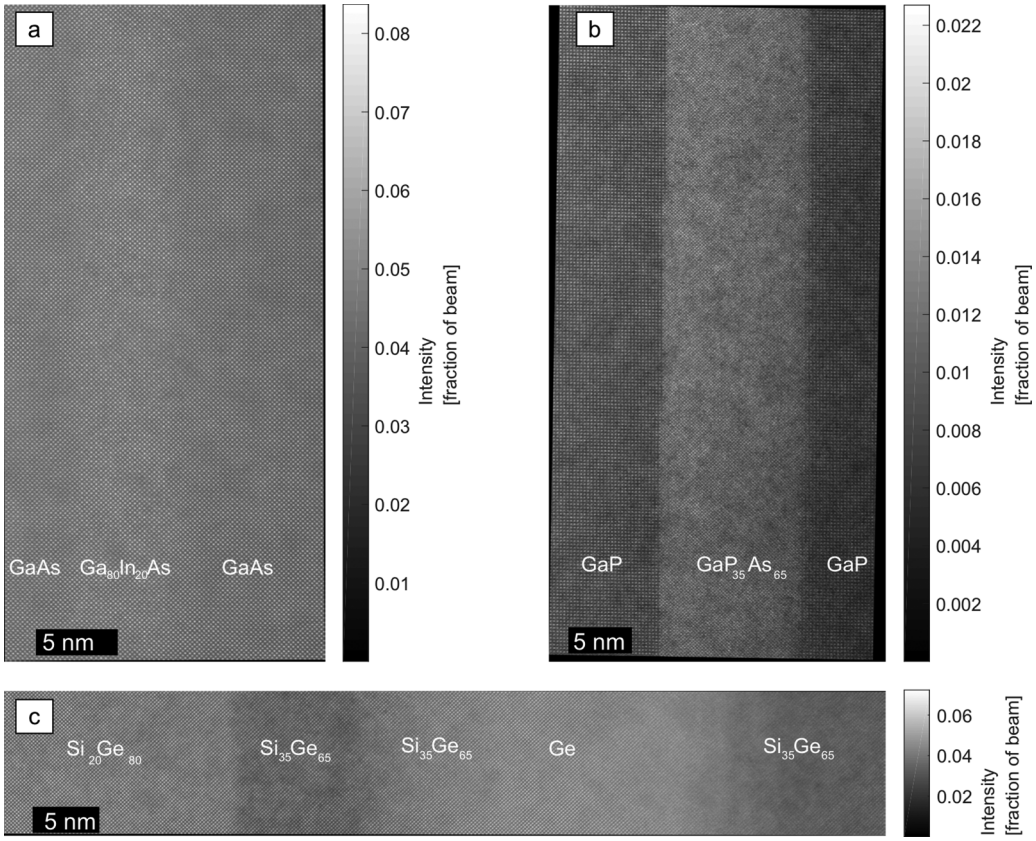

Fig. 3. STEM images of all three samples normalised to the impinging electron beam. (a) Sample I, a (Ga,InAs)-QW between GaAs barriers. (b) Sample II, a Ga(P,As)-QW between GaP barriers. (c) Sample III, SiGe with different Ge concentrations. Growth direction is from left to right.

With increasing thickness *t*, the percentage of exactly determined atomic columns drops and the percentage of atomic columns with some atoms deviation increases accordingly. Up to a sample thickness of 50 atoms the maximum deviation is in the range of 2 atoms. At thicknesses higher than 50 atoms, a small fraction of atomic columns are determined with a deviation of 3 atoms or higher.

To check how the atomic deviations influences the total determined composition of the sample, Fig 2b shows the deviation from the real composition in percent versus the sample thickness *t*. The black dots represent the deviation from real composition if the correct thickness is assumed. The deviation from the real composition starts at 0.5% at 10 atoms thickness and decreases with increasing sample thickness down to 0.1% at 50 atoms thickness. This means, that the mean of the determined atomic columns is still very accurate with a deviation under 0.5% for (Ga,In)As with 20% indium and thicknesses below 70 atoms. The deviation from real composition is given in absolute percentage, i.e. a deviation of 0.5% would mean that In content 19.5% or 20.5% would be determined instead of the 20% being present in reality.

If the assumed thickness of the sample is incorrect by 1 or two atoms, deviation from the real composition increases. The green dots, depict the total deviation with a thickness error of 1 atom. The deviation increases tremendously to 20% whilst still remaining centered symmetrically around 0% deviation. The deviation starts at (±) 20% indium concentration at 10 atoms sample thickness. This deviation decreases with increasing sample thickness down to (±) 3% at 70 atoms thickness. With a thickness error of two atoms the deviation starts at (±) 37% at 10 atoms thickness and decreases down to (±) 6% at 70 atoms thickness whilst also remaining symmetrically distributed around 0%.

This analysis summarizes the capability of the composition determination via STEM HAADF intensities using the example of (Ga,In)As with 20% indium concentration. The accuracy of the method is determined mainly by the thickness of the sample and the slope of the intensity composition relationship (compare Fig. 1). The steeper the slope is, the higher is the accuracy of the intensity method.

The analysis shows that the precision of correct determined number of atoms is higher at thinner samples. The thicker the sample is, the higher is the deviation in determined number of substitute atoms. Nevertheless, it can be said that the deviation is in the range of 1–2 atoms per atomic column. Furthermore, the analysis of the mean composition determined from the atomic columns shows a negligible deviation from the real composition for all investigated thicknesses *t* at a correctly assumed sample thickness. This stresses the fact, that calculating the correct sample thickness is crucial for the composition determination. If the assumed thickness is off by one or two atoms, it has a tremendous effect on the composition determination. However, since the deviations are symmetrically around zero when over/underestimating the thickness, they are likely to cancel out in experimental images due to statistics. This will be shown in later paragraphs.

3.3. Collocation of raw experimental data

With the capabilities of the presented method in mind, the next paragraph addresses the application on experimental samples. A $(Ga_{1-x}In_x)As$ quantum well (QW) is investigated, potentially being part of a 'W'-type or a multi QW heterostructure used in an infrared laser device. Furthermore, a $Ga(P_{1-x}As_x)$ QW structure, that might be used as a barrier in several different laser designs is investigated. Moreover, a $Si_{1-x}Ge_x$ QW heterostructure is investigated, where the Ge fraction *x* is varied in the attempt of obtaining a parabolic confining potential. [24]

For all three samples, STEM images were acquired under HAADF conditions. These are shown in Fig. 3. Due to the dominant Z-contrast under HAADF conditions, the different QWs are clearly visible within the respective barriers. For all samples the substituting atoms are heavier than the atoms in the matrix (i.e. In (49) vs. Ga (31), As (33) vs. P (15) and Ge (32) vs. Si (14)), therefore the QW appears brighter than the matrix material in all cases.

For a quantitative analysis of these raw STEM images, intensities are

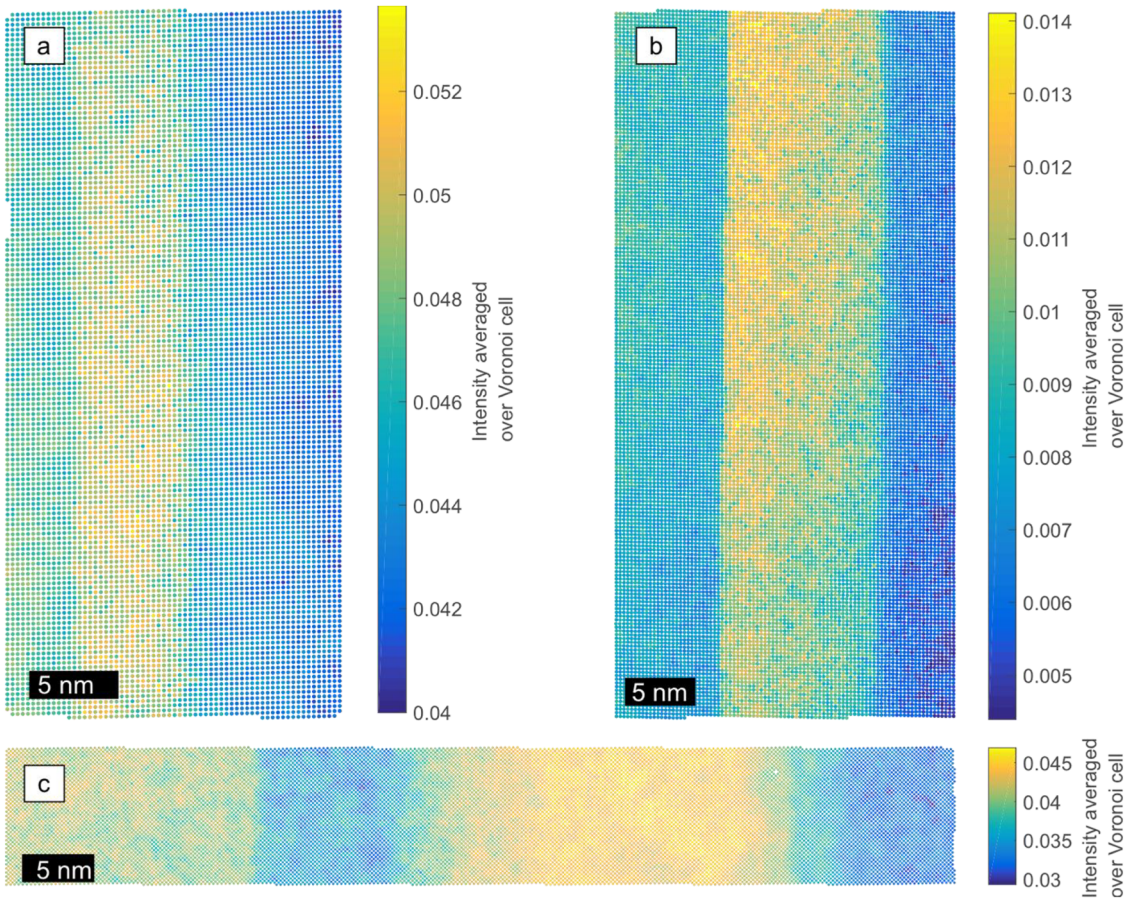

Fig. 4. Intensity maps showing the intensities of every atomic column averaged using Voronoi cells. For sample I (a), only the group III sub lattice is shown, for sample II (b) only the group V lattice is shown. In (c), all atomic columns of sample III are shown. Growth direction is from left to right.

evaluated by Voronoi cells and assigned to every atomic column [21,45]. In a Voronoi cell, every pixel is belonging to its closest atomic column and for every column the intensity of the appropriate pixels is averaged. These Voronoi intensities have the advantage of being robust regarding most experimental influences [45] especially including surface relaxation that is important for our samples [50]. Using these Voronoi cells, Voronoi intensity maps are created as shown in Fig. 4. For clarity, only the sub lattice on which the composition change is taking place is shown in the Voronoi intensity map. This is the group III sub lattice for sample I (Fig. 4a), the group V sub lattice for sample II (Fig. 4b) and the group IV lattice for sample III (Fig. 4c) which is the only lattice present in this sample. To determine the influence of cross scattering to neighboring columns and show the thickness gradient (see later chapter), additionally Voronoi intensity profiles are shown for the group III and V sub lattices in the case of sample I and II and for group IV for sample III (Fig. 5).

3.4. Matching of simulation and experiment

To determine the composition of semiconductor alloys by intensity comparison of experiment and simulation, the simulation has to reproduce the experiment as closely as possible. Considering the influences mentioned above, a parameter for the Lorentzian convolution of the simulation remains to be determined. This takes into account the size of the electron source [40].

The adaption of the simulation to the experiment has to take place in a region with known composition, i.e. the barrier, and at the correct thickness.

In sample I, this adaption is done for GaAs. Here, for every peak of one sub lattice the surrounding unit cell is found and the average experimental unit cell (AEUC) of GaAs is generated as shown in Fig. 6a. For the simulated image of GaAs, which has a size of 5 × 5 unit cells, the average simulated unit cell (ASUC) is also calculated (Fig. 6b). Now, the most suitable thickness – that is number of atoms – for the simulation is chosen so that the mean intensity of the ASUC is matching the mean intensity of the AEUC. As the composition is the same in both experiment and simulation, thickness is the decisive parameter for matching both. A thickness intensity relationship can be obtained by evaluating the ASUC for different thicknesses. This relationship and the best fitting thickness are shown in Fig. 6d.

At this thickness, a Lorentzian convolution of the simulated image is performed using a range of different widths of the Lorentzian. Minimizing the total deviation between AEUC and ASUC for all pixels, the correct width $\sigma = 0.049$ nm is found. The resulting ASUC with correct thickness and width σ is shown in Fig. 6b. A pixel wise 2D representation of the relative difference between both AEUC and ASUC is presented in Fig. 6c already showing the good overall agreement. To get an exact comparison of both images, they are aligned using the software SmartAlign [30] beforehand. The good agreement between experiment and simulation is also supported by a diagonal line scan across both ASUC and AEUC plotted in Fig. 6e. The difference in 2D pixel wise intensity between the experimental and simulated intensity can be calculated to 1.6% in this case for GaAs in sample I.

The corresponding figures for sample II and sample III, respectively, can be found in the supplements. Here, a difference between experimental and simulated 2D pixel wise intensity of 1.1% (GaP in sample II) and 1.4% ($Si_{0.2}Ge_{0.8}$ in sample III) is achieved.

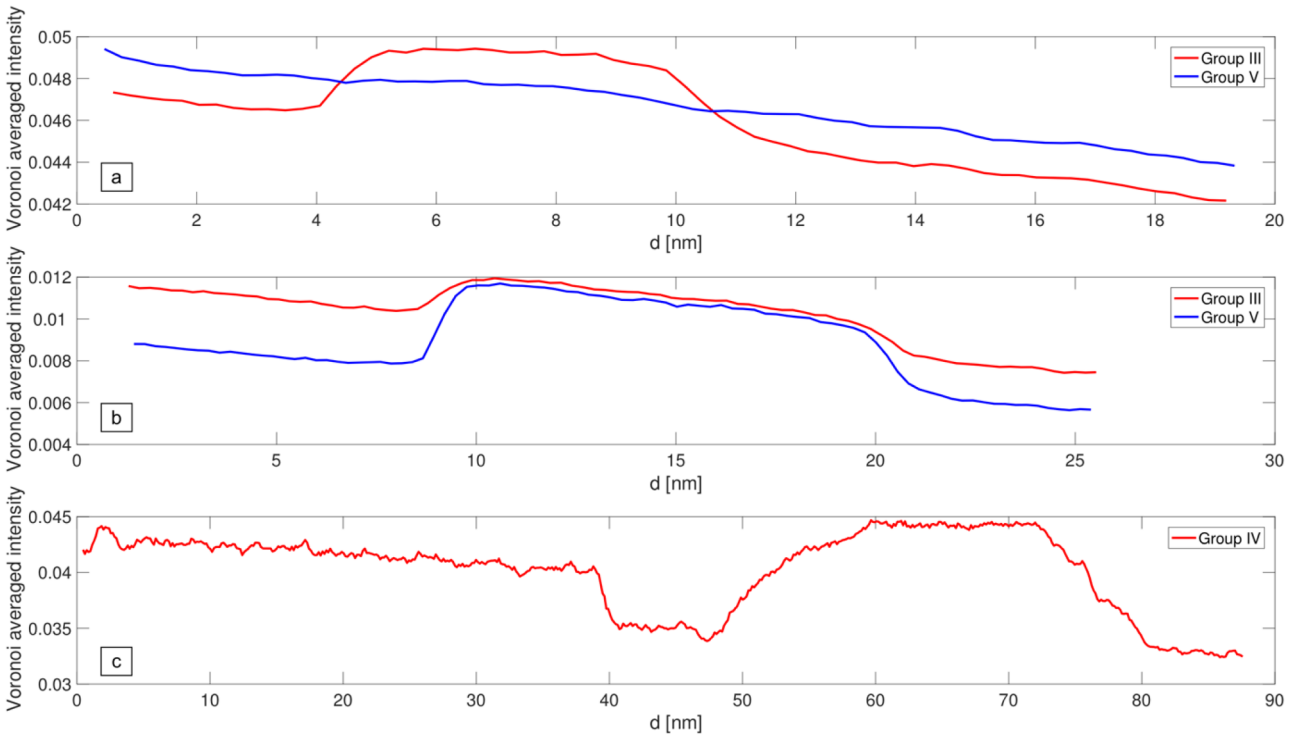

Fig. 5. Voronoi averaged intensity profiles of all three samples. In (a) and (b) both sub lattices of sample I ((Ga,In)As-QW in GaAs barrier) and sample II (Ga(P,As)-QW in GaP barrier) are shown. The intensity profile for sample II (SiGe-QW in SiGe barrier) is shown in (c). Growth direction is from left to right.

3.5. Local thickness determination

In this way, suitable parameters for a matching between experiment and simulation were determined. To be able to find the composition of every atomic column, for each column the thickness, i.e. the number of atoms in this column, has to be specified. A determination of the thickness is only possible with a known composition of the atomic column. In order to assign a thickness to a column with unknown composition, thickness information about the material itself or the surrounding atomic columns are necessary. There are several

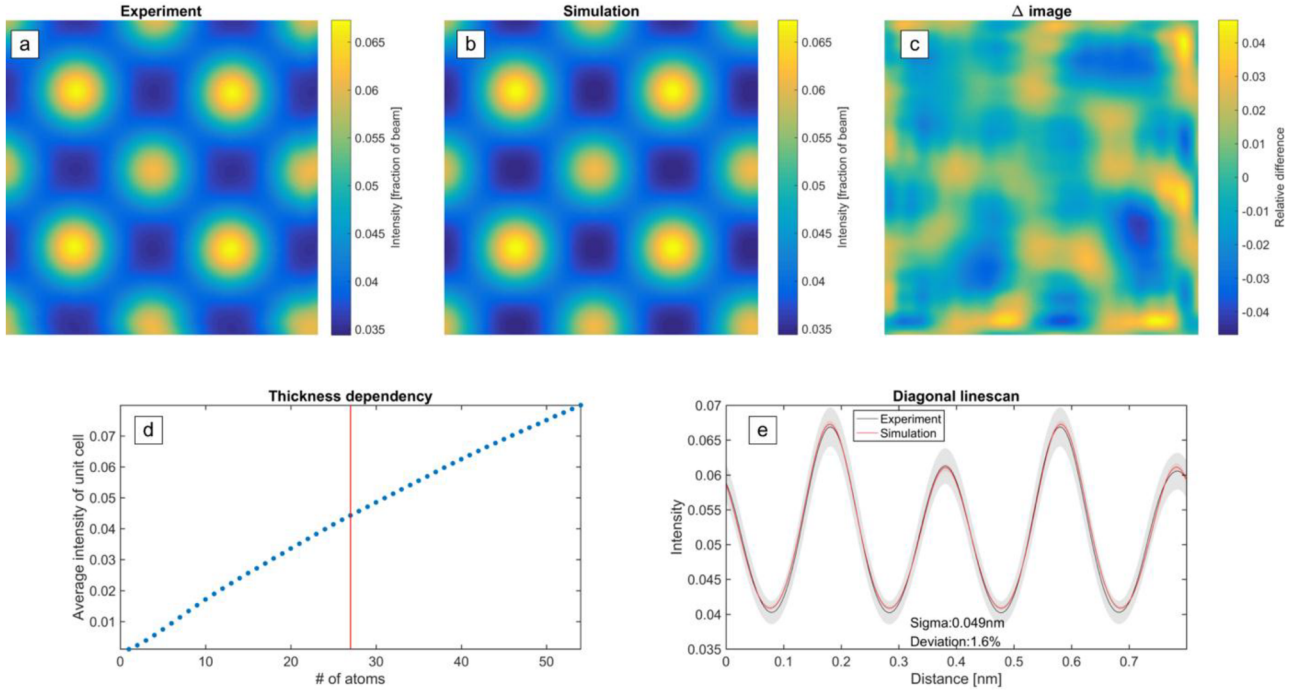

Fig. 6. Adapting simulation to experiment for GaAs. The correct thickness is found by matching the unit cell averaged intensities with the simulated thickness intensity relationship shown in (d). The respective unit cells are shown in (a) and (b) for experiment and simulation, respectively. By choosing a suitable width for the Lorentzian convolution, representing the source size, both show a good agreement as proven in 1D by a diagonal line scan (e) across both images as well as in 2D by difference image (c), normalized to the intensity of the simulated unit cell. A deviation in Voronoi intensity of only 1.6% was achieved.

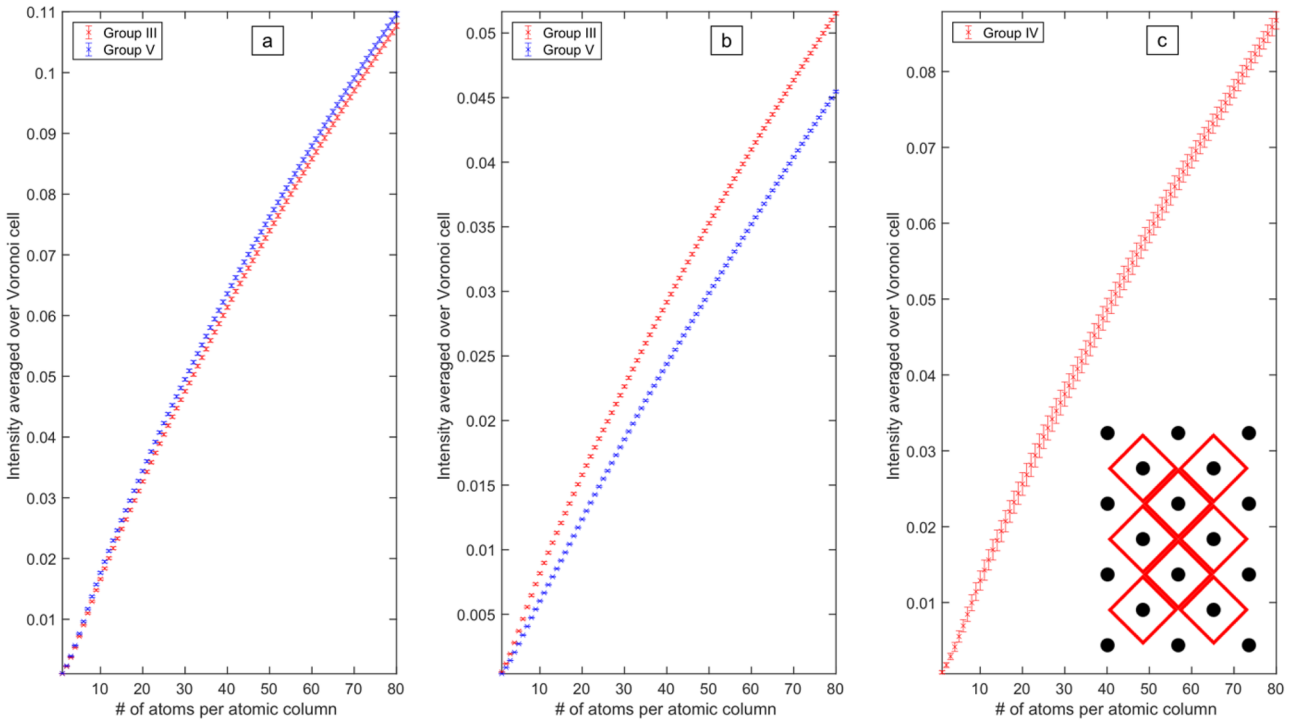

Fig. 7. Thickness dependencies for Voronoi intensities. The different barrier materials are presented: GaAs in (a), GaP in (b) and $Si_{0.2}Ge_{0.8}$ in (c). The inset in (c) illustrates the concept of the Voronoi cell.

possibilities to do so, which will be explained for the different samples in the following.

In sample I, there is a composition change on one sub lattice only, as group V columns are consisting of As in the barrier and the QW region. In contrast, the group III sub lattice composition is changing across the sample: there is only Ga in barrier regions but Ga and In in the QW region. Since the sample is thin enough (thickness determined by unit cell average is 27 atoms), there is no substantial influence of one sub lattice on the other during the electron scattering process, i.e. there is no cross scattering. This assumption is supported by the line plots depicted in Fig. 5(a) and (b). Comparing subfigure (a) to subfigure (b), one can see the clear effect of cross scattering in subfigure (b) but not in (a). Therefore, the group V sub lattice can be used to determine the thickness of the sample. The intensity is compared to simulated Voronoi intensities, As in the case of sample I (see Fig. 7a), and the suitable thickness is assigned. Since finally the thickness of group III sub lattice atomic columns is needed, for every group III column the thickness of the 4 neighboring group V columns is averaged and assigned to the group III column. The resulting thickness map of group III atomic columns only is shown in Fig. 8a. Thicknesses are ranging from 25 to 33 atoms per column. This thickness gradient is induced by the preparation method as explained earlier. The thickness map shows a reasonable thickness distribution considering the last preparation step of Ar ion milling.

In sample II, the composition change is also taking place on one sub lattice only. Here, group III atomic columns consist of Ga atoms everywhere, while group V atomic columns consist of P atoms in the barrier regions and P and As in the QW. As can be seen in Fig. 5b, cross scattering plays a more important role in this sample. Thus, even if the composition stays constant on the group III sub lattice it cannot be used for a thickness determination in the QW. Instead, the thickness in the QW region is interpolated by fitting a plane to the intensities of the group V columns in the barrier. There, the original intensities of every column are taken for thickness determination while in the QW region the intensities are interpolated. The QW region is found by setting an intensity threshold for gradient normalized column intensities. Intensities above this threshold are then assigned to the QW region. The intensities assigned to each peak are then compared to the thickness dependent simulated P intensities and the thicknesses are determined. In Fig. 8b the resulting thickness map for the group V sub lattice is shown. Thicknesses range from 8 to 18 atoms per column. In the interpolated region, the small length scale features are necessarily gone but the fitted plane is the best approximation of the thickness in this region.

In sample III, there is only one sub lattice on which Si and Ge concentration are changing. Additionally, there is no region consisting only of Si or pure Ge. Instead, there is a region where the Ge concentration is nominally 80%. However, as can be seen from the intensity profile (see Fig. 5c) the intensity is also fluctuating in this region suggesting that the concentration may not be constant here. Therefore, only a mean concentration of 80% Ge is assumed. A plane is fitted to the linear decreasing region (see Fig. 5c) and intensities are assigned to the columns based on this plane both in the buffer layer of $Si_{0.2}Ge_{0.8}$ and in the region of unknown composition. This technique is only suitable if the reference region is large enough (40×40 nm in this case) and shows a linear behavior. Using a simulation of $Si_{0.2}Ge_{0.8}$ and its mean Voronoi intensity, thicknesses are specified for every column. Hence, extrapolation is used to determine local thicknesses in this sample. The thickness map resulting is shown in Fig. 8c where the thickness ranges from 29 to 35 atoms per column.

3.6. Composition maps

With the composition intensity relationships explained above, the experimental Voronoi intensities can now be converted to a composition of the corresponding material. For this, every atomic column's intensity is compared to its corresponding *intensity composition relationship*. For this, the local thickness of every column is used and its corresponding *intensity composition relationship* is calculated. This ensures that no intensity that originates from thickness is mistaken for

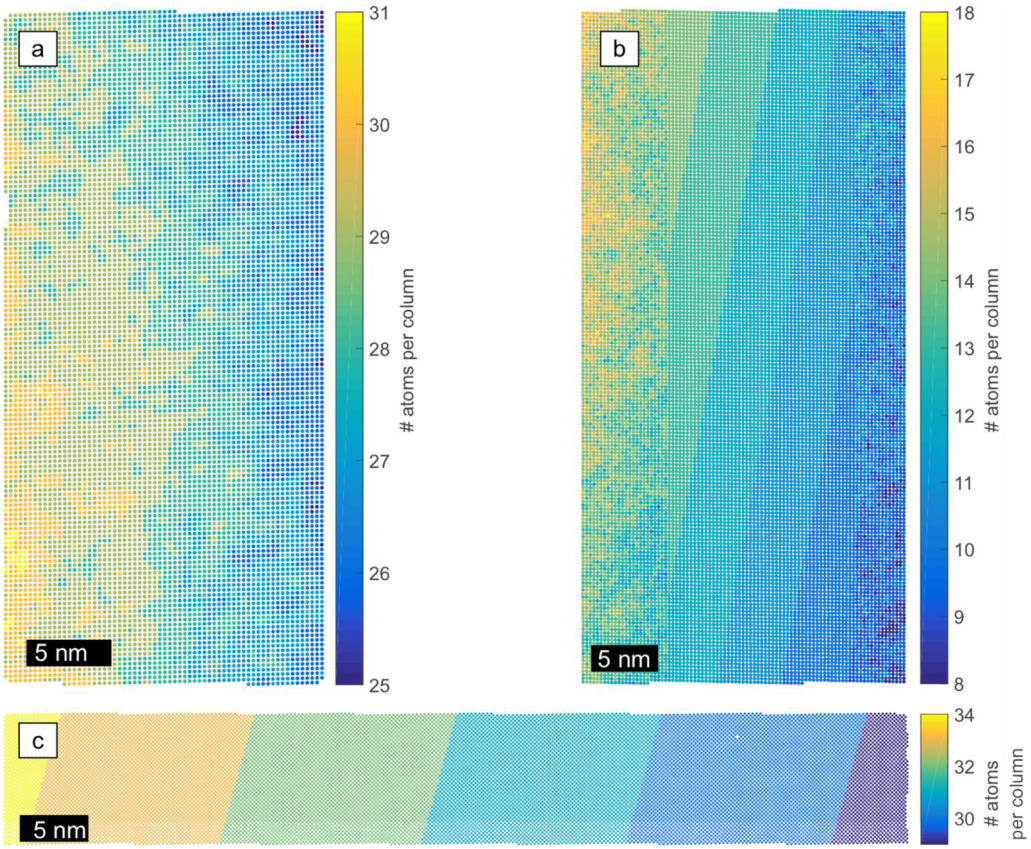

Fig. 8. Thickness maps for all three samples. In (a), the thicknesses in atoms per column are given for the group III sub lattice of sample I. For sample II, thicknesses of the group V sub lattice are shown in (b). In (c) the thicknesses of the atomic columns of sample III are presented. Growth direction is from left to right.

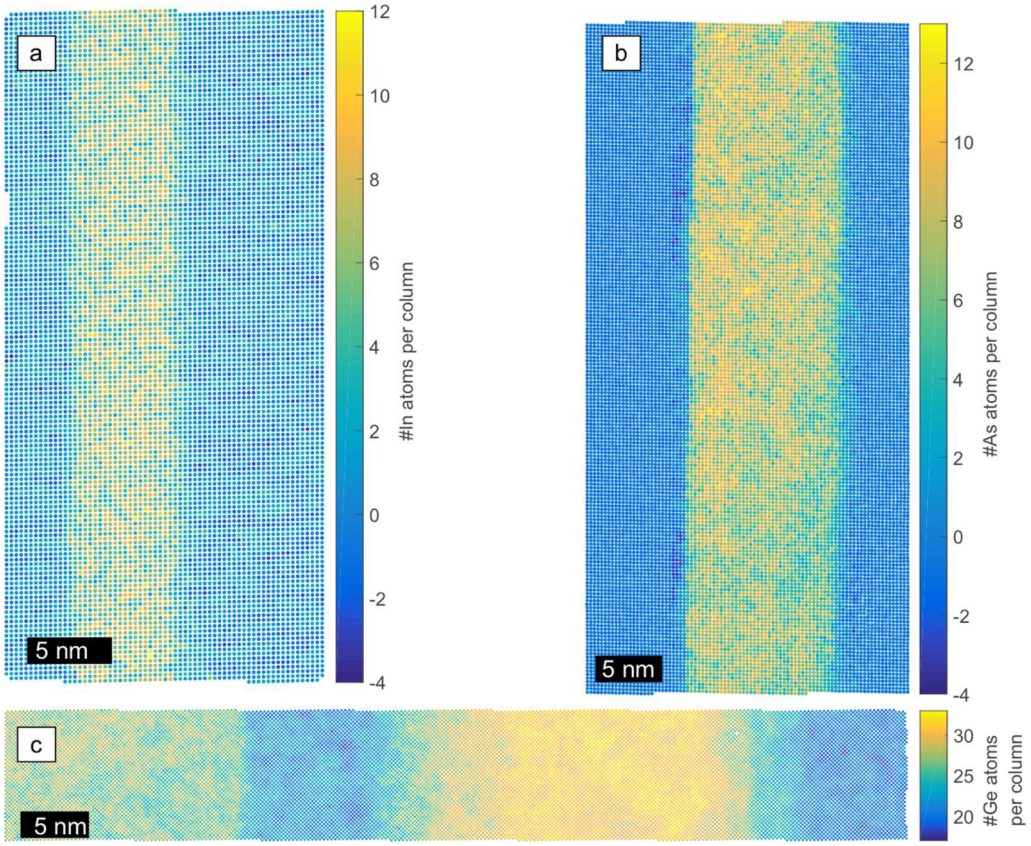

Fig. 9. Composition maps of all three samples. The number of substitute atoms per atomic column is given for the group III sub lattice of sample I (a), the group V sub lattice of sample II (b) and for sample III (c). Note, that the thickness of each atomic column differs as indicated in the thickness maps in Fig. 6. This was taken into account for composition determination.

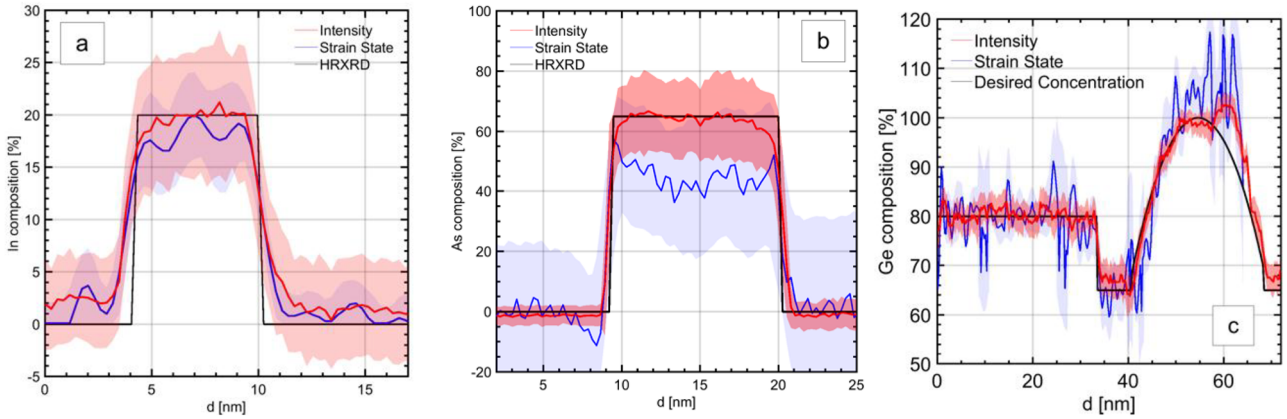

Fig 10. Horizontal line scans, acquired by averaging the 2D maps perpendicular to the growth direction. Sample I is depicted in (a) where the red line represents the composition derived from the intensity method, the solid blue line originates from the strain state, calculated from the local lattice constant and the black line visualizes the output of HRXRD measurements. Sample II is visualized in (b) and sample III in (c). The red and blue shaded areas depict the concentration standard deviation perpendicular to the growth direction. (For interpretation of the references to color in this figure legend, the reader is referred to the web version of this article.)

composition variation. The Voronoi intensities can now be converted into the corresponding number of substitute atoms. Fig. 9a shows the color coded 2D composition map of sample I. The GaAs barrier is clearly visible with a mean number of In atoms of 0 which increases up to a maximum of 12 in the QW region. The local thickness in the QW region ranges between 27 and 29 atoms in total. The mean number of In atoms in the QW area is around 6 which translates to a composition of 20% In. Additionally to the 2D map, Fig. 10a shows a line scan in growth direction of sample I. This is done by averaging the composition of the atomic columns perpendicular to the growth direction. In this way, the results of the different methods can be compared more easily. The red solid line represents the composition determined by the intensity method, explained above. The shaded area around the solid line is not the accuracy of the method but rather the composition deviation perpendicular to growth direction. The deviation of the composition in the GaAs barrier material as well as in the QW region is around ± 5%. Additionally an offset in the pure GaAs barrier of ~1.5% is visible. The black line in Fig. 10a shows the geometry retrieved from HRXRD with a QW width of 6.1 nm and an In composition of around 20%. Furthermore, the concentration derived from the lattice constant analysis of the sample is visualized with the blue line. The In concentration was calculated via the local lattice constant, derived from the image and combining Vegard's law with tetragonal distortion due to pseudomorphic growth. This method is considerably more sensitive to the surface relaxation of the sample. An increase of the concentration in the upper barrier region of the QW is visible which is due to the elastic surface relaxation of the sample. The concentration deviation along the QW is smaller than for the intensity method with ± 4%. Nevertheless, the composition derived from the intensity method is in good agreement with the composition derived from HRXRD.

The effect of the noise from the experimental intensity can be seen in the GaAs barrier in Fig. 9a. The mean concentration of In atoms in the GaAs is zero, but due to the noise, the minimum of the calculated In atoms is negative. Surface damage introduced during the preparation of the sample enhances the effect.

Fig. 9b shows the 2D composition maps for sample II. The GaP barrier is clearly visible and distinguishable from the QW region. The number of As atoms in the barrier is around 0 with a total number of group V atoms of 10 − 18. The number of As atoms increases to maximum of 13 atoms in the QW with a local thickness between 11 and 16 total atoms. Fig. 10b shows the corresponding line scans for sample II. The composition line scan (red) derived from the intensity method shows a very good agreement with the sample geometry derived from HRXRD (black). The parameters of the QW, according to XRD are 11.7 nm width with an As concentration of 65.5%, which is also reproduced by the intensity method. The concentration deviation is small in the barrier region and increases to around ± 4% in the QW area. This is due to the averaging of the intensities perpendicular to the growth direction. The distribution of atoms in a QW consisting of a compound semiconductor is not completely homogeneous, which leads to different compositions on the atomic columns. The composition deviation in the barrier is small and results from the intensity deviation, introduced by surface damage. The concentration profile derived from the lattice constant (blue line) shows a prominent discrepancy with the HRXRD profile (black). The concentration in the QW is between 40% and 50%. Due to the sample geometry, the elastic surface relaxation is very prominent. The intensities, derived from the Voronoi cells compensate the elastic relaxation very well, which is why the influence is not present, whereas the lattice constant is influenced tremendously. A detailed description how the elastic surface relaxation influences the lattice constant and thus the concentration derived from it can be found in.

Fig. 9c depicts the 2D composition map for sample III. The sample geometry is different than the one of sample I & II. The barrier consists of a $Si_{0.35}Ge_{0.65}$ alloy grown on the relaxed $Si_{0.2}Ge_{0.8}$ buffer. In the QW region the Ge content increases gradually in a parabolic form to 100% Ge. The composition drops back to $Si_{0.35}Ge_{0.65}$ after the QW area. The Ge content profile is such to ensure strain balance between the tensile strained barrier regions and the compressively strained QW regions. This geometry cannot be clearly distinguished from that a conventional box like QW by means of X-ray diffraction, therefore the nominal parabolic profile has been estimated from the calibrated deposition rate and alloy composition at varying precursor gas fluxes. The relaxed buffer material with $Si_{0.2}Ge_{0.8}$ is visible in the 2D color map from Fig. 9c with a total number of atoms between 35 and 33. The drop to $Si_{0.35}Ge_{0.65}$ is clearly visible with a number of Ge atoms between 19 and 22 with a total number of atoms of 32. The QW area with a higher Ge concentration is clearly visible whereas the parabolic form is not clearly distinguishable. The highest point of the parabola consists of 32 Ge atoms with a total number of 32 atoms. After the QW region, the Ge concentration drops back to 20 atoms with a thickness between 29 and 30 atoms in total. The line scans in Fig. 10c visualize the desired sample geometry more in detail. The concentration derived from the intensity method fluctuates around 80% of Ge in the barrier and the drop to 65% is clearly visible. The intensity method shows a small offset of around 3% to the desired sample geometry. The increase to 100% Ge is visible and peaks at around 102% Ge, which is due to the deviation of the Voronoi intensity. The drop in Ge concentration after the QW results in

a Ge concentration of 68%. The concentration derived from the lattice constant shows an enormous fluctuation around the desired concentration (black). This underlines that the proposed intensity method is more stable in comparison to the composition derived from the lattice constant.

4. Discussion

In this paragraph, we discuss composition determination by comparing simulated and experimental STEM intensities with regards to its extension towards single-atom accuracy. First, a general assessment of the method and its capabilities is done. Then, the application to experimental STEM images and accompanying influences are assessed.

Composition determination by comparing STEM intensities is based on the assumption that a certain composition of an atomic column leads to a unique intensity. In this work, Voronoi intensities [21] are considered. However, due to different possible z-height configurations of the substitute atom(s) inside the atomic column different intensities result. This leads to the intensity distribution for a given composition shown in Fig. 1. For the composition determination, the whole intensity distributions are reduced to a mean intensity that reflects a certain composition. The intensity distributions lead to the statistical character of the composition determination that is inherent in the composition intensity relationships of STEM experiments.

Therefore, the overlap of the intensity distributions determines the accuracy of the composition determination. To be more exactly, it is that overlap of the intensity distributions that is closer to the mean intensity of another composition. This is referred to as overlap from now on. In this work, an estimation of this accuracy was done with help of standard deviations of the intensity distributions. With this, 68% of the atomic columns are considered. An assessment of the error for all atomic columns can be done with the simulation study performed for the example of (Ga,In)As.

Atomic columns that have a z-height configuration leading a “non-overlap intensity” are determined correctly. If an atomic column has an intensity that is part of the overlap to another composition, its composition is not determined correctly.

The overlap of the intensity distributions and hence the accuracy of composition determination depends on the material system, the number of substitute atoms in an atomic column and its thickness. The HAADF-STEM images used for this study exhibit strong Z-contrast. Consequently, if the difference between the atomic number of the substitute atom and the replaced atom is higher, the overlap between different intensity distributions is smaller. Therefore, the achievable accuracy depends decisively on the studied material system and for example for Ga(As,Bi), where the difference in atomic number is $\Delta Z = 50$, the accuracy of composition determination is higher than for (Ga,In)As where the difference in atomic number is only $\Delta Z = 18$. For a higher number of substitute atoms in an atomic column, there are more possible arrangements of these substitute atoms and therefore a larger overlap of intensity distributions. If the number of total atoms in an atomic column is higher, this leads to more possible z-height configurations and a larger overlap between intensity distributions.

The influence of thickness can be clearly seen in the simulation study on (Ga,In)As. With increasing thickness, the percentage of atomic columns for which the composition was determined correctly decreases since the overlap of intensities increases. From a statistical point of view, this means that there is certain probability that the composition of a given atomic column is determined correctly. This probability depends on the material system and the composition and decreases with increasing thickness.

The errors in composition determination increase with increasing thickness since there is overlap with more compositions. However, overall these errors cancel out on average, since plus and minus deviations are equally frequent independently of the thickness. Consequently, the overall composition is determined very accurately at every thickness for the investigated sample size.

For the application to an experimental STEM image, all experimental parameters are determined and all influences are treated carefully. Since the evaluation method solely relies on STEM HAADF intensities, every potential influence on the intensities has to be understood very precisely. In the following, the influences of local thickness, amorphous layers, detector angles, clustering of substitute atoms and surface relaxation are discussed.

As already apparent during the evaluation, the thickness of each atomic column has a major influence on its intensity. In the simulation study for (Ga,In)As, it is found that below thicknesses of 30 atoms it is impossible to determine the correct number of In atoms if the thickness is of by one atom. At higher thicknesses, the probability of correct composition determination becomes almost equally likely for wrong thicknesses.

The process of sample preparation where Ar ion milling is used as a final step leads to thickness variation within the field of view of one image. Therefore, the thickness of each atomic column has to be considered locally. Several options to do so have been introduced tailored to the demands of different samples. These demands depend on experimental sample thickness and present atomic columns/regions with known composition that can be used as reference for thickness determination. If the assumption for the thickness of an atomic column is wrong, this will lead to a locally wrong composition. However, the deviations in composition for under- and overestimated thickness of an atomic column cancel at every thickness. Hence, for the experiment contributions from wrong thicknesses will cancelout, leading to an overall correctly determined composition as shown for the three samples.

Thickness determination is realized by comparison of experimental intensities to simulation resulting in a certain number of atoms per atomic column. In the simulation, only crystalline material is considered. However, due to sample preparation there are amorphous layers on top and bottom of the sample. For the case of GaAs based material, an amorphous layer of 3.5 nm was found on both sides of the sample [51]. These amorphous layers lead to two main effects: One is beam broadening [40] and the other one is different intensity compared to only crystalline material [52] leading to a thickness determination deviating from only crystalline material.

The beam broadening caused by the upper amorphous layer leads to a two-dimensional redistribution of intensity in the image, which is the same effect as caused by the finite source size. As this is taken into account by a Lorentzian convolution, the width of this convolution will increase due to the amorphous layers and lead to a higher effective source size.

Since the thickness is determined via intensity comparison to simulation which only considers crystalline material, this crystalline thickness is overestimated. The real crystalline thickness is smaller: Considering the intensity of amorphous material to be about 50% [53] of crystalline material, the real crystalline thickness would be about 3.5 nm smaller than the one determined by intensity comparison. The real crystalline thickness is not considered in this case but could be taken into account by for example measuring position averaged convergent beam electron diffraction (PACBED) patterns [53]. However, since there is still a linear relationship between thickness and intensity there is only a minor influence by the amorphous layers present due to our sample preparation. Amorphous and crystalline material seems to behave similar despite of the different compositions present. This is supported by the good agreement of the presented composition results to other methods.

Additionally, to these two main effects, the amorphous layers are probably also causing the non-zero concentration of substitute atoms in the barrier of samples I and II (see Fig. 10). In the case of sample I, the In concentration is slightly higher than zero (~2%, ~0.5 atoms per column), in sample II As concentration is slightly smaller than zero (~1.3%, ~0.2 atoms per column). This will be explained in the

following with the example of Fig. 6.

In Fig. 6, the adaption of simulation to experiment for GaAs is shown. In the diagonal line scan, the central peak is a Ga peak (group III), while both neighboring peaks are As peaks (group V). Using the best possible adaption of the simulation to the experimental image, the group III intensity is slightly underestimated by simulation, while the group V intensity is slightly overestimated. In the case of GaP (see SI), the simulation is overestimating both group II and group V peaks. This leads to a small amount of In that increases the intensity of group III atomic columns being necessary to match experiment and simulation for sample (~1.3% intensity increase per substitute In at 27 atoms thickness). For sample II, a small negative concentration of As that decreases the intensity of group V atomic columns gives the best match between simulation and experiment in GaP (~5.8% intensity decrease per negative substitute As at 14 atoms thickness). While these deviations in adapting simulation to experiment cause the non-zero concentrations of substitute atoms in the barriers of samples I and II, the deviations themselves are probably caused by the two main effects of amorphous layers on intensity evaluations that are differing thickness and differing effective source size discussed above.

A possible solution to deal with the residual amorphous layers is to use very low kV ion milling to remove them [54]. This is work in progress, which should improve both adaption of simulation to experiment and composition determination.

However, amorphous layers are most influential on STEM intensities in a lower angular detector range. This is also the case for inelastic scattering and diffuse scattering caused by SADs. While the two former ones are not considered in simulation, SADs are taken into account. However, since the angular range used for the measurements is in the HAADF regime all three effects do not contribute majorly.

Detector angles were determined following the ansatz from [29]. Thickness determination is performed assuming this certain angular range of the detector. Since these thicknesses and the same angular range are used for composition determination, final compositions are relatively robust against small angle deviations.

The distribution of substitute atoms within the supercells that are used for simulations is done statistically in both the *x*–*y*-plane and their *z*-height within one atomic column. The distribution of substitute atoms in the *x*–*y*-plane only influences the Voronoi averaged intensities of atomic columns if the sample exceeds a certain thickness so that cross scattering comes into play. However, for samples that show clustering effects in the *x*-*y*-plane and are quite thick this assumption of statistical distribution leads to a wrong treatment of the influence of neighboring atomic columns on the intensity. This is only a minor effect while clustering in *z*-direction would have a larger influence. Here, the statistical distribution of substitute atoms leads to the intensity distribution and its mean value for a certain number of atoms per atomic column (see Fig. 1). If there is clustering in z-direction, the mean intensity of an atomic column will deviate from the one determined by evaluation of the simulated super cells. However, for all samples investigated no clustering effects are expected. Indeed, for a similar structure as sample I it was already shown that In atoms are statistically distributed [55].

Surface relaxation was shown to have a possibly severe influence on HAADF-STEM images [26,50]. It changes not only the intensity in the QW region but also in the barrier. Thus, it can be difficult to find a suitable reference for quantitative evaluations. However, the influence of surface relaxation on composition determination by intensity evaluation is decreased by the use of Voronoi cells [45]. To fully treat surface relaxation and its influence on composition determination is very complex since it is a self-consistent problem for both intensity evaluations and strain state analysis.

The composition determined by strain state analysis is severely influenced by surface relaxation [26] in the case of sample II (Fig. 10b) where the lattice mismatch of barrier and QW is the highest for the three samples investigated. Here, strain state analysis gives lower compositions than both other methods. However, in general the overall accuracy of the composition determination where a single-atom ansatz is chosen is also very good experimentally. This is confirmed by the comparisons to XRD and strain state analysis results.

5. Summary

In this paper, an extension of the established procedure that is used to determine compositions of materials by comparing STEM multislice simulations to experimental images is presented. A special focus lies on the comprehensive investigation of the capabilities and limitations of the extended method presented and the question whether single-atom accuracy is achievable. With the help of a simulation study on (Ga,In)As, the extended technique was benchmarked by calculating the percentage of correctly determined atomic columns as a function of assumed sample thickness. The results show that a correct determination of the composition of all atomic columns is possible up to a sample thickness of 3 atoms only. Above a sample thickness of 3 atoms, locally a deviation in composition of one atom is visible. Above 30 atoms sample thickness, the fraction of atomic columns which have a composition deviation of one atom or above increases substantially. This inaccuracy is caused by the fact that there is a certain intensity range for a fixed number of substitute atoms caused by the different z-heights of the substitute atoms as well as their local environment. Accordingly, the intensities for different number of substitute atoms overlap, leading to an over- or underestimation of the local composition. Since, over- and underestimation of the composition is as likely, the global composition, however, is determined very accurately.

Furthermore, the simulation study showed that the assumed sample thickness is a crucial parameter when determining compositions. With a correctly assumed thickness, the mean total deviation is below 0.5% for the example of (Ga,In)As with 20% indium. Moreover, the analysis of intentionally wrong chosen thicknesses shows that the resulting deviation in composition is symmetrical around zero. This means, that the errors in global composition determination again cancel out, since plus and minus deviations are equally frequent independently of the thickness. With the capabilities of the evaluation method in mind, three technologically important semiconductor samples, namely (Ga,In)As QW, a Ga(P,As) and a SiGe QW, were used to prove the applicability of the method. The concentration resulting from the intensity method presented here shows a good agreement with HRXRD measurements and strain state analysis. However, it has the advantages of atomic lateral resolution and insensitivity to surface relaxation. Of course, in the future this allows to investigate samples, which cannot be characterized accurately by XRD, e.g. due to gradients in the composition or interface roughness present.

Acknowledgments

Support by the German Research Foundation (DFG) in the framework of the research training group “Functionalization of Semiconductors” (GRK 1782) is gratefully acknowledged. P. Kükelhan also acknowledges support in the framework of the Collaborative Research Center “Structure and Dynamics of internal interfaces” (SFB 1083). S. Firoozabadi acknowledges support of the European Union's Horizon 2020 in the framework of the project microSPIRE (ID: 766955). A. Ballabio acknowledges support from Regione Lombardia ID: 242092, under the TEINVEIN project, Call “Accordi per laRicerca e l'Innovazione”, co-funded by POR FESR 2014-2020 (ID: 242092).

Supplementary materials

Supplementary material associated with this article can be found, in the online version, at doi:10.1016/j.ultramic.2019.02.009.

References

[1] O.L. Krivanek, M.F. Chisholm, V. Nicolosi, T.J. Pennycook, G.J. Corbin, N. Dellby, M.F. Murfitt, C.S. Own, Z.S. Szilagyi, M.P. Oxley, S.T. Pantelides, S.J. Pennycook, Atom-by-atom structural and chemical analysis by annular dark-field electron microscopy, Nature 464 (March (7288)) (2010) 571–574.

[2] P.D. Nellist, M.F. Chisholm, N. Dellby, O.L. Krivanek, M.F. Murfitt, Z.S. Szilagyi, A.R. Lupini, A. Borisevich, W.H. Sides, S.J. Pennycook, Direct sub-angstrom imaging of a crystal lattice, Science (80-.) 305 (September (5691)) (2004) 1741.

[3] A. Singhal, J.C. Yang, J.M. Gibson, STEM-based mass spectroscopy of supported Re clusters, Ultramicroscopy 67 (June (1–4)) (1997) 191–206.

[4] P.M. Voyles, D.A. Muller, J.L. Grazul, P.H. Citrin, H.-J.J.L. Gossmann, Atomic-scale imaging of individual dopant atoms and clusters in highly n-type bulk Si, Nature 416 (April (6883)) (2002) 826–829.

[5] S.J. Pennycook, L.A. Boatner, Chemically sensitive structure-imaging with a scanning transmission electron microscope, Nature 336 (December (6199)) (1988) 565–567.

[6] J.M. LeBeau, S.D. Findlay, L.J. Allen, S. Stemmer, Quantitative atomic resolution scanning transmission electron microscopy, Phys. Rev. Lett. 100 (May (20)) (2008) 206101.

[7] S.J. Pennycook, D.E. Jesson, High-resolution Z-contrast imaging of crystals, Ultramicroscopy 37 (August (1–4)) (1991) 14–38.

[8] V. Grillo, E. Carlino, F. Glas, Influence of the static atomic displacement on atomic resolution Z-contrast imaging, *Phys. Rev. B – Condens. Matter Mater. Phys.* 77 (5) (2008).

[9] V. Grillo, The effect of surface strain relaxation on HAADF imaging, Ultramicroscopy 109 (November (12)) (2009) 1453–1464.

[10] A. Rosenauer, K. Gries, K. Müller, A. Pretorius, M. Schowalter, A. Avramescu, K. Engl, S. Lutgen, Measurement of specimen thickness and composition in AlxGa1–xN/GaN using high-angle annular dark field images, Ultramicroscopy 109 (August (9)) (2009) 1171–1182.

[11] L. Jones, Quantitative ADF STEM: acquisition, analysis and interpretation, IOP Conf. Ser. Mater. Sci. Eng. 109 (1) (2016) 012008.

[12] P.L. Galindo, S. Kret, A.M. Sanchez, J.Y. Laval, A. Yáñez, J. Pizarro, E. Guerrero, T. Ben, S.I. Molina, The Peak Pairs algorithm for strain mapping from HRTEM images, Ultramicroscopy 107 (November (12)) (2007) 1186–1193.

[13] J.M. LeBeau, S.D. Findlay, L.J. Allen, S. Stemmer, Standardless atom counting in scanning transmission electron microscopy, Nano Lett 10 (November (11)) (2010) 4405–4408.

[14] A. De Backer, G.T. Martinez, A. Rosenauer, S. Van Aert, Atom counting in HAADF STEM using a statistical model-based approach: methodology, possibilities, and inherent limitations, Ultramicroscopy 134 (November) (2013) 23–33.

[15] A. De wael, A. De Backer, L. Jones, P.D. Nellist, S. Van Aert, Hybrid statistics-simulations based method for atom-counting from ADF STEM images, Ultramicroscopy 177 (June) (2017) 69–77.

[16] S. Van Aert, A. De Backer, G.T. Martinez, B. Goris, S. Bals, G. Van Tendeloo, A. Rosenauer, Procedure to count atoms with trustworthy single-atom sensitivity, Phys. Rev. B - Condens. Matter Mater. Phys. 87 (Feburary (6)) (2013) 064107.

[17] G.T. Martinez, A. Rosenauer, A. De Backer, J. Verbeeck, S. Van Aert, Quantitative composition determination at the atomic level using model-based high-angle annular dark field scanning transmission electron microscopy, Ultramicroscopy 137 (Feburary) (2014) 12–19.

[18] T. Grieb, K. Müller, R. Fritz, V. Grillo, M. Schowalter, K. Volz, A. Rosenauer, Quantitative chemical evaluation of dilute GaNAs using ADF STEM: avoiding surface strain induced artifacts, Ultramicroscopy 129 (June) (2013) 1–9.

[19] T. Grieb, K. Müller, R. Fritz, M. Schowalter, N. Neugebohrn, N. Knaub, K. Volz, A. Rosenauer, Determination of the chemical composition of GaNAs using STEM HAADF imaging and STEM strain state analysis, Ultramicroscopy 117 (June) (2012) 15–23.

[20] T. Grieb, K. Müller, E. Cadel, A. Beyer, M. Schowalter, E. Talbot, K. Volz, A. Rosenauer, Simultaneous Quantification of Indium and Nitrogen Concentration in InGaNAs Using HAADF-STEM, Microsc. Microanal. 20 (December (06)) (2014) 1740–1752.

[21] A. Rosenauer, T. Mehrtens, K. Müller, K. Gries, M. Schowalter, P. Venkata Satyam, S. Bley, C. Tessarek, D. Hommel, K. Sebald, M. Seyfried, J. Gutowski, A. Avramescu, K. Engl, S. Lutgen, Composition mapping in InGaN by scanning transmission electron microscopy, Ultramicroscopy 111 (July (8)) (2011) 1316–1327.

[22] T. Grieb, K. Müller, R. Fritz, M. Schowalter, N. Neugebohrn, N. Knaub, K. Volz, A. Rosenauer, Determination of the chemical composition of GaNAs using STEM HAADF imaging and STEM strain state analysis, Ultramicroscopy 117 (June) (2012) 15–23.

[23] C. Fuchs, A. Beyer, K. Volz, W. Stolz, MOVPE growth of (GaIn)As/Ga(AsSb)/(GaIn)As type-II heterostructures on GaAs substrate for near infrared laser applications, J. Cryst. Growth 464 (April) (2017) 201–205.

[24] A. Ballabio, “Germanium and SiGe epitaxial growth for mid-infrared applications.”, Dissertation, Italy 2018.

[25] J.O. Oelerich, L. Duschek, J. Belz, A. Beyer, S.D. Baranovskii, K. Volz, STEMsalabim: a high-performance computing cluster friendly code for scanning transmission electron microscopy image simulations of thin specimens, Ultramicroscopy 177 (June) (2017) 91–96.

[26] A. Beyer, L. Duschek, Jü. Belz, J.O. Oelerich, K. Jandieri, K. Volz, Surface relaxation of strained Ga(P,As)/GaP heterostructures investigated by HAADF STEM, J. Microsc. 268 (December (3)) (2017) 239–247.

[27] C. Rosenblad, H.R. Deller, A. Dommann, T. Meyer, P. Schroeter, H. von Känel, Silicon epitaxy by low-energy plasma enhanced chemical vapor deposition, J. Vac. Sci. Technol. A 16 (October (5)) (1998) 2785–2790.

[28] S. Marchionna, A. Virtuani, M. Acciarri, G. Isella, H. von Kaenel, Defect imaging of SiGe strain relaxed buffers grown by LEPECVD, Mater. Sci. Semicond. Process. 9 (August (4–5)) (2006) 802–805 SPEC. ISS..

[29] J.M. LeBeau, S. Stemmer, Experimental quantification of annular dark-field images in scanning transmission electron microscopy, Ultramicroscopy 108 (November (12)) (2008) 1653–1658.

[30] L. Jones, H. Yang, T.J. Pennycook, M.S.J. Marshall, S. Van Aert, N.D. Browning, M.R. Castell, P.D. Nellist, Smart Align—a new tool for robust non-rigid registration of scanning microscope data, Adv. Struct. Chem. Imaging 1 (December (1)) (2015) 8.

[31] D.S. He, Z.Y. Li, A practical approach to quantify the ADF detector in STEM, J. Phys. Conf. Ser. 522 (June (1)) (2014) 012017.

[32] K.T. Jacob, S. Raj, L. Rannesh, Vegard's law: a fundamental relation or an approximation? Int. J. Mater. Res. 98 (September (9)) (2007) 776–779.

[33] W. Li, M. Pessa, J. Likonen, Lattice parameter in GaNAs epilayers on GaAs: deviation from Vegard's law, Appl. Phys. Lett. 78 (May (19)) (2001) 2864–2866.

[34] O. Rubel, I. Németh, W. Stolz, K. Volz, Modeling the compositional dependence of electron diffraction in dilute GaAs- and GaP-based compound semiconductors, Phys. Rev. B - Condens. Matter Mater. Phys. 78 (August (7)) (2008) 075207.

[35] P.N. Keating, Effect of invariance requirements on the elastic strain energy of crystals with application to the diamond structure, Phys. Rev. 145 (May (2)) (1966) 637–645.

[36] T.G. Ramesh, S. Ramaseshan, Determination of the static displacement of atoms in a binary alloy system using anomalous scattering, Acta Crystallogr. Sect. A 27 (November (6)) (1971) 569–572.

[37] E.J. Kirkland, Advanced Computing in Electron microscopy: Second Edition, Springer, 2010.

[38] E.J. Kirkland, Image simulation in transmission electron microscopy, Simulation (2006) 1–14.

[39] B.D. Forbes, A.J. D'Alfonso, S.D. Findlay, D. Van Dyck, J.M. LeBeau, S. Stemmer, L.J. Allen, Thermal diffuse scattering in transmission electron microscopy, Ultramicroscopy 111 (December (12)) (2011) 1670–1680.

[40] A. Beyer, J. Belz, N. Knaub, K. Jandieri, K. Volz, Influence of spatial and temporal coherences on atomic resolution high angle annular dark field imaging, Ultramicroscopy 169 (October) (2016) 1–10.

[41] C. Dwyer, R. Erni, J. Etheridge, Method to measure spatial coherence of sub-angstrom electron beams, Appl. Phys. Lett. 93 (July (2)) (2008) 021115.

[42] C. Dwyer, R. Erni, J. Etheridge, Measurement of effective source distribution and its importance for quantitative interpretation of STEM images, Ultramicroscopy 110 (8) (2010) 952–957.

[43] D. Nguyen, S. Findlay, J. Etheridge, The spatial coherence function in scanning transmission electron microscopy and spectroscopy, Ultramicroscopy 146 (2014) 6–16.

[44] S.D. Findlay, J.M. LeBeau, Detector non-uniformity in scanning transmission electron microscopy, Ultramicroscopy 124 (January) (2013) 52–60.

[45] H. E, K.E. MacArthur, T.J. Pennycook, E. Okunishi, A.J. D'Alfonso, N.R. Lugg, L.J. Allen, P.D. Nellist, Probe integrated scattering cross sections in the analysis of atomic resolution HAADF STEM images, Ultramicroscopy 133 (October) (2013) 109–119.

[46] J. Belz, A. Beyer, L. Nattermann, K. Volz, On the effects of column occupancy and static atomic disorder on the analysis of chemical ordering in Ga(P(1-x)Bix) compounds, Microsc. Microanal. 23 (July (S1)) (2017) 1474–1475.

[47] K.H.W. van den Bos, L. Janssens, A. De Backer, P.D. Nellist, S. Van Aert, The atomic lensing model: new opportunities for atom-by-atom metrology of heterogeneous nanomaterials, Ultramicroscopy (December) (2018).

[48] J. Fertig, H. Rose, Resolution and contrast of crystalline objects in high-resolution scanning transmission electron microscopy, Optik (Stuttg) 59 (1981) 407–429.

[49] P.D. Nellist, S.J. Pennycook, Incoherent imaging using dynamically scattered coherent electrons, in *Ultramicroscopy* 78 (1–4) (1999) 111–124.

[50] A. Beyer, L. Duschek, J. Belz, J.O. Oelerich, K. Jandieri, K. Volz, Influence of surface relaxation of strained layers on atomic resolution ADF imaging, Ultramicroscopy 181 (October) (2017) 8–16.

[51] J. Belz, A. Beyer, T. Torunski, W. Stolz, K. Volz, Direct investigation of (sub-) surface preparation artifacts in GaAs based materials by FIB sectioning, Ultramicroscopy 163 (2016) 19–30.

[52] K.A. Mkhoyan, S.E. Maccagnano-Zacher, E.J. Kirkland, J. Silcox, Effects of amorphous layers on ADF-STEM imaging, Ultramicroscopy 108 (July (8)) (2008) 791–803.

[53] T. Grieb, M. Tewes, M. Schowalter, K. Müller-Caspary, F.F. Krause, T. Mehrtens, J.M. Hartmann, A. Rosenauer, Quantitative HAADF STEM of SiGe in presence of amorphous surface layers from FIB preparation, Ultramicroscopy 184 (2018) 29–36.

[54] R.R. Cerchiara, P.E. Fischione, J. Liu, J.M. Matesa, A.C. Robins, H.L. Fraser, A. Genc, Raising the standard of specimen preparation for aberration-corrected TEM and STEM, Micros. Today 19 (01) (2011) 16–19.

[55] P. Kükelhan, A. Beyer, C. Fuchs, M.J. Weseloh, S.W. Koch, W. Stolz, K. Volz, Atomic structure of ‘W’-type quantum well heterostructures investigated by aberration-corrected STEM, J. Microsc. 268 (December (3)) (2017) 259–268.

6.3 Segregation at Interfaces in *(GaIn)As/Ga(AsSb)/(GaIn)As*-Quantum Well Heterostructures Explored by Atomic Resolution STEM

P. Kükelhan, S. Firoozabadi, A. Beyer, L. Duschek, C. Fuchs, J. O. Oelerich, W. Stolz, K. Volz. *Journal of Crystal Growth* 524 (2019), 125180. doi: 10.1016/j.jcrysgro.2019.125180

Abstract Surface segregation and interaction effects of *In* and *Sb* in *(GaIn)As/Ga(AsSb)/-(GaIn)As-* "W"-type quantum well heterostructures ("W"-QWHs) are investigated by high angle annular dark field scanning transmission electron microscopy with atomic resolution. "W"-QWHs are promising candidates for type-II laser applications in telecommunications. In this study, independent textit(GaIn)As and *Ga(AsSb)* quantum wells as well as complete "W"-QWHs are grown by metal organic vapor phase epitaxy on *GaAs* substrate. The composition is determined with atomic resolution by comparison of the experimental data to complementary contrast simulations. From concentration profiles, an altered segregation in "W"-QWHs in comparison to single *(GaIn)As* and *Ga(AsSb)* quantum wells grown on *GaAs* is detected. *In* and *Sb* are clearly influencing each other during the growth, including blocking effects of *In* incorporation by *Sb* and vice versa. Especially, growth rate and total amount of *Sb* incorporated into *Ga(AsSb)* are decreased by *In* being present.

Contributions of the Author For this work, I performed all STEM investigations and evaluations and the analysis of the segregation with the Muraki model.

The manuscript was written by me.

Journal of Crystal Growth 524 (2019) 125180

Contents lists available at ScienceDirect

Journal of Crystal Growth

journal homepage: www.elsevier.com/locate/jcrysgro

Segregation at interfaces in *(GaIn)As/Ga(AsSb)/(GaIn)As*- quantum well heterostructures explored by atomic resolution STEM

P. Kükelhan, S. Firoozabadi, A. Beyer*, L. Duschek, C. Fuchs, J.O. Oelerich, W. Stolz, K. Volz

Materials Science Centre and Faculty of Physics, Philipps University Marburg, Hans-Meerwein-Straße 6, Marburg, Germany

ARTICLE INFO

Communicated by Roberto Fornari

Keywords:
A1. Characterization
A3. Metalorganic vapour phase epitaxy
A3. Quantum wells
B2. Semiconducting III–V materials
B3. Solid state lasers

ABSTRACT

Surface segregation and interaction effects of *In* and *Sb* in *(GaIn)As/Ga(AsSb)/(GaIn)As*- "W"-type quantum well heterostructures ("W"-QWHs) are investigated by high angle annular dark field scanning transmission electron microscopy with atomic resolution. "W"-QWHs are promising candidates for type-II laser applications in telecommunications. In this study, independent *(GaIn)As* and *Ga(AsSb)* quantum wells as well as complete "W"-QWHs are grown by metal organic vapour phase epitaxy on *GaAs* substrate. The composition is determined with atomic resolution by comparison of the experimental data to complementary contrast simulations. From concentration profiles, an altered segregation in "W"-QWHs in comparison to single *(GaIn)As* and *Ga(AsSb)* quantum wells grown on *GaAs* is detected. *In* and *Sb* are clearly influencing each other during the growth, including blocking effects of *In* incorporation by *Sb* and vice versa. Especially, growth rate and total amount of *Sb* incorporated into *Ga(AsSb)* are decreased by *In* being present.

1. Introduction

Modern semiconductor lasers emitting in the infrared regime are promising for application in telecommunications [1]. So called "W"-type quantum heterostructures ("W"-QWHs) are candidates for laser applications at 1300 nm, which allow more efficient optical telecommunications. In our case, "W"-QWHs are type-II laser systems with an active region consisting of a *Ga(AsSb)* quantum well (QW) embedded between two *(GaIn)As-QWs*. The name "W"-QWH is based on the shape of the resulting band structure. In type-II laser systems, electrons and holes are spatially separated in those different QWs and recombination takes place across the interfaces. Hence, the structure of these interfaces is of major importance for a device's performance.

The "W"-QWH was theoretically proposed [2–4], successfully grown [5] and was already used for a vertical-external-cavity surface-emitting laser emitting at 1200 nm [6]. To finally achieve efficient laser devices at high emission wavelength, optimization is based on additional characterization of the structures. First optical characterization can be carried out by photoluminescence measurements, while structural characterization is possible by X-ray diffraction (XRD) [5]. To achieve structural characterization with atomic resolution, high angle annular dark field scanning transmission electron microscopy (HAADF-STEM) is suitable. Due to dominant Z-contrast in HAADF-STEM images, also composition quantification is possible. This can lead to composition determination at an atomic scale [7,8]. Complementary contrast simulations are a common option to achieve this [9]. These simulations can precisely match experimental results [10,11]. Given an atomically resolved composition, effects during growth like surface segregation or interactions between different elements can be investigated at an atomic level.

Surface segregation was shown to play an important role for the growth of *(GaIn)As*- [12] and *Ga(AsSb)*-QWs [13] on *GaAs* and is especially altering their respective interfaces. Several models were proposed to describe the resulting concentration profiles. Among others, these include a phenomenological model by Muraki et al. [14] and a three-layer exchange model proposed by Godbey and Ancona [15]. The Muraki model was successfully applied to *(GaIn)As*- and *Ga(AsSb)*-QWs characterized by TEM methods [16–19] and is widely accepted. The three-layer exchange model was originally tailored for describing surface segregation for *SiGe/Si* but was also used to describe a material system with simultaneous segregation of *In* and *Sb* [20]. Furthermore, interaction mechanisms between *In* and *Sb* during growth were reported before [21].

Beforehand, the "W"-QWH were investigated by HAADF-STEM and intensity profiles obtained were discussed to explore the general structure [22].

In this work, a superior method for local composition determination is applied that is used to isolate the interaction effects in the "W"-QWH

* Corresponding author.
E-mail addresses: pirmin.kuekelhan@physik.uni-marburg.de (P. Kükelhan), andreas.beyer@physik.uni-marburg.de (A. Beyer).

https://doi.org/10.1016/j.jcrysgro.2019.125180
Received 15 January 2019; Received in revised form 29 July 2019; Accepted 1 August 2019
Available online 02 August 2019
0022-0248/

by comparison to single QWs.

The "W"-QWH as well as single *(GaIn)As*- and *Ga(AsSb)*-QWs are investigated by HAADF-STEM and through comparison with complementary contrast simulations the composition of these QWHs is determined on an atomic level. For the composition profiles obtained, the Muraki model as well as the three-layer exchange model are applied to all QWHs to quantify segregation. Growth conditions are kept the same for all *(GaIn)As*-QWs and *Ga(AsSb)*-QWs, respectively. Hence, the interaction of *In* and *Sb* in the "W"-QWH can be investigated. In particular, the influence of *Sb* on the surface segregation of *In* and vice versa is analysed.

To this end, first experimental methods used are described in detail. A close discussion of surface segregation and models to characterize it is following. Then, the determined composition of the QWHs and modelling of their present surface segregation are shown. Finally, the accuracy of the composition determination and interaction effects of *In* and *Sb* during the growth are discussed.

2. Materials and methods

The investigated sample includes a single *(GaIn)As*-QW, a single *Ga(AsSb)*-QW and a "W"-QWH between *GaAs*-barriers. It was grown for the purpose of TEM investigations by MOVPE using an AIXTRON AIX 200 GFR (Gas Foil Rotation) reactor system (Aixtron SE, Herzogenrath, Germany). The growth was carried out on exactly oriented, semi-insulating *GaAs* (0 0 1) substrates. As group III precursors triethylgallium (TEGa) and trimethylindium (TMIn) were used, while group V precursors were tertiarybutylarsine (TBAs) and triethylantimony (TESb). The partial pressures of the precursors which were smaller than 1 mbar and the high-purity H_2 carrier gas added up to a reactor pressure of 50 mbar. Prior to the sample growth at 550 °C [5], the native oxide layer was removed from the substrates by a TBAs-stabilised bake-out procedure. The V/III ratios were chosen as 5.2 for *GaAs*, 3.9 for *(GaIn)As* and 7.4 for *Ga(AsSb)*. In more detail, the ratio of the partial pressure of TMIn to all group III precursors was 0.75, while the ratio of the partial pressure of TESb to all group V precursors was 0.808. The growth of the *(GaIn)As*- and *Ga(AsSb)*-QWs in the "W"-QWH took place under the exact same conditions as for the single *(GaIn)As*- and *Ga(AsSb)*-QWs. No special gas switching sequence was applied at the interfaces. This allows to investigate the presence of any interaction between In and Sb at the interfaces of the "inner" QW, where both elements are present at the same time.

The sample described above was conventionally prepared for cross-sectional TEM investigations in [0 1 0]-direction. Mechanical grinding and polishing was carried out with a Multiprep™ system (Allied High Tech Products, Inc., Rancho Dominguez, CA, United States) down to a thickness of approximately 20 µm, whereas the final thinning and polishing through *Ar*-ion bombardment took place with a precision ion polishing system (model 691 Gatan, Inc., Pleasanton, CA, United States). To limit amorphous layers, the acceleration voltage was gradually decreased from 5 kV to 1.2 kV with an inclination angle of the ion beam on the sample surface of 6°. Due to this preparation procedure, the resulting TEM sample shows a wedge shape, i.e. a thickness gradient. Prior to STEM investigations, the sample was plasma cleaned to remove contaminations (model 1020 E. A. Fischione Instruments, Inc., Export, PA, United States).

HAADF-STEM investigations were performed with a double C_s-corrected JEOL JEM2200FS (JEOL Ltd., Tokyo, Japan) at 200 kV acceleration voltage. The convergence semi-angle of the electron probe of α= 21.3 mrad was formed by a condenser aperture with a size of 40 µm. The JEOL EM-24590YPDFI dark-field image detector was detecting electrons scattered to an angular range of 63–252 mrad, 60–240 mrad and 62–248 mrad for the evaluated STEM images of the single *(GaIn)As*-QW, the single *Ga(AsSb)*-QW and the "W"-QWH, respectively. This angular range was determined by measuring the shadow of the detector on a CCD camera to identify the inner angle [23] while the outer angle is four times the inner angle. Slightly different detector angles are most likely caused by slight changes in the excitation of the filter lenses in different sessions. Each STEM image is the average of ten images with a dwell time of 3 µs per pixel which have been aligned using the software Smart Align [24]. Additionally, the images were normalised to the impinging beam with the help of a beam image [25] on a CCD camera.

Table 1
Parameters used for simulation of *(GaIn)As* and *Ga(AsSb)* with varying composition. The parameters were determined from the electron microscope used.

Electron energy	200 kV
Aperture angle	21.3 mrad
Two-fold astigmatism	0 nm
C_S	2 µm
C_5	5 mm
C_C	1.5 mm

To be able to determine the composition of the QWs, complementary image simulations were performed with the software package STEMsalabim [26] which is based on the multi slice method [27]. Chromatic aberration is taken into account by a defocus series [28] of 7 different defoci centred at Δf= 0 nm with a full width half maximum of 7.5 nm [11]. Thermal diffuse scattering is incorporated by the frozen phonon approximation [29] with 10 different atomic configurations per defocus. Each atomic configuration represents a thermal vibration by statistically displacing atoms from their resting positions. All main parameters for the image simulation corresponding to experimental conditions are found in Table 1. 20 different super cells with a size of 5 × 5 × 80 unit cells (X × Y × Z) were simulated. For ten of them, *(GaIn)As* was simulated for *In* concentrations ranging from 0% to 45%. Likewise, ten super cells of *Ga(AsSb)* with *Sb* concentrations from 0% to 45% were simulated. In all super cells, *In* respectively *Sb* were statistically distributed while fixing the concentration in the whole super cell to the desired value. All super cells were relaxed by valence force field relaxation [30] to consider static atomic displacements.

3. Segregation models

Surface segregation is well known for III-V heterostructures both grown by molecular beam epitaxy (MBE) [12] and by MOVPE [14]. After its first observation [31,32] and further studies [12] several models to describe it were developed. Moison et al. [33] came up with a thermodynamic model that worked well for high temperatures and small bulk layer concentrations. For lower temperatures, Dehaese et al. [34] proposed a kinetic model that is equivalent to the one by Moison et al. for higher temperatures. However, both models are only working for small bulk concentrations [35,36]. Muraki et al. [14] used a phenomenological model in which for every layer a certain fraction S (segregation coefficient) of incoming atoms is segregating to the surface layer while the rest is incorporated into the crystal. With this, for every layer the concentration x(n) of the segregating element in layer n can be described as

$$x(n) = \begin{cases} x_0(1 - S^n): & 1 \le n \le N \\ x_0(1 - S^n)S^{n-N}: & n > N \end{cases} \quad (1)$$

where x_0 is the final concentration of the segregating element and N is the total number of deposited layers. The segregation model by Muraki et al. was used for several studies of segregation in III-V heterostructures by TEM, especially for *(GaIn)As* [17–19]. In the case of *Sb* segregation, there are also studies available [37]. Additionally, the Muraki model was applied to *InAs/GaSb* super lattices [38]. In all these cases, the Muraki model gives a reasonable description of the experimental findings.

However, it was shown that in certain cases the Muraki model

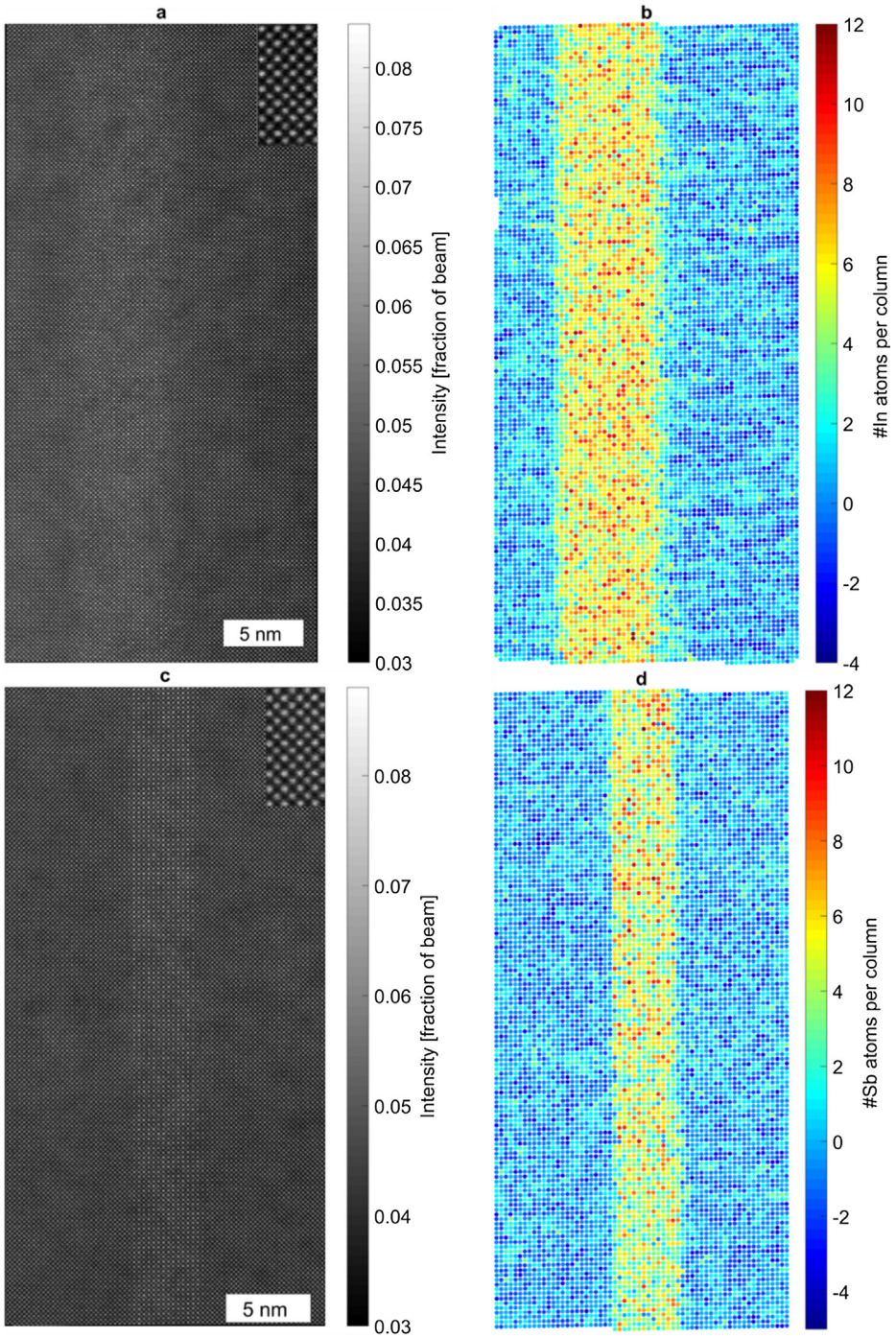

Fig. 1. HAADF-STEM images of the single *(GaIn)As-QW* (A) and the single *Ga(AsSb)*-QW (C). The intensity in both images is normalized to the impinging beam. Magnified insets show the high resolution. Composition maps of the single *(GaIn)As*-QW and the single *Ga(AsSb)*-QW are shown in (B) and (D), respectively. The number of *In* respectively *Sb* is given per atomic column with atomic resolution. Note, that the total number of atoms per column (i.e. the thickness) is not constant within the image. Negative compositions are explained in the main text. Growth direction is from left to right.

breaks down and the fluid three-layer exchange (F3LE) model proposed by Godbey and Ancona [15] can offer a better description. This was found initially for *SiGe/Si* where extended tails in the concentration profile, i.e. a slow decay of the concentration, were present [39,40]. Additionally, this was reported for a material system where both *In* and *Sb* segregation are taking place and competing with one another [20]. In contrast to the previous models where only exchange between two layers is considered, in the F3LE model exchange can take place between the three topmost layers and an infinite surface diffusion rate is assumed. When the growth of new layer s starts, the exchange takes place between the topmost layer s and the second topmost layer s-1 and between the second topmost layer s-1 and the third topmost layer s-2. Once layer s is fully grown, layer s-2 is not included in the exchange mechanism anymore and a new layer starts to grow. Hence, growth and exchange take place simultaneously.

For better readability, the following equations describing the F3LE model are given for the case of *In/Ga* but can analogously be used for *Sb/As*. The composition of the three topmost layers taking part in the exchange is given as

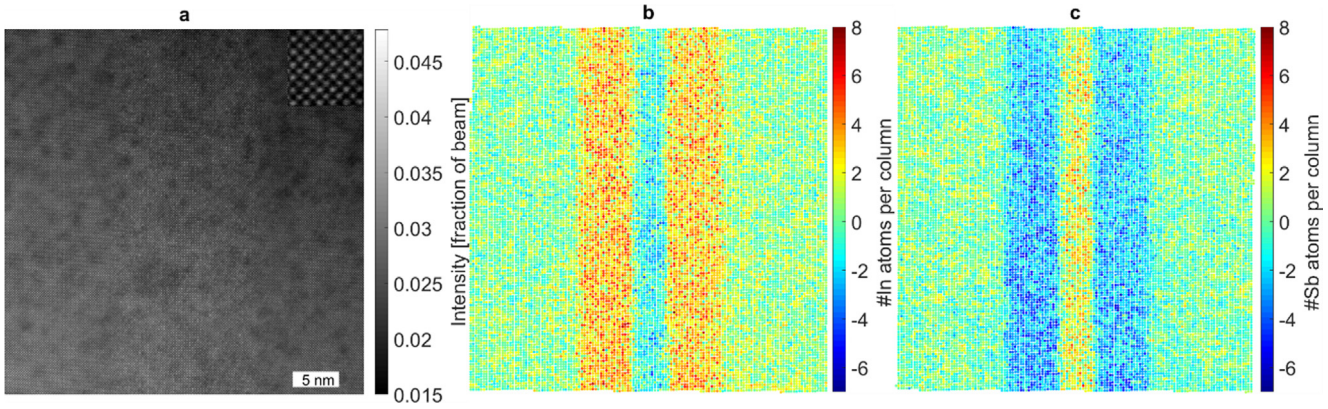

Fig. 2. HAADF-STEM image of the "W"-QWH (A). The intensity is normalized to the impinging beam. A magnified inset shows the high resolution. The composition of *In* is shown in B, while the composition of *Sb* is presented in C. Again, note the varying thickness of the atomic columns. Negative compositions are explained in the text. Growth direction is from left to right.

$$X_{In}^{(s)} + X_{Ga}^{(s)} = \frac{t}{\tau} \tag{2}$$

$$X_{In}^{(s-1)} + X_{Ga}^{(s-1)} = 1 \tag{3}$$

$$X_{In}^{(s-2)} + X_{Ga}^{(s-2)} = 1 \tag{4}$$

Here $X_{In/Ga}^{(s)}$, $X_{In/Ga}^{(s-1)}$, $X_{In/Ga}^{(s-2)}$ denote the concentration of *In* respectively *Ga* in the topmost, second topmost and third topmost layer, t is the time and τ is the time needed to complete the growth of one monolayer. Note, that group III and group V lattices are treated separately. The concentrations of *In* in all three layers underlie mass balance equations:

$$\frac{dX_{In}^{(s)}}{dt} = \Phi_{In} + E_{s,s-1} \tag{5}$$

$$\frac{dX_{In}^{(s-1)}}{dt} = E_{s-1,s} + E_{s-1,s-2} \tag{6}$$

$$\frac{dX_{In}^{(s-2)}}{dt} = E_{s-2,s-1} \tag{7}$$

Here $\Phi_{In} = \frac{x}{\tau}$ is the *In* incorporation rate and $E_{i,j}$ describes the exchange process. Thereby, $E_{i,j}$ is given as

$$E_{i,i-1} = P_1 X_{Ga}^{(i)} X_{In}^{(i-1)} - P_2 X_{Ga}^{(i-1)} X_{In}^{(i)} \tag{8}$$

with exchange probabilities P_1 and P_2 that are described as $P_1 = \nu_1 e^{-E_1/kT}$ and $P_2 = \nu_2 e^{-E_2/kT}$. E_1 and E_2 are surface and bulk energies, while ν_1 and ν_2 are vibrational frequencies. They describe a combination of surface and bulk lattice vibration and are normally chosen as $10^{13}\ 1/s$ [34,41]. T is the temperature and k the Boltzmann constant.

In this work, both the Muraki and the F3LE model are used to describe the composition profiles of the different QWHs.

4. Results

In a first step, composition maps of the QWHs are determined from the experimental HAADF-STEM images. The resulting concentration profiles are used to investigate the surface segregation taking place during the growth of QWHs by MOVPE. Therefore, both Muraki and F3LE model are fitted to the concentration profiles.

4.1. Composition determination

To be able to determine the composition of the QWHs from the HAADF-STEM images, first experimental images and the simulated composition series are carefully matched considering detector sensitivity [42] and source size [11]. Here, the source size parameter fitted is not only representing the source size of the electron source. It also involves the influence of amorphous layers that have been introduced by sample preparation. These amorphous layers lead to a general redistribution of intensity from the peaks to the background which can be inherently modelled by the source size parameter. Additional influences of amorphous layers [43] are not taken into account. Consequences following from this will be discussed later.

The composition of each atomic column is determined by a comparison of Voronoi intensities [8] of simulation and experiment. By using Voronoi intensities, the influence of surface relaxation of thin TEM samples [44–46] on the intensity assigned to atomic columns is reduced. For composition determination, the local thickness of each atomic column is taken into account. A detailed description and discussion of the composition determination procedure can be found in [47].

The HAADF-STEM images of the single *(GaIn)As*-QW (Fig. 1A) and the single *Ga(AsSb)*-QW (Fig. 1C) together with the composition maps derived are shown in Fig. 1. In the composition maps, for the *(GaIn)As*-QW (Fig. 1B) only group III columns are shown. For the *Ga(AsSb)*-QW (Fig. 1D), only group V columns are shown. The absolute number of *In* atoms or *Sb* atoms per column is given while the thickness of every atomic column differs. In both cases, the mean concentration of *In* or *Sb* is varying around zero in the *GaAs* barriers. The thickness ranges from 25 to 31 atoms per atomic column in the case of *(GaIn)As* and from 24 to 28 atoms per atomic column in the case of *Ga(AsSb)*. The thickness maps are not shown.

For the "W"-QWH, HAADF-STEM image (Fig. 2A) and the composition maps of *In* where only group III columns are shown (Fig. 2B) and *Sb* where only group V columns are shown (Fig. 2C) are presented in Fig. 2.

Here, the thickness of the atomic columns ranges from 10 to 19 atoms per atomic column as the total field of view of the HAADF-STEM image is roughly twice as large as in case of the single QWs. The thickness of every atomic column is determined by using the other sub lattice given a negligible influence of cross scattering [47].

An apparently negative composition of *In* in the *Ga(AsSb)*-QW and an apparently negative composition of *Sb* in the *(GaIn)As*-QWs is determined. This is caused by the local thickness determination that uses the other sub lattice. Consequently, the increased intensity of the other sub lattice due to compositional changes leads to a wrong thickness determination of the group III sub lattice in the *Ga(AsSb)*-QW and the group V sub lattice in the *(GaIn)As*-QWs. Hence, the composition is determined for a wrong thickness which is assumed to be higher than the actual thickness. This leads to unphysical negative compositions. However, since all QWs in the "W"-QWH are ternary the same composition determination procedure can still be used and the negative concentrations in the other QW can be omitted. So, the *In* composition

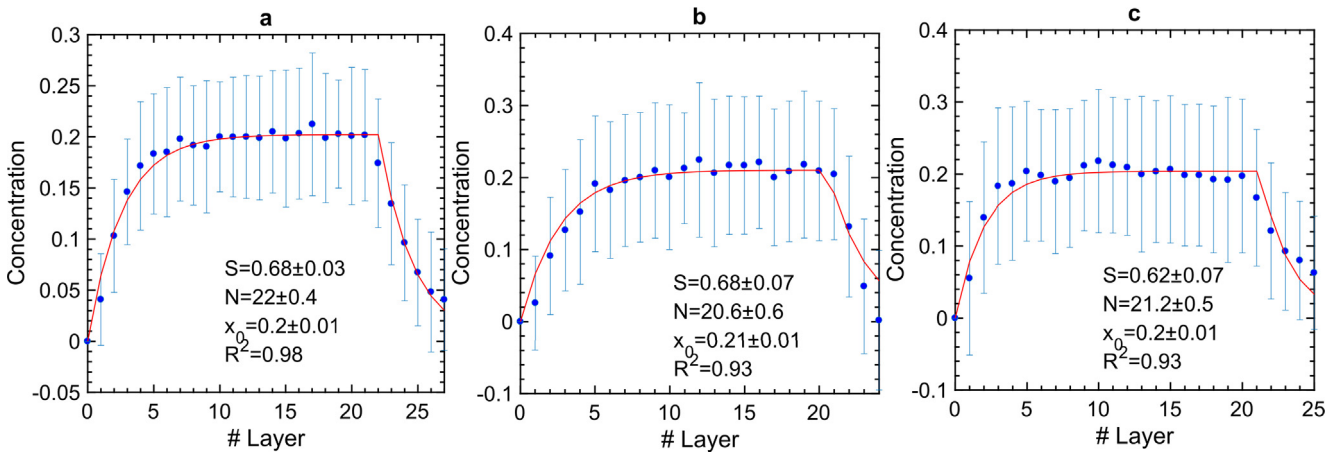

Fig. 3. Muraki model fitted to the composition profiles of the single *(GaIn)As*-QW (A), the first *(GaIn)As*-QW in the "W"-QWH (B) and the second *(GaIn)As*-QW in the "W"-QWH (C). The concentration of *In* is given as fraction averaged over one atomic layer considering the local thickness of each atomic column. Shown error bars do not indicate the error of composition determination but the standard deviation per lattice plane. Fit parameters are given as insets.

is trustable everywhere but in the *GaAsSb*-QW, while the *Sb* composition is only wrong in the *GaInAs*-QWs. In *GaAs* barriers, the mean concentration of *In* or *Sb* determined is almost zero as expected.

4.2. Surface segregation

From the composition maps, concentration profiles of the QWHs can be obtained by averaging the composition of each lattice plane considering the local thickness of each atomic column. This yields a layer-by-layer concentration profile of the QWHs. For the single *(GaIn)As*-QWs and the *(GaIn)As*-QWs in the "W"-QWH, the concentration profiles are shown in Fig. 3. The "error bars" do not give the accuracy of concentration determination but instead they give the standard deviation of the concentration per lattice plane. As discussed in previous work [22], this standard deviation reflects a Poisson-like distribution of *In* in the QWs considering the experimental noise present in the measurement. The experimental noise can be determined in the *GaAs* barrier and could be subtracted to reveal the actual chemical fluctuation of the ternary materials assuming quadratic addition of standard deviations. However, this was not done in the given profiles.

The concentration profile of the single *(GaIn)As*-QW clearly shows surface segregation well known for III-V heterostructures [16]. In a first step, the Muraki model is fitted to all *(GaIn)As*-QWs using the Levenberg-Marquardt algorithm [48]. The concentration profiles together with the fitted models are shown in Fig. 3. As inset, the fitting parameters of the Muraki model are given together with the R^2-value of the fit. For better visualization, for every concentration the data point (0/0) was added. However, this does not change the fit of the Muraki model.

To specify the different interfaces, for each QW the first interface in growth direction is called lower interface, while the second interface in growth direction is called the upper interface. This nomenclature is chosen based on the geometry during growth.

For the single *(GaIn)As*-QW (Fig. 3A), a very good description of the concentration profile is achieved with the Muraki model. This is true for both the lower and the upper interface. The segregation coefficient determined as $S = 0.68 \pm 0.03$ is in good agreement with the value of $S = 0.65 \pm 0.05$ found by Piscopiello et al. [17] for *(GaIn)As* also grown by MOVPE at 550 °C.

Furthermore, the Muraki model is fitted to all the *(GaIn)As*-QWs in the "W"-QWH. For the first *(GaIn)As*-QW in the "W"-QWH (in growth direction, Fig. 3B), the same segregation coefficient as for the single *(GaIn)As*-QW was found ($S = 0.68 \pm 0.07$). However, the fit is not describing the data as well as in the previous case. Especially at the upper interface where the concentration decreases and the Ga(AsSb)-QW is already grown, the concentration profile is not well matched.

For the second *(GaIn)As*-QW in the "W"-QWH (Fig. 3C), the segregation coefficient determined is slightly lower $S = 0.62 \pm 0.07$ but within the errors the segregation coefficients of both *(GaIn)As*-QWs agree. Again, the data is not well matched by the Muraki model everywhere: Lower (growth on *Ga(AsSb)*) as well as upper interface (followed by *GaAs*) show some deviations from the Muraki model.

The Muraki model is also applied to the *Ga(AsSb)*-QWs. For the single *Ga(AsSb)*-QW (Fig. 4A), the Muraki model is reasonably describing the concentration profile of *Sb* in the QW. In case of the *Ga*

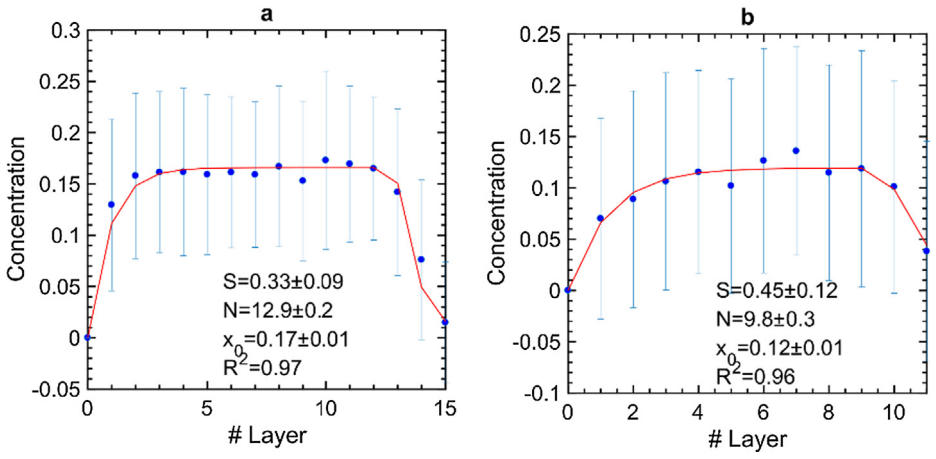

Fig. 4. Muraki model fitted to the composition profiles of the single *Ga(AsSb)*-QW (A) and the *Ga(AsSb)*-QW in the "W"-QWH (B). The concentration of *Sb* is given as fraction averaged over one atomic layer considering the local thickness of each atomic column. Shown error bars do not indicate the error of composition determination but the standard deviation per lattice plane. Fit parameters are given as insets.

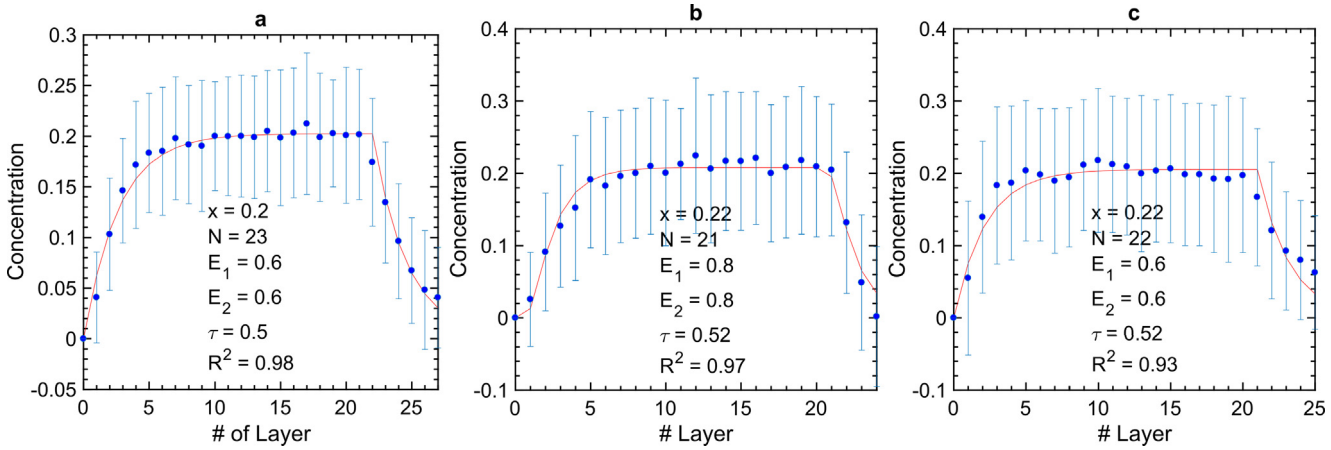

Fig. 5. F3LE model fitted to *(GaIn)As*-QWs. The results for the single QW (A) and the first (B) and second (C) QW in the "W"-QWH are shown together with the parameters used. Energies are given in eV. The parameter N describes the layer after which In deposition stops.

(AsSb)-QW in the "W"-QWH (Fig. 4B), the Muraki model is also matching the *Sb* concentration profile reasonably.

Since the Muraki model is not matching all concentration profiles additionally the F3LE model by Godbey and Ancona is considered to describe the concentration profiles. This model is chosen because in previous studies it has been shown that the F3LE model can describe concentration profiles in certain cases where the Muraki model fails [39,40].

For this, the resulting partial differential equations have to be solved and fitted to the concentration profiles. Fitting is performed with the Nelder-Mead method [49].

The time to grow one monolayer τ is determined from the growth time for the QWs which is 11 s in case of the *(GaIn)As*-QWs and 13 s in case of the *Ga(AsSb)*-QWs and the number of layers as determined by the Muraki model.

The results for the *(GaIn)As*-QWs are shown in Fig. 5. For the single *(GaIn)As*-QW (a), a very good description can be achieved. In case of the first *(GaIn)As*-QW in the "W"-QWH, the data is also described well by the model with slightly changed energies. For the second *(GaIn)As*-QW in the "W"-QWH, the description is less accurate at the interfaces.

For the single *Ga(AsSb)*-QW, also a very good description of the concentration profile by the F3LE model is possible (Fig. 6(a)). In case of the *Ga(AsSb)*-QW in the "W"-QWH, the agreement of model and data is reasonable considering the small amount of data especially at the interfaces.

5. Discussion

Below, the results for both composition determination and surface segregation are discussed.

5.1. Accuracy of composition determination

The composition determination of the different QWHs is performed on an atomic scale. Composition determination by comparing experimental and simulated STEM intensities is a statistical process. Different z-height distributions of the substitute atoms can yield the same Voronoi intensity which leads to an inherent uncertainty. For a given atomic column, its composition can be determined with single-atom accuracy with a certain probability depending on material system and thickness. However, if the number of analysed atomic columns is large enough, the overall composition is determined correctly [47].

For composition determination, the local thickness of each atomic column is considered. Additionally, the simulation includes static atomic displacements and accurate modelling of the electron microscope. However, there are still several parameters which were not thoroughly considered in the evaluation process: surface relaxation, amorphous layers on the samples and inelastic scattering.

The surface relaxation of thin TEM samples can have a severe influence on the intensities used for quantitative STEM evaluations [45,46]. This influence is reduced by the use of Voronoi cells as already stated above. Additionally, the influence of surface relaxation is picked

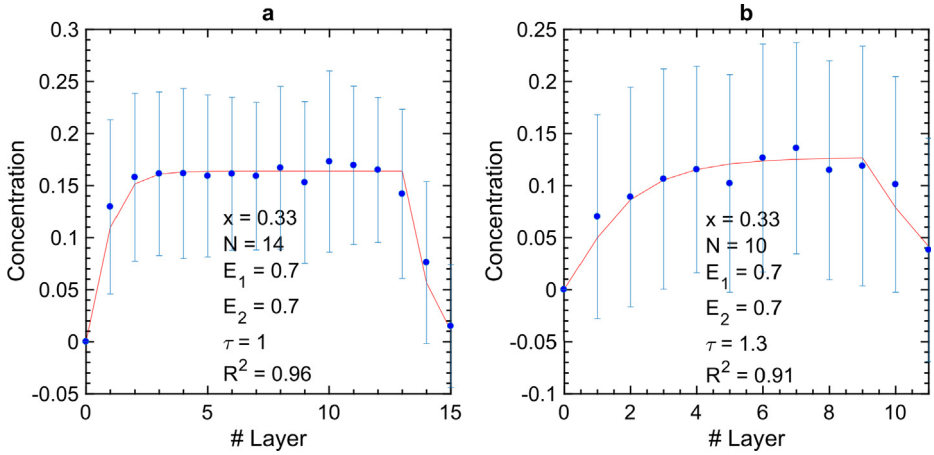

Fig. 6. F3LE model fitted to single *Ga(AsSb)*-QW (A) and *Ga(AsSb)*-QW in the "W"-QWH (B). The fitting parameters are given as insets. Energies are given in eV. The parameter N describes the layer after which Sb deposition stops.

up by local thickness treatment that factors in the local intensity of each column. If surface relaxation changes Voronoi intensities locally, this leads to a thickness determination deviating from the real one. Finally, this also has an influence on the concentration determination. However, for the QWs investigated surface relaxation plays a minor role, since the strain is comparably low. Furthermore, a thorough consideration of surface relaxation is not trivial since the actual sample structure and geometry, e.g. QW width, composition and sample thickness, affect the way surface relaxation alters the intensity [45].

Amorphous layers occur both on top and bottom of the crystalline centre as ion bombardment during sample preparation is destroying the crystalline sample. For *GaAs* based materials prepared in the same way as in this work, the thickness of the amorphous layers both on top and bottom was found to be 3.5 nm [50]. Hence, the thickness of the amorphous layers present on the investigated sample is expected to be in a similar range. Both amorphous layers lead to an increase of the detected scattered intensity whereby the influence is larger for smaller detector angles. The true crystalline thickness will be smaller than the one determined without considering amorphous layers. However, if different amorphous materials behave very similar for their intensity increase as proposed for the case of *Si* and *Ge* by Grieb et al. [51], then the concentration finally derived should not change. Besides the general intensity increase, the amorphous layer on the top surface also broadens the beam and leads to enhanced cross scattering compared to a fully crystalline sample. Taking into account amorphous layers for quantitative STEM in general and for thickness determination in particular can be achieved by considering them in simulations or removing them on the experimental sample by very low voltage ion milling [52]. Simulation involving methods can be based on position averaged convergent electron beam diffraction for the determination of crystalline thickness, e.g. like suggested by Grieb et al. [51].

Inelastic scattering is not considered for the simulation when comparing experimental and simulated intensities. However, inelastic scattering is less important for high angles used here [53] so the measurements in this work performed for an angular range above 60 mrad are not affected.

In the composition maps, non-zero concentrations of *In* respectively *Sb* in *GaAs* regions are present. On the one hand, these can be caused by the determination of the local thickness as discussed in detail elsewhere [47]. On the other hand, the non-zero concentrations are a consequence of the material system investigated. The local thickness of each column is determined through *Ga* or *As* columns with a precision of one atom by comparison of its Voronoi intensity to simulations. The atomic number of the column is the main factor for the scattered intensity of that atomic column. If the thickness of a column is increased by one *Ga* or *As* column, the total atomic number Z of that column is increased by 31 or 33, respectively. In comparison, replacing a *Ga* atom by an *In* atom or *As* by *Sb* increases the total atomic number of that column by only 18. Hence, one additional *Ga* or *As* atom (i.e. changing the thickness) has a larger impact on the intensity of that column than changing the composition: The "composition sampling" of the intensity is smaller than the "thickness sampling" of the intensity. Since all thicknesses and compositions are found by matching intensities of simulation and experiment, this leads to non-zero compositions of columns in *GaAs*. Of course, the same effect is also happening in QWs. An ideal material system for composition determination consists of materials where the influence of a thickness change is smaller than that of a composition change. The small deviation from zero of the mean concentrations in *GaAs* is most likely caused by the presence of the amorphous layer. For further discussion of the composition determination, also see [47].

In general, the composition determination method used is giving an excellent agreement of the composition of the *(GaIn)As*-QW with the composition determined by XRD and a reasonable agreement for the *Ga(AsSb)*-QW. The deviations in case of *Ga(AsSb)* could be explained by a stronger oxidation of the surfaces of the TEM specimen in the *Sb* containing layer [54].

5.2. Interaction of In and Sb during growth

Since the growth conditions of the single QWs and the QWs in the "W"-QWH are exactly the same, a comparison of the resulting concentration profiles of the QWs gives insight into the influences of *In* and *Sb* on each other during the growth.

First, the single *(GaIn)As*-QW and the two *(GaIn)As*-QWs in the "W"-QWH are compared to each other.

All *(GaIn)As*-QWs have the same maximum *In* concentration of $x \approx 0.2$ but the shape, i.e. the surface segregation, differs depending on the material at the interface that is either *GaAs* or *Ga(AsSb)*.

In case of the single *(GaIn)As*-QW, the Muraki model gives an adequate description of the concentration profile obtained and the surface segregation present as was already reported in several cases before [16–18]. Additionally, the segregation coefficient obtained is in good agreement with results published before for a *(GaIn)As*-QW grown by MOVPE at the same growth temperature. This supports the validity of both concentration profile and segregation coefficient determined.

In the following, descriptions of the segregation for the *(GaIn)As*-QWs in the "W"-QWH are referring to the segregation for the single *(GaIn)As*-QW where all interfaces consist of *GaAs*. To allow for quantitative comparison, the Muraki model is slightly modified. For the lower interface, a segregation coefficient S_l is used while the upper interface is described by segregation coefficient S_u. This is motivated by the inequivalence of lower and upper interface. The resulting model is

$$x(n) = \begin{cases} x_0(1 - S_l^n): & 1 \le n \le N \\ x_0(1 - S_l^n)S_u^{n-N}: & n > N \end{cases} \tag{9}$$

so that both interfaces can be treated independently. In Fig. 7, the fits obtained for the *(GaIn)As*-QWs in the "W"-QWH are shown. Both give a good description of the concentration profiles at both interfaces. The resulting segregation coefficients at both interfaces differ from each other which is discussed hereafter.

The first *(GaIn)As*-QW in the "W"-QWH shows a very similar segregation at the lower interface. This is supported by the segregation coefficients determined with the Muraki model ($S_l^I = 0.74 \pm 0.04$). Since both QWs are grown on *GaAs* under the same growth conditions this is the expected result. A decrease in concentration takes place when the *In* supply during growth is stopped. Depending on the present segregation, this concentration decrease can take place slowly as it is the case for the single *(GaIn)As*-QW. In contrast, the first *(GaIn)As*-QW in the "W"-QWH shows an abrupt decay of *In* concentration. Consequently, a smaller segregation coefficient for the upper interface of $S_u^I = 0.31 \pm 0.15$ is connected to this abrupt decay. Since only a limited amount of data points is used for fitting, a larger error results. The abrupt decay is in agreement with results published by Sanchez et al. [21] who found blocking of incorporation of segregating *In* by *Sb*. The growth of *Ga(AsSb)* on the first *(GaIn)As*-QW can stop *In* incorporation. So, the blocking of segregating *In* leads to an abrupt interface. While the segregation at the lower interface of the first *(GaIn)As*-QW in the "W"-QWH is the same as for the single *(GaIn)As*-QW, the upper interface is altered and surface segregation is suppressed due to the interface to the *Ga(AsSb)*-QW in the "W"-QWH.

In line with blocking of *In* incorporation by *Sb*, the lower interface of the second *(GaIn)As*-QW in the "W"-QWH deviates from the one of the other *(GaIn)As*-QWs that is dominated by segregation. It does not show the same degree of surface segregation and is more abrupt ($S_l^{II} = 0.58 \pm 0.06$). This can be explained by the fact that this *(GaIn)As*-QW is grown on *Ga(AsSb)* instead on *GaAs*.

Furthermore, this is connected to blocking of *In* incorporation. The amount of *Sb* still present from the growth of the *Ga(AsSb)*-QW has to drop below a certain value before the growth of the second *(GaIn)As*-QW can start. Once this value is undercut, the incorporation of *In*

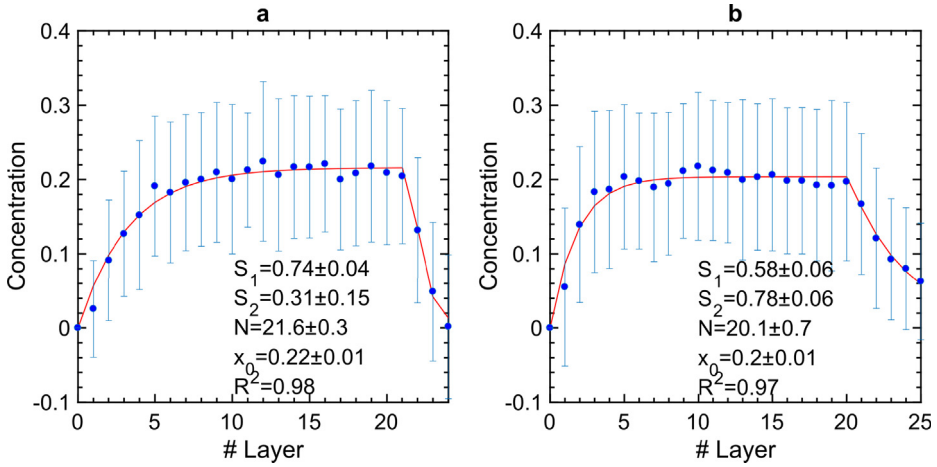

Fig. 7. Modified Muraki model with two different segregation coefficients fitted to the concentration profiles of the first (A) and the second (B) *(GaIn)As*-QW in the "W"-QWH. In both cases, a reasonable description of both interfaces is reached. Fit parameters are given as insets.

already offered and presumably floating on the surface can begin which leads to a more abrupt interface and less surface segregation developing.

The concentration decrease at the upper interface is taking place with a higher segregation coefficient again ($S_u^{II} = 0.76 \pm 0.06$). This surface segregation is similar to the single *(GaIn)As*-QW as both QWs are followed by *GaAs*. However, the segregation coefficient is slightly increased. This can be connected to the growth on already strained layers in the "W"-QWH. Summarized, the surface segregation of the second *(GaIn)As*-QW in the "W"-QWH at the lower interface is changed due to the *Ga(AsSb)*-QW it is grown on and the *Sb* blocking *In* incorporation until the *Sb* content has undercut a certain value whereas the upper interface remains almost unchanged.

All in all, the *(GaIn)As*-QWs in the "W"-QWH are severely altered with regard to their surface segregation where they have interfaces to the *Ga(AsSb)*-QW but show the same surface segregation as in case of the single *(GaIn)As*-QW otherwise.

A comparison of the single *Ga(AsSb)*-QW and the one inside the "W"-QWH shows huge differences. The concentration of *Sb* in the *Ga(AsSb)*-QW inside the "W"-QWH is significantly decreased. Apparently, the growth of *Ga(AsSb)* on *(GaIn)As* (in combination with *In* possibly still floating on the surface) decreases the incorporation of *Sb* even more severely as the other way around. This is in agreement with findings reported by Sanchez et al. [21]. They found a *GaSb* layer on *(GaIn)As* that was intended to contain 100% of *Sb* to have an *Sb* concentration of only 5%. A possible explanation would be disruption of the surface coverage of *Sb* by the floating *In* layer since a critical amount is needed [13].

Additionally, the QW inside the "W"-QWH has a noticeably smaller width than the single one (10 vs. 13 atomic layers). Here, the combination of a *(GaIn)As*-QW before the *Ga(AsSb)*-QW, *In* possibly still floating on the surface and a *(GaIn)As*-QW grown afterwards (i.e. newly incoming *In* floating on the surface) is limiting the incorporation of *Sb*, i.e. the growth rate of *Ga(AsSb)* is changed by the floating layer of *In*. This could also be connected to the critical surface coverage of *Sb* needed.

The Muraki model gives a reasonable description of the concentration profile of the single *Ga(AsSb)*-QW and the *Ga(AsSb)*-QW in the "W"-QWH. *Sb* surface segregation was described by the Muraki model before [37] so that the single *Ga(AsSb)*-QW is expected to be describable by the Muraki model. The *Ga(AsSb)*-QW in the "W"-QWH has two interfaces to *(GaIn)As*-QWs (lower and upper interface) which is in contrast to the *(GaIn)As*-QWs in the "W"-QWH that have interfaces to two different materials. Hence, the *Ga(AsSb)*-QW in the "W"-QWH can be described by the Muraki model with one segregation coefficient while the *(GaIn)As*-QWs in the "W"-QWH cannot as has been shown above.

Schowalter et al. [16] empirically related the segregation efficiency to the lattice mismatch between the materials grown. A smaller lattice mismatch leads to a smaller segregation coefficient, i.e. a more abrupt interface.

This relationship was tailored for single QWs and can therefore not easily be applied to QWHs where strain builds up and additional interaction between elements is present as outlined above.

Haxha et al. [20] showed that the F3LE model can be used to describe both *In* and *Sb* segregation of *Ga(AsSb)/InAs* grown by MBE. Here, next to the single QWs we apply it to the "W"-QWH grown by MOVPE. The F3LE model can be used to describe the growth of the first *(GaIn)As*-QW in the "W"-QWH and also the second *(GaIn)As*-QW in the "W"-QWH in presence of *Sb* with reasonable agreement. Additionally, the *Ga(AsSb)*-QW in the "W"-QWH is reasonably described. Hence, the description of the growth is possible when incorporating three layers. The energies describing the exchange between layers are slightly changed compared to the single QWs used as a reference pointing to different growth behaviour in presence of In/*Sb*.

The results from the F3LE model support the statements made about the growth before.

6. Summary

Concentration profiles of single *(GaIn)As*- and *Ga(AsSb)*-QWs as well as of the whole "W"-QWH were determined on an atomic level by STEM and complementary contrast simulations. With these concentration profiles, growth in general and surface segregation in particular were investigated with regard to influences of *In* and *Sb* on each other. Several findings were made: (i) Surface segregation plays a decisive role in growth of "W"-QWH. (ii) *In* and *Sb* alter surface segregation of each other. (iii) Different segregation coefficients are needed to describe the interfaces of the *(GaIn)As*-QWs in the "W"-QWH as they differ for interfaces to *GaAs* and to *Ga(AsSb)*. (iv) On the one hand, *Sb* is blocking *In* incorporation both after and before the growth of *(GaIn)As*. (v) On the other hand, *In* is changing the growth of *Ga(AsSb)* altering both the total amount of incorporated *Sb* and the growth rate.

In conclusion, surface segregation and interactions between *In* and *Sb* during the growth of "W"-QWHs were revealed using atomic resolution STEM.

Declaration of Competing Interest

The authors declare no conflicting interests.

Acknowledgements

Financial support by the German Research Foundation (DFG) in the framework of SFB 1083 and GRK 1782 is gratefully acknowledged. S. Firoozabadi acknowledges support of the European Union's Horizon 2020 in the framework of the project microSPIRE (ID: 766955).

References

[1] E. Murphy, Enabling optical communication, Nat. Photon. 4 (2010) 287, https://doi.org/10.1038/nphoton.2010.107.
[2] J.R. Meyer, C.A. Hoffman, F.J. Bartoli, L.R. Ram-Mohan, Type-II quantum-well lasers for the mid-wavelength infrared, Appl. Phys. Lett. 67 (1995) 757–759, https://doi.org/10.1063/1.115216.
[3] M. Kudo, K. Ouchi, J. Kasai, T. Mishima, Low-Lattice-strain long-wavelength GaAsSb/GaInAs type-II quantum wells grown on GaAs substrates, Jpn. J. Appl. Phys. 41 (2002) L1040–L1042, https://doi.org/10.1143/JJAP.41.L1040.
[4] C. Berger, C. Möller, P. Hens, C. Fuchs, W. Stolz, S.W. Koch, A. Ruiz Perez, J. Hader, J.V. Moloney, Novel type-II material system for laser applications in the near-infrared regime, AIP Adv. 5 (2015) 047105, https://doi.org/10.1063/1.4917180.
[5] C. Fuchs, A. Beyer, K. Volz, W. Stolz, MOVPE growth of (GaIn)As/Ga(AsSb)/(GaIn)As type-II heterostructures on GaAs substrate for near infrared laser applications, J. Cryst. Growth 464 (2017) 201–205, https://doi.org/10.1016/j.jcrysgro.2016.10.052.
[6] C. Möller, C. Fuchs, C. Berger, A. Ruiz Perez, M. Koch, J. Hader, J.V. Moloney, S.W. Koch, W. Stolz, Type-II vertical-external-cavity surface-emitting laser with Watt level output powers at 1.2 µm, Appl. Phys. Lett. 108 (2016), https://doi.org/10.1063/1.4942103.
[7] S. Van Aert, J. Verbeeck, R. Erni, S. Bals, M. Luysberg, D. Van Dyck, G. Van Tendeloo, Quantitative atomic resolution mapping using high-angle annular dark field scanning transmission electron microscopy, Ultramicroscopy 109 (2009) 1236–1244, https://doi.org/10.1016/j.ultramic.2009.05.010.
[8] A. Rosenauer, T. Mehrtens, K. Müller, K. Gries, M. Schowalter, P. Venkata Satyam, S. Bley, C. Tessarek, D. Hommel, K. Sebald, M. Seyfried, J. Gutowski, A. Avramescu, K. Engl, S. Lutgen, Composition mapping in InGaN by scanning transmission electron microscopy, Ultramicroscopy 1316–1327 (2011) 111, https://doi.org/10.1016/j.ultramic.2011.04.009.
[9] J.M. LeBeau, S.D. Findlay, L.J. Allen, S. Stemmer, Quantitative atomic resolution scanning transmission electron microscopy, Phys. Rev. Lett. 100 (2008) 206101, https://doi.org/10.1103/PhysRevLett. 100.206101.
[10] J.M. LeBeau, S.D. Findlay, X. Wang, A.J. Jacobson, L.J. Allen, S. Stemmer, High-angle scattering of fast electrons from crystals containing heavy elements: simulation and experiment, Phys. Rev. B 79 (2009) 214110, https://doi.org/10.1103/PhysRevB.79.214110.
[11] A. Beyer, J. Belz, N. Knaub, K. Jandieri, K. Volz, Influence of spatial and temporal coherences on atomic resolution high angle annular dark field imaging, Ultramicroscopy 169 (2016) 1–10, https://doi.org/10.1016/j.ultramic.2016.06.006.
[12] J. Massies, F. Turco, A. Saletes, J.P. Contour, Experimental evidence of difference in surface and bulk compositions of AlGaAs, AlInAs and GaInAs epitaxial layers grown by molecular beam epitaxy, J. Cryst. Growth 80 (1987) 307–314, https://doi.org/10.1016/0022-0248(87)90076-5.
[13] M. Pristovsek, M. Zorn, U. Zeimer, M. Weyers, Growth of strained GaAsSb layers on GaAs (001) by MOVPE, J. Cryst. Growth 276 (2005) 347–353, https://doi.org/10.1016/j.jcrysgro.2004.11.420.
[14] K. Muraki, S. Fukatsu, Y. Shiraki, Surface segregation of In atoms during molecular beam epitaxy and its influence on the energy levels in InGaAs/GaAs quantum wells, Appl. Phys. Lett. 61 (1992) 557–559, https://doi.org/10.1063/1.107835.
[15] D.J. Godbey, M.G. Ancona, Modeling of Ge segregation in the limits of zero and infinite surface diffusion, J. Vac. Sci. Technol. A Vac., Surf., Film. 15 (1997) 976–980, https://doi.org/10.1116/1.580790.
[16] M. Schowalter, A. Rosenauer, D. Litvinov, D. Gerthsen, Investigation of segregation by quantitative transmission electron microscopy, Opt. Appl. 36 (2006) 297–308.
[17] E. Piscopiello, A. Rosenauer, A. Passaseo, E.H. Montoya Rossi, G. Van, Tendeloo, segregation in InGaAs/GaAs Stranski-Krastanow layers grown by metal–organic chemical vapour deposition, Philos. Mag. 85 (2005) 3857–3870, https://doi.org/10.1080/147830500269402.
[18] D. Litvinov, D. Gerthsen, A. Rosenauer, M. Schowalter, T. Passow, M. Hetterich, The role of segregation in InGaAs heteroepitaxy, Mater. Sci. Forum. 539–543 (2007) 3540–3545, https://doi.org/10.4028/www.scientific.net/MSF.539-543.3540.
[19] T. Mehrtens, K. Müller, M. Schowalter, D. Hu, D.M. Schaadt, A. Rosenauer, Measurement of indium concentration profiles and segregation efficiencies from high-angle annular dark field-scanning transmission electron microscopy images, Ultramicroscopy 131 (2013) 1–9, https://doi.org/10.1016/j.ultramic.2013.03.018.
[20] V. Haxha, I. Drouzas, J.M. Ulloa, M. Bozkurt, P.M. Koenraad, D.J. Mowbray, H.Y. Liu, M.J. Steer, M. Hopkinson, M.A. Migliorato, Role of segregation in InAs/GaAs quantum dot structures capped with a GaAsSb strain-reduction layer, Phys. Rev. B 80 (2009) 165334, https://doi.org/10.1103/PhysRevB.80.165334.
[21] A.M. Sanchez, A.M. Beltran, R. Beanland, T. Ben, M.H. Gass, F. De La Pëa, M. Walls, A.G. Taboada, J.M. Ripalda, S.I. Molina, Blocking of indium incorporation by antimony in III-V-Sb nanostructures, Nanotechnology 21 (2010) 145606, https://doi.org/10.1088/0957-4484/21/14/145606.
[22] P. Kükelhan, A. Beyer, C. Fuchs, M.J. Weseloh, S.W. Koch, W. Stolz, K. Volz, Atomic structure of 'W'-type quantum well heterostructures investigated by aberration-corrected STEM, J. Microsc. 268 (2017) 259–268, https://doi.org/10.1111/jmi.12647.
[23] J.M. LeBeau, S. Stemmer, Experimental quantification of annular dark-field images in scanning transmission electron microscopy, Ultramicroscopy 108 (2008) 1653–1658, https://doi.org/10.1016/j.ultramic.2008.07.001.
[24] L. Jones, H. Yang, T.J. Pennycook, M.S.J. Marshall, S. Van Aert, N.D. Browning, M.R. Castell, P.D. Nellist, S.I. Molina, D.L. Sales, P.L. Galindo, D. Fuster, Y. González, B. Alén, L. González, M. Varela, S.J. Pennycook, R. Erni, H. Heinrich, G. Kostorz, V. Grillo, E. Carlino, F. Glas, F. Rossi, E.J. Kirkland, Z. Yu, P.E. Batson, J. Silcox, E. Carlino, V. Grillo, Smart align-a new tool for robust non-rigid registration of scanning microscope data, Ultramicroscopy 109 (2009) 8, https://doi.org/10.1186/s40679-015-0008-4.
[25] D.S. He, Z.Y. Li, A practical approach to quantify the ADF detector in STEM, J. Phys. Conf. Ser. 522 (2014) 012017, https://doi.org/10.1088/1742-6596/522/1/012017.
[26] J.O. Oelerich, L. Duschek, J. Belz, A. Beyer, S.D. Baranovskii, K. Volz, STEMsalabim: a high-performance computing cluster friendly code for scanning transmission electron microscopy image simulations of thin specimen, Ultramicroscopy 177 (2017) 91–96, https://doi.org/10.1016/j.ultramic.2017.03.010.
[27] E.J. Kirkland, Advanced Computing in Electron Microscopy, 2010.
[28] K. Kuramochi, T. Yamazaki, Y. Kotaka, M. Ohtsuka, I. Hashimoto, K. Watanabe, Effect of chromatic aberration on atomic-resolved spherical aberration corrected STEM images, Ultramicroscopy 110 (2009) 36–42, https://doi.org/10.1016/j.ultramic.2009.09.003.
[29] R.F. Loane, P. Xu, J. Silcox, Thermal vibrations in convergent-beam electron diffraction, Acta Crystallogr. Sect. A 47 (1991) 267–278, https://doi.org/10.1107/S0108767391000375.
[30] P.N. Keating, Effect of invariance requirements on the elastic strain energy of crystals with application to the diamond structure, Phys. Rev. 145 (1966) 637–645, https://doi.org/10.1103/PhysRev. 145.637.
[31] T.-C. Chiang, R. Ludecke, D.E. Eastman, Photoemission studies of AlGaAs(100) surfaces grown by molecular-beam epitaxy, Phys. Rev. B 25 (1982) 6518–6521, https://doi.org/10.1103/PhysRevB.25.6518.
[32] A. Stall, J. Zilko, V. Swaminathan, N. Schumaker, Morphology of GaAs and AlGaAs grown by molecular beam epitaxy, J. Vac. Sci. Technol. B 3 (1985).
[33] J.M. Moison, C. Guille, F. Houzay, F. Barthe, M. Van Rompay, Surface segregation of third-column atoms in group III-V arsenide compounds: ternary alloys and heterostructures, Phys. Rev. B 40 (1989) 6149–6162, https://doi.org/10.1103/PhysRevB.40.6149.
[34] O. Dehaese, X. Wallart, F. Mollot, Kinetic model of element III segregation during molecular beam epitaxy of III-III′-V semiconductor compounds, Appl. Phys. Lett. 66 (1995) 52–54, https://doi.org/10.1063/1.114180.
[35] J.M. Gerard, In situ probing at the growth temperature of the surface composition of (InGa)As and (InAl)As, Appl. Phys. Lett. 61 (1992) 2096–2098, https://doi.org/10.1063/1.108318.
[36] A. Rosenauer, D. Gerthsen, D. Van Dyck, M. Arzberger, G. Böhm, G. Abstreiter, Quantification of segregation and mass transport in InGaAs/GaAs Stranski-Krastanow layers, Phys. Rev. B 64 (2001) 245334, https://doi.org/10.1103/PhysRevB.64.245334.
[37] M. Schowalter, A. Rosenauer, D. Gerthsen, M. Grau, M.C. Amann, Quantitative measurement of the influence of growth interruptions on the Sb distribution of GaSb/GaAs quantum wells by transmission electron microscopy, Appl. Phys. Lett. 83 (2003) 3123–3125, https://doi.org/10.1063/1.1618380.
[38] X. Li, Y. Zhang, D. Jiang, F. Guo, D. Wang, L. Zhao, Atomic intermixing and segregation at the interface of InAs/GaSb type II superlattices, Superlattices Microstruct. 104 (2017) 390–396, https://doi.org/10.1016/j.spmi.2017.02.052.
[39] T. Walther, C.J. Humphreys, D.J. Robbins, Diffusion and surface segregation in thin SiGe/Si layers studied by scanning transmission electron microscopy, Defect Diffus. Forum. 143–147 (1997) 1135–1140, https://doi.org/10.4028/www.scientific.net/DDF.143-147.1135.
[40] D.J. Norris, Y. Qiu, A. Dobbie, M. Myronov, T. Walther, Similarity of Stranski-Krastanow growth of Ge/Si and SiGe/Si (001), J. Appl. Phys. 115 (2014), https://doi.org/10.1063/1.4837975.
[41] R. Magri, A. Zunger, Effects of interfacial atomic segregation and intermixing on the electronic properties of InAs/GaSb superlattices, Phys. Rev. B - Condens. Matter Mater. Phys. 65 (2002) 1653021–16530218, https://doi.org/10.1103/PhysRevB.65.165302.
[42] S.D. Findlay, J.M. LeBeau, Detector non-uniformity in scanning transmission electron microscopy, Ultramicroscopy 124 (2013) 52–60, https://doi.org/10.1016/j.ultramic.2012.09.001.
[43] K.A. Mkhoyan, S.E. Maccagnano-Zacher, E.J. Kirkland, J. Silcox, Effects of amorphous layers on ADF-STEM imaging, Ultramicroscopy 108 (2008) 791–803, https://doi.org/10.1016/j.ultramic.2008.01.007.
[44] V. Grillo, The effect of surface strain relaxation on HAADF imaging, Ultramicroscopy 109 (2009) 1453–1464, https://doi.org/10.1016/j.ultramic.2009.07.010.
[45] A. Beyer, L. Duschek, J. Belz, K. Jandieri, K. Volz, Influence of surface relaxation of strained layers on atomic resolution ADF imaging, Ultramicroscopy 181 (2017) 8–16, https://doi.org/10.1016/j.ultramic.2017.04.019.
[46] A. Beyer, L. Duschek, J. Belz, J.O. Oelerich, K. Jandieri, K. Volz, Surface relaxation of strained Ga(P, As)/GaP heterostructures investigated by HAADF STEM, J. Microsc. 268 (2017) 239–247, https://doi.org/10.1111/jmi.12622.
[47] L. Duschek, P. Kükelhan, A. Beyer, S. Firoozabadi, J.O. Oelerich, A. Ballabio, G. Isella, K. Volz, Composition determination of semiconductor alloys towards atomic accuracy by HAADF-STEM, Ultramicroscopy 200 (2019) 84–96, https://doi.

org/10.1016/j.ultramic.2019.02.009.
[48] K. Levenberg, A method for the solution of certain non-linear problems in least squares, Q. Appl. Math. 2 (1944) 164–168, https://doi.org/10.1090/qam/10666.
[49] J.A. Nelder, R. Meadf, A simplex method for function minimization, Comput. J. 7 (1964) 308–313.
[50] J. Belz, A. Beyer, T. Torunski, W. Stolz, K. Volz, Direct investigation of (sub-) surface preparation artifacts in GaAs based materials by FIB sectioning, Ultramicroscopy 163 (2016) 19–30, https://doi.org/10.1016/j.ultramic.2016.01.001.
[51] T. Grieb, M. Tewes, M. Schowalter, K. Müller-Caspary, F.F. Krause, T. Mehrtens, J.M. Hartmann, A. Rosenauer, Quantitative HAADF STEM of SiGe in presence of amorphous surface layers from FIB preparation, Ultramicroscopy 184 (2018) 29–36, https://doi.org/10.1016/j.ultramic.2017.09.012.
[52] R.R. Cerchiara, P.E. Fischione, J. Liu, J.M. Matesa, A.C. Robins, H.L. Fraser, A. Genc, Raising the standard of specimen preparation for aberration-corrected TEM and STEM, Micros. Today. 19 (2011) 16–19, https://doi.org/10.1017/S1551929510001197.
[53] R.F. Egerton, Electron Energy-Loss Spectroscopy in the Electron Microscope, 3rd ed., 2011.
[54] Y. Mizokawa, O. Komoda, S. Miyase, Long-time air oxidation and oxide-substrate reactions on GaSb, GaAs, adn GaP at room temperature studied by x-ray photoelectron spectroscopy, Thin Solid Films 156 (1988) 127–143, https://doi.org/10.1016/0040-6090(88)90288-X.

6.4 Simultaneous Determination of Local Thickness and Composition for Ternary III-V Semiconductors by Aberration-Corrected STEM

P. Kükelhan, A. Beyer, S. Firoozabadi, T. Hepp, K. Volz. *Ultramicroscopy* 201 (2019), pp. 49-57. doi: 10.1016/j.ultramic.2019.03.005

Abstract Scanning transmission electron microscopy (STEM) is a suitable method for the quantitative characterization of nano-materials. For an absolute composition determination on an atomic scale, the thickness of the specimen has to be known locally with high accuracy. Here, we propose a method to determine both thickness and composition of ternary III-V semiconductors locally from one STEM image as shown for the example material systems *Ga(AsBi)* and *(GaIn)As*. In a simulation study, the feasibility of the method is proven and the influence of specimen thickness and detector angles used is investigated. An application to an experimental STEM image of a textitGa(AsBi) quantum well grown by metal organic vapor phase epitaxy yields an excellent agreement with composition results from high resolution X-ray diffraction.

Contributions of the Author For this work, I developed the method proposed and performed all STEM investigations and evaluations, both in simulation and experiment.

The manuscript was written by me except for one paragraph dealing with MOVPE and XRD measurements.

Ultramicroscopy 201 (2019) 49–57

Contents lists available at ScienceDirect

Ultramicroscopy

journal homepage: www.elsevier.com/locate/ultramic

Simultaneous determination of local thickness and composition for ternary III-V semiconductors by aberration-corrected STEM

P. Kükelhan, A. Beyer*, S. Firoozabadi, T. Hepp, K. Volz

Materials Science Centre and Faculty of Physics, Philipps University Marburg, Hans-Meerwein-Straße 6, Marburg, Germany

ARTICLE INFO

Keywords:
Quantitative STEM
composition determination
III-V semiconductors
image simulations

ABSTRACT

Scanning transmission electron microscopy (STEM) is a suitable method for the quantitative characterization of nanomaterials. For an absolute composition determination on an atomic scale, the thickness of the specimen has to be known locally with high accuracy. Here, we propose a method to determine both thickness and composition of ternary III-V semiconductors locally from one STEM image as shown for the example material systems Ga(AsBi) and (GaIn)As. In a simulation study, the feasibility of the method is proven and the influence of specimen thickness and detector angles used is investigated. An application to an experimental STEM image of a Ga(AsBi) quantum well grown by metal organic vapour phase epitaxy yields an excellent agreement with composition results from high resolution X-ray diffraction.

1. Introduction

Scanning transmission electron microscopy (STEM) became a widely used technique for the atomic-scale analysis of nanomaterials, especially technologically relevant ones. For the optimization of these nanomaterials, the atomic-scale characterization by STEM plays an important role in the interplay of theoretical predictions, growth and material characterization with the aim of improving the performance of the final device.

In particular, annular dark field (ADF) STEM proved to be suited for a quantitative analysis of material properties that includes locating, counting and distinguishing atoms in a material matrix. To achieve these goals, two main ideas were established. One is based on imaging models with statistical parameter estimation theory and the other one relies on the comparison of experimental and simulated images.

With the former one, relative composition determination [1] and atom counting with single atom sensitivity [2] were accomplished. By combining the statistical framework with image simulations, atom counting could be further improved [3] and atomic-scale composition determination was brought to an absolute scale [4]. Additionally, for composition determination on an atomic scale, an atomic lensing model was developed [5,6].

The direct comparison of experimental and simulated image intensities will be discussed in more detail since this is the ansatz followed in this work.

For this direct comparison of experimental and simulated image intensities, a normalisation of the intensities to the impinging electron beam is crucial [7]. To be able to analyse each atomic column separately, pixel intensities are assigned to the atomic columns which could either be done by circular integration [8], Voronoi intensities [9] or pixel integrated cross sections [10].

For highest accuracy in the comparison of experimental and simulated intensities, electron probe, specimen, probe-specimen interaction and detector have to be known and modelled precisely. In case of the electron probe, this especially includes the effect of chromatic aberration [11] and of a finite source size [12–14] and coherent lens aberrations [15]. Static atomic displacements [16], strain [17], tilt [18], surface relaxation [19,20] and amorphous layers [21–23] are characteristics of the specimen that influence ADF-STEM image intensities. Alongside a general knowledge of the probe-specimen interaction [24,25], especially the influence of thermal diffuse scattering [26,27] is of importance.

For the electron detector, next to the general geometry [28], the detector angles [7] and the non-uniform detector sensitivity [7,29,30] influence experimental results.

Taking into account all these parameters, atom counting [31] and composition determination can be conducted. Composition determination was performed on non-atomic [30] and atomic scale [9,32,33] for III-V semiconductors.

To be able to determine absolute atomic scale composition, the specimen thickness has to be known locally. Already small thickness deviations can make accurate, i.e. single-atom accuracy, composition

* Corresponding author.
E-mail addresses: pirmin.kuekelhan@physik.uni-marburg.de (P. Kükelhan), andreas.beyer@physik.uni-marburg.de (A. Beyer).

https://doi.org/10.1016/j.ultramic.2019.03.005
Received 17 January 2019; Received in revised form 8 March 2019; Accepted 14 March 2019
Available online 15 March 2019

determination impossible depending on the material system [33]. Determination of local thickness is normally achieved by an inter- or extrapolation of thickness in regions with known composition [9,30] but this will obviously lead to local thickness deviations. Another possibility is the usage of atomic columns with known composition being justified by a small influence of cross-scattering due to small specimen thicknesses but failing for thicker specimens [4,33]. Furthermore, a method was developed where the composition and thickness characteristic electron scattering was detected in two ADF-STEM images taken at different angular ranges [32]. Complementary methods for thickness determination like electron energy loss spectroscopy [34] or convergent beam electron diffraction [35] do not offer the necessary accuracy or have other limitations.

In this work, we propose a method to simultaneously determine the local thickness and composition for ternary III-V semiconductors from a single ADF-STEM image using complementary image simulations. For the composition determination, the sub lattice where the matrix atom is replaced by the substitute atom is utilized while for thickness determination the other sub lattice with known composition is employed. The latter is prevented by the influence of cross-scattering at a certain thickness. However, this influence and the knowledge about it drawn from simulation are used to determine thickness and composition locally on an atomic scale. This process is performed iteratively analysing both sub lattices separately.

For this, the outline is as follows: After general information about STEM image simulations and experimental setups, the method itself is explained in detail. Then, a proof of principle is given by applying the method to a simulated STEM image of Ga(AsBi) which is a promising material for optoelectronic applications and for which the composition is fully known. Additionally, it is also applied to a simulated STEM image of (GaIn)As. In a simulation study, the influence of detector angles and specimen thickness are investigated leading to preferred conditions that are considered for applying the method to experimental STEM images of a Ga(AsBi)-QW grown by metal organic vapour phase epitaxy (MOVPE). Finally, the obtained results are discussed.

2. STEM image simulations

STEM image simulations are performed for quantitative evaluation of STEM image intensities. For this, the software package STEMsalabim [36] is employed. STEMsalabim is based on the multi slice algorithm [37] and optimized to run on parallelized computing clusters. Thermal diffuse scattering is included by the frozen phonon approximation [27] and a defocus series [11] of seven different defoci centred around $\Delta f = 0$ nm with a full with half maximum of 7.5 nm considers the effect of chromatic aberration. A detector scan allows to consider the non-uniform detector sensitivity [7,9,29,30]. The finite source size is built in by a Lorentzian convolution [14] for which the width is carefully adjusted. All parameters for image simulations are chosen in accordance with the microscope at hand and are summarized in Table 1.

Super cells are generated for Ga(AsBi) with a varying average Bi concentration of $x = 0, 0.02, 0.04, \ldots, 0.14$ and a size of $5 \times 5 \times 80$ unit cells ($x \times y \times z$). Thereby, Bi atoms are statistically distributed inside the super cell. Slicing of the super cell was done in a way that one slice contains one atom per atomic column. A valence force field relaxation of Keating's potential [38] takes into account the effect of static atomic displacements. For Ga(AsBi), 700 group V and 567 group III atomic columns are evaluated. Equivalent image simulations are also performed for (GaIn)As with an average In composition varying from $x = 0, 0.05, 0.10, \ldots, 0.50$. Here, 539 group III and 704 group V atomic columns are evaluated.

Table 1
Parameters for STEM image simulations as determined for the microscope at hand.

Electron energy	200 kV
Aperture angle	21.3 mrad
Astigmatism	0 nm
C_S	2 µm
C_5	5 mm
C_C	1.5 mm

3. Experimental

The Ga(AsBi)/GaAs multi quantum well (MQW) structure was grown in an Aixtron AIX 200 reactor with gas foil rotation. The reactor pressure was kept constant at 50 mbar and H_2 was used as carrier gas. For growth at low temperatures Triethylgallium ($Ga(C_2H_5)_3$), Tertiarybutylarsine ($As(C_4H_9)H_2$) and Trimethylbismuth ($Bi(CH_3)_3$) were chosen as *Gallium, Arsenic* and *Bismuth* source, respectively. First, a GaAs buffer layer was deposited at 625°C on top of the exact n^+-GaAs substrate to ensure a smooth growth surface. The Ga(AsBi) quantum well (QW) was grown at a reduced growth temperature of 400°C whilst the barrier was grown at 550°C to prevent segregation of Bi into the GaAs barrier [39]. Growth interruptions between the layers were established to change the growth temperature of the layer, respectively.

Multi QW thickness and strain were determined by simulation of a high-resolution X-Ray (HR-XRD) diffractogram around the (004)-reflection. Using a GaBi lattice constant of 6.33 Å [40], the Bi fraction was calculated to 5.8% from the strain. The QW thicknesses were determined to 7.2 nm separated by 34.9 nm thick GaAs barriers.

For TEM investigations, a cross-sectional lamella was prepared of this sample using a dual beam scanning electron microscope focused ion beam (FIB) machine (JEOL JIB-4601F, JEOL Ltd., Tokyo, Japan). Applied milling voltages for the Ga ions were progressively reduced from 30 kV to 10 kV. The specimen thickness after this initial FIB preparation was roughly 140 nm.

Further sample thinning was performed using a NanoMill TEM specimen preparation system (model 1040, E. A. Fischione Instruments, Inc., Export, PA, United States) [41] using a milling voltage of 900 eV for the Ar ions utilized. Milling was continued with an inclination angle of ± 10° until the final specimen thicknesses were reached.

STEM measurements were realized with an aberration-corrected JEOL JEM 2200FS (JEOL Ltd., Tokyo, Japan) operating at 200 kV acceleration voltage. Electrons scattered into an angular range of 67–268 mrad were detected by the annular dark-field detector (JEOL EM-24590YPDFI). The inner detector angle was determined according to [7] while the outer detector angle is determined by the geometry of the detector. A convergence angle of 21 mrad was used resulting from a condenser aperture with a diameter of 40 µm. The hexapole lenses of the imaging corrector were turned off to avoid a cut-off in the diffraction plane [42]. Images were recorded as a stack of 10 images with a dwell time of 3 µs and aligned afterwards using the SmartAlign software [43] to reduce the influence of sample drift and scan distortions. For comparison with simulated STEM images, image intensities were normalized to the impinging electron beam [44]. Peak position finding in the STEM images was achieved by applying the peak finding software PeakPairs [45].

4. Method

In the following, we describe the method developed to determine thickness and composition simultaneously for ternary III-V semiconductors using an STEM image.

The first crucial step is to fix the width of the Lorentzian convolution needed to take into account the finite source size for all following simulations. For a given experimental image, this is achieved by a pixel wise comparison of a simulated and an experimental average unit cell at the same thickness. In detail, this procedure can be found in [33].

Voronoi intensities [9] are assigned to every atomic column of the experimental image and will also be used for simulations. They are

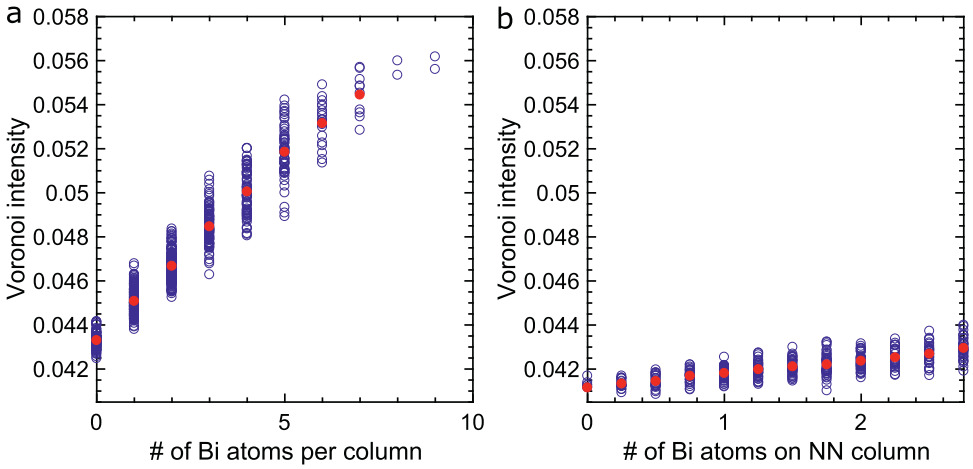

Fig. 1. Relationship between group V Voronoi intensity and Bi composition (a) and group III Voronoi intensity and average NN Bi composition (b) for GaAsBi at a total thickness of 30 atoms per atomic column. For both cases, all events within the simulated super cell (blue) are shown together with the mean intensity (red). (For interpretation of the references to color in this figure legend, the reader is referred to the web version of this article.)

chosen as they are robust against surface relaxation that can strongly influence STEM intensities in semiconductor heterostructures [19,20].

Then, the thickness of every atomic column is determined initially. This is achieved by the comparison of the Voronoi intensities of every atomic column of the sub lattice with known composition with simulated Voronoi intensities of the same sub lattice in the matrix material. Hence, in the case of Ga(AsBi) group III atomic columns containing only Ga atoms are compared to simulated group III atomic columns in a GaAs super cell. By this comparison, the thickness of every atomic column can be fixed given in number of atoms in this column. The thickness of group V atomic columns with unknown composition is found by averaging the thickness of the 4 next neighbor (NN) group III atomic columns that are present in [010]-direction that is used.

After this initial thickness determination, a first initial composition determination can be performed. The obtained intensity composition relationship is shown in Fig. 1(a). For this, for all thicknesses present in the experimental image the simulated super cells with varying Bi concentration have to be evaluated. For every group V atomic column, the number of Bi atoms contained in this column and the Voronoi intensity is read. Because of different z-heights of Bi atoms within each atomic column, this leads to an intensity distribution for every Bi composition. However, a mean Voronoi intensity can be determined for every Bi composition that will be used to determine the Bi composition of every experimental atomic column by comparison of Voronoi intensities. This is also described in more detail in [33].

With this initially determined composition, the thickness can be determined again. For this, the simulated super cells with varying Bi concentration are evaluated in a different way. Using a range of thicknesses, for every group III atomic column the Voronoi intensity together with the columns thickness and the average NN Bi composition is read. Again this gives a distribution of Voronoi intensities for every NN composition for which a mean value is found. This dependency between intensity and average NN Bi composition for group III atomic columns is shown in Fig. 1(b). The thickness of every group III column in the experimental image can then be determined by comparison to simulated Voronoi intensities considering the average NN Bi composition that was determined in the step before. Then, the thickness of group V atomic columns is again determined by averaging the thickness of NN group III atomic columns. With these adapted thicknesses, the Bi composition of group V atomic column is again determined by comparison to simulation as described before.

These last two steps are performed iteratively until a stable thickness composition configuration is found. For the simulated cases investigated, this was always the case after five iterations.

5. Proof of principle using simulated STEM image

To prove the feasibility of the method described above, it will first be applied to a simulated STEM image for which the super cell and its composition generating this image are fully known. Hence, one can compare thickness and composition obtained to the real values for every atomic column.

For this, a super cell with a composition of $GaAs_{0.94}Bi_{0.06}$ is chosen with a thickness of 30 atoms in every atomic column. To generate the STEM image, a virtual detector range of 70–280 mrad is chosen and the experimentally obtained non-uniform detector sensitivity is applied to closely resemble the experiment. A Lorentzian convolution with a width of $\sigma = 0.05$ nm is applied in accordance with experimental conditions. The resulting STEM image is shown in Fig. 2(a). First, the initial thickness determination is performed as described above and the resulting thickness map is shown in Fig. 2(b) for the group V columns only. Note, that atomic columns at the edges are removed due to incomplete, open Voronoi cells and unfulfilled NN relationships. As can be seen, the thickness is generally overestimated by 1–2 atoms since the intensity of group III atomic columns is increased compared to GaAs due to the influence of cross scattering from group V atomic columns. The thickness is determined correctly only for 40% of the 81 group V atomic columns highlighting the necessity of taking cross scattering into account at this thickness.

The initial composition map resulting from this initial thickness determination is shown in Fig. 2(c). Due to the generally overestimated thickness of atomic columns, the Bi composition is generally underestimated. Though, the Bi composition is still determined correctly for 56% of the group V atomic columns. This leads to a total deviation of −35 Bi atoms compared to the real composition in the simulated super cell that contains 140 Bi atoms. The column wise deviation to the real composition is shown in Fig. 2(d).

After three cycles of iteratively determining the thickness of every atomic column considering the Bi composition derived before and the composition of every atomic column considering the current thickness, the configuration of thickness and Bi composition is stable. The resulting thickness, composition and composition deviation maps are shown in Fig. 3(a)–(c), respectively. The thickness is determined correctly for all but one column (99%) while the Bi composition is correct for 78% of the columns. The summed total deviation of Bi atoms is +2 for the 140 Bi atoms contained in the super cell so the total composition is well reflected.

As a comparison, the composition is also determined for that case if the thickness of all atomic columns is known correctly. In this case, the composition is determined for 79% of the group V atomic columns and the total deviation is −1 Bi atom. Hence, the method introduced above essentially reaches the inherently present limitations of this

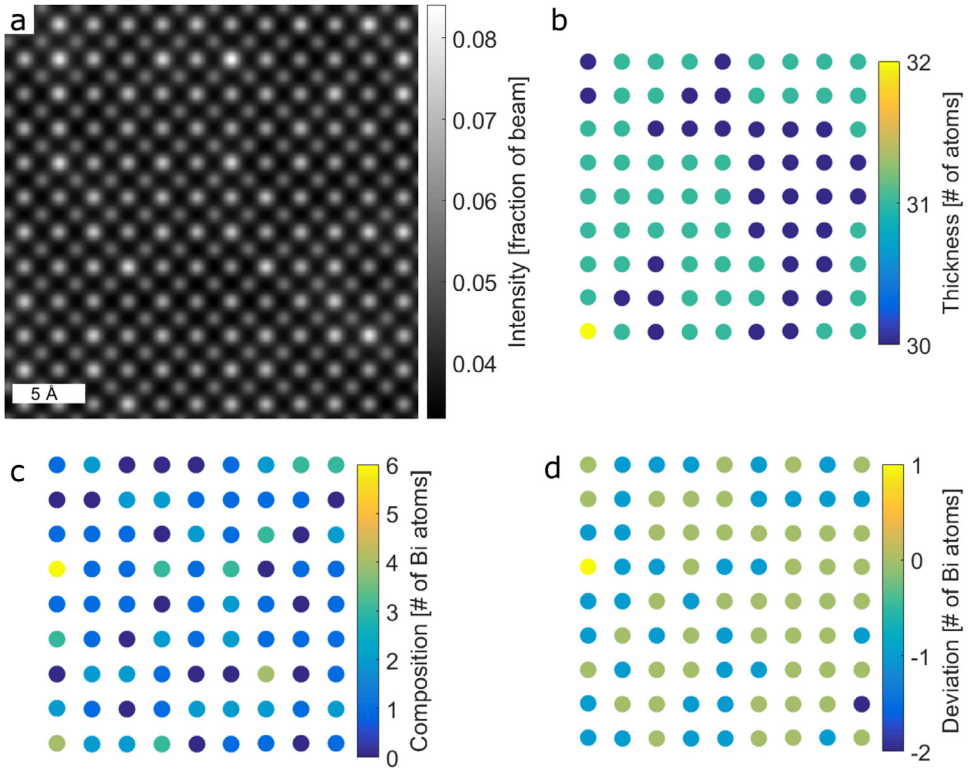

Fig. 2. (a) Simulated STEM image of GaAsBi containing 6% Bi at a thickness of 30 atoms per atomic column. (b) Thickness of group V atomic column determined initially via the group III sub lattice and comparison of Voronoi intensities to simulations. (c) Bi composition determined at the thicknesses shown in (b) by comparing to intensity composition relationships. (d) Deviation of determined composition shown in (c) to the real composition of the super cell. When comparing STEM image in (a) and column representations in (b)–(d) note that only group V atomic columns are shown and edge regions of the image are excluded. (For interpretation of the references to color in this figure legend, the reader is referred to the web version of this article.)

composition determination via comparison to mean Voronoi intensities of atomic columns. These limitations exist due to different z-height distributions of the substitute (Bi) atoms inside the atomic columns and following different intensities. However, these limitations are of statistical nature and are discussed in detail later on.

To show that the proposed method is not only working in the special case of Ga(AsBi), it is also applied to a simulated STEM image of $(Ga_{0.7}In_{0.3})As$ at a thickness of 35 atoms per atomic column and detector angles of 70–280 mrad (Fig. 4). With the proposed method, the thickness is determined correctly for 92% of 49 group III atomic columns which leads to a composition determination that is correct in 33% of the group III atomic columns. The overall deviation of the composition is 4 In atoms for 495 In atoms contained in the super cell. If the thickness is known correctly for every atomic column the composition is determined correctly for 33% of the group III atomic columns and a deviation of 4 In atoms results which is dictated by the statistical nature of composition determination. Hence, the same accuracy is reached with the method proposed.

For now, it is concluded that the method introduced allows us to determine thickness and composition of the atomic columns shown in the simulated STEM images with good accuracy.

6. Influence of detector range and specimen thickness

To get a more comprehensive understanding of the method described, the influence of the detector range employed and of specimen thickness is investigated in a simulation study. For this purpose, the proof of principle described for the simulated STEM image above in detail is performed for the $GaAs_{0.94}Bi_{0.06}$ super cell but with varying thickness and images recorded with different virtual detector ranges.

Specimen thicknesses range from 10 to 35 atoms per atomic column in steps of 5 atoms per atomic column while for every thickness inner detector angles from 30 mrad to 100 mrad in steps of 10 mrad were evaluated. The outer detector angle was chosen as four times the inner detector angle which corresponds to the geometry of the detector used in this work. A maximum simulation angle of 300 mrad was chosen since intensity scattered to higher angles hardly affects the intensity finally collected by the detector because of the θ^{-4} dependency of the scattered intensity.

For each thickness-detector configuration, we evaluated the total deviation of Bi atoms between determined and real composition and the percentage of correctly determined columns for both composition and thickness.

In a first step, for a given thickness of 30 atoms per atomic column

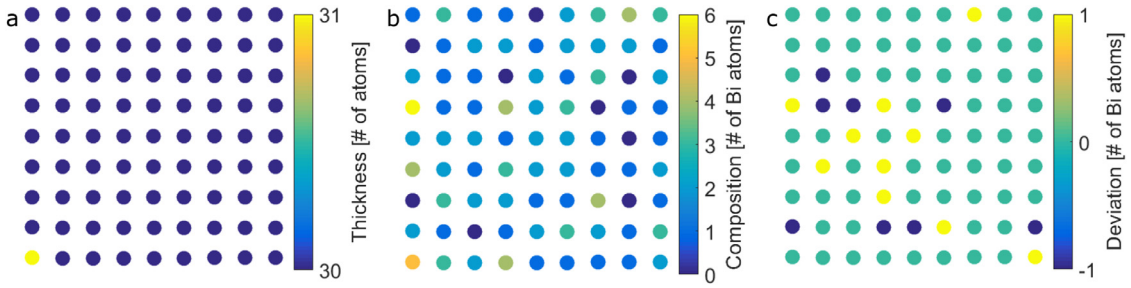

Fig. 3. Thickness (a), Bi composition (b) and deviation to the real composition (c) for the same simulated STEM image shown in 2(a) after applying the proposed method for thickness and composition determination with 3 cycles. (For interpretation of the references to color in this figure legend, the reader is referred to the web version of this article.)

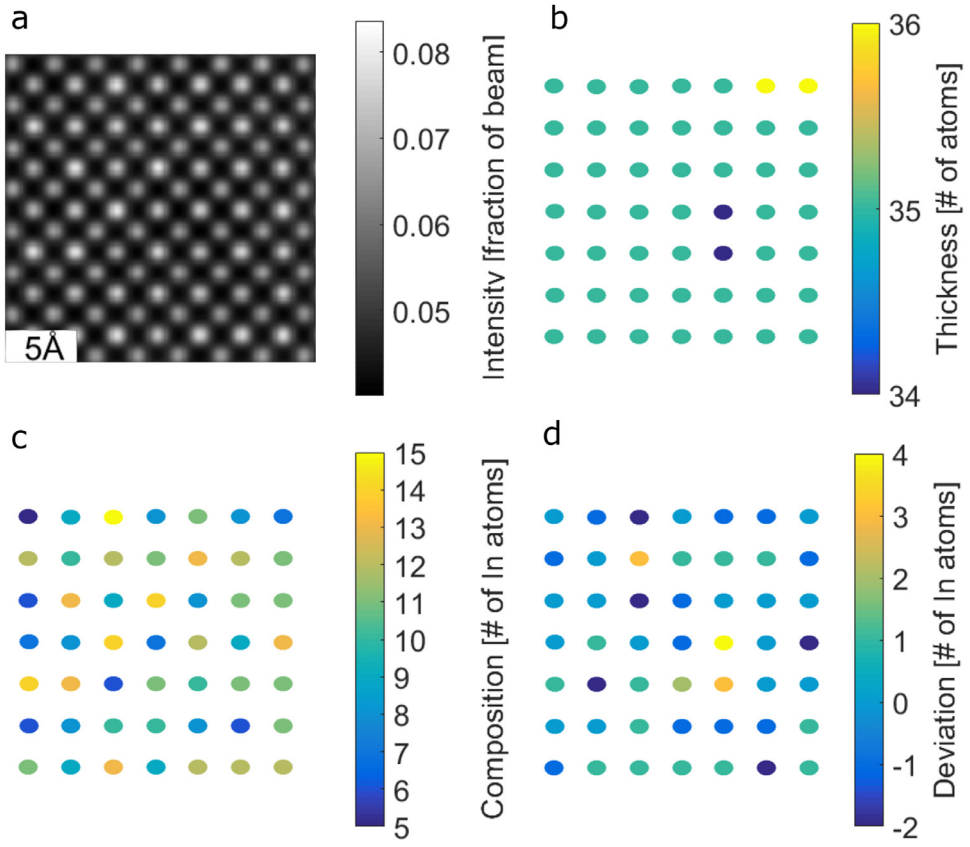

Fig. 4. STEM image of $(Ga_{0.7}In_{0.3})As$ for a thickness of 35 atoms per atomic column (a), together with the thickness (b), the composition (c) and the deviation to the real composition (d) determined by applying the proposed method. When comparing STEM image in (a) and column representations in (b)–(d) note that only group III atomic columns are shown and edge regions of the image are excluded. (For interpretation of the references to color in this figure legend, the reader is referred to the web version of this article.)

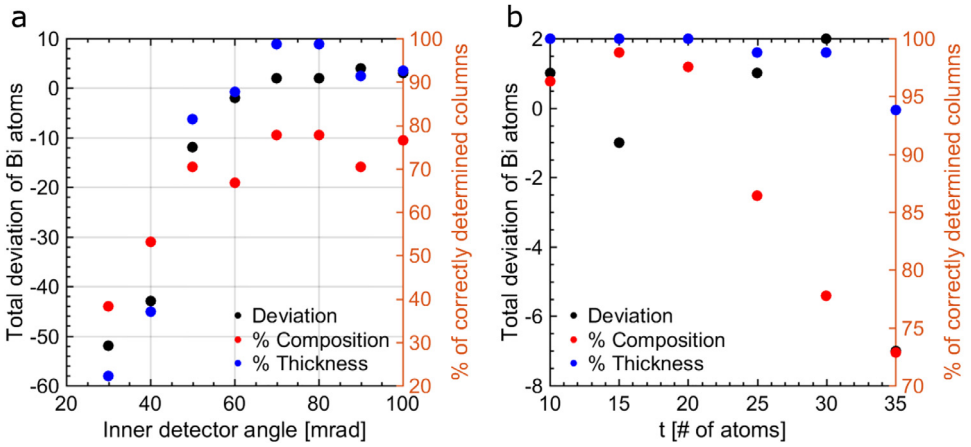

Fig. 5. Detector angle dependency of the proposed method for a super cell of Ga(AsBi) with 6% Bi and a thickness of 30 atoms (a). Thickness dependency of the proposed method for the same super cell (b). In a simualtion study, the deviation of the total Bi composition determined to the real composition of the super cell (black) and the fraction of group V atomic columns for which the composition (red) and the thickness (blue) were determined correctly were analysed. (For interpretation of the references to color in this figure legend, the reader is referred to the web version of this article.)

the influence of the detector range is evaluated. The results are shown in Fig. 5(a) for the total deviation of Bi atoms and the percentages of correctly determined atomic columns. With increasing inner detector angle from 30 mrad to 70 mrad, the total deviation to the real composition tends to zero while the number of correctly determined columns increases for both thickness and composition. For inner detector angles of 70 mrad and 80 mrad, thicknesses are determined correctly for almost every atomic column while this leads to the composition being determined correctly in almost 80% of the cases. The total deviation of the composition is 2 Bi atoms for both detector ranges. Increasing the inner detector angle leads to a decline in correctly determined atomic columns and an increase in the deviation. Hence, experimentally one should aim to work with an inner detector angle of 70–80 mrad for the given thickness of 30 atoms per atomic column.

Secondly, it is investigated whether the proposed method is working for every thickness range. Thicknesses are investigated up to 35 atoms per atomic column. Up to this thickness, for the given super cell size edge effects can be excluded. In Fig. 5(b), the absolute total deviation between the real and the determined Bi composition together with the percentage of correctly determined atomic columns for both thickness and composition is shown. For very thin samples up to 20 atoms per atomic column composition and thickness can be determined correctly for (almost) every atomic column, whereas this percentage decreases with increasing thickness afterwards. However, up to a thickness of 30 atoms per atomic column the total composition can be deduced accurately with a deviation of only 2 Bi atoms, at most. For a thickness of 35 atoms per atomic column, the deviation to the real composition increases to 7 Bi atoms and the percentage of correctly determined columns drops to 73% while the thickness is determined for 94% of the atomic columns. However, with 2835 group V atoms and 163 Bi atoms in the super cell the absolute concentration deviation is only 0.2%.

Hence, for all investigated thicknesses the proposed method works

accurately for the total composition but the local accuracy decreases. The thickness of every atomic column can be determined with 99% accuracy up to a thickness of 30 atoms per atomic column. For taking experimental STEM images, working in specimen regions with a thickness of 35 atoms per atomic column (~20 nm) is possible depending on the goal of the investigation. If one is interested in high local accuracy for the composition determination in contrast to more global information, thinner specimens have to be investigated. This has to be considered for sample preparation but is definitely achievable experimentally.

7. Application to experimental STEM image

The proposed method was also applied to an experimental STEM image of a Ga(AsBi)-QW with GaAs barriers grown on a GaAs substrate for which the composition is known from HR-XRD measurements. For acquiring the STEM image, the detector range was chosen as 67–268 mrad which is in agreement with the optimal detector range determined by the simulation study above. Additionally, we aimed for a specimen thickness below the upper limit of 20 nm which was also ascertained above.

The STEM image of the Ga(AsBi)-QW is shown in Fig. 6(a) already being normalized to the impinging electron beam. Here, the Ga(AsBi)-QW is on the left side of the image while on the right side GaAs is present. The small field of view due to high magnification is sufficient since no binary reference material is needed on both sides of the QW. The method proposed was applied with 15 thickness-composition refinement cycles to this image. The resulting thickness map is shown in Fig. 6(b). As can be seen, the thickness of the atomic columns ranges from 26 to 31 atoms per column and therefore is below the thickness limit of 35 atoms per atomic column discussed before. Using this thickness map for composition determination, the composition map presented in Fig. 6(c) was retrieved. For the composition determination, the intensity composition relationships were extrapolated to negative compositions of Bi both for on- and off-column relationships to take into account the possibility of experimental noise. Resulting compositions range from −1 to 6 Bi atoms per atomic column clearly showing that the QW just begins on the left side of the image and that there is GaAs on the right side of the image. Within the QW, also clustering of Bi atoms is apparent which was reported for this material system before [8].

By averaging over the lattice planes in the vertical direction, i.e. parallel to the interface, a composition profile of the Ga(AsBi)-QW is generated. To take into account the differing thickness of atomic columns and enable a comparison, Bi composition is given as concentration. The resulting concentration profile is shown in Fig. 6(d) (red profile). Here, it has to be noted that the shaded region does not show the error of the composition determination but rather the standard deviation of the concentration along one lattice plane that contains 34 atomic columns in the present case. Additionally, the concentration profile that would result from an initial thickness and composition determination without applying the refinement steps is given (blue profile). Finally, also the concentration profile obtained by HR-XRD is shown in Fig. 6(d) (black profile). A comparison between the final concentration profile obtained and the box-like concentration profile obtained by HR-XRD with a QW width of 7.2 nm and a Bi concentration of 5.8% yields a very good agreement and therefore confirms the validity of the method also experimentally. In contrast, the concentration

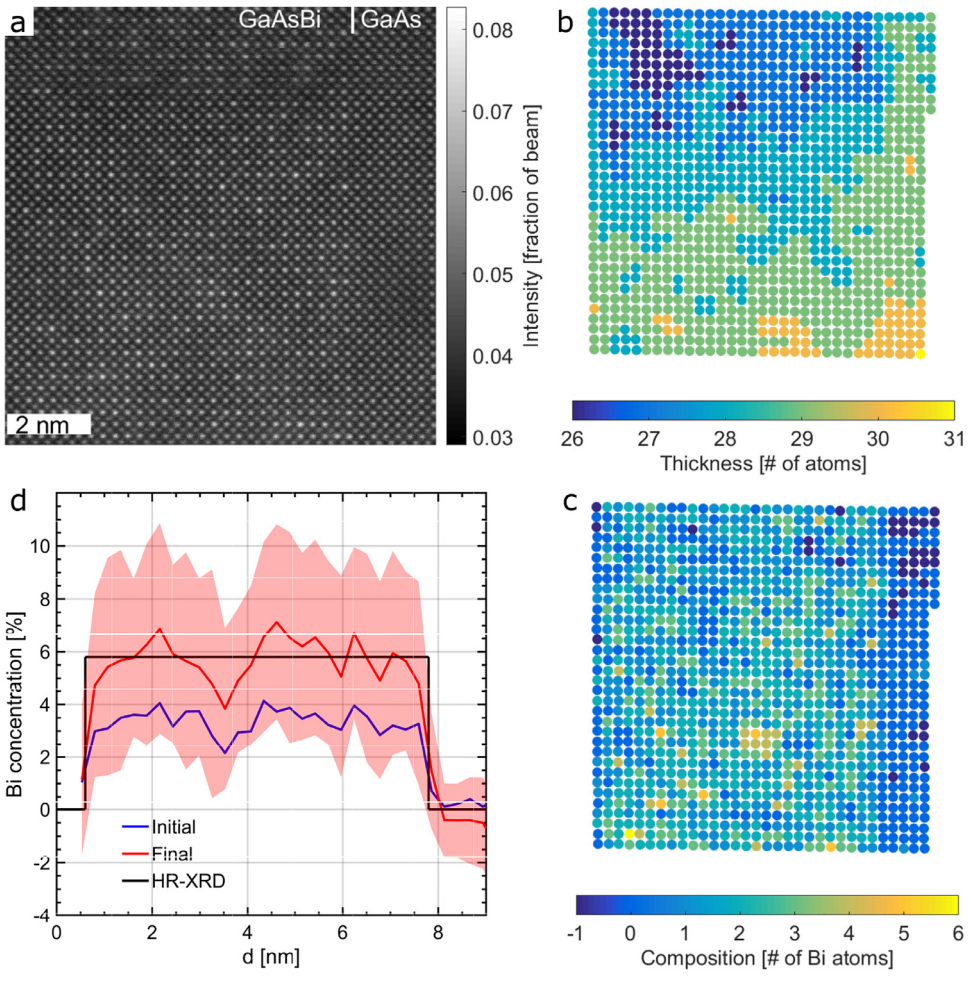

Fig. 6. Application of the proposed method to an STEM image of a GaAsBi-QW grown by MOVPE. The STEM image (a) shows the GaAsBi-QW on the left and GaAs barrier on the right. Thickness map (b) after 15 iterative cycles. Composition map (c) for thicknesses shown in (b). The QW is clearly distinguishable. Concentration profile (d) of the initial (blue) and final (red) composition determination together with its standard deviation within one lattice plane (shaded red). For comparison reasons, also the concentration profile as determined by HR-XRD (black) is shown. (For interpretation of the references to color in this figure legend, the reader is referred to the web version of this article.)

profile resulting from the initial composition determination distinctly differs from the HR-XRD profile and the final concentration profile and underestimates the Bi concentration due to overestimating the thickness of the atomic columns.

8. Discussion

In the following, the proposed method and its application is discussed regarding several aspects. This starts with the method in general and its statistical character as well as its accuracy. Then the best imaging conditions for a successful composition determination and the experimental results are explained.

The proposed method was developed out of the need for an accurate knowledge of the thickness of every atomic column in order to determine its thickness. As was shown in [33], already a difference between the assumed thickness and the real thickness of one atom per atomic column leads to an incorrect composition determination in most cases. Hence, a correct knowledge about the thickness is crucial to determine the composition with atomic accuracy and avoid making assumptions of the thickness in the region with unknown composition [9,30,33]. Furthermore, the method proposed works with only one STEM image detected for one detector range in comparison to the angular resolved STEM ansatz [32] that detects composition and thickness characteristic scattering at different angular ranges.

Cross-scattering limits the use of the sub lattice with constant composition in ternary III-V semiconductors for thickness determination to very small thicknesses (10–15 atoms per atomic column in the case of Ga(AsBi)) as for these the influence of cross scattering is marginal. For the proposed method, it is this existence of cross-scattering that is exploited by reading this information from image simulations. These image simulations are at the heart of simulation-based quantitative STEM analysis and therefore an exact modeling of probe, specimen and detector is necessary. By using the iterative composition and thickness determination described above, an ensemble of a cohesive thickness and composition configuration can be found.

Thereby, the composition determination has a strong statistical character as discussed in detail in [33]. For a given thickness, for every quantity of substitute atoms in an atomic column an intensity distribution arises due to different possible z-configurations of these substitute atoms, i.e. z-heights with respect to the impinging beam. These intensity distributions have a certain overlap depending on material system, specimen thickness and number of substitute atoms. However, for the evaluation these intensity distributions are only represented by mean values that inherently lead to errors in composition determination for extremal z distributions. For example, atoms placed on top of the column will have a higher intensity than the mean intensity for this composition and vice versa. Nonetheless, on average this composition determination still yields the correct value given a large enough value of atomic columns to evaluate. For the simulation study presented above, only 81 atomic columns out of one super cell were evaluated but for experimental images there are typically several thousand atomic columns within one image (1098 group V atomic columns in the experimental STEM image used). Hence, the statistically determined mean value for the composition is still correct.

The percentage of atomic columns for which the composition is determined correctly, i.e. the exact number of substitute atoms in that column, decreases with increasing thickness since with increasing thickness there are more possibilities to arrange a given number of substitute atoms within one column and overlap between the resulting intensity distributions increases. This decreasing percentage of atomic columns for which the composition can be determined correctly also leads to a decreasing percentage of atomic columns for which the thickness can be determined correctly. The thickness determination depends on the average NN composition that is not correct anymore. Hence, the thickness is not correct anymore which then leads to a wrong composition of that atomic column as the thickness is crucial. This explains why the performance of the method proposed decreases with increasing thickness as found in the simulation study.

Therefore, the statistical character of the experimental method prevents a correct composition determination of every single atomic column whereas the overall composition is determined correctly given a large enough number of atomic columns. These effects are then exaggerated for the simultaneous thickness and composition determination as these two characteristics are strongly mutually dependent.

The fact that the composition of an atomic column is not determined correctly for 100% of the atomic columns also leads to the necessity to assess the accuracy of the present method. As previously explained, this accuracy depends on the overlap of the intensity distributions that for a given material system increases both with increasing thickness and composition. Hence, these three factors have to be considered when determining the accuracy of the proposed method. One way to assess this accuracy is an evaluation of the results of the simulation study. For the super cell with a Bi concentration of 6% (140 Bi atoms of 2430 total group V atoms) and a thickness of 30 atoms per atomic column that closely resembles the experimentally investigated QW, the detailed evaluation performed above yielded deviations of $\pm$ 1 Bi atom for 22% of the atomic columns while for 78% of the atomic columns the composition was determined correctly. Since the Bi atoms were statistically distributed within the super cell, this value of 78% correctly determined atomic columns and an error $\pm$ 1 Bi atom for the remaining atomic columns can be assumed to reflect the accuracy of the given combination of material system, thickness, and composition.

The influence of the material system on the accuracy of composition determination manifests itself through the difference in atomic number between the matrix atom and the substitute atom replacing it. Therefore, Ga(PBi) would give a more accurate composition determination than Ga(AsBi), whilst Ga(AsSb) would be less accurate. For thickness determination, it would be the other way around. For Ga(PBi) the thickness determination is expected to perform worse than for Ga(AsBi), while Ga(AsSb) is expected to yield more accurate results.

The concentration itself is also influencing the accuracy of composition determination and therefore also the accuracy of the proposed method. If the amount of both the substitute and the matrix atom is equal, i.e. a concentration of 50%, the number of possible arrangements of these atoms within an atomic column is highest. Therefore, the statistically determined composition determination performs worst for this concentration and this also converts to the proposed method.

However, these material system and concentration considerations are only of a theoretical nature since most of the time the material system to investigate is technologically dictated. Hence, the only remaining “free parameter” is the specimen thickness that is measured at. Then, the optimum thickness becomes a matter of specimen preparation and in particular the amorphous layers emerging during it.

The best detector range for simultaneous thickness and composition determination is determined by the potential to detect both the matrix and the substitute atom. Generally, atoms with higher atomic number scatter electrons to higher angular ranges while atoms with lower atomic number like N mostly scatter to a lower angular range [32]. Since the total atomic number of one atomic column increases with thickness the best detector range for composition determination also depends on thickness. This was also found for atom counting [46]. A detailed analysis of the best imaging conditions for composition determination will be done in future work. For now, it is stated that the choice of the detection range is highly influential and offers great potential for future optimization and application.

The experimental results that were obtained considering the optimized angular range and thickness for STEM measurements are in very good agreement with the HR-XRD results. For these HR-XRD results, it has to be considered that HR-XRD yields only box-like concentration profiles that do not reflect the real concentration profile due to non-abrupt interfaces and non-constant concentration within the QW. Taking this into account, the composition profiles obtained by STEM

investigations give a more detailed description even in 2D and furthermore, closely resemble the concentration profile assumed for HR-XRD.

The 2D composition map also reveals clustering effects for Bi atoms in Ga(AsBi) that have also been found before [8] and can be confirmed for this sample by considering the absolute atomic numbers for the composition.

Negative composition values for an atomic column are allowed with the purpose of taking into account the experimental noise present in the STEM image that will lead to intensity values that would belong to these negative compositions. Not allowing these negative compositions would bias the average concentration of one lattice plane to higher concentrations which is especially important for binary material where the average concentration of the substitute atom should be zero.

Locally, the experimental noise causes composition values of -1 Bi atoms and therefore gives a good estimation of the loss of accuracy that must be considered in addition to the inherent accuracy of the method of $\pm$ 1 Bi atoms for the given material system, composition and thickness.

The magnitude of experimental noise for a lattice plane can be detected within the binary material. Here, the standard deviation of the concentration within one lattice plane can be solely attributed to experimental noise since there are no composition fluctuations in binary material. In contrast, the higher standard deviations of concentration within one lattice plane within the Ga(AsBi)-QW is a combination of experimental noise and real composition fluctuations that are further increased by the clustering effects detected.

Non-zero average concentrations of the substitute atom within the binary matrix have been attributed to the presence of amorphous layers before [33]. There, the concentration of the substitute atoms for specimens prepared by conventional sample preparation and final treatment with a precision ion polishing system with an ion energy of 1.2 kV was substantially higher than 1%. Here, improved specimen preparation by using the NanoMill TEM specimen preparation system with ion energies of 900 V could decrease the non-zero concentration as the Bi concentration detected in the GaAs barrier is -0.4%. This supports the argument that indeed the amorphous layers due to specimen preparation are responsible for non-zero concentrations of the substitute atom in the binary region. Hence, it is expected that further improvement of specimen preparation, i.e. the use of even lower ion energy and the reduction of the amorphous layers will bring the concentration of the substitute atom even closer to zero.

9. Summary

We showed a method to determine the thickness and composition of ternary III-V semiconductors on an atomic scale while aiming for single-atom accuracy. The statistical character of the experimental method allows this single-atom accuracy only for a certain fraction of atomic columns but looking at a high number of atomic columns an accurate overall composition determination is possible. In a simulation study, a proof of principle was given and the best detector range for image acquisition as well as limiting specimen thickness was investigated. When applying the method to an experimental STEM image excellent agreement with HR-XRD composition measurements was found.

Acknowledgments

Financial support by the German Research Foundation (DFG) in the framework of SFB 1083 “Structure and Dynamics of Internal Interfaces” is greatly appreciated. S. Firoozabadi acknowledges support of the European Union’s Horizon 2020 in the framework of the project microSPIRE (ID: 766955). T. Hepp acknowledges financial support by the DFG in the framework of the research training group “Functionalization of Semiconductors” (GRK 1782).

References

[1] S. Van Aert, J. Verbeeck, R. Erni, S. Bals, M. Luysberg, D. Van Dyck, G. Van Tendeloo, Quantitative atomic resolution mapping using high-angle annular dark field scanning transmission electron microscopy, Ultramicroscopy 109 (2009) 1236–1244, https://doi.org/10.1016/j.ultramic.2009.05.010.

[2] S. Van Aert, A. De Backer, G.T. Martinez, B. Goris, S. Bals, G. Van Tendeloo, A. Rosenauer, Procedure to count atoms with trustworthy single-atom sensitivity, Phys. Rev. B 87 (2013) 064107, , https://doi.org/10.1103/PhysRevB.87.064107.

[3] A. De wael, A. De Backer, L. Jones, P.D. Nellist, S. Van Aert, Hybrid statistics-simulations based method for atom-counting from ADF STEM images, Ultramicroscopy 177 (2017) 69–77, https://doi.org/10.1016/j.ultramic.2017.01.010.

[4] G.T. Martinez, A. Rosenauer, A. De Backer, J. Verbeeck, S. Van Aert, Quantitative composition determination at the atomic level using model-based high-angle annular dark field scanning transmission electron microscopy, Ultramicroscopy 137 (2014) 12–19, https://doi.org/10.1016/j.ultramic.2013.11.001.

[5] K.H.W. Van Den Bos, A. De Backer, G.T. Martinez, N. Winckelmans, S. Bals, P.D. Nellist, S. Van Aert, Unscrambling mixed elements using high angle annular dark field scanning transmission electron microscopy, Phys. Rev. Lett. 116 (2016) 246101, , https://doi.org/10.1103/PhysRevLett.116.246101.

[6] K.H.W. Van den Bos, L. Janssens, A. De Backer, P.D. Nellist, S. Van Aert, The atomic lensing model: new opportunities for atom-by-atom metrology of heterogeneous nanomaterials, Ultramicroscopy (2018), https://doi.org/10.1016/j.ultramic.2018.12.004.

[7] J.M. LeBeau, S. Stemmer, Experimental quantification of annular dark-field images in scanning transmission electron microscopy, Ultramicroscopy 108 (2008) 1653–1658, https://doi.org/10.1016/j.ultramic.2008.07.001.

[8] A. Beyer, N. Knaub, P. Rosenow, K. Jandieri, P. Ludewig, L. Bannow, S.W. Koch, R. Tonner, K. Volz, Local Bi ordering in MOVPE grown Ga(As,Bi) investigated by high resolution scanning transmission electron microscopy, Appl. Mater. Today 6 (2017) 22–28, https://doi.org/10.1016/j.apmt.2016.11.007.

[9] A. Rosenauer, T. Mehrtens, K. Müller, K. Gries, M. Schowalter, P. Venkata Satyam, S. Bley, C. Tessarek, D. Hommel, K. Sebald, M. Seyfried, J. Gutowski, A. Avramescu, K. Engl, S. Lutgen, Composition mapping in InGaN by scanning transmission electron microscopy, Ultramicroscopy 111 (2011) 1316–1327, https://doi.org/10.1016/j.ultramic.2011.04.009.

[10] H. E, K.E. MacArthur, T.J. Pennycook, E. Okunishi, A.J. D'Alfonso, N.R. Lugg, L.J. Allen, P.D. Nellist, Probe integrated scattering cross sections in the analysis of atomic resolution HAADF STEM images, Ultramicroscopy 133 (2013) 109–119, https://doi.org/10.1016/j.ultramic.2013.07.002.

[11] K. Kuramochi, T. Yamazaki, Y. Kotaka, M. Ohtsuka, I. Hashimoto, K. Watanabe, Effect of chromatic aberration on atomic-resolved spherical aberration corrected STEM images, Ultramicroscopy 110 (2009) 36–42, https://doi.org/10.1016/j.ultramic.2009.09.003.

[12] C. Dwyer, R. Erni, J. Etheridge, Measurement of effective source distribution and its importance for quantitative interpretation of STEM images, Ultramicroscopy 110 (2010) 952–957, https://doi.org/10.1016/j.ultramic.2010.01.007.

[13] C. Maunders, C. Dwyer, P.C. Tiemeijer, J. Etheridge, Practical methods for the measurement of spatial coherence—a comparative study, Ultramicroscopy 111 (2011) 1437–1446, https://doi.org/10.1016/j.ultramic.2011.05.011.

[14] A. Beyer, J. Belz, N. Knaub, K. Jandieri, K. Volz, Influence of spatial and temporal coherences on atomic resolution high angle annular dark field imaging, Ultramicroscopy 169 (2016) 1–10, https://doi.org/10.1016/j.ultramic.2016.06.006.

[15] S. Uhlemann, M. Haider, Residual wave aberrations in the first spherical aberration corrected transmission electron microscope, Ultramicroscopy 72 (1998) 109–119, https://doi.org/10.1016/S0304-3991(97)00102-2.

[16] V. Grillo, E. Carlino, F. Glas, Influence of the static atomic displacement on atomic resolution Z-contrast imaging, Phys. Rev. B 77 (2008) 054103, , https://doi.org/10.1103/PhysRevB.77.054103.

[17] V. Grillo, The effect of surface strain relaxation on HAADF imaging, Ultramicroscopy 109 (2009) 1453–1464, https://doi.org/10.1016/j.ultramic.2009.07.010.

[18] S.E. Maccagnano-Zacher, K.A. Mkhoyan, E.J. Kirkland, J. Silcox, Effects of tilt on high-resolution ADF-STEM imaging, Ultramicroscopy 108 (2008) 718–726, https://doi.org/10.1016/j.ultramic.2007.11.003.

[19] A. Beyer, L. Duschek, J. Belz, K. Jandieri, K. Volz, Influence of surface relaxation of strained layers on atomic resolution ADF imaging, Ultramicroscopy 181 (2017) 8–16, https://doi.org/10.1016/j.ultramic.2017.04.019.

[20] A. Beyer, L. Duschek, J. Belz, J.O. Oelerich, K. Jandieri, K. Volz, Surface relaxation of strained Ga(P,As)/GaP heterostructures investigated by HAADF STEM, J. Microsc 268 (2017) 239–247, https://doi.org/10.1111/jmi.12622.

[21] K.A. Mkhoyan, S.E. Maccagnano-Zacher, E.J. Kirkland, J. Silcox, Effects of amorphous layers on ADF-STEM imaging, Ultramicroscopy 108 (2008) 791–803, https://doi.org/10.1016/j.ultramic.2008.01.007.

[22] T. Grieb, M. Tewes, M. Schowalter, K. Müller-Caspary, F.F. Krause, T. Mehrtens, J.M. Hartmann, A. Rosenauer, Quantitative HAADF STEM of SiGe in presence of amorphous surface layers from FIB preparation, Ultramicroscopy 184 (2018) 29–36, https://doi.org/10.1016/j.ultramic.2017.09.012.

[23] J. Belz, A. Beyer, T. Torunski, W. Stolz, K. Volz, Direct investigation of (sub-) surface preparation artifacts in GaAs based materials by FIB sectioning, Ultramicroscopy 163 (2016) 19–30, https://doi.org/10.1016/j.ultramic.2016.01.001.

[24] L.J. Allen, S.D. Findlay, M.P. Oxley, C.J. Rossouw, Lattice-resolution contrast from a

focused coherent electron probe. Part I, Ultramicroscopy 96 (2003) 47–63, https://doi.org/10.1016/S0304-3991(02)00380-7.
[25] S.D. Findlay, L.J. Allen, M.P. Oxley, C.J. Rossouw, Lattice-resolution contrast from a focused coherent electron probe. Part II, Ultramicroscopy 96 (2003) 65–81, https://doi.org/10.1016/S0304-3991(02)00381-9.
[26] R.F. Loane, P. Xu, J. Silcox, Thermal vibrations in convergent-beam electron diffraction, Acta Crystallogr. Sect. A 47 (1991) 267–278, https://doi.org/10.1107/S0108767391000375.
[27] B.D. Forbes, A.J.D. Alfonso, S.D. Findlay, D. Van Dyck, J.M. Lebeau, S. Stemmer, L.J. Allen, Thermal diffuse scattering in transmission electron microscopy, Ultramicroscopy 111 (2011) 1670–1680, https://doi.org/10.1016/j.ultramic.2011.09.017.
[28] S. Hillyard, J. Silcox, Detector geometry, thermal diffuse scattering and strain effects in ADF STEM imaging, Ultramicroscopy 58 (1995) 6–17, https://doi.org/10.1016/0304-3991(94)00173-K.
[29] S.D. Findlay, J.M. LeBeau, Detector non-uniformity in scanning transmission electron microscopy, Ultramicroscopy 124 (2013) 52–60, https://doi.org/10.1016/j.ultramic.2012.09.001.
[30] A. Rosenauer, K. Gries, K. Müller, A. Pretorius, M. Schowalter, A. Avramescu, K. Engl, S. Lutgen, Measurement of specimen thickness and composition in AlGaN/GaN using high-angle annular dark field images, Ultramicroscopy 109 (2009) 1171–1182, https://doi.org/10.1016/j.ultramic.2009.05.003.
[31] J.M. LeBeau, S.D. Findlay, L.J. Allen, S. Stemmer, Standardless atom counting in scanning transmission electron microscopy, Nano Lett. 10 (2010) 4405–4408, https://doi.org/10.1021/nl102025s.
[32] K. Müller-Caspary, O. Oppermann, T. Grieb, F.F. Krause, A. Rosenauer, M. Schowalter, T. Mehrtens, A. Beyer, K. Volz, P. Potapov, Materials characterisation by angle-resolved scanning transmission electron microscopy, Sci. Rep. 6 (2016) 37146, https://doi.org/10.1038/srep37146.
[33] L. Duschek, P. Kükelhan, A. Beyer, S. Firoozabadi, J.O. Oelerich, A. Ballabio, G. Isella, K. Volz, Composition determination of semiconductor alloys towards atomic accuracy by HAADF-STEM, Ultramicroscopy 200 (2019) 84–96, https://doi.org/10.1016/j.ultramic.2019.02.009.
[34] S.I. Molina, D.L. Sales, P.L. Galindo, D. Fuster, Y. Gonzalez, B. Alen, L. Gonzalez, M. Varela, S.J. Pennycook, Column-by-column compositional mapping by Z-contrast imaging, Ultramicroscopy 109 (2009) 172–176, https://doi.org/10.1016/j.ultramic.2008.10.008.
[35] J.M. LeBeau, S.D. Findlay, L.J. Allen, S. Stemmer, Position averaged convergent beam electron diffraction: theory and applications, Ultramicroscopy 110 (2010) 118–125, https://doi.org/10.1016/j.ultramic.2009.10.001.
[36] J.O. Oelerich, L. Duschek, J. Belz, A. Beyer, S.D. Baranovskii, K. Volz, STEMsalabim: a high-performance computing cluster friendly code for scanning transmission electron microscopy image simulations of thin specimen, Ultramicroscopy 177 (2017) 91–96, https://doi.org/10.1016/j.ultramic.2017.03.010.
[37] E.J. Kirkland, Advanced Computing in Electron Microscopy, (2010).
[38] P.N. Keating, Effect of invariance requirements on the elastic strain energy of crystals with application to the diamond structure, Phys. Rev. 145 (1966) 637–645, https://doi.org/10.1103/PhysRev.145.637.
[39] P. Ludewig, Z.L. Bushell, L. Nattermann, N. Knaub, W. Stolz, K. Volz, Growth of Ga(AsBi) on GaAs by continuous flow MOVPE, J. Cryst. Growth 396 (2014) 95–99, https://doi.org/10.1016/j.jcrysgro.2014.03.041.
[40] S. Tixier, M. Adamcyk, T. Tiedje, S. Francoeur, A. Mascarenhas, P. Wei, F. Schiettekatte, Molecular beam epitaxy growth of molecular beam epitaxy growth of GaAsBi, Appl. Phys. Lett. 82 (2013) 2245, https://doi.org/10.1063/1.1565499.
[41] R.R. Cerchiara, P.E. Fischione, J. Liu, J.M. Matesa, A.C. Robins, H.L. Fraser, A. Genc, Raising the standard of specimen preparation for aberration-corrected TEM and STEM, Micros. Today 19 (2011) 16–19, https://doi.org/10.1017/S1551929510001197.
[42] F.F. Krause, M. Schowalter, T. Grieb, K. Müller-Caspary, T. Mehrtens, A. Rosenauer, Effects of instrument imperfections on quantitative scanning transmission electron microscopy, Ultramicroscopy 161 (2016) 146–160, https://doi.org/10.1016/j.ultramic.2015.10.026.
[43] L. Jones, H. Yang, T.J. Pennycook, M.S.J. Marshall, S. Van Aert, N.D. Browning, M.R. Castell, P.D. Nellist, S.I. Molina, D.L. Sales, P.L. Galindo, D. Fuster, Y. González, B. Alén, L. González, M. Varela, S.J. Pennycook, R. Erni, H. Heinrich, G. Kostorz, V. Grillo, E. Carlino, F. Glas, F. Rossi, E.J. Kirkland, Z. Yu, P.E. Batson, J. Silcox, E. Carlino, V. Grillo, Smart Align-a new tool for robust non-rigid registration of scanning microscope data, Ultramicroscopy 109 (2009) 8, https://doi.org/10.1186/s40679-015-0008-4.
[44] D.S. He, Z.Y. Li, A practical approach to quantify the ADF detector in STEM, J. Phys. Conf. Ser. 522 (2014) 012017, , https://doi.org/10.1088/1742-6596/522/1/012017.
[45] P.L. Galindo, S. Kret, A.M. Sanchez, J.Y. Laval, A. Yáñez, J. Pizarro, E. Guerrero, T. Ben, S.I. Molina, The Peak Pairs algorithm for strain mapping from HRTEM images, Ultramicroscopy 107 (2007) 1186–1193, https://doi.org/10.1016/j.ultramic.2007.01.019.
[46] A. De Backer, A. De, J. Gonnissen, S. Van Aert, Optimal experimental design for nano-particle atom-counting from high-resolution STEM images, Ultramicroscopy 151 (2015) 46–55, https://doi.org/10.1016/j.ultramic.2014.10.015.

6.5 Composition Determination for Quaternary III-V Semiconductors by Aberration-Corrected STEM

P. Kükelhan, T. Hepp, S. Firoozabadi, A. Beyer, K. Volz. *Ultramicroscopy* 206 (2019), 112814. doi: 10.1016/j.ultramic.2019.112814

Abstract Quantitative scanning transmission electron microscopy (STEM) is a powerful tool for the characterization of nano-materials. Absolute composition determination for ternary III-V semiconductors by direct comparison of experiment and simulation is well established. Here, we show a method to determine the composition of quaternary III-V semiconductors with two elements on each sub lattice from the intensities of one STEM image. As an example, this is applied to *(GaIn)(AsBi)*. The feasibility of the method is shown in a simulation study that also explores the influence of detector angles and specimen thickness. Additionally, the method is applied to an experimental STEM image of a *(GaIn)(AsBi)* quantum well grown by metal organic vapor phase epitaxy. The obtained concentrations give good agreement with X-ray diffraction and photoluminescence results.

Contributions of the Author For this work, I developed the method proposed and performed all STEM investigations and evaluations, in simulation and experiment.

The manuscript was written by me except for one paragraph dealing with MOVPE and XRD and PL measurements.

Ultramicroscopy 206 (2019) 112814

Contents lists available at ScienceDirect

Ultramicroscopy

journal homepage: www.elsevier.com/locate/ultramic

Composition determination for quaternary III–V semiconductors by aberration-corrected STEM

P. Kükelhan, T. Hepp, S. Firoozabadi, A. Beyer*, K. Volz

Materials Science Centre and Faculty of Physics, Philipps University Marburg, Hans-Meerwein-Straße 6, Marburg, Germany

ARTICLE INFO

Keywords:
Quantitative STEM
Quaternary III-V semiconductors
Composition determination
Image simulation

ABSTRACT

Quantitative scanning transmission electron microscopy (STEM) is a powerful tool for the characterization of nano-materials. Absolute composition determination for ternary III–V semiconductors by direct comparison of experiment and simulation is well established. Here, we show a method to determine the composition of quaternary III–V semiconductors with two elements on each sub lattice from the intensities of one STEM image. As an example, this is applied to (GaIn)(AsBi). The feasibility of the method is shown in a simulation study that also explores the influence of detector angles and specimen thickness. Additionally, the method is applied to an experimental STEM image of a (GaIn)(AsBi) quantum well grown by metal organic vapour phase epitaxy. The obtained concentrations are in good agreement with X-ray diffraction and photoluminescence results.

1. Introduction

Scanning transmission electron microscopy (STEM) emerged as an excellent tool for the quantitative analysis of nanostructures at atomic scale. In particular, annular dark field (ADF) STEM is established for composition determination of semiconductor compounds. This information is essential to support the development of new semiconductor devices.

Composition determination on an absolute scale can be achieved by comparison of experimental results to complementary image simulations. For these simulations, a precise modelling of the electron probe, the specimen, their interaction and the detector characteristics is necessary. Past developments made excellent agreement between experiment and simulation possible [1–3].

For material systems with one unknown substitute element, composition determination by ADF-STEM was demonstrated frequently [4–7] and showed good agreement to other methods, e.g. high resolution x-ray diffraction (XRD), but superior lateral resolution. Particularly, ternary III-V semiconductors were investigated. Obtained concentration profiles can be used to analyse further characteristics of the material system, e.g. surface segregation [8].

For material systems with two substitute elements, i.e. quaternary III–V semiconductors, several methods were considered. By analysing a single XRD measurement of the quasi-forbidden (002)-reflection, Tilli et al. determined the composition of Ga(NAsP) [9]. Grillo et al. combined the measurement of lattice distortions from high resolution transmission electron microscopy (HR-TEM) and (002) dark field TEM reflections to analyse the composition of (GaIn)(NAs) on a nanometre scale [10]. With atomic resolution, Grieb et al. determined the composition of (GaIn)(NAs) by evaluating high angle ADF-STEM intensity and strain state yielding good agreement to XRD results [11]. Additionally, there are more TEM studies of (GaIn)(NAs) by Müller et al. evaluating strain and contrast in TEM two-beam images [12] and using three-beam TEM lattice fringe images [13]. Duschek et al. proposed a method to determine the composition of Ga(NAsP) from several ADF-STEM images taken at different detector angles [14]. The atomic lensing model can also analyse the composition of mixed atomic columns [15,16]. Recently, Balades et al. pointed out the importance of cross talk for an intensity based composition evaluation of ADF-STEM images [17].

Here, we propose a method to determine the composition of quaternary III–V semiconductors with two elements on each sub lattice. It is applied to (GaIn)(AsBi) which is a promising material for optoelectronic applications. The method works with a single ADF-STEM image and utilizes the cross talk and knowledge about it from image simulations.

The feasibility of the proposed method is proven by the application to a simulated ADF-STEM image for which the composition is fully known. In a simulation study, the influence of detector angles and specimen thickness is evaluated. Then, the composition of (GaIn)(AsBi) quantum wells (QWs) grown on GaAs by metal organic vapour phase epitaxy (MOVPE) is determined from a high resolution ADF-STEM image. The obtained concentrations are compared to XRD and

* Corresponding author.
E-mail address: andreas.beyer@physik.uni-marburg.de (A. Beyer).

https://doi.org/10.1016/j.ultramic.2019.112814
Received 25 April 2019; Received in revised form 4 July 2019; Accepted 7 July 2019
Available online 08 July 2019
0304-3991/

photoluminescence (PL) results. Finally, the results are discussed.

2. Experimental

Growth of the sample is conducted at 400 °C and a reactor pressure of 50 mbar in a MOVPE machine with horizontal reactor system (Aixtron AIX 200). H_2 is used as carrier gas for the precursors triethylgallium (TEGa), trimethylindium (TMIn), tertiarybutylarsine (TBAs) and trimethylbismuth (TMBi) as Gallium (Ga), Indium (In), Arsenic (As) and Bismuth (Bi) sources, respectively. Flow modulated epitaxy (FME) is utilized to deposit the quaternary (GaIn)(AsBi) QW structure with three QWs on s.i. GaAs (001) substrates. Bi and In are pulsed separately for 2 s each without a break in between while GaAs is grown continuously. A growth interruption is established to increase the temperature to 550 °C in order to grow the GaAs barrier. XRD measurements around the (004) reflection are carried out to determine the strain of the quaternary layer. To determine the composition of the quaternary layer, a second information is needed since Bi and In both contribute to the compressive strain. Therefore, PL is performed in order to determine the energy gap. Bi shows a stronger influence on strain and band gap energy than In which makes it possible to determine the composition. For the given strain, a set of compositions can be calculated. From these compositions, the corresponding band gap energies are calculated based on tight binding theory simulations [18]. Finally, the calculated band gap energies are fitted to the experimental ones to extract the correct composition of the quaternary layer. More details of the growth of this quaternary material system and the composition determination by XRD and PL can be found in [19].

Using a dual beam focused ion beam scanning electron microscope (FIB-SEM) machine (JEOL JIB 4601F), a cross-sectional TEM lamella of this sample is prepared in [010] direction. The energy of the Ga ion beam is gradually decreased from 30 kV to 10 kV. After this FIB preparation, the specimen thickness is approximately 100 nm. Subsequently, the specimen is further thinned using a NanoMill TEM specimen preparation system (model 1040, E. A. Fischione Instruments, Inc., Export, PA, United States) [20] with milling energies of the Ar ions gradually decreasing from 900 eV to 500 eV. This milling is performed under an angle of ± 10°. Directly before the STEM investigations, plasma cleaning of the sample is performed.

For STEM investigations, a double C_s-corrected JEOL JEM2200FS (JEOL Ltd., Tokyo, Japan) is employed at an acceleration voltage of 200 kV. A condenser aperture with a diameter of 40 µm results in a convergence semi-angle of $\alpha = 21.3$ mrad. Scattered electrons are detected by the JEOL EM-24590YPDFI dark-field image detector at an angular range of 67–268 mrad. The inner angle is determined by measuring the shadow of the detector on a CCD camera and the outer angle is four times the inner angle. The hexapoles of the imaging corrector are switched off to avoid the cut-off in the diffraction plane introduced otherwise [21]. To reduce sample drift and scan distortions, ten images with dwell times of 3 µs are averaged using the software SmartAlign [22]. Normalisation of STEM intensities to the impinging beam is done with a beam image on a CCD camera [23].

3. STEM image simulations

For quantitative evaluation of STEM image intensities, complementary image simulations are used. These are conducted by the software STEMsalabim [24] which is based on the multi-slice algorithm by Kirkland [25] and optimized for highly parallelized computing on high-performance clusters. Thermal diffuse scattering is taken into account by the frozen phonon approximation [26] while the influence of chromatic aberration is included via a defocus series [27] of seven different defoci being centred at $\Delta f = 0$ nm with a full width half maximum of 7. 5 nm. The non-uniform detector sensitivity is taken into account after conducting a detector scan [1,4,5,28]. The effect of finite source size is considered by a Lorentzian convolution [3] whereby the width of this Lorentzian convolution is carefully adjusted to the experiment as described in [7]. All parameters for image simulation are chosen in accordance to experimental values and are summarized in Table 1.

Table 1
Parameters for STEM image simulations in accordance to the microscope at hand.

Electron energy	200 kV
Aperture angle	21.3 mrad
Astigmatism	0 nm
C_S	2 µm
C_5	5 mm
C_C	1.5 mm

$Ga_{1-x}In_xAs_{1-y}Bi_y$ super cells with sizes of $5 \times 5 \times 80$ unit cells are created resembling all possible compositions for $x = 0$–0.6 and $y = 0$–0.2 in steps of 0.05. In and Bi atoms are randomly distributed within the respective super cells while the overall composition was fixed to the value given. The effect of static atomic displacements is considered by valence force field relaxation using a Keating potential [29].

4. Method

In this section, the method developed to determine the composition of quaternary III–V semiconductors with two elements per sub lattice is described in detail.

First, the width of the Lorentzian convolution used to consider the finite source size [3] has to be determined as this parameter is used for evaluation of all image simulations following. For this, a barrier region with a material of known composition is needed. An averaged unit cell is calculated for this region. From this averaged unit cell, the thickness can be determined by comparison of the average intensity to the average intensity of an average simulated unit cell of the same composition. At this thickness, the width of the Lorentzian convolution can then be identified by matching both average unit cells as closely as possible in 2D. This procedure is also described in more detail in [7]. For all simulations following hereafter, this width is used for the Lorentzian convolution. For the simulation study, a reasonable value of $\sigma = 50$ pm is chosen while for the experimental image evaluated later $\sigma = 55$ pm is determined.

To determine the composition of a specific column, a measure of its intensity is needed. For this, Voronoi intensities [5] are assigned to every atomic column. These are chosen since they limit the influence of surface relaxation that can drastically alter the intensity in STEM images of semiconductor heterostructures [30,31]. Voronoi intensities are used for both experiment and simulation.

To be able to determine the composition of an atomic column, it is crucial to know its thickness. This is done by using a region of known composition, i.e. the barrier, and by interpolating the determined thickness from here to the region of unknown composition [4,5]. This is necessary since the composition of both sub lattices changes. The thickness gradient is modelled by a plane.

The thickness in the region of known composition is determined by comparison of the Voronoi intensities of both sub lattices to simulated Voronoi intensities of a super cell with the same composition. By finding the best fitting intensity, the thickness is fixed for every atomic column and can then be interpolated to atomic columns of unknown composition [5]. Thicknesses are determined as total number of atoms in a specific column.

Knowing the thickness of every atomic column, one can then evaluate all simulations with varying compositions at the present thicknesses. For every present thickness, for every atomic column the composition of this column, the composition of neighbouring atomic columns and the Voronoi intensity is evaluated. Since the STEM images

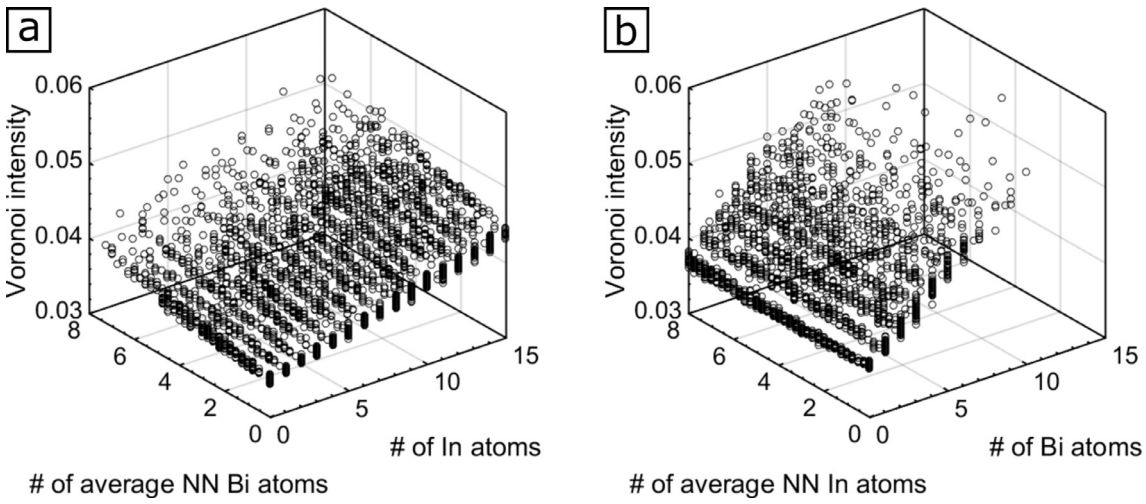

Fig. 1. Voronoi intensities depending on in-column and NN composition (simulated reference data). All group III (a) and group V (b) atomic columns are evaluated for the simulated super cells at a thickness of 25 atoms per atomic column and for a detector range of 70–280 mrad.

are taken in [010] direction, every atomic column has four next neighbour (NN) atomic columns that are belonging to the other sub lattice. This means that for every group III atomic column the number of In atoms in this atomic column, the average number of Bi atoms within the four NN group V columns (which can therefore feature quarter atoms) and the Voronoi intensity is evaluated. For group V atomic columns, the analogous procedure is done for Bi atoms in that column and average number of In atoms within NN atomic columns. Because of the statistical distribution of substitute atoms within the super cells, a wide range of different neighbourhoods is present for every composition.

These data are shown in Fig. 1 for a thickness of 25 atoms per atomic column, a detector range of 70–280 mrad and a width for the Lorentzian convolution of $\sigma = 50$ pm. In Fig. 1(a), the Voronoi intensity of group III atomic columns is illustrated depending on the number of In atoms in that column and the average number of neighbouring Bi atoms. Correspondingly, Fig. 1(b) shows this relationship for the group V lattice with Bi atoms and neighbouring In. One can see that for the given material system (GaIn)(AsBi) the Voronoi intensity increases with increasing number of In and Bi atoms in the respective column as well as with increasing average number of In and Bi atoms in the neighbourhood. As expected for Z-contrast images, the dependence of the Voronoi intensity on the number of Bi atoms is higher than on the number of In atoms for both in-column and NN atoms. This is made use of later on.

Now one has a certain Voronoi intensity distribution for every value pair of number of in-column atoms and average number of NN atoms. This originates from the different z-height distributions of substitute atoms in atomic columns due to the statistical distribution of substitute atoms within the super cells. To ascertain an average Voronoi intensity for every value pair of number of in-column atoms and average number of NN atoms, polynomial planes of second degree are fitted to the data. A polynomial relationship of second degree emerged as the most reasonable approximation.

If there are at least 10 data points for one value pair, the mean Voronoi intensity is assigned. Otherwise the value of the fitted plane is used. This ascertains the consideration of a minimum amount of possible z-height configurations.

The resulting relationships between Voronoi intensity, number of in-column atoms and average number of NN atoms are shown in Fig. 2(a) and (b) for group III and group V atomic columns, respectively. The sampling of this data space is set to one atom for the in-column composition and a quarter atom for the average NN composition.

The actual composition determination is then done in several steps. During the whole process, for every atomic column the intensity composition relationship for the atomic column's thickness has to be employed.

In a first step, the composition is determined for one sub lattice only. Here, one should use the sub lattice for which the dependence of the Voronoi intensity on the composition of the substitute atom is higher. In the case of the given material system (GaIn)(AsBi), this is the group V lattice containing Bi atoms. Hence, for the group V lattice the composition is determined without considering influences of neighbouring atomic columns on the Voronoi intensity. This means that only the data of the intensity composition relationship for the group V atomic columns are taken, where no NN In atoms are present. For these, the number of Bi atoms in the group V atomic columns is then set by comparing the simulated Voronoi intensities to the experimental one.

In the next step, the composition of the other sub lattice which is the group III lattice in this case is determined. For this, for every group III atomic column the In composition is determined by considering the average NN Bi composition just determined and using only this data from the intensity composition relationship for the group III lattice. Then, the In composition of every atomic column is found by comparing experimental and simulated Voronoi intensities.

Afterwards, the Bi composition of the group V atomic columns is refined analogously by considering the NN In composition and finally this step is performed one more time for the In composition of the group III atomic columns by considering the NN Bi composition of the group V lattice.

The last two steps can be performed iteratively.

5. Application to simulated STEM images

To show that the method described above is actually working, it is tested for a simulated STEM image. For this, the simulated super cell and its composition are fully known for every atomic column. The chosen super cell contains 5% of Bi and 5% of In on average while the substitute atoms are randomly distributed on the respective sub lattice. A thickness of 25 atoms per atomic column is chosen with the image being generated by a virtual detector with inner and outer detection angle of 70 and 280 mrad, respectively. Finally, a width of $\sigma = 50$ pm for the Lorentzian convolution is applied. The resulting STEM image is shown in Fig. 3(a). Different intensities of the atomic columns can be clearly distinguished due to their different composition.

The thickness of every atomic column is treated as already known so for every column the correct thickness of 25 atoms per atomic column is used. With the intensity composition relationships shown in Fig. 2 the

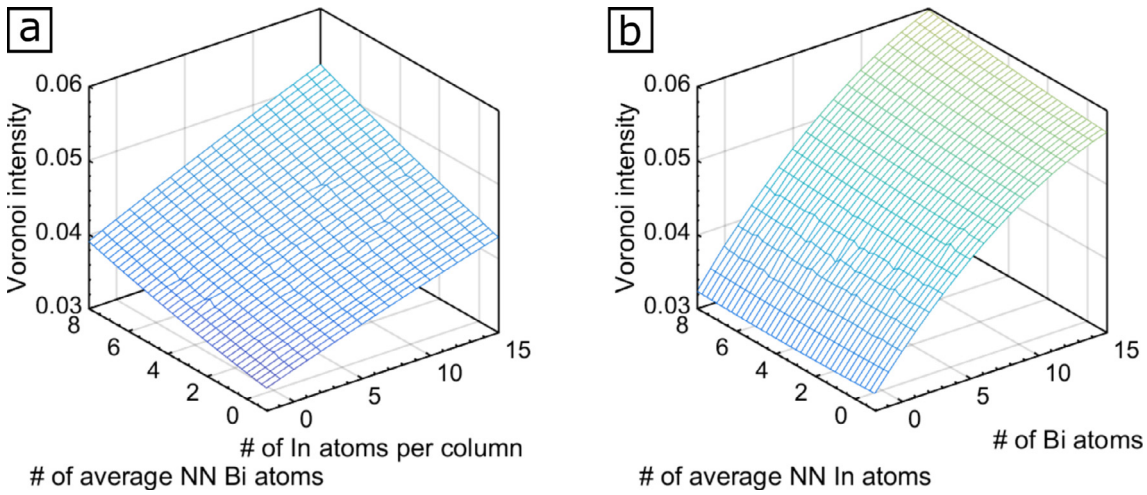

Fig. 2. Intensity composition relationships for group III (a) and group V (b) atomic columns drawn from the data shown in Fig. 1 (simulated reference data at thickness of 25 atoms per atomic column). A polynomial fit was used to account for missing statistics. Otherwise the mean intensity for a composition and its NN composition is chosen.

composition for every atomic column can be determined. The resulting composition map after two composition determination cycles is shown in Fig. 3(b) while the deviation to the real composition of every atomic column is shown in Fig. 3(c). As can be seen, the deviation to the real composition is $\pm$ 1 atoms per atomic column at most while there are up to 5 substitute atoms contained in one column in reality. This leads to a total deviation of -2 In atoms to the overall In composition of 65 In atoms and a total deviation of -1 Bi atoms to the overall Bi composition of 63 Bi atoms. For 85% of the atomic columns, the composition is determined correctly.

Hence, an accurate composition determination is possible for the given super cell. A perfect composition determination is not possible since the z-height distribution of the substitute atoms inside an atomic column influences its Voronoi intensity which leads to an intensity distribution for the same composition of an atomic column while only a mean intensity value can be used for the evaluation. This is discussed in more detail below.

To explore possibilities and limitations of the proposed method, it is also applied to a range of different detector angles and super cell thicknesses. By this, the best detector range can be found and the influence of specimen thickness can be determined.

The inner detector angle is varied from 50 to 100 mrad in steps of 10 mrad while the outer detector angle is chosen as the minimum value of four times the inner detector angle which is the detector geometry for the microscope at hand and 300 mrad which is the maximum value simulated. Above 300 mrad the change of the total signal is rather small. For a thickness of 25 atoms per atomic column, the influence of the detector angles is illustrated in Fig. 4(a). For small inner detector angles, the Bi composition is underestimated first while with increasing inner detector angle also the determined Bi composition is increasing. An optimum is reached at 70 mrad but afterwards the Bi composition is underestimated again. The In composition is also underestimated first, reaches its lowest deviation at an inner detector angle of 70 mrad and is underestimated for higher inner detector angles. The percentage of atomic columns for which the composition is determined correctly also has its highest value (85%) at an inner detector angle of 70 mrad while other detector angles give worse results.

Hence, for taking experimental images at the given thickness one should aim to work with an inner detector angle of 70 mrad resulting in an outer detector angle of 280 mrad for the evaluated detector geometry. It is found that the optimum inner detector angle increases with increasing specimen thickness.

Furthermore, the thickness of the super cell has been varied from 10 atoms to 35 atoms per atomic column in steps of 5 atoms. The evaluation stops at a thickness of 35 atoms per atomic column since the limited edge exclusion in the STEM image leads to edge effects beyond this thickness. These edge effects are caused by the self-interference of the convergent electron beam in the finite size of the simulated super cell.

For each thickness, the smallest deviation to the real composition is found in dependence of the detector range. The resulting dependence of the performance of the method on the specimen thickness is shown in

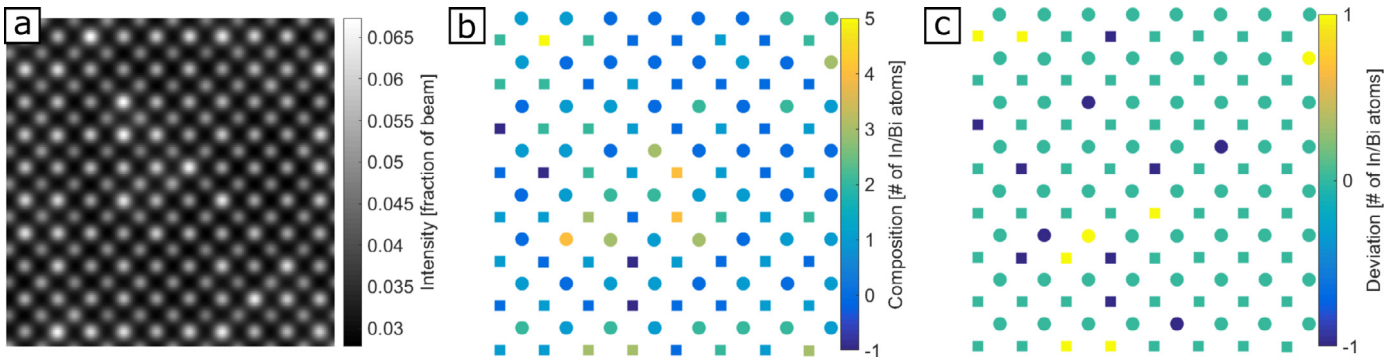

Fig. 3. Proof of feasibility with simulated STEM image of $Ga_{0.95}In_{0.05}As_{0.95}Bi_{0.05}$. The STEM image (a) was used to determine the composition (b) by the method described. Here, squares indicate group III atomic columns, while circles indicate group V atomic columns. The deviation to the real composition of the super cell is shown in (c). When comparing STEM image and compositions, take into account that edge columns are removed due to unclosed Voronoi cells and wrong NN relationships.

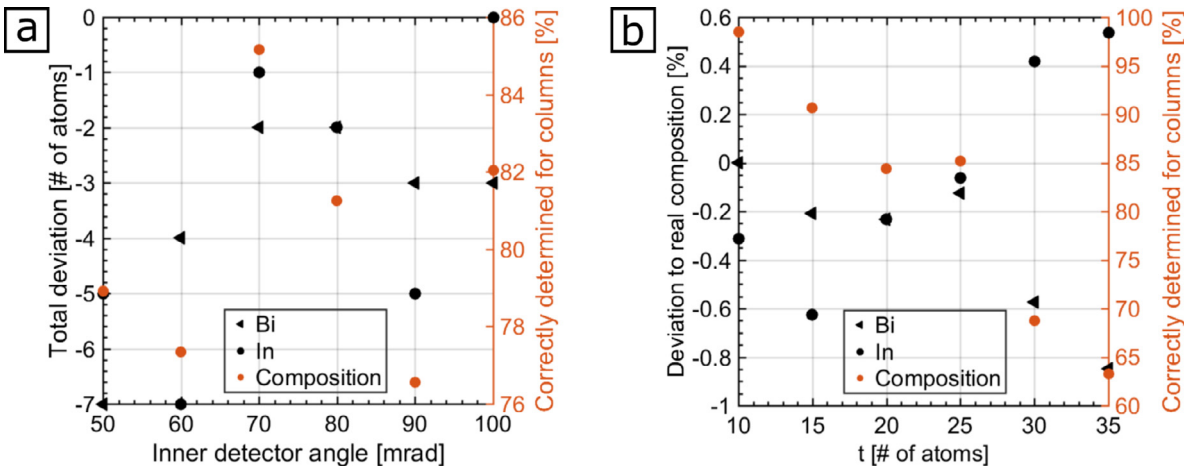

Fig. 4. Simulation study on the influence of detector range (a) and specimen thickness (b) for $Ga_{0.95}In_{0.05}As_{0.95}Bi_{0.05}$. The total deviation is evaluated for Bi (black triangle) and In (black circle). Additionally, the percentage of atomic columns for which the composition is determined correctly (red circle) is analysed. The detector angle study is performed at a thickness of 25 atoms per atomic column while for each thickness the best detector angle is chosen. (For interpretation of the references to colour in this figure legend, the reader is referred to the web version of this article.)

Fig. 4(b).

For thicknesses of 10 to 25 atoms per column, the total composition of In and Bi can be determined with very good agreement and deviations of 3 atoms maximum while the composition is determined correctly for more than 80% of the atomic columns.

At a thickness of 30 atoms, the Bi composition is underestimated by 11 atoms (80 Bi atoms and 1800 total group V atoms in the super cell) and for the In composition the deviation increases to 5 In atoms with 86 In atoms (1800 total group III atoms) contained in the super cell. Additionally, the percentage of correctly determined columns drops to 69%.

At a thickness of 35 atoms, for 62% of the atomic columns the composition is determined correctly and the Bi composition is underestimated by 18 atoms (91 Bi atoms and 2240 total group V atoms) while the In composition is overestimated by 8 atoms (96 In atoms and 2240 total group III atoms).

This thickness dependence means that for experimental investigations the most accurate results are achieved for thin samples with a thickness below 25 atoms per atomic column (~15 nm) for the case of (GaIn)(AsBi) which is possible to reach during sample preparation.

6. Application to experimental STEM image

Having proven that the proposed method is actually capable to determine the composition of quaternary (GaIn)(AsBi) from its HAADF-STEM image, it is applied to an experimental STEM image. The investigated material system is a (GaIn)(AsBi)-QW grown on GaAs by MOVPE. As found in the simulation study, the combination of thickness and detector range has to be chosen appropriately in the experiment. This is considered when acquiring the experimental STEM image shown in Fig. 5(a). Due to the dominant Z-contrast, the quaternary (GaIn)(AsBi)-QW in the centre of the image can be clearly distinguished from the binary GaAs regions. Following the method introduced above, the thickness is determined for every atomic column in the binary GaAs regions and then interpolated linearly to the quaternary region. The resulting thickness map is shown in Fig. 5(b). Thicknesses range from 22 to 26 atoms per atomic column. For these thicknesses, the composition of both In and Bi is determined iteratively as described above using three cycles. The resulting composition maps for In and Bi are shown in Fig. 5(c) and (d), respectively. These composition maps only show one sub lattice each. The In composition ranges from −3 to 8 In atoms per atomic column while the Bi composition ranges from −1 to 2 Bi atoms per atomic column. Negative compositions are allowed to consider experimental noise and to account for wrong thickness assumptions in the region where the thickness is interpolated. These wrong assumptions are apparent at the transition from one thickness to another where edges are visible within the composition maps. However, overall the thickness interpolation is resembling the thickness trend reasonably as confirmed by the thickness profile shown in Fig. 5(e). Averaging the compositions of all atomic columns along the lattice planes while considering the local thickness of each atomic column yields layer-by-layer concentration profiles. These profiles are shown in Fig. 5(f). Here, the shaded regions represent the standard deviation of the concentration across one lattice plane. While In and Bi growths start simultaneously, In continues to grow longer than Bi. This is caused by the pulsed growth with In being the last growth pulse. Averaging the concentrations within the QW, this gives a concentration of 4.5% In and 1.3% Bi.

With these average concentrations, the XRD diffractogram can be simulated and is compared to the experimental one in Fig. 6. A good agreement between both is present. Width of QW and barrier are adjusted to give the best agreement of both diffractograms as the QW width is found to vary locally.

7. Discussion

In this section, the proposed method for composition determination for quaternary III–V semiconductors with two elements on each sub lattice is discussed with regards to the general idea, its statistical character and the attainable accuracy. Furthermore, the best imaging conditions in terms of detector range as well as the experimental results are analysed.

The general idea of the method proposed is to make use of the cross-scattering [32] between the two sub lattices in quaternary III–V semiconductors that was also recently highlighted to be very influential [17]. However, although it might prevent the direct composition determination detailed knowledge about this cross-scattering from image simulations is utilized to determine the composition in an iterative manner for each sub lattice separately. For this, the NN atomic columns are considered as these heavily influence the intensity of neighbouring atomic columns from the other sub lattice. In this way, a cohesive composition neighbourhood can be found.

In general, composition determination by comparing experimental and simulated mean STEM intensities has a strong statistical character as discussed in detail in [7]. This is caused by the spread in intensities for a given composition of an atomic column due to different possible z-height distributions within this atomic column. Consequently, extreme z-height distributions could be assigned to a different composition

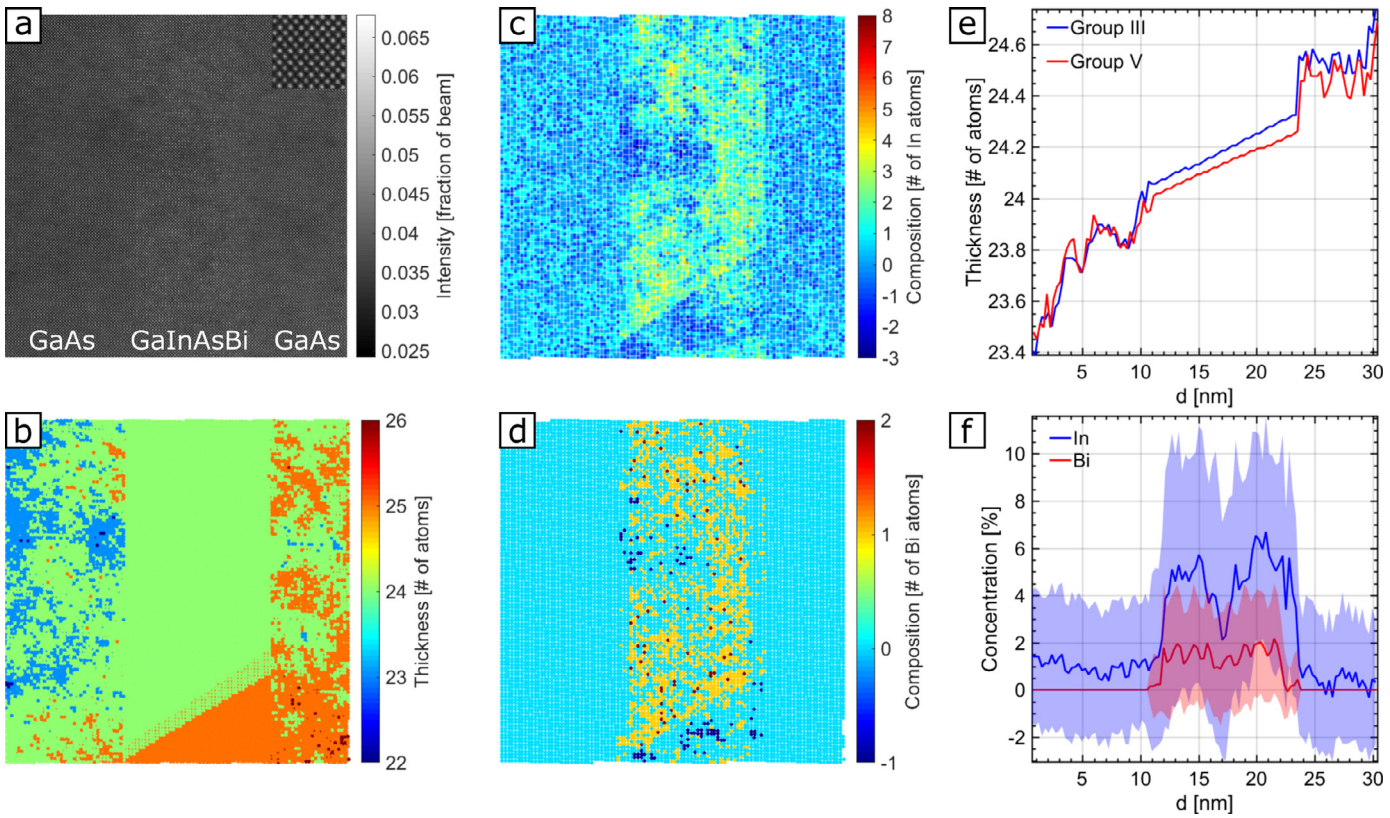

Fig. 5. Experimental results for a (GaIn)(AsBi)-QW between GaAs barriers. In the STEM image, the (GaIn)(AsBi)-QW is distinguishable due to its higher intensity. The small inset proves the atomic resolution. The thickness of every atomic column (b) is interpolated from the GaAs barriers. Applying the described method gives the In (c) and Bi composition (d). Profiles are obtained by averaging along the lattice planes. The thickness profile in (e) ensures a reasonable interpolation of the thickness. The resulting concentration profiles for In and Bi are given in (f). Shaded regions show the standard deviations along one lattice plane.

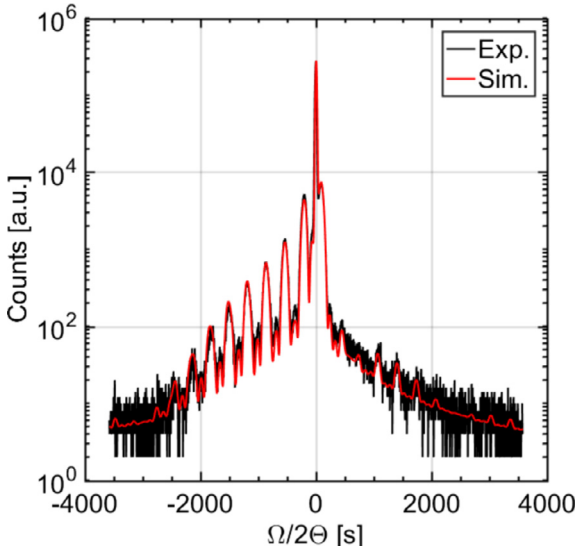

Fig. 6. Experimental XRD diffractogram and simulated XRD diffractogram for concentrations obtained by STEM. The width of the three (GaIn)(AsBi)-QWs is set to 10.4 nm and the barrier width is 48.1 nm.

based on their intensity. The width of the intensity distribution determines the attainable accuracy of the composition determination and is influenced by material system, thickness and composition of the respective atomic column. Hence, only for a certain fraction of all atomic columns the composition can be determined correctly. The capability for accurate composition determination decreases with decreasing difference in atomic number between substitute and matrix atom, with increasing thickness and with increasing number of substitute atoms per atomic column [7]. The last two aspects reflect the increased number of possible z-height configurations and consequently the decreased uniqueness of Voronoi intensities.

Nonetheless, given a sufficiently high number of atomic columns the overall composition is determined correctly since statistically positive and negative deviations from the correct composition for a single atomic column cancel.

In the case of a quaternary material system, this statistical character is even more important. The correct composition determination for an atomic column relies on the correct composition determination of its neighbouring atomic columns as these are highly influential on each other's Voronoi intensity. Since even with correct knowledge of the composition of neighbouring columns only for a fraction of the atomic columns the composition could be determined correctly, this amplifies for two sub lattices. The unavoidable wrong composition of some atomic columns leads to more wrongly determined columns on the other sub lattice. Thus, for the quaternary case a lower fraction of atomic columns can be determined correctly.

Additionally, the composition of all 4 NN atomic columns is described by the average composition only while there is a large range of possible z-height distributions for this average NN composition. However, this effect is weakened by approaching the composition determination separately for each sub lattice under consideration of the NN composition. Just looking for the most suitable composition based on comparing the atomic column's intensity with all intensities within the intensity composition data space does not work.

Despite the influence of increasing thickness, also at a thickness of 35 atoms the overall accuracy is still good. Nonetheless, the fraction of correctly determined atomic columns decreases so a thinner specimen allows a more accurate composition determination also locally.

An estimation of the local accuracy of composition determination by the method proposed can be done by means of the simulation study as here local deviations to the real composition are known. As already discussed, this accuracy is different regarding on material system, thickness and composition. It can be assessed for each case separately with the help of simulations where atoms are statistically distributed with a fixed mean concentration. For the investigated experimental example, the accuracy is estimated by evaluating a simulated STEM image of a super cell with 5% In and 5% Bi at a thickness of 25 atoms per atomic column and with a detector range of 70 –280 mrad. This yields deviations in the composition of up to ± 1 atoms per atomic column for In and Bi. Hence, it can be concluded that this is the expected local accuracy of the method not considering wrongly assumed thickness and experimental noise. It has to be stated that this local accuracy is inherent for using scattering intensities of ADF-STEM experiments.

For an experimental STEM image, the accuracy is worse than this inherent accuracy of the method since the thickness of each atomic column has to be known.

In the case of quaternary III–V semiconductors with two elements on each sub lattice, there is no sub lattice of constant composition that could be used for local thickness determination [33]. Therefore, a thickness determination could either be performed by a complementary method, e.g. convergent beam electron diffraction [34], or has to be interpolated from a region of known composition [4]. Obviously, this interpolation leads to local thickness deviations but it is the best possible solution working with a given ADF-STEM image. These local thickness deviations are apparent in the composition map for group III atomic columns (Fig. 5(c)) where the In composition resembles the pattern of the thickness map. All in all, the thickness assumption is not correct locally but still a linear interpolation is the best option available with a single STEM image.

The influence of local thickness deviations is also estimated with the help of simulations. To this end, the STEM image used for the accuracy estimation is utilized again. However, the thickness that is assumed for the evaluation is 24 and 26 atoms per atomic column, respectively. For an assumed thickness of 24 atoms per atomic column, i.e. an underestimation of the thickness by one atom, the composition is determined correctly for only 26% of the atomic columns resulting in a deviation of 2.0% for the Bi composition and 5.2% for the In composition. For an overestimation of the thickness by one atom, for 12% of the atomic columns the composition is determined correctly and a deviation of −3.2% for the Bi composition and −6% for the In composition results. These values result if for all atomic columns the thickness is under- or overestimated. Experimentally, thickness assumptions should be wrong only locally while the overall trend is correct. Hence, deviations from wrongly assumed thicknesses cancel since generally composition deviations for under- and overestimation of the thickness are expected to be symmetric [7]. However, due to the limited number of atomic columns evaluated this is not the case for this simulation study.

The influence of wrongly assumed thickness on composition determination is stronger for In than for Bi. This is caused by characteristics of the material system and the dominant Z-contrast of the HAADF-STEM imaging mode. Replacing a Ga atom by an In atom increases the atomic number of that atomic column by 18 while adding or subtracting one Ga atom changes it by 31. For Bi, a substitution leads to an increase of the atomic number by 50 while an As atom causes a change of 33. Hence, for In composition determination the thickness is more influential than for Bi composition determination. This is also reflected in the experimental results.

The best imaging conditions are determined in a simulation study. Here, the best detector range is a compromise between detecting the characteristic scattering of both substitute atoms. Hence, it highly depends on the material system. However, the optimal inner detector angle increases with increasing thickness. This is in accordance with results by De Backer et al. for atom-counting. This behaviour is explained by the non-monotonic increase of scattering cross-sections for low angle ADF-STEM at small thicknesses. This non-monotonic increase is caused by coherent contributions [35].

A detailed study on the influence of the detector range on composition determination will be carried out in separate work. The exploitation of different angular ranges for detecting characteristic scattering of different elements is promising and offers great potential.

For an experimental application of the proposed method, several influences are important. Accurate knowledge of all instrumental parameters is necessary. In particular, these include the electron probe and characteristics of the detector that have to be taken into account for image simulations. Additionally, amorphous layers at the surfaces of the sample are influential. These originate from sample preparation. Amorphous layers cause a deviation of crystalline and total specimen thickness experimentally while in the simulations only crystalline material is considered. However, crystalline and amorphous material seem to behave similarly so that the composition determination is still correct [7]. Since the specimen was treated with low-voltage ion milling, the amorphous layers are limited here. Therefore, their influence is less severe than in other cases where the influence is discussed in detail [7].

The accuracy of possible strain measurements is deteriorated by surface relaxation of the thin TEM specimen [30,31].

With a combination of XRD and PL results, the concentration can also be determined. There are many theoretical assumptions necessary for this, e.g. the energetic level of Bi impurities in (GaIn)As. By combining XRD and PL, an In concentration of 3.9 ± 0.4% and a Bi concentration of 1.3 ± 0.2% are determined. The STEM results indicate a slightly higher In concentration which can also explain small deviations between simulated and experimental XRD. Since thickness is really influential on composition determination of In, wrong thickness estimations can lead to this slightly higher In concentration.

Additionally, the composition of both In and Bi is fluctuating within the QW, so that local differences within one QW and between all three QWs can be present and are then averaged by XRD and PL results. Contrarily, the STEM image shows only a small field of view. Nonetheless, STEM offers superior resolution and can reveal the present clustering effects.

This superior resolution offered by the proposed method can be obtained for quaternary III–V semiconductors with two elements on each sub lattice and offers new possibilities for structural characterization of these materials.

8. Summary

In this work, we showed a method to determine the composition of quaternary III–V semiconductors with two elements on each sub lattice from the intensities of one STEM image for the example of (GaIn)(AsBi). The method is based on an iterative composition determination of both sub lattices considering the composition of neighbouring atomic columns. In a simulation study, the feasibility of the method was proven and confirmed for thicknesses up to 35 atoms per atomic columns. The detector angles can be optimized to improve the performance. Applying the method to an experimental STEM image of a (GaIn)(AsBi)-QW gives good agreement to concentration results obtained by XRD and PL.

Acknowledgements

Financial support in the framework of SFB 1083 and GRK 1782 by the German Research Foundation (DFG) is greatly appreciated. S. Firoozabadi acknowledges financial support by the European Union's Horizon 2020 in the framework of the project microSPIRE (ID: 766955).

References

[1] J.M. LeBeau, S. Stemmer, Experimental quantification of annular dark-field images

in scanning transmission electron microscopy, Ultramicroscopy 108 (2008) 1653–1658, https://doi.org/10.1016/j.ultramic.2008.07.001.
[2] C. Dwyer, C. Maunders, C.L. Zheng, M. Weyland, P.C. Tiemeijer, Sub-0.1nm-resolution quantitative scanning transmission electron microscopy without adjustable parameters, Appl. Phys. Lett. 100 (2012) 191915, , https://doi.org/10.1063/1.4711766.
[3] A. Beyer, J. Belz, N. Knaub, K. Jandieri, K. Volz, Influence of spatial and temporal coherences on atomic resolution high angle annular dark field imaging, Ultramicroscopy 169 (2016) 1–10, https://doi.org/10.1016/j.ultramic.2016.06.006.
[4] A. Rosenauer, K. Gries, K. Müller, A. Pretorius, M. Schowalter, A. Avramescu, K. Engl, S. Lutgen, Measurement of specimen thickness and composition in AlGaN/GaN using high-angle annular dark field images, Ultramicroscopy 109 (2009) 1171–1182, https://doi.org/10.1016/j.ultramic.2009.05.003.
[5] A. Rosenauer, T. Mehrtens, K. Müller, K. Gries, M. Schowalter, P. Venkata Satyam, S. Bley, C. Tessarek, D. Hommel, K. Sebald, M. Seyfried, J. Gutowski, A. Avramescu, K. Engl, S. Lutgen, Composition mapping in InGaN by scanning transmission electron microscopy, Ultramicroscopy 111 (2011) 1316–1327, https://doi.org/10.1016/j.ultramic.2011.04.009.
[6] G.T. Martinez, A. Rosenauer, A. De Backer, J. Verbeeck, S. Van Aert, Quantitative composition determination at the atomic level using model-based high-angle annular dark field scanning transmission electron microscopy, Ultramicroscopy 137 (2014) 12–19, https://doi.org/10.1016/j.ultramic.2013.11.001.
[7] L. Duschek, P. Kükelhan, A. Beyer, S. Firoozabadi, J.O. Oelerich, C. Fuchs, W. Stolz, A. Ballabio, G. Isella, K. Volz, Composition determination of semiconductor alloys towards atomic accuracy by HAADF-STEM, Ultramicroscopy 200 (2019) 84–96, https://doi.org/10.1016/j.ultramic.2019.02.009.
[8] T. Mehrtens, K. Müller, M. Schowalter, D. Hu, D.M. Schaadt, A. Rosenauer, Measurement of indium concentration profiles and segregation efficiencies from high-angle annular dark field-scanning transmission electron microscopy images, Ultramicroscopy 131 (2013) 1–9, https://doi.org/10.1016/j.ultramic.2013.03.018.
[9] J. Tilli, H. Jussila, K.M. Yu, T. Huhtio, M. Sopanen, Composition determination of quaternary GaAsPN layers from single X-ray diffraction measurement of quasi-forbidden (002) reflection, J. Appl. Phys. 115 (2014) 203102, , https://doi.org/10.1063/1.4878939.
[10] V. Grillo, M. Albrecht, T. Remmele, H.P. Strunk, A.Y. Egorov, H. Riechert, Simultaneous experimental evaluation of In and N concentrations in InGaAsN quantum wells, J. Appl. Phys. 90 (2001) 3792, https://doi.org/10.1063/1.1402139.
[11] T. Grieb, K. Müller, E. Cadel, A. Beyer, M. Schowalter, E. Talbot, K. Volz, A. Rosenauer, Simultaneous quantification of indium and nitrogen concentration in InGaNAs using HAADF-STEM, Microsc. Microanal. 20 (2014) 1740–1752, https://doi.org/10.1017/S1431927614013051.
[12] K. Müller, M. Schowalter, A. Rosenauer, O. Rubel, K. Volz, Effect of bonding and static atomic displacements on composition quantification in InGaNAs, Phys. Rev. B. 81 (2010) 075315, , https://doi.org/10.1103/PhysRevB.81.075315.
[13] K. Müller, M. Schowalter, A. Rosenauer, D. Hu, D.M. Schaadt, M. Hetterich, P. Gilet, O. Rubel, R. Fritz, K. Volz, Atomic scale annealing effects on InGaNAs studied by TEM three-beam imaging, Phys. Rev. B. 84 (2011) 045316, , https://doi.org/10.1103/PhysRevB.84.045316.
[14] L. Duschek, A. Beyer, J.O. Oelerich, K. Volz, Composition determination of multinary III/V semiconductors via STEM HAADF multislice simulations, Ultramicroscopy 185 (2018) 15–20, https://doi.org/10.1016/j.ultramic.2017.11.002.
[15] K.H.W. Van Den Bos, A. De Backer, G.T. Martinez, N. Winckelmans, S. Bals, P.D. Nellist, S. Van Aert, Unscrambling mixed elements using high angle annular dark field scanning transmission electron microscopy, Phys. Rev. Lett. 116 (2016) 246101, , https://doi.org/10.1103/PhysRevLett.116.246101.
[16] K.H.W. Van den Bos, L. Janssens, A. De Backer, P.D. Nellist, S. Van Aert, The atomic lensing model: new opportunities for atom-by-atom metrology of heterogeneous nanomaterials, Ultramicroscopy (2018), https://doi.org/10.1016/j.ultramic.2018.12.004.
[17] N. Balades, M. Herrera, D.L. Sales, M.P. Guerrero, E. Guerrero, P.L. Galindo, S.I. Molina, Influence of the crosstalk on the intensity of HAADF-STEM images, J. Microsc 273 (2019) 81–88, https://doi.org/10.1111/jmi.12763.
[18] M. Usman, C.A. Broderick, A. Lindsay, E.P.O. Reilly, Tight-binding analysis of the electronic structure of dilute bismide alloys of GaP and GaAs, Phys. Rev. B. 84 (2011) 245202, , https://doi.org/10.1103/PhysRevB.84.245202.
[19] T. Hepp, O. Maßmeyer, D.A. Duffy, S.J. Sweeney, K. Volz, MOVPE growth and characterization of quaternary (Ga, In)(As, Bi) on GaAs substrates, Submitt. to J. Appl. Phys. (2019).
[20] R.R. Cerchiara, P.E. Fischione, J. Liu, J.M. Matesa, A.C. Robins, H.L. Fraser, A. Genc, Raising the standard of specimen preparation for aberration-corrected TEM and STEM, Micros. Today 19 (2011) 16–19, https://doi.org/10.1017/S1551929510001197.
[21] F.F. Krause, M. Schowalter, T. Grieb, K. Müller-Caspary, T. Mehrtens, A. Rosenauer, Effects of instrument imperfections on quantitative scanning transmission electron microscopy, Ultramicroscopy 161 (2016) 146–160, https://doi.org/10.1016/j.ultramic.2015.10.026.
[22] L. Jones, H. Yang, T.J. Pennycook, M.S.J. Marshall, S. Van Aert, N.D. Browning, M.R. Castell, P.D. Nellist, S.I. Molina, D.L. Sales, P.L. Galindo, D. Fuster, Y. González, B. Alén, L. González, M. Varela, S.J. Pennycook, R. Erni, H. Heinrich, G. Kostorz, V. Grillo, E. Carlino, F. Glas, F. Rossi, E.J. Kirkland, Z. Yu, P.E. Batson, J. Silcox, E. Carlino, V. Grillo, Smart Align-a new tool for robust non-rigid registration of scanning microscope data, Ultramicroscopy 109 (2009) 8, https://doi.org/10.1186/s40679-015-0008-4.
[23] D.S. He, Z.Y. Li, A practical approach to quantify the ADF detector in STEM, J. Phys. Conf. Ser. 522 (2014) 012017, , https://doi.org/10.1088/1742-6596/522/1/012017.
[24] J.O. Oelerich, L. Duschek, J. Belz, A. Beyer, S.D. Baranovskii, K. Volz, STEMsalabim: a high-performance computing cluster friendly code for scanning transmission electron microscopy image simulations of thin specimen, Ultramicroscopy 177 (2017) 91–96, https://doi.org/10.1016/j.ultramic.2017.03.010.
[25] E.J. Kirkland, Advanced computing in electron microscopy, 2010.
[26] B.D. Forbes, A.J. D'Alfonso, S.D. Findlay, D. Van Dyck, J.M. LeBeau, S. Stemmer, L.J. Allen, Thermal diffuse scattering in transmission electron microscopy, Ultramicroscopy 111 (2011) 1670–1680, https://doi.org/10.1016/j.ultramic.2011.09.017.
[27] K. Kuramochi, T. Yamazaki, Y. Kotaka, M. Ohtsuka, I. Hashimoto, K. Watanabe, Effect of chromatic aberration on atomic-resolved spherical aberration corrected STEM images, Ultramicroscopy 110 (2009) 36–42, https://doi.org/10.1016/j.ultramic.2009.09.003.
[28] S.D. Findlay, J.M. LeBeau, Detector non-uniformity in scanning transmission electron microscopy, Ultramicroscopy 124 (2013) 52–60, https://doi.org/10.1016/j.ultramic.2012.09.001.
[29] P.N. Keating, Effect of invariance requirements on the elastic strain energy of crystals with application to the diamond structure, Phys. Rev. 145 (1966) 637–645, https://doi.org/10.1103/PhysRev.145.637.
[30] A. Beyer, L. Duschek, J. Belz, K. Jandieri, K. Volz, Influence of surface relaxation of strained layers on atomic resolution ADF imaging, Ultramicroscopy 181 (2017) 8–16, https://doi.org/10.1016/j.ultramic.2017.04.019.
[31] A. Beyer, L. Duschek, J. Belz, J.O. Oelerich, K. Jandieri, K. Volz, Surface relaxation of strained Ga(P,As)/GaP heterostructures investigated by HAADF STEM, J. Microsc. 268 (2017) 239–247, https://doi.org/10.1111/jmi.12622.
[32] S.J. Pennycook, L.A. Boatner, Chemically sensitive structure-imaging with a scanning transmission electron microscope, Nature 336 (1988) 565–567.
[33] P. Kükelhan, A. Beyer, S. Firoozabadi, T. Hepp, K. Volz, Simultaneous determination of local thickness and composition for ternary III-V semiconductors by aberration-corrected STEM, Ultramicroscopy 201 (2019) 49–57, https://doi.org/10.1016/j.ultramic.2019.03.005.
[34] J.M. LeBeau, S.D. Findlay, L.J. Allen, S. Stemmer, Position averaged convergent beam electron diffraction: theory and applications, Ultramicroscopy 110 (2010) 118–125, https://doi.org/10.1016/j.ultramic.2009.10.001.
[35] A. De Backer, A. De wael, J. Gonnissen, S. Van Aert, Optimal experimental design for nano-particle atom-counting from high-resolution STEM images, Ultramicroscopy 151 (2015) 46–55, https://doi.org/10.1016/j.ultramic.2014.10.015.

6.6 Conference Contributions

- P. Kükelhan, A. Beyer, C. Fuchs, A. Bäumner, S. W. Koch, W. Stolz, K. Volz. Atomic Structure of "W"-Quantum Well Heterostructures Investigated by Aberration-Corrected STEM. Microscopy of Semiconducting Materials, 2017, contributed talk

- P. Kükelhan, A. Beyer, L. Duschek, C. Fuchs, W. Stolz, K. Volz. Atomic Structure of "W"-Quantum Well Heterostructures Investigated by Aberration-Corrected STEM and Complementary Contrast Simulation. Microscopy Conference, 2017, contributed poster

- P. Kükelhan, A. Beyer, L. Duschek, C. Fuchs, J.O. Oelerich, W. Stolz, K. Volz. Surface Segregation in "W"-type Quantum Well Heterostructures Revealed by Atomic Resolution STEM. International Microscopy Conference, 2018, contributed digital poster and mini oral presentation

- P. Kükelhan, A. Beyer, S. Firoozabadi, T. Hepp, K. Volz. Simultaneous Determination of Local Thickness and Composition for Ternary III-V Semiconductors by Aberration-Corrected STEM. Microscopy of Semiconducting Materials, 2019, contributed talk

- P. Kükelhan, T. Hepp, S. Firoozabadi, A. Beyer, K. Volz. Composition Determination for Quaternary III-V Semiconcuctors by Aberration-Corrected STEM. PICO, 2019, contributed poster

Bibliography

[1] S. J. Pennycook and D. E. Jesson. High-Resolution Incoherent Imaging of Crystals. *Physical Review Letters*, 64(8):938–941, 1990.

[2] S. J. Pennycook and D. E. Jesson. High-resolution Z-contrast imaging of crystals. *Ultramicroscopy*, 37(1-4):14–38, 1991.

[3] P. D. Nellist and S. J. Pennycook. Incoherent imaging using dynamically scattered coherent electrons. *Ultramicroscopy*, 78(1-4):111–124, 1999.

[4] S. J. Pennycook and L. A. Boatner. Chemically sensitive structure-imaging with a scanning transmission electron microscope. *Nature*, 336:565–567, 1988.

[5] S. J. Pennycook. Z-contrast stem for materials science. *Ultramicroscopy*, 30:58–69, 1989.

[6] P. M. Voyles, David A. Muller, J. L. Grazul, P. H. Citrin, and H.-J. J.L. Gossmann. Atomic-scale imaging of individual dopant atoms and clusters in highly n-type bulk Si. *Nature*, 416(6883):826–829, apr 2002.

[7] M. Haider, H. Rose, S. Uhlemann, E. Schwan, B. Kabius, and K. Urban. A spherical-aberration-corrected 200 kV transmission electron microscope. *Ultramicroscopy*, 75:53–60, 1998.

[8] B. Kabius, M. Haider, S. Uhlemann, E. Schwan, K. Urban, and H. Rose. First application of a spherical-aberration corrected transmission electron microscope in materials science. *Journal of Electron Microscopy*, 51:51–58, 2002.

[9] P. E. Batson, N. Dellby, and O. L. Krivanek. Sub-Angstrom resolution using aberration corrected electron optics. *Nature*, 418:617–620, 2002.

[10] R. Erni, M. D. Rossell, C. Kisielowski, and U. Dahmen. Atomic-Resolution Imaging with a Sub-50 pm Electron Probe. *Physical Review Letters*, 102:096101, 2009.

[11] C. Dwyer, C. Maunders, C. L. Zheng, M. Weyland, P. C. Tiemeijer, and J. Etheridge. Sub-0.1 nm-resolution quantitative scanning transmission electron microscopy without adjustable parameters. *Appl. Phys. Lett.*, 100:191915, 2012.

[12] M. J. Hÿtch and A. M. Minor. Observing and measuring strain in nanostructures and devices with transmission electron microscopy. *MRS Bull.*, 39:138–146, 2014.

[13] D. Cooper, T. Denneulin, N. Bernier, A. Béché, and J.-L. Rouvière. Strain mapping of semiconductor specimens with nm-scale resolution in a transmission electron microscope. *Micron*, 80:145–165, 2016.

[14] S. Van Aert, J. Verbeeck, R. Erni, S. Bals, M. Luysberg, D. Van Dyck, and G. Van Tendeloo. Quantitative atomic resolution mapping using high-angle annular dark field scanning transmission electron microscopy. *Ultramicroscopy*, 109:1236–1244, 2009.

[15] A. J. Den Dekker, S. Van Aert, A. Van Den Bos, and D. Van Dyck. Maximum likelihood estimation of structure parameters from high resolution electron microscopy images . Part I : A theoretical framework. *Ultramicroscopy*, 104:83–106, 2005.

[16] S. Van Aert, A. J. Den Dekker, A. Van Den Bos, D. Van Dyck, and J. H. Chen. Maximum likelihood estimation of structure parameters from high resolution electron microscopy images . Part II : A practical example. *Ultramicroscopy*, 104:107–125, 2005.

[17] J. Verbeeck and S. Van Aert. Model based quantification of EELS spectra. *Ultramicroscopy*, 101(2-4):207–224, 2004.

[18] S. Van Aert, A. De Backer, G. T. Martinez, B. Goris, S. Bals, G. Van Tendeloo, and A. Rosenauer. Procedure to count atoms with trustworthy single-atom sensitivity. *Physical Review B*, 87:064107, 2013.

[19] A. De Backer, G. T. Martinez, A. Rosenauer, and S. Van Aert. Atom counting in HAADF STEM using a statistical model-based approach: Methodology, possibilities, and inherent limitations. *Ultramicroscopy*, 134:23–33, 2013.

[20] A. De wael, A. De Backer, L. Jones, P. D. Nellist, and S. Van Aert. Hybrid statistics-simulations based method for atom-counting from ADF STEM images. *Ultramicroscopy*, 177:69–77, 2017.

[21] G. T. Martinez, A. Rosenauer, A. De Backer, J. Verbeeck, and S. Van Aert. Quantitative composition determination at the atomic level using model-based high-angle annular dark field scanning transmission electron microscopy. *Ultramicroscopy*, 137:12–19, 2014.

[22] K. H.W. Van Den Bos, A. De Backer, G. T. Martinez, N. Winckelmans, S. Bals, P. D. Nellist, and S. Van Aert. Unscrambling Mixed Elements using High Angle Annular Dark Field Scanning Transmission Electron Microscopy. *Physical Review Letters*, 116:246101, 2016.

[23] K. H. W. Van den Bos, L. Janssens, A. De Backer, P. D. Nellist, and S. Van Aert. The atomic lensing model: New opportunities for atom-by-atom metrology of heterogeneous nanomaterials. *Ultramicroscopy*, 2018.

[24] S. C. Anderson, C. R. Birkeland, G. R. Anstis, and D. J.H. Cockayne. An approach to quantitative compositional profiling at near-atomic resolution using high-angle annular dark field imaging. *Ultramicroscopy*, 69(2):83–103, 1997.

[25] E. Carlino and V. Grillo. Atomic-resolution quantitative composition analysis using scanning transmission electron microscopy Z-contrast experiments. *Physical Review B*, 71:235303, 2005.

[26] D. O. Klenov and S. Stemmer. Contributions to the contrast in experimental high-angle annular dark-field images. *Ultramicroscopy*, 106(10):889–901, 2006.

[27] V. Grillo, E. Carlino, and F. Glas. Influence of the static atomic displacement on atomic resolution Z-contrast imaging. *Physical Review B*, 77:054103, 2008.

[28] J. M. LeBeau, S. D. Findlay, L. J. Allen, and S. Stemmer. Quantitative atomic resolution scanning transmission electron microscopy. *Physical Review Letters*, 100:206101, 2008.

[29] J. M. LeBeau and S. Stemmer. Experimental quantification of annular dark-field images in scanning transmission electron microscopy. *Ultramicroscopy*, 108:1653–1658, 2008.

[30] A. Rosenauer, K. Gries, K. Müller, A. Pretorius, M. Schowalter, A. Avramescu, K. Engl, and S. Lutgen. Measurement of specimen thickness and composition in AlGaN/GaN using high-angle annular dark field images. *Ultramicroscopy*, 109:1171–1182, 2009.

[31] R. Ishikawa, A. R. Lupini, S. D. Findlay, and S. J. Pennycook. Quantitative Annular Dark Field Electron Microscopy Using Single Electron Signals. *Microscopy and Microanalysis*, 20:99–10, 2014.

[32] D. S. He and Z. Y. Li. A practical approach to quantify the ADF detector in STEM. *Journal of Physics: Conference Series*, 522:012017, 2014.

[33] G. T. Martinez, L. Jones, A. De Backer, A. Béché, J. Verbeeck, S. Van Aert, and P. D. Nellist. Quantitative STEM normalisation: The importance of the electron flux. *Ultramicroscopy*, 159:46–58, 2015.

[34] F. F. Krause, M. Schowalter, T. Grieb, K. Müller-Caspary, T. Mehrtens, and A. Rosenauer. Effects of instrument imperfections on quantitative scanning transmission electron microscopy. *Ultramicroscopy*, 161:146–160, 2016.

[35] A. Rosenauer, T. Mehrtens, K. Müller, K. Gries, M. Schowalter, P. Venkata Satyam, S. Bley, C. Tessarek, D. Hommel, K. Sebald, M. Seyfried, J. Gutowski, A. Avramescu, K. Engl, and S. Lutgen. Composition mapping in InGaN by scanning transmission electron microscopy. *Ultramicroscopy*, 111:1316–1327, 2011.

[36] J. M. LeBeau, S. D. Findlay, L. J. Allen, and S. Stemmer. Standardless atom counting in scanning transmission electron microscopy. *Nano Letters*, 10:4405–4408, 2010.

[37] J. M. Cowley and A F Moodie. The Scattering of Electrons by Atoms and Crystals. I. A New Theoretical Approach. *Acta Crystallographica*, 10:609–619, 1957.

[38] P. Goodman and A. F. Moodie. Numerical Evaluation of N-Beam Wave Functions in Electron Scattering by the Multi-slice Method. *Acta Cryst. A*, 30:280–290, 1970.

[39] T. Grieb, K. Müller, R. Fritz, M. Schowalter, N. Neugebohrn, N. Knaub, K. Volz, and A. Rosenauer. Determination of the chemical composition of GaNAs using STEM HAADF imaging and STEM strain state analysis. *Ultramicroscopy*, 117:15–23, 2012.

[40] T. Grieb, K. Müller, R. Fritz, V. Grillo, M. Schowalter, K. Volz, and A. Rosenauer. Quantitative chemical evaluation of dilute GaNAs using ADF STEM: Avoiding surface strain induced artifacts. *Ultramicroscopy*, 129:1–9, 2013.

[41] T. Mehrtens, K. Müller, M. Schowalter, D. Hu, D. M. Schaadt, and A. Rosenauer. Measurement of indium concentration profiles and segregation efficiencies

from high-angle annular dark field-scanning transmission electron microscopy images. *Ultramicroscopy*, 131:1–9, 2013.

[42] J. Tilli, H. Jussila, K. M. Yu, T. Huhtio, and M. Sopanen. Composition determination of quaternary GaAsPN layers from single X-ray diffraction measurement of quasi-forbidden (002) reflection. *Journal of Applied Physics*, 115:203102, 2014.

[43] V. Grillo, M. Albrecht, T. Remmele, H. P. Strunk, A. Yu Egorov, and H. Riechert. Simultaneous experimental evaluation of In and N concentrations in InGaAsN quantum wells. *Journal of Applied Physics*, 90:3792, 2001.

[44] T. Grieb, K. Müller, E. Cadel, A. Beyer, M. Schowalter, E. Talbot, K. Volz, and A. Rosenauer. Simultaneous quantification of indium and nitrogen concentration in InGaNAs using HAADF-STEM. *Microscopy and Microanalysis*, 20(6):1740–1752, 2014.

[45] L. Duschek, A. Beyer, J. O. Oelerich, and K. Volz. Composition determination of multinary III/V semiconductors via STEM HAADF multislice simulations. *Ultramicroscopy*, 185:15–20, 2018.

[46] M. Grundmann. *The Physics of Semiconductors*. 2010.

[47] G. B. Stringfellow. *Organometallic Vapor-Phase Epitaxy: Theory and Practice*. 1999.

[48] M. Behet, A. Kohl, A. Mesquida, B. Opitz, and K. Heime. MOVPE growth of III-V compounds for optoelectronic and electronic applications. 27:297–334, 1996.

[49] J. E. Ayers. *Heteroepitaxy of Semiconductors: Theory, Growth and Characterization*. 2007.

[50] A. Stukowski. Visualization and analysis of atomistic simulation data with OVITO - the Open Visualization Tool. *Modelling and Simulation in Materials Science and Engineering*, 18:015012, 2010.

[51] K. Alberi, J. Wu, W. Walukiewicz, K. M. Yu, O. D. Dubon, S. P. Watkins, C. X. Wang, X. Liu, Y.-J. Cho, and J. Furdyna. Valence-band anticrossing in mismatched III-V semiconductor alloys. *Physical Review B*, 75:045203, 2007.

[52] C. Fuchs, A. Brüggemann, M. J. Weseloh, C. Berger, C. Möller, S. Reinhard, and J. Hader. High-temperature operation of electrical injection type-II

(GaIn)As/Ga(AsSb)/(GaIn)As "W"-quantum well lasers emitting at 1300 nm. *Scientific Reports*, 8:1422, 2018.

[53] J. R. Meyer, C. L. Felix, W. W. Bewley, I. Vurgaftman, E. H. Aifer, L. J. Olafsen, J. R. Lindle, C. A. Hoffman, M. J. Yang, B. R. Bennett, B. V. Shanabrook, H. Lee, C. H. Lin, S. S. Pei, and R. H. Miles. Auger coefficients in type-II InAs/GaInSb quantum wells. *Applied Physics Letters*, 73(20):2857–2859, 1998.

[54] G. G. Zegrya and A. D. Andreev. Mechanism of suppression of Auger recombination processes in typeâII heterostructures. *Applied Physics Letters*, 67(18):2681–2683, 1995.

[55] C. Berger, C. Möller, P. Hens, C. Fuchs, W. Stolz, S. W. Koch, A. Ruiz Perez, J. Hader, and J. V. Moloney. Novel type-II material system for laser applications in the near-infrared regime. *AIP Advances*, 5:047105, 2015.

[56] C. Fuchs, A. Beyer, K. Volz, and W. Stolz. MOVPE growth of (GaIn)As/Ga(AsSb)/(GaIn)As type-II heterostructures on GaAs substrate for near infrared laser applications. *Journal of Crystal Growth*, 464:201–205, 2017.

[57] R. Erni. *Aberration-corrected imaging in transmission electron microscopy: An introduction*. World Scientific Publishing Company, 2010.

[58] R. Brydson (Ed.). *Aberration-corrected analytical transmission electron microscopy*. 2011.

[59] P. M. Voyles, J. L. Grazul, and D. A. Muller. Imaging individual atoms inside crystals with ADF-STEM. *Ultramicroscopy*, 96:251–273, 2003.

[60] L. Dieterle, B. Butz, and E. Müller. Optimized Ar-ion milling procedure for TEM cross-section sample preparation. *Ultramicroscopy*, 111(11):1636–1644, 2011.

[61] Jürgen Belz, Andreas Beyer, Torsten Torunski, Wolfgang Stolz, and Kerstin Volz. Direct investigation of (sub-) surface preparation artifacts in GaAs based materials by FIB sectioning. *Ultramicroscopy*, 163:19–30, 2016.

[62] M. Schaffer, B. Schaffer, and Q. Ramasse. Sample preparation for atomic-resolution STEM at low voltages by FIB. *Ultramicroscopy*, 114:62–71, 2012.

[63] R. R. Cerchiara, P. E. Fischione, J. Liu, J. M Matesa, A. C. Robins, H. L. Fraser, and A. Genc. Raising the Standard of Specimen Preparation for Aberration-Corrected TEM and STEM. *Microscopy Today*, 19(01):16–19, 2011.

[64] E. J. Kirkland. *Advanced computing in electron microscopy: Second edition.* Springer, 2010.

[65] B. Fultz and J. M. Howe. *Transmission Electron Microscopy and Diffractometry of Materials.* Springer, 2001.

[66] D. Van Dyck and M. Op De Beeck. A simple intuitive theory for electron diffraction. *Ultramicroscopy*, 64:99–107, 1996.

[67] D. B. Williams and C. B. Carter. Transmission electron microscopy: a textbook for materials science., 2009.

[68] O. L. Krivanek, G. J. Corbin, N. Dellby, B. F. Elston, R. J. Keyse, M. F. Murfitt, C. S. Own, Z. S. Szilagyi, and J. W. Woodruff. An electron microscope for the aberration-corrected era. *Ultramicroscopy*, 108:179–195, 2008.

[69] 0. Scherzer. Über einige Fehler von Elektronenlinsen. *Zeitschrift für Physik*, 101(9-10):593–603, 1936.

[70] M. Born and E. Wolf. *Principles of Optics.* 2001.

[71] O. L. Krivanek, N. Dellby, A. J. Spence, R. A. Camps, and L. M. Brown. Aberration correction in the STEM. *Institute of Physics Conference Series*, 153:35–40, 1997.

[72] M. Haider, S. Uhlemann, and J. Zach. Upper limits for the residual aberrations of a high-resolution aberration-corrected STEM. *Ultramicroscopy*, 81(3-4):163–175, 2000.

[73] O. L. Krivanek, N. Dellby, R. J. Keyse, M. F. Murfitt, C. S. Own, and Z. S. Szilagyi. Advances in aberration-corrected scanning transmission electron microscopy and electron energy-loss spectroscopy. *Advances in Imaging and Electron Physics: Aberration-corrected Electron Microscopy*, 153:121, 2009.

[74] H. Rose. Correction of aberrations, a promising means for improving the spatial and energy resolution of energy-filtering electron microscopes. *Ultramicroscopy*, 56:11–25, 1994.

[75] A. V. Crewe and D. Kopf. Limitations of sextupole correctors. *Optik*, 56(4):391–399, 1980.

[76] H. Rose. Outline of a spherically corrected semiaplanatic medium-voltage transmission electron microscope. *Optik*, 85:19–24, 1990.

[77] H. Müller, S. Uhlemann, P. Hartel, and M. Haider. Advancing the Hexapole Cs-Corrector for the Scanning Transmission Electron Microscope. *Microscopy and Microanalysis*, 12(6):442–455, 2006.

[78] D. A. Muller, L. Fitting Kourkoutis, M. Murfitt, J. H. Song, H. Y. Hwang, J. Silcox, N. Dellby, and O. L. Krivanek. Atomic-scale chemical imaging of composition and bonding by aberration-corrected microscopy. *Science*, 319(5866):1073–6, 2008.

[79] F. Zemlin, K. Weiss, P. Schiske, W. Kunath, and K. Herrmann. Coma-free alignment of high resolution electron microscopes with the aid of optical diffractograms. *Ultramicroscopy*, 3:49–60, 1978.

[80] S. Uhlemann and M. Haider. Residual wave aberrations in the first spherical aberration corrected transmission electron microscope. *Ultramicroscopy*, 72:109–119, 1998.

[81] V. Intaraprasonk, H. L. Xin, and D. A. Muller. Analytic derivation of optimal imaging conditions for incoherent imaging in aberration-corrected electron microscopes. *Ultramicroscopy*, 108:1454–1466, 2008.

[82] O. L. Krivanek, P. D. Nellist, N. Dellby, M. F. Murfitt, and Z. Szilagyi. Towards sub-0.5 A electron beams. *Ultramicroscopy*, 96:229–237, 2003.

[83] C. Dwyer, R. Erni, and J. Etheridge. Method to measure spatial coherence of subangstrom electron beams. *Applied Physics Letters*, 93(2):021115, jul 2008.

[84] A. Amali and P. Rez. Theory of Lattice Resolution in High-angle Annular Dark-field Images. *Microsc. & Microanal.*, 3(1):28–46, 1997.

[85] K. Watanabe, T. Yamazaki, I. Hashimoto, and M. Shiojiri. Atomic-resolution annular dark-field STEM image calculations. *Physical Review B*, 64(11):115432, 2001.

[86] A. Rosenauer and M. Schowalter. STEMSIM - a new software tool for simulation of STEM HAADF Z-contrast imaging. In *Microscopy of Semiconducting Materials 2007*, pages 170–172. Springer, 2008.

[87] V. Grillo and E. Rotunno. STEM_CELL: A software tool for electron microscopy: Part I simulations. *Ultramicroscopy*, 125:97–111, 2013.

[88] I. Lobato, S. van Aert, and J. Verbeeck. Progress and new advances in simulating electron microscopy datasets using MULTEM. *Ultramicroscopy*, 168:17–27, 2016.

[89] J. O. Oelerich, L. Duschek, J. Belz, A. Beyer, S. D. Baranovskii, and K. Volz. STEMsalabim: A high-performance computing cluster friendly code for scanning transmission electron microscopy image simulations of thin specimen. *Ultramicroscopy*, 177:91–96, 2017.

[90] K. Kuramochi, T. Yamazaki, Y. Kotaka, M. Ohtsuka, I. Hashimoto, and K. Watanabe. Effect of chromatic aberration on atomic-resolved spherical aberration corrected STEM images. *Ultramicroscopy*, 110:36–42, 2009.

[91] C. L. Zheng and J. Etheridge. Measurement of chromatic aberration in STEM and SCEM by coherent convergent beam electron diffraction. *Ultramicroscopy*, 125:49–58, 2013.

[92] C. Dwyer, R. Erni, and J. Etheridge. Measurement of effective source distribution and its importance for quantitative interpretation of STEM images. *Ultramicroscopy*, 110:952–957, 2010.

[93] C. Maunders, C. Dwyer, P. C. Tiemeijer, and J. Etheridge. Practical methods for the measurement of spatial coherence - A comparative study. *Ultramicroscopy*, 111:1437–1446, 2011.

[94] J. Verbeeck, A. Beche, and W. Van den Broek. A holographic method to measure the source size broadening in STEM. *Ultramicroscopy*, 120:35–40, 2012.

[95] A. Beyer, J. Belz, N. Knaub, K. Jandieri, and K. Volz. Influence of spatial and temporal coherences on atomic resolution high angle annular dark field imaging. *Ultramicroscopy*, 169:1–10, 2016.

[96] T. G. Ramesh and S. Ramaseshan. Determination of the static displacement of atoms in a binary alloy system using anomalous scattering. *Acta Crystallographica Section A*, 27(6):569–572, nov 1971.

[97] P. N. Keating. Effect of invariance requirements on the elastic strain energy of crystals with application to the diamond structure. *Physical Review*, 145(2):637–645, 1966.

[98] O. Rubel, I. Németh, W. Stolz, and K. Volz. Modeling the compositional dependence of electron diffraction in dilute GaAs- and GaP-based compound semiconductors. *Physical Review B - Condensed Matter and Materials Physics*, 78(7):075207, aug 2008.

[99] V. Grillo. The effect of surface strain relaxation on HAADF imaging. *Ultramicroscopy*, 109:1453–1464, 2009.

[100] A. Beyer, L. Duschek, J. Belz, J. O. Oelerich, K. Jandieri, and K. Volz. Surface relaxation of strained Ga(P,As)/GaP heterostructures investigated by HAADF STEM. *Journal of Microscopy*, 268(3):239–247, 2017.

[101] A. Beyer, L. Duschek, J. Belz, K. Jandieri, and K. Volz. Influence of surface relaxation of strained layers on atomic resolution ADF imaging. *Ultramicroscopy*, 181:8–16, 2017.

[102] A. Rosenauer, D. Gerthsen, and V. Potin. Strain state analysis of InGaN/GaN - sources of error and optimized imaging conditions. *Phys. Stat. Sol. A*, 2003(1):176–184, 2006.

[103] L. J. Allen, S. D. Findlay, M. P. Oxley, and C. J. Rossouw. Lattice-resolution contrast from a focused coherent electron probe. Part I. *Ultramicroscopy*, 96(1):47–63, 2003.

[104] S. D. Findlay, L. J. Allen, M. P. Oxley, and C. J. Rossouw. Lattice-resolution contrast from a focused coherent electron probe. Part II. *Ultramicroscopy*, 96:65–81, 2003.

[105] F. F. Krause, D. Bredemeier, M. Schowalter, T. Mehrtens, T. Grieb, and A. Rosenauer. Using molecular dynamics for multislice TEM simulation of thermal diffuse scattering in AlGaN. *Ultramicroscopy*, 189:124–135, 2018.

[106] R. F. Loane, P. Xu, and J. Silcox. Thermal vibrations in convergent-beam electron diffraction. *Acta Crystallographica Section A*, 47(3):267–278, 1991.

[107] D. A. Muller, B. Edwards, E. J. Kirkland, and J. Silcox. Simulation of thermal diffuse scattering including a detailed phonon dispersion curve. *Ultramicroscopy*, 86:371–380, 2001.

[108] M. Schowalter, A. Rosenauer, J. T. Titantah, and D. Lamoen. Computation and parametrization of the temperature dependence of Debye-Waller factors for group IV, III-V and II-VI semiconductors. *Acta Crystallographica Section A*, 65:5–17, 2009.

[109] V. Grillo. An advanced study of the response of ADF detector. *Journal of Physics: Conference Series*, 326(1), 2011.

[110] K. E. MacArthur, L. Jones, and P. D. Nellist. How flat is your detector? Non-uniform annular detector sensitivity in STEM quantification. *Journal of Physics: Conference Series*, 522(1):012018, 2014.

[111] L. Jones, A. Varambhia, H. Sawada, and P.D. Nellist. An optical configuration for fastidious STEM detector calibration and the effect of the objective-lens pre-field. *Journal of Microscopy*, 00(0):1–12, 2018.

[112] J. M. LeBeau and S. Stemmer. Experimental quantification of annular dark-field images in scanning transmission electron microscopy. *Ultramicroscopy*, 108(12):1653–1658, nov 2008.

[113] K. E. MacArthur, A. J. D'Alfonso, D. Ozkaya, L. J. Allen, and P. D. Nellist. Optimal ADF STEM imaging parameters for tilt-robust image quantification. *Ultramicroscopy*, 156:1–8, 2015.

[114] S. E. Maccagnano-Zacher, K. A. Mkhoyan, E. J. Kirkland, and J. Silcox. Effects of tilt on high-resolution ADF-STEM imaging. *Ultramicroscopy*, 108:718–726, 2008.

[115] T. Yamazaki, K. Watanabe, N. Nakanishi, and I. Hashimoto. Role of surface amorphous film in high-resolution high-angle annular dark field STEM imaging. *Ultramicroscopy*, 99(2-3):125–135, 2004.

[116] K. A. Mkhoyan, S. E. Maccagnano-Zacher, E. J. Kirkland, and J. Silcox. Effects of amorphous layers on ADF-STEM imaging. *Ultramicroscopy*, 108:791–803, 2008.

[117] T. Grieb, M. Tewes, M. Schowalter, K. Müller-Caspary, F. F. Krause, T. Mehrtens, J. M. Hartmann, and A. Rosenauer. Quantitative HAADF STEM of SiGe in presence of amorphous surface layers from FIB preparation. *Ultramicroscopy*, 184:29–36, 2018.

[118] P. Kükelhan, A. Beyer, C. Fuchs, M. J. Weseloh, S. W. Koch, W. Stolz, and K. Volz. Atomic structure of 'W'-type quantum well heterostructures investigated by aberration-corrected STEM. *Journal of Microscopy*, 268(3):259–268, 2017.

[119] L. Duschek, P. Kükelhan, A. Beyer, S. Firoozabadi, J. O. Oelerich, C. Fuchs, W. Stolz, A. Ballabio, G. Isella, and K. Volz. Composition determination of semiconductor alloys towards atomic accuracy by HAADF-STEM. *Ultramicroscopy*, 200:84–96, 2019.

[120] C. Rosenblad, H. R. Deller, A. Dommann, T. Meyer, P. Schroeter, and H. von Känel. Silicon epitaxy by low-energy plasma enhanced chemical vapor deposition. *Journal of Vacuum Science & Technology A: Vacuum, Surfaces, and Films*, 16(5):2785–2790, oct 1998.

[121] S. Marchionna, A. Virtuani, M. Acciarri, G. Isella, and H. von Kaenel. Defect imaging of SiGe strain relaxed buffers grown by LEPECVD. *Materials Science in Semiconductor Processing*, 9(4-5 SPEC. ISS.):802–805, aug 2006.

[122] T.-C. Chiang, R Ludecke, and D. E. Eastman. Photoemission studies of AlGaAs(100) surfaces grown by molecular-beam epitaxy. *Physical Review B*, 25(10):6518–6521, 1982.

[123] J. Massies, F. Turco, A. Saletes, and J. P. Contour. Experimental evidence of difference in surface and bulk compositions of AlGaAs, AlInAs and GaInAs epitaxial layers grown by molecular beam epitaxy. *Journal of Crystal Growth*, 80:307–314, 1987.

[124] K. Muraki, S. Fukatsu, and Y. Shiraki. Surface segregation of In atoms during molecular beam epitaxy and its influence on the energy levels in InGaAs/GaAs quantum wells. *Applied Physics Letters*, 61(5):557–559, 1992.

[125] P. Kükelhan, A. Beyer, L. Duschek, S. Firoozabadi, J. O. Oelerich, W. Stolz, and K. Volz. Segregation at Interfaces in (GaIn)As/Ga(AsSb)/(GaIn)As-Quantum Well Heterostructures Explored by Atomic Resolution STEM. *submitted to Journal of Crystal Growth*, 2019.

[126] E. Piscopiello, A. Rosenauer, A. Passaseo, E. H. Montoya Rossi, and G. Van Tendeloo. Segregation in InGaAs/GaAs Stranski-Krastanow layers grown by metal organic chemical vapour deposition. *Philosophical Magazine*, 85(32):3857–3870, 2005.

[127] A. M. Sanchez, A. M. Beltran, R. Beanland, T. Ben, M. H. Gass, F. De La Pá^{o}œa, M. Walls, A. G. Taboada, J. M. Ripalda, and S. I. Molina. Blocking of indium incorporation by antimony in III-V-Sb nanostructures. *Nanotechnology*, 21:145606, 2010.

[128] K. Müller-Caspary, O. Oppermann, T. Grieb, F. F. Krause, A. Rosenauer, M. Schowalter, T. Mehrtens, A. Beyer, K. Volz, and P. Potapov. Materials characterisation by angle-resolved scanning transmission electron microscopy. *Scientific Reports*, 6:37146, 2016.

[129] P. Kükelhan, A. Beyer, S. Firoozabadi, T. Hepp, and K. Volz. Simultaneous determination of local thickness and composition for ternary III-V semiconductors by aberration-corrected STEM. *Ultramicroscopy*, 2019.

[130] A. Beyer, N. Knaub, P. Rosenow, K. Jandieri, P. Ludewig, L. Bannow, S. W. Koch, R. Tonner, and K. Volz. Local Bi ordering in MOVPE grown Ga(As,Bi) investigated by high resolution scanning transmission electron microscopy. *Applied Materials Today*, 6:22–28, 2017.

[131] N. Balades, M. Herrera, D. L. Sales, M. P. Guerrero, E. Guerrero, P. L. Galindo, and S. I. Molina. Influence of the crosstalk on the intensity of HAADF-STEM images. *Journal of Microscopy*, 273(1):81–88, 2019.

[132] P. Kükelhan, T. Hepp, S. Firoozabadi, A. Beyer, and K. Volz. Composition determination for quaternary III-V semiconductors by aberration-corrected STEM. *submitted to Ultramicroscopy*, 2019.

[133] A. De Backer, A. De wael, J. Gonnissen, and S. Van Aert. Optimal experimental design for nano-particle atom-counting from high-resolution STEM images. *Ultramicroscopy*, 151:46–55, 2015.

Zusammenfassung

Quantitative Rastertransmissionselektronenmikroskopie (STEM) kann die Entwicklung von modernen Halbleiterbauelementen mit atomar aufgelösten strukturellen Informationen unterstützen. Die Auswertung kann nur auf STEM Bildintensitäten, einer Kombination von STEM Bildintensitäten mit anderen Methoden und dem Vergleich von STEM Bildintensitäten mit Bildsimulationen beruhen.

Basierend auf STEM Bildintensitäten können Halbleiter-Heterostrukturen wie die hier betrachtete „W"-Struktur quantitativ untersucht werden. Wenn diese Bildintensitäten mit Konzentrationen aus Röntgenbeugung kombiniert werden, können einfache Konzentrationsprofile berechnet werden.

Mit höherer Genauigkeit und mit zweidimensionaler atomarer Auflösung kann die Komposition auch nur basierend auf STEM-Ergebnissen bestimmt werden, ohne Annahmen aus anderen Methoden hinzuzuziehen. Der dominante Z-Kontrast von STEM-Bildern ermöglicht die Kompositionsbestimmung durch den direkten Vergleich von Bildsimulationen und experimentellen Ergebnissen. Mit diesen genaueren Konzentrationsprofilen kann insbesondere die Oberflächensegregation an Grenzflächen in Heterostrukturen untersucht werden. Für die „W"-Strukturen ergab diese Untersuchung eine starke Wechselwirkung von In und Sb während des Wachstums mit metallorganischer Gasphasenepitaxie. Diese Wechselwirkung führt zu einer Änderung der Grenzflächen im Vergleich zu $GaAs$-Grenzflächen.

Das Ziel der quantitativen STEM ist es, Atome zu lokalisieren, zu zählen und zu unterscheiden. Für ternäre III-V Halbleiter ist die Kompositionsbestimmung durch STEM bereits etabliert. Diese wird hinsichtlich einer möglichen atomgenauen Kompositionsbestimmung weiterentwickelt. Inwieweit diese Möglichkeit besteht, kann mit Bildsimulationen untersucht werden. Die Wahrscheinlichkeit, die Komposition einer Atomsäule atomgenau richtig zu bestimmen, ist statistisch festgelegt: Eine gegebene Anzahl an Austauschatomen in einer Atomsäule kann zu einer Verteilung von STEM-Intensitäten mit gewisser Breite führen. Die Ursache dieser Verteilung sind die vielen verschiedenen Möglichkeiten zur Anordnung dieser Atome in der Atomsäule. Daher wird die Wahrscheinlichkeit für die richtige Kompositionsbestimmung durch die Kompo-

sition und die Dicke der Atomsäule beeinflusst. Beides erhöht die Anzahl der Anordnungsmöglichkeiten und verringert damit die Wahrscheinlichkeit, die Komposition der Atomsäule richtig zu bestimmen. Außerdem wird diese Wahrscheinlichkeit durch das untersuchte Materialsystem beeinflusst. Hier ist der Unterschied der Ordnungszahlen zwischen Austausch- und Matrixatom entscheidend. Da aber technologisch relevante Proben untersucht werden, sind das Materialsystem und seine Komposition durch die Anforderungen an das jeweilige Bauelement bereits vorgegeben. Damit bleibt nur die Probendicke als freier Parameter, der durch die Probenpräparation festgelegt wird. Die Probenpräparation muss außerdem eine gute Qualität der Proben sicherstellen, d.h. insbesondere geringe Oberflächenschäden.

Während die Komposition einer Atomsäule mit einer gewissen Wahrscheinlichkeit richtig bestimmt wird, ist die Genauigkeit der Kompositionsbestimmung für viele Atomsäulen sehr gut. Lokale statistische Abweichungen heben sich gegenseitig auf und führen zu einer genauen Bestimmung der Gesamtkomposition. Experimentell werden meistens viele Atomsäulen untersucht, sodass die Gesamtkomposition korrekt ist.

Um die Atome in einer Atomsäule unterscheiden zu können, muss man zuerst ihre Anzahl kennen. Da STEM die effektive Ordnungszahl einer Atomsäule untersucht, können Komposition und Dicke den gleichen Einfluss auf die Bildintensität haben. Eine falsche Annahme über die Dicke der Atomsäule verhindert eine genaue Kompositionsbestimmung. Daher ist es notwendig, die lokale Dicke einer Probe zu kennen. Typischerweise wird die Dicke einer zu untersuchenden Schicht aus Schichten bekannter Komposition interpoliert. Dies führt aber offensichtlich zu lokalen Ungenauigkeiten. In dieser Arbeit wird eine Methode gezeigt, mit der für ternäre III-V Halbleiter Dicke und Komposition aus nur einem STEM-Bild lokal bestimmt werden können. Hierbei werden sowohl die Kristallstruktur in [010]-Richtung als auch Wissen über Streueffekte aus Bildsimulationen ausgenutzt. Dicke und Komposition können auf diese Weise iterativ bestimmt werden.

Da Dicke und Komposition den gleichen Einfluss auf die Bildintensität haben können, kann das Prinzip dieser Methode auch für quaternäre III-V Halbleiter mit zwei Elementen auf jedem Untergitter benutzt werden. Dafür muss die Dicke allerdings wieder interpoliert oder auf eine andere Art und Weise bestimmt werden. Das Wissen über Streueffekte aus Simulationen sowie die Intensität beider Untergitter können zusammen für eine iterative Kompositionsbestimmung genutzt werden.

Der Winkelbereich des STEM-Detektors kann für die Kompositionsbestimmung optimiert werden. Eine detaillierte Untersuchung der Winkelbereiche der Elektronenstreuung bietet viele Verbesserungs- und Entwicklungsmöglichkeiten und wird insbesondere

durch die verfügbaren experimentellen Geräte wie einen ortsaufgelösten Detektor begünstigt. Dadurch kann nicht nur die Kompositionsbestimmung für bereits in dieser Arbeit untersuchte Materialsysteme verbessert, sondern auch für andere III/V-Halbleiter oder kristalline Materialien mit unbekannter Zusammensetzung ermöglicht werden.

Nomenclature

ADF	annular dark field
CBED	convergent beam electron diffraction
CCD	charged coupled device
fcc	face centered cubic
MOVPE	metal organic vapor phase epitaxy
NN	next neighbor
OL	objective lens
PL	photo-luminescence
QW	quantum well
QWH	quantum well heterostructure
STEM	scanning transmission electron microscopy
TDS	thermal diffuse scattering
TEM	transmission electron microscopy
XRD	X-ray diffraction

List of Figures

List of Tables

Danksagung

Ich möchte allen Personen danken, die mich im Laufe dieser Arbeit unterstützt und damit zum Gelingen beigetragen haben. Besonders bedanken möchte ich mich bei

... Prof. Dr. Kerstin Volz für die Möglichkeit der Promotion in ihrer Arbeitsgruppe, die Betreuung während der Arbeit und die immer entspannte Atmosphäre. Darüber hinaus bin ich für die Teilnahme an zahlreichen (internationalen) Konferenzen dankbar.

... Prof. Dr. Wolfram Heimbrodt für die freundliche Übernahme des Zweitgutachtens.

... Prof. Dr. Florian Gebhard für die Vervollständigung der Prüfungskommission.

... Dr. Andreas Beyer für die tägliche Betreuung, fortlaufende Diskussionen und Hilfe. Außerdem möchte ich mich für das Korrekturlesen dieser Arbeit bedanken.

... Dr. Jan Oliver Oelerich und Dr. Kakhaber Jandieri für Hilfe in allen Belangen der Simulationen und die Bereitstellung der Infrastruktur.

... Thilo Hepp, Dr. Christian Fuchs und Prof. Dr. Wolfgang Stolz für die Bereitstellung der untersuchten Proben, die gute Zusammenarbeit und die Diskussionen zur Epitaxie.

... Lennart Duschek für die gute Zusammenarbeit und die Unterstützung in Sachen Simulationen, insbesondere ClusterUtils.

... Jürgen Belz für Hilfe und Tipps zu zahlreichen Fragestellungen der TEM.

... Saleh Firoozabadi for the good collaboration and his readiness to help.

... all guys in my office for contributing to the good working atmosphere.

... Celina Becker und Michael Hellwig TEM-seitig, aber auch Stefan Reinhard und Thomas Ochs für die technische Unterstützung.

... Elke Vaupel, Marina Koch, Isabelle Kimmel und Marieke Sycha für die Übernahme aller organisatorischen Aufgaben.

... all members of our international group for the nice atmosphere and the good times I had with the group.

... Jule, meinen Eltern und meiner ganzen Familie für ihre Unterstützung.